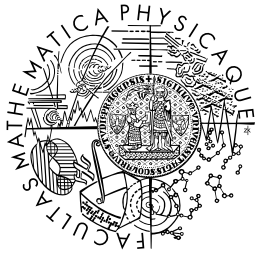

FACULTY
OF MATHEMATICS
AND PHYSICS
Charles University

DOCTORAL THESIS

Michal Karamazov

Gravitational Lensing by Substructures in Dark Matter Halos

Institute of Theoretical Physics

Supervisor of the doctoral thesis: doc. Mgr. David Heyrovský, Ph.D.

Study programme: Physics

Study branch: Theoretical Physics, Astronomy and Astrophysics

Prague 2022

I declare that I carried out this doctoral thesis independently, and only with the cited sources, literature and other professional sources. It has not been used to obtain another or the same degree.

I understand that my work relates to the rights and obligations under the Act No. 121/2000 Sb., the Copyright Act, as amended, in particular the fact that the Charles University has the right to conclude a license agreement on the use of this work as a school work pursuant to Section 60 subsection 1 of the Copyright Act.

In ..... date ....

Author's signature

I wish to thank my supervisor David Heyrovský for guiding my work, for all kinds of support, and friendly collaboration in general.

Work on the thesis was supported by Charles University Grant Agency project GA UK 1000218.

Title: Gravitational Lensing by Substructures in Dark Matter Halos

Author: Michal Karamazov

Institute: Institute of Theoretical Physics

Supervisor: doc. Mgr. David Heyrovský, Ph.D., Institute of Theoretical Physics

Abstract: Gravitational lensing serves as an invaluable tool for studying the distribution of matter in the universe. This matter is predominantly dark and clumped into centrally concentrated hierarchically structured halos of galaxies and galaxy clusters. Early comparisons suggested discrepancies between the high population of substructures predicted by cosmological simulations and the lack of corresponding observational data. More recently, a major discrepancy in the opposite sense was reported from analyses of lensing galaxy clusters: the lensing efficiency of their substructures was found to be much higher than predictions based on cosmological simulations. In this thesis, we examine gravitational lensing by substructures embedded in dark-matter halos with Navarro—Frenk—White (NFW) density profiles. We start by a detailed investigation of a simple model with a single point mass perturbing the halo. Using analytical methods, we study its critical curves, caustics and their transitions. Next, we explore the geometry of lensed images and the weak-lensing characteristics of the same simple model, developing novel ways of their visualization. Finally, we construct a more realistic lens model of a galaxy cluster consisting of an ellipsoidal cluster halo combined with a population of truncated ellipsoidal galaxy halos. For both types of halos we present analytical deflection-angle formulae. We choose parameters of the galaxy cluster based on observations and cosmological simulations. We generate source-plane and image-plane maps of the shear, phase and other lensing quantities and discuss them, applying insights derived from our study of the simpler model. The developed code can be used for advanced modeling and detailed studies of cluster lensing, which may possibly indicate routes toward resolving the substructure lensing-efficiency discrepancy.

Keywords: gravitational lensing, galaxy clusters, dark matter halos

Contents

1. Introduction

In 1915 Albert Einstein published his general theory of relativity, which describes spacetime as being curved by the presence of its matter content. Objects including light then propagate along geodesics. These are curves that generalise the notion of a straight line for the case of a curved space. In simple terms, massive objects bend light rays. This phenomenon was first observed by Sir Arthur Eddington in 1919 (Dyson et al. 1920), who measured an apparent change in the positions of stars close to the eclipsed sun. Since his experimental results were in agreement with the quantitative prediction of general relativity, it is considered the first major experimental success of Einstein's great theory.

Later in the 1930s it was proposed (Einstein 1936, Zwicky 1937), that sufficiently massive and compact astrophysical objects could be used to observe more distant suitably positioned sources of light. Therefore, these massive objects would effectively act as *gravitational lenses* forming images of background sources, affecting their position, shape, brightness and even breaking the wavefront of the incoming radiation and thus creating multiple images of a single source. The theory was later developed by Refsdal (1964) and since the first observation of a multiply imaged quasar (Walsh et al. 1979) gravitational lensing has become an invaluable astronomical tool and, due to the progress in imaging technology, it is now extensively used to examine a broad spectrum of astrophysical and cosmological phenomena.

Three distinct modes of gravitational lensing are studied. In *strong lensing*, lenses are massive and concentrated enough to distort the images of distant sources in a highly non-linear fashion, potentially forming multiple images, long arcs or other spectacular shapes. In *weak lensing*, the projected mass density and other related quantities of the lens have low values and linearised lens equations thus hold sufficiently well. Only mildly distorted and reoriented images of background sources are then observed. When the shapes and orientations of a substantial number of these images are measured and statistically processed, they can be used to compute the projected matter distribution in the lens. The third regime of gravitational lensing is called *microlensing*. In this case, no change in the position or shape of the images can be discerned. However, its brightness changes over time non-trivially, as the microlensing object passes between the source and the observer.

All three modes of gravitational lensing (but mostly strong and weak) are being used in the astrophysical context of galaxy clusters. Already by the end of the 18th century, Charles Messier noticed that what he back then called "nebulae" tend to cluster together (Messier 1781). Of course today we know that many of his "nebulae" are actually distant galaxies. Important progress in the study of galaxy clusters was made in 1950s when the extensive Abell catalogue with 1,682 clusters was composed (Abell 1958). A typical cluster consists of hundreds of galaxies and its mass is circa 10^{15} solar masses ($M_\odot$). However, a vast majority of this mass is not contained in the individual galaxies. Roughly 85% of cluster mass is in the form of a dark matter halo, around 10% amounts to hot intracluster gas radiating in the X-ray spectrum and the individual galaxies make up only less then 5%. Most of the matter in galaxy clusters thus cannot be directly observed.

Figure 1.1: Galaxy cluster Abell S1063. Many thin arc-shaped tangentially oriented images and several multiple images of background galaxies are visible. Source: Hubble Frontier Field program.

This is where gravitational lensing comes into play as the light from the galaxies that lie in the background gets deflected by the *total mass* distribution in the cluster. This provides an excellent opportunity to survey the distribution and properties of the dark matter.

In the rest of this chapter, we present brief overviews of fundamental concepts of gravitational lensing theory, the phenomenology of dark matter halos and gravitational lensing studies of dark matter halos.

1.1 Fundamentals of gravitational lensing

Gravitational lensing occurs when the light-emitting source and the massive lensing object are aligned along the line of sight of the observer. A rigorous and precise study of such a configuration would require to compute the propagation of electromagnetic waves in the spacetime dynamically curved by its matter content. This is a daunting task. Thankfully, several reasonable assumptions and approximations can be made to formulate an elegant theory of gravitational lensing feasible for practical computations. Detailed overview of the theory and its many applications was provided in several comprehensive books including, e.g., Schneider et al. (1992, 2006) or Congdon and Keeton (2018).

The assumptions and approximations are the following. Instead of propagating waves, light is described in the framework of geometric optics as rays and

bundles of rays travelling from the source to the lens and from the lens to the observer along straight lines if distances are sufficiently small, or along appropriate photon geodesics in cases where cosmology must be taken into account. The so-called thin lens approximation is also employed and the *lens* L is modeled as a two-dimensional density distribution limited to a single *lens plane* (also called *image plane*) perpendicular to the line of sight of the *observer* O. It is then only at the intersection with this plane that the light ray gets deflected. The projected two-dimensional density distribution can be computed from the three-dimensional density by integrating along the line of sight.

There are three important angles used to describe the typical lensing scenario, which can be seen in Figure 1.2. The angle $\boldsymbol{\beta}$ denotes the angular position where the *source* S is located from the lens, as it would be seen by the observer in absence of light deflection. The angle $\boldsymbol{\theta}$ denotes the position where the observer sees an image I of the source. Finally, $\boldsymbol{\alpha}$ denotes the angle by which the light ray is deflected at the lens plane. These angles are assumed to by very small, so that their trigonometric functions can be approximated by their linear expansions.

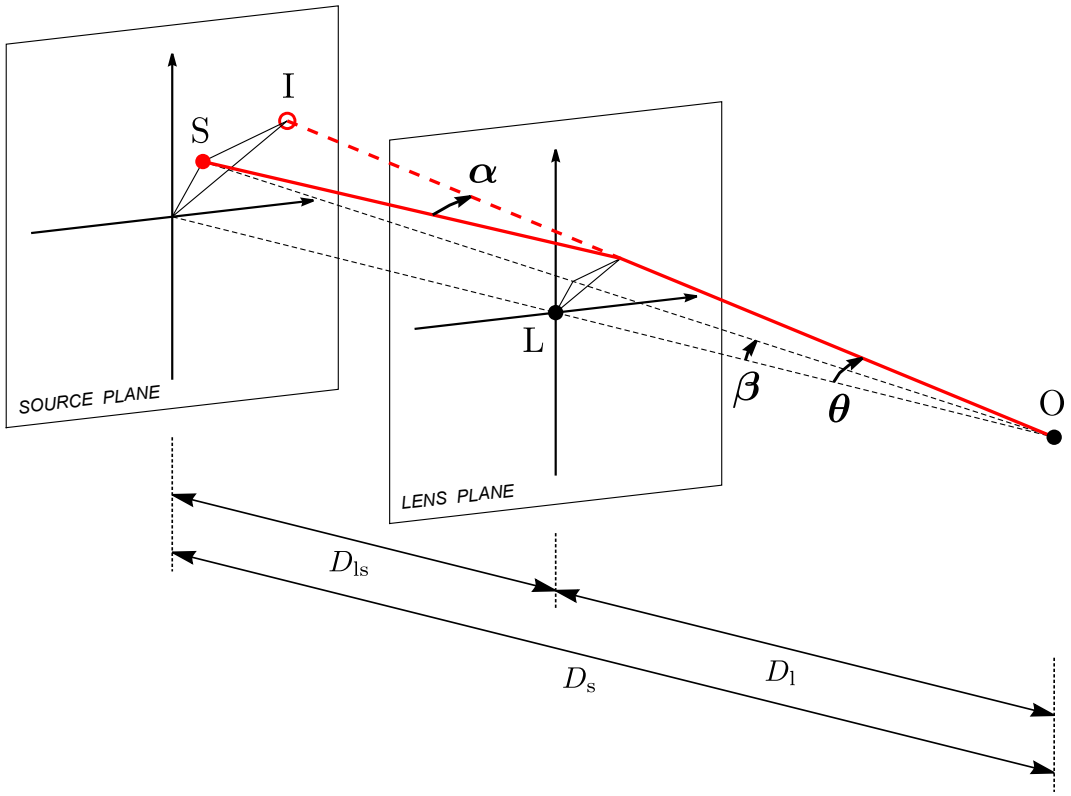

Figure 1.2: Layout of a typical lensing scenario. The observer O is observing the source S that is located at the angular position $\boldsymbol{\beta}$. However, as the incoming light is deflected by the angle $\boldsymbol{\alpha}$ due to the lens L, the observer actually sees image I at the angular position $\boldsymbol{\theta}$. The source lies in the source plane and the thin lens is located in the lens plane. These lie at distances D_s and D_l from the observer, respectively. D_{ls} denotes the distance between both planes. The figure is adapted with permission from Heyrovský (2021).

Finally, a quasi-static configuration is assumed with the relative velocities of observer, lens and source being non-relativistic.

Using the approximations just mentioned, it can be shown that angles $\boldsymbol{\alpha}$, $\boldsymbol{\beta}$ and $\boldsymbol{\theta}$ are related by the *lens equation*

$$\boldsymbol{\beta} = \boldsymbol{\theta} - \frac{D_{\mathrm{ls}}}{D_{\mathrm{s}}}\,\boldsymbol{\alpha}(\boldsymbol{\theta})\,. \tag{1.1}$$

Here D_{s} and D_{ls} are the distances from the observer to the *source plane* and from the lens plane to the source plane, respectively (see Figure 1.2). We also use D_{l} to denote the distance from the observer to the lens plane. These are angular diameter distances and in general they are not additive. Equation (1.1) is the explicit expression of the angular position of the source in terms of the angular position of its image. To get the position of the image from the position of the source, one has to solve the equation for $\boldsymbol{\theta}$. In general, there may be multiple solutions representing different observed images of a single source.

The well-known Schwarzschild solution to the Einstein equation can be used to derive the deflection angle $\boldsymbol{\alpha}$ of the simplest possible gravitational lens – the point mass lens,

$$\boldsymbol{\alpha}(\boldsymbol{\theta}) = \frac{4\,G\,M}{c^2\,D_{\mathrm{l}}}\,\frac{\boldsymbol{\theta}}{\theta^2}\,, \tag{1.2}$$

where G is the gravitational constant, c is the speed of light and M is the mass of the point lens. To obtain the deflection angle of a spatially extended gravitational lens, one has to integrate over the lens plane,

$$\boldsymbol{\alpha}(\boldsymbol{\theta}) = \frac{1}{\pi}\,\frac{D_{\mathrm{s}}}{D_{\mathrm{ls}}}\int \kappa(\boldsymbol{\theta}')\,\frac{\boldsymbol{\theta}-\boldsymbol{\theta}'}{|\boldsymbol{\theta}-\boldsymbol{\theta}'|^2}\,\mathrm{d}^2\boldsymbol{\theta}'\,. \tag{1.3}$$

The *convergence* κ is defined using the two-dimensional mass density Σ, which can be obtained by the integration of three-dimensional density ρ of the lens along the line of sight,

$$\kappa(\boldsymbol{\theta}) = \frac{\Sigma(\boldsymbol{\theta})}{\Sigma_{\mathrm{cr}}}\,. \tag{1.4}$$

The critical density Σ_{cr} is merely a constant factor given by the combination of distances,

$$\Sigma_{\mathrm{cr}} = \frac{c^2}{4\pi G}\,\frac{D_{\mathrm{s}}}{D_{\mathrm{l}}\,D_{\mathrm{ls}}}\,. \tag{1.5}$$

The form of Equation (1.3) is analogous to those of Newton's law of gravitation or Coulomb's law of electrostatics. This analogy can be extended further and the *lensing potential* ψ can be introduced. The deflection angle can then be expressed as its gradient,

$$\boldsymbol{\alpha}(\boldsymbol{\theta}) = \frac{D_{\mathrm{s}}}{D_{\mathrm{ls}}}\,\nabla_{\boldsymbol{\theta}}\,\psi(\boldsymbol{\theta})\,, \tag{1.6}$$

while the potential itself is the solution to the two-dimensional Poisson's equation with the convergence on the right hand side,

$$\Delta\psi(\boldsymbol{\theta}) = 2\,\kappa(\boldsymbol{\theta})\,. \tag{1.7}$$

One of the most important quantities in the study of gravitational lensing is the Jacobian matrix the lens equation,

$$J(\boldsymbol{\theta}) = \frac{\partial\,\boldsymbol{\beta}}{\partial\,\boldsymbol{\theta}} \tag{1.8}$$

and its determinant $\det J(\boldsymbol{\theta})$. The inverse of the absolute value of this determinant, $|\det J(\boldsymbol{\theta})|^{-1}$, is the magnification or amplification of an infinitesimal source observed at the image-plane position $\boldsymbol{\theta}$. To compute the total amplification of such a source, one has to sum amplifications associated with each of its images formed by the lens

$$A(\boldsymbol{\beta}) = \sum_i |\det J(\boldsymbol{\theta}_i)|^{-1} \,. \tag{1.9}$$

One of the ways to obtain the source-plane amplification map $A(\boldsymbol{\beta})$, and the one that we will be using in the following chapters, is inverse ray shooting (Kayser et al. 1986). In this method, a high number of light-rays is randomly sampled in the image plane and followed back to the source plane using the lens equation, where they are binned and counted in a pixel grid.

Zero contours of the Jacobian determinant,

$$\det J(\boldsymbol{\theta}) = 0, \tag{1.10}$$

are called *critical curves*. These curves represent positions in the image plane, where amplification diverges to infinity. Of course such a concept is not strictly physical as it pertains only to amplification of an infinitesimal point source, while real sources are spatially extended. Nevertheless, images that appear along critical curves are in general extremely amplified, magnified and deformed. The critical curves are images of *caustics*. Caustics are curves in the source plane, that can be obtained by projecting critical curves back to the source plane using the lens equation. In addition to their relation to the amplification divergence they also represent important boundaries in the source plane, at which the number of observed images changes by two, if the point source crosses them.[1]Caustics, their topology and their metamorphoses are of particular interest in the context of gravitational microlensing and the apparatus of catastrophe theory is usually employed to study them.

It is often useful to decompose the Jacobian matrix of the lens equation as

$$J(\boldsymbol{\theta}) = \frac{\partial\,\boldsymbol{\beta}}{\partial\,\boldsymbol{\theta}} = \begin{pmatrix} 1-\kappa-\gamma\cos 2\varphi & -\gamma\sin 2\varphi \\ -\gamma\sin 2\varphi & 1-\kappa+\gamma\cos 2\varphi \end{pmatrix} , \tag{1.11}$$

where the already mentioned convergence $\kappa(\boldsymbol{\theta})$ as well as *shear* $\gamma(\boldsymbol{\theta})$ and *phase* $\varphi(\boldsymbol{\theta})$ can be expressed in terms of the second derivatives of the lens potential,

$$\kappa = \frac{\psi_{,11} + \psi_{,22}}{2} \,, \tag{1.12}$$

$$\gamma\,(\cos 2\varphi,\, \sin 2\varphi) = \left(\frac{\psi_{,11} - \psi_{,22}}{2},\, \psi_{,12} \right) . \tag{1.13}$$

Subsequently, the Jacobian determinant can then be expressed as

$$\det J(\boldsymbol{\theta}) = [\,1 - \kappa(\boldsymbol{\theta}) - \gamma(\boldsymbol{\theta})\,]\;[\,1 - \kappa(\boldsymbol{\theta}) + \gamma(\boldsymbol{\theta})\,] \,. \tag{1.14}$$

[1]However, in Appendix A.2 we describe and discuss a peculiar exception to this rule, that we have encountered in our inquiry.

The Jacobian matrix can also be used to formulate the linear approximation of the lens equation. Assuming a small source centered at $\boldsymbol{\beta}_0$ with an image centered at $\boldsymbol{\theta}_0$ the lens equation can be expanded to the linear order as

$$\boldsymbol{\beta} - \boldsymbol{\beta}_0 \approx J(\boldsymbol{\theta}_0)(\boldsymbol{\theta} - \boldsymbol{\theta}_0) \tag{1.15}$$

and conversely

$$\boldsymbol{\theta} - \boldsymbol{\theta}_0 \approx \mathbb{A}(\boldsymbol{\theta}_0)(\boldsymbol{\beta} - \boldsymbol{\beta}_0)\,, \tag{1.16}$$

where $\mathbb{A}(\boldsymbol{\theta})$ is the inverse to the lens-equation Jacobian matrix

$$\mathbb{A}(\boldsymbol{\theta}) = \frac{1}{(1-\kappa)^2 - \gamma^2} \begin{pmatrix} 1 - \kappa + \gamma\cos 2\varphi & \gamma \sin 2\varphi \\ \gamma \sin 2\varphi & 1 - \kappa - \gamma \cos 2\varphi \end{pmatrix}. \tag{1.17}$$

The Equations (1.15, 1.16) hold for sufficiently small deviations of $\boldsymbol{\beta}$ and $\boldsymbol{\theta}$. In Section 3.2.3 we discuss in detail the eigendecomposition of matrix $\mathbb{A}(\boldsymbol{\theta})$ and how it relates to the geometry of images of small circular sources. In this linear regime, the images of such sources are small ellipses. Their semi-axes are given by the eigenvalues and the orientation of the ellipse by the eigenvectors of $\mathbb{A}(\boldsymbol{\theta})$. In weak lensing surveys, the lengths of semi-axes a, b of numerous background-galaxy images are measured and used to estimate the shear,

$$1 - b/a \;=\; 1 - \frac{1-\kappa-\gamma}{1-\kappa+\gamma} \;\simeq\; 2\,\gamma\,. \tag{1.18}$$

A distribution of shear estimated in this way, which we call *weak shear* (see Section 3.2.4), together with orientations of images can, after statistical processing and adjustment for intrinsic shapes of source galaxies, be used to compute an estimate of the convergence κ, which yields the projected matter distribution in the lens. A direct approach for obtaining the convergence from the shear was devised by Kaiser and Squires (1993). The Fourier transform of Equation (1.13) is used to express the Fourier transform of Equation (1.12). The obtained Fourier image of the convergence κ is then transformed back into real space.

1.2 Dark matter halos

At present time, the most widely accepted physical model of the universe and its content is the ΛCDM model. Greek letter Λ denotes the cosmological constant of Einstein's equations representing the dark energy, which is thought to dominate the current universe constituting roughly 68% of its content (Planck Collaboration et al. 2016). The abbreviation CDM means *cold dark matter*. Although directly unobservable, it makes up 26% of the universe's content, while everyday baryonic matter makes only 5%. The dark matter, or shortly DM, is being indirectly observed already since 1920s (Kapteyn 1922, Zwicky 1933) – first in the form of unexpected stellar and galactic motions – and today it constitutes an integral part of our understanding of galaxies, structure formation, cosmic microwave background anisotropies, Big Bang nucleosynthesis, etc. Gravitational lensing is an invaluable tool for studying dark matter, as the light gets deflected by the total mass irrespective of its nature, while most of this total mass can be attributed to dark matter. The coldness of dark matter means that its hypothetical particles move with non-relativistic velocities.

In the ΛCDM model, the universe starts with a nearly uniform power spectrum of density fluctuations. From them, structure grows in hierarchical order due to gravitational instability, meaning that smaller structures form earlier, while bigger structures form later and aggregate smaller ones. First, the primordial density fluctuations collapse along one direction forming two-dimensional sheets or, in other words, "Zel'dovich pancakes" (Zel'dovich 1970). These then collapse further into a network of interconnected filaments separated by vast voids. This macrostructure of the universe is usually called the "cosmic web". Finally, dark matter further accretes along filaments forming halos at their intersections – roughly ellipsoidal structures of dark matter strongly concentrated towards their centers. In general, the dark matter collapses first, forming potential wells into which the baryonic matter is then attracted. An overview of structure formation in the early universe can be found for example in Peter and Uzan (2009), Lyth and Liddle (2009).

Over the past half-century, this growth of structure and the formation of dark-matter halos have been studied extensively using N-body computer simulations, in which the movement of dark-matter (macro)particles is traced from primordial fluctuations to present times. Growth of computational power allowed for a vast increase in the number of simulated particles, from 300 particles used by Peebles (1970) to reproduce the profile of the Coma cluster, to the PKDGRAV3 simulation (Potter et al. 2017) with more than 1 trillion particles. Once the simulation is complete, its resulting matter distribution can be used to find individual dark-matter halos. Several methods with varying results have been proposed for this, since the definition of a halo is necessarily somewhat arbitrary. Usually, however, a center of the halo is placed at the local minimum of the gravitational potential. The halo then consists of the dark matter within a sphere with radius r_{vir} determined according to the spherical collapse model with an average density inside the sphere being equal to the virial overdensity $\Delta_{\mathrm{vir}}(z)$ times the critical density at redshift z. The mass of such a halo is then denoted M_{vir}. Alternatively, the virial overdensity can be fixed as $\Delta = 200$, for example. In that case, the halo is then defined by a radius r_{200} and its mass M_{200}. Once halos are found in the simulation results, typically circa 80% of dark matter is present in the form of halos and only 20% remains unclustered. The properties of the halos can then be studied. A useful review of morphology of dark-matter halos formed in simulations can be found in Zavala and Frenk (2019).

During their development, halos gradually acquire more mass by gravitationally accreting surrounding smooth diffuse dark matter, by trapping and disrupting smaller halos and by merging with other halos. Those smaller halos enclosed in bigger halos are called *subhalos*. Today, halos are mostly composed of dark matter from disrupted subhalos and only roughly 15% of their mass was accreted smoothly (e.g., Wang et al. 2011). Moreover, only 10% of halo mass is gravitationally bound in its subhalos, while most of the original subhalo mass was stripped from them by the process called tidal stripping and is now part of the greater halo, in which they are embedded. The whole structure of halos, subhalos, subhalos of subhalos and so on is nearly self-similar. As per their masses, the count n of halos with mass M follows the *mass function*, which behaves approximately as (Frenk et al. 1988)

$$\frac{\mathrm{d}n}{\mathrm{d}M} \sim M^{-1.9}\,. \tag{1.19}$$

The density profiles of halos in dark-matter-only simulations are significantly centrally concentrated, forming a characteristic cusp. Asymptotically, the density at the center of the halo depends on the radial distance as $\rho(r \to 0) \sim r^{-1}$. The physical origin of this cusp is not yet fully understood. However, it was suggested (e.g., Angulo et al. 2017) that first, an even steeper $\rho \sim r^{-1.5}$ cusp forms and only then it is flattened to $\rho \sim r^{-1}$. Remarkably, the density profile of dark-matter halos appears to be universal over the vast range of halo masses (Ludlow et al. 2013).

The Navarro–Frenk–White (NFW) profile (Navarro et al. 1996, 1997) has been used to fit the dark-matter distribution in simulated halos,

$$\rho_{\mathrm{NFW}}(r) = \frac{\rho_{\mathrm{s}}}{\frac{r}{r_{\mathrm{s}}}\left(1+\frac{r}{r_{\mathrm{s}}}\right)^2}\,. \tag{1.20}$$

Here, ρ_{s} is a characteristic density of the halo and r_{s} is its scale radius. The concentration parameter c, which can then be (together with r_{s}) used as a parameter to describe the halo profile, is usually defined as $c_{200} = r_{200}/r_{\mathrm{s}}$ or $c_{\mathrm{vir}} = r_{\mathrm{vir}}/r_{\mathrm{s}}$. There is a correlation between the concentration parameter and halo mass (Navarro et al. 1997), with lighter halos being more concentrated. In the hierarchical structure formation paradigm, lower-mass halos collapsed earlier, when the universe was less expanded and its density was higher. The density of the inner regions of halos reflects the mean density of the universe at the time of their collapse (Wang et al. 2011). This explains why smaller halos tend to be more concentrated.

Other density profiles than NFW have been proposed to fit simulated halos even more closely (e.g., Einasto 1965). However, the NFW profile continues to be used as it still provides a good fit, especially close to the halo center. Moreover, it was pointed out (Newman et al. 2013) that the NFW profile is even more suitable to model the total mass distribution of galaxy clusters including the mass of baryons. This is particularly convenient for the purposes of gravitational lensing.

The three-dimensional shape of a dark-matter halo is roughly a triaxial ellipsoid. That is an ellipsoid with all three semi-axes having different lengths. Nonetheless, the inner parts of halos tend to be more prolate, and the outskirts tend to be more oblate (Vera-Ciro et al. 2011). A prolate ellipsoid has two semi-axes distinctively shorter than the third one, while an oblate ellipsoid has two semi-axes longer than the third one. Schneider (2006) uses the terms "cigars" and "hamburgers" to illustrate the prolate and oblate shapes, respectively. The inner parts of the halos were formed earlier by accretion along the filaments, thus their prolate shape. On the other hand, the outer parts formed later in a more isotropic manner. In general, more massive halos tend to be more aspherical as they formed more recently and thus retain more influence from the merger events (Despali et al. 2014).

For heavy halos of the galactic and galaxy-cluster scales, the astronomical observations are in good agreement with cosmological simulations of structure growth in terms of halo properties and abundancies. However, several discrepancies between observations and simulations were pointed out for lower-mass halos with $M \lesssim 10^{11} M_{\odot}$. A review of the research on these small-scale challenges to the ΛCDM paradigm was recently provided by Bullock and Boylan-Kolchin (2017).

Four small-scale problems are usually mentioned.

First, there is the "missing satellites" problem. By this, it is meant that simulations predict several orders of magnitude more low-mass halos than what is observed in the vicinity of the Milky Way galaxy. Naturally, it was proposed that these low-mass halos in fact do exist, but cannot be easily observed, since they aren't heavy enough to form a sufficient stellar population. This takes us directly to the second problem, which is called "too-big-to-fail", because according to the theoretical predictions, many of the these low-mass halos should still be too massive to fail to form a substantial population of stars. Third is the "core–cusp" problem. As mentioned above, halos formed in dark-matter-only simulations have the characteristic density cusp at the center. On the other hand, various observations show that at least some halos actually have a flattened central density profile or, in other words, a "core". The fourth and final problem that is usually mentioned are "satellite planes". It seems that low-mass satellite halos around Milky Way are preferentially located in a thin plane, in which they orbit. This was claimed to be incompatible with predictions.

These suggested problems of the ΛCDM cosmological model remain controversial. Some recent reviews (Zavala and Frenk 2019) consider them more or less "solved" within the ΛCDM paradigm once several important mechanisms of baryonic feedback are included in the simulations and improved observations and statistics are used. Others remain critical (Bullock and Boylan-Kolchin 2017) and propose alternative cosmologies to obtain simulation results that would be in better agreement with current observations.

In any case, gravitational lensing is an important tool for surveying the properties of dark-matter halos down to the scale of the controversial galactic satellites. These properties are difficult to study in other ways due to the nature of dark matter.

1.3 Gravitational lensing by dark matter halos of galaxies and galaxy clusters

A couple of strong-lensing methods were devised in order to indirectly observe and quantify low-mass halos that are predicted by simulations yet thought to be missing in observations. The primary goal of these methods is thus to shed more light on the "missing satellites" problem.

One of the methods is based on so called "flux-ratio anomalies". Since the magnification in multiply lensed images is determined by higher-order derivatives of the lens potential, it is highly sensitive to its perturbations. The perturbations may be caused for example by the presence of small-scale halo substructures. For a smooth mass distribution of the lens and nearby images in the vicinity of the caustic, ratios of fluxes were shown to follow an asymptotic relation, which however does not hold if sufficient substructures are positioned along the line of sight. Such anomalous flux-ratios were indeed observed (Metcalf and Madau 2001, Dalal and Kochanek 2002) and they hint at an abundance of subhalos that is in agreement with CDM simulations. On the other hand, it was also claimed (Xu et al. 2015) that the magnitudes of flux-anomalies cannot be wholly attributed to the dark-matter substructures and other effects must be in play.

Another method for detecting dark-matter substructures could use distortions of strongly lensed images. When the background galaxy acting as a source is sufficiently aligned with the dark-matter halo of a foreground lens galaxy, an image in the form of a curved arc or even an "Einstein ring" is formed. If the subhalo is located in a position that is projected onto the image, this image gets distorted slightly. The influences from hundreds of subhalos accumulate in the residual pattern of correlations in the lensed image. These correlations depend on the properties of the subhalo population. It was estimated (Li et al. 2016) that few hundred strong-lensing systems need to carefully analysed in this manner in order to possibly conclude that results disagree with the ΛCDM structure-formation predictions.

On the other end of the mass spectrum, there are galaxy-cluster halos. Galaxy clusters are the largest gravitationally bound structures formed in the present universe and due to their mass, composition and density profiles they can serve as very powerful gravitational lenses. They exhibit a wide range of lensing phenomena, which in turn can be used to measure many astrophysical and cosmological quantities (Kneib and Natarajan 2011). Lensing-based methods are widely used to reconstruct the density distributions of clusters. The galaxy clusters also serve as giant natural telescopes, allowing us to see very distant sources that would otherwise be too dim and too small to be observed.

In the strong-lensing regime, galaxy clusters create multiple images and frequently form thin arc-shaped images (Hennawi et al. 2008) of the background galaxies. The morphology of the arcs hints towards a mostly smooth and somewhat asymmetric mass distribution in clusters. The mass distribution in the central parts of the cluster is well determined by the positions and shapes of the strongly-lensed images. This fact can be practically utilised to reconstruct the density profile of the cluster. Such reconstruction is done by choosing an initial model of the lens and varying its parameters to fit the observed images. Parametric (e.g., Halkola et al. 2006) or non-parametric (e.g., Diego et al. 2005) lens models can be used for the task. Parametric models consist of predefined density profiles placed and centered at locations of peak luminosity with some parameters fixed using scaling relations. Remaining parameters are estimated during the fitting procedure. Non-parametric models involve a general density distribution on a discrete plane grid. The fitting of the lens model can be done iteratively. A simple initial model is fitted and used to predict the positions of additional images. These can then be located and used to further constrain the mass distribution. Repeating these steps leads to further refinement of the model.

Individual cluster members, i.e., galaxies and their associated subhalos, also produce strong-lensing systems. The first observed lens, the "Twin Quasar" (Walsh et al. 1979), itself is a galaxy–galaxy strong lens. By today, hundreds of such systems have been discovered and in the near future this number is expected to increase substantially thanks to upcoming large-scale imaging surveys (Metcalf et al. 2019). Surprisingly, a recent parametric strong-lensing study of 11 galaxy clusters (Meneghetti et al. 2020) indicated a stark discrepancy of the efficiency of galaxy–galaxy strong lensing between real observed clusters and those from cosmological simulations. It seems that the observed clusters posses an order of magnitude more substructures than their simulated counterparts. This discrepancy differs from the one mentioned in the previous section. While the

"missing satellites" problem indicates a lack of observed halo substructures, these new lensing results indicate the opposite. However, this remains a controversial subject. Robertson (2021) and Bahé (2021) suggest that the problem may be caused by the insufficient resolution of used simulations, while Granata et al. (2022) argue against this idea.

Once the mass distribution in the strong lensing cluster or substructure is determined, it can potentially be used to measure or constrain various cosmological parameters. The time delay between multiple images of time-dependant phenomena like supernovae or active galactic nuclei provides comparatively precise measurement of the Hubble constant H_0 (Suyu et al. 2017). Moreover, spectroscopical analysis of redshifts of many multiple images constrains the density parameters Ω_m and Ω_Λ (Golse and Kneib 2002).

Weak lensing methods can also be used to reconstruct the mass distribution in galaxy clusters. They require measuring the ellipticities and orientations of a substantial amount of weakly lensed background galaxies. After statistical processing and filtering out the influence of the intrinsic ellipticity of sources, these measurements provide image-plane maps of shear and phase. Since the observed weakly lensed images are often only a few pixels in size, special care must also be taken to adjust for the point spread function of the imaging device. Estimated maps of the weak-lensing quantities can then be used to directly compute the convergence κ representing projected density in the cluster (Kaiser and Squires 1993, Kaiser et al. 1995). Apart from these *direct* methods, several *inverse* weak-lensing methods were also devised to estimate the mass distribution in galaxy clusters. In them, the potential is varied on a grid in order to minimise a penalty function, which measures the agreement with observed image geometries. Inverse methods based on maximum likelihood (e.g., Bartelmann et al. 1996) or maximum entropy (e.g., Seitz et al. 1998) and also Bayesian and Markovian Monte Carlo methods (e.g., Jullo et al. 2007) were all used for cluster-mass reconstruction.

Although to this day many clusters were studied using the weak-lensing methods, the Bullet Cluster (1E 0657-56) remains to be the most famous of them. Clowe et al. (2004) used weak lensing to show that the Bullet Cluster is actually composed of two large total-density peaks located at the highest accumulations of cluster galaxies.. On the other hand, X-ray observations show that hot baryon gas is concentrated mostly in between them, forming a distinct shock front. The whole configuration is explained as a merger event of two sub-clusters. Their dark-matter halos that make up most of the total mass passed through each other, while their baryon-gas components collided and slowed down substantially. This observation is commonly cited as a strong evidence for the collisionless nature of dark matter.

The weak-lensing signals from multiple galaxy clusters or even individual galaxies can be stacked and processed together to reveal the mean density profiles (Okabe et al. 2013, Umetsu and Diemer 2017). The galaxy clusters that serve as inputs for these analyses are often grouped based on their properties (redshift, luminosity, etc.) to uncover relations between the shape of the density profile and these properties.

Powerful state-of-the-art methods for cluster-density reconstruction combine the advantages of both strong and weak gravitational lensing (Bradač et al. 2005, Limousin et al. 2007, Finney et al. 2018, Jauzac et al. 2018). Strongly lensed

images constrain the mass distribution near the cluster center, while weak lensing helps to resolve the halo outskirts. The fitting of such a combined model is done by minimising a penalty function, which is now a sum of a strong-lensing term, a weak-lesning term and a regularisation term used to suppress the influence of small-scale fluctuations.

Besides strong and weak lensing, microlensing is the third major mode of lensing that is being studied. Although it is not the regime typically considered in the context of galaxy clusters, some work on this subject has been done nonetheless. For example Kelly et al. (2018) investigated microlensing of an individual star in a background galaxy by the cluster caustic.

1.4 Structure of the thesis

We have seen that although gravitational lensing by dark-matter halos of galaxies and galaxy clusters is now a mature field of study, several open questions still remain that are related especially to halo substructures. In the context of galaxy clusters, this was recently demonstrated by Meneghetti et al. (2020), who have found a major discrepancy between the efficiency of the galaxy–galaxy strong lensing observed within galaxy clusters and predictions based on cosmological simulations. As already mentioned, these results remain controversial and ask for further investigation.

In this thesis, we take a bottom-up and mostly analytical approach to study dark-matter halos perturbed by substructures. We start with a lens that consists of a single point mass embedded in a continuous Navarro–Frenk–White mass distribution. Such a configuration can be used as a simplest model for an individual galaxy or subhalo in the galaxy cluster or as a dwarf halo in a galactic halo. Our analysis of this model also applies to gravitational lensing by a supermassive black hole within the galaxy halo, as already acknowledged by Mahler et al. (2022). The simplicity of the model allows for the use of analytic methods and for systematic exploration of its parameter space. We find that in terms of gravitational lensing, this seemingly simple model already exhibits unexpectedly complex properties.

Detailed analysis of this NFW lens perturbed by a point mass is the subject of the next two chapters. The content of these chapters corresponds to the content of our two papers (Karamazov et al. 2021, Karamazov and Heyrovský 2022) published in The Astrophysical Journal.

In Chapter 2, we continue the work that was initiated by Lukáš Timko in his bachelor's thesis (Timko 2017) and focus on the critical curves and caustics of the system while varying the mass and the location of the point mass within the halo. We locate boundaries in the parameter space at which caustic metamorphoses appear. An unexpectedly high number of caustic transitions of different types is present in the system. We demonstrate the existence of a critical mass of the added object, at which the radial caustics of the cluster vanish in an unusual non-local transition.

Then, in Chapter 3, our focus moves to the second derivatives of the lens potential and to the geometry of images formed by this lens. We study the shear, the phase and their weak-lensing estimates. We derive analytical expressions to explain patterns that appear in obtained plots of lensing quantities. We reveal the

relation between zero-shear points and umbilics of the caustic. We use eigenvalue-decomposition of the inverse-Jacobian matrix to asses the geometry of images and to introduce novel ways of visualisation.

In Chapter 4, we proceed to study the gravitational lensing by a more realistic model of a galaxy cluster that consists of numerous ellipsoidal truncated NFW subhalos within the main ellipsoidal NFW cluster halo. We choose the main-halo parameters based on real galaxy clusters analysed in lensing surveys and we generate parameters of the subhalos using probability distributions fitted from N-body cosmological simulations. Then, we present formulae for deflection angles of both truncated and untruncated ellipsoidal NFW halo lenses and use them to generate image-plane and source-plane of lensing quantities, which we analyse.

This thesis is also supplemented by an Appendix chapter. It consists of several sections that appeared as appendices to our original papers. In Appendix A.1, we gather several analytic results and approximations for the model with a point mass embedded in the NFW halo. In Appendix A.2 we discuss the peculiar properties of the vanishing radial critical curves and caustics that we have discovered in the same model. In Appendix A.3, we describe how the image geometry is related to the convergence and shear and how these relations can be visualised in a compact way.

2. Gravitational Lensing by a Massive Object in a Dark Matter Halo. I. Critical Curves and Caustics[1]

Abstract

We study the gravitational lensing properties of a massive object in a dark matter halo, concentrating on the critical curves and caustics of the combined lens. We model the system in the simplest approximation by a point mass embedded in a spherical Navarro–Frenk–White density profile. The low number of parameters of such a model permits a systematic exploration of its parameter space. We present galleries of critical curves and caustics for different masses and positions of the point in the halo. We demonstrate the existence of a critical mass, above which the gravitational influence of the centrally positioned point is strong enough to eliminate the radial critical curve and caustic of the halo. In the point-mass parameter space we identify the boundaries at which critical-curve transitions and corresponding caustic metamorphoses occur. The number of transitions as a function of position of the point is surprisingly high, ranging from three for higher masses to as many as eight for lower masses. On the caustics we identify the occurrence of six different types of caustic metamorphoses. We illustrate the peculiar properties of the single radial critical curve and caustic appearing in an additional unusual non-local metamorphosis for a critical mass positioned at the halo center. Although we constructed the model primarily to study the lensing influence of individual galaxies in a galaxy cluster, it can also be used to study the lensing by dwarf satellite galaxies in the halo of a host galaxy, as well as (super)massive black holes at a general position in a galactic halo.

Keywords: gravitational lensing — galaxy clusters — dark matter halos — dwarf galaxies — supermassive black holes

[1]Karamazov et al. (2021)

2.1 Introduction

Galaxy clusters provide a unique setting in which gravitational lensing plays an important role, uncovering information about the background universe as well as about the cluster itself (Kneib and Natarajan 2011). On the one hand, clusters act as gravitational telescopes for studying the more distant populations of high-redshift galaxies and protogalaxies. On the other hand, combined analyses of weak and strong gravitational lensing can be used to map the total mass distribution in the cluster (e.g., Finney et al. 2018, Jauzac et al. 2018). A number of different techniques have been developed for joining the statistical information on weak image deformations in the outer parts of the cluster with the information on specific multiply imaged systems in its inner parts (Meneghetti et al. 2017).

These techniques have advanced to a state in which properties of analyzed clusters can be compared with properties of simulated clusters formed in cosmological structure-formation simulations. In a recent study, Meneghetti et al. (2020) compared the lensing effects of substructure in a set of observed clusters and in their simulated counterparts. They found a substantial discrepancy in the population of small-scale gravitational lenses: their lensing efficiency in the observed clusters was more than an order of magnitude higher than in the simulated clusters. Lacking an obvious single explanation for this surprising result, Meneghetti et al. (2020) suggested its possible resolution might involve either systematic issues with simulations, or incorrect assumptions about dark matter properties.

Instead of simulating lensing by an advanced realistic model of a galaxy cluster with all its different components, in this work we take a first step in a bottom-up approach. We study the lensing effect of a single massive object in the dark matter halo of a galaxy cluster. Using a simple model with few parameters allows us to systematically explore the lensing behavior of the system and its parameter-space variations. Results of such a study can be used as a stepping stone to exploring the properties of more advanced models. At the same time, they may aid the interpretation of the local lensing behavior in the vicinity of individual galaxies in a cluster.

We model the mass distribution of the cluster by a spherical Navarro–Frenk–White (hereafter NFW) density profile (Navarro et al. 1996), which has been shown to describe adequately the combined dark matter and baryonic gas distribution in galaxy clusters (Newman et al. 2013). For our purposes, the NFW profile has the additional advantage of yielding a simple analytic expression for the gravitational deflection angle. This in turn permits an analytic derivation of the Jacobian and other lensing quantities, as well as more efficient inverse-ray-shooting computations. We model the massive object using the simplest approximation, i.e., that of a point mass. While this is a rather poor model for describing a galaxy, at a sufficient distance the gravitational field of any massive object can be described by its monopole. At the scale of the galaxy cluster it is not unreasonable as a first approximation.

The results of structure-formation simulations indicate that the NFW profile is suitable not just for galaxy-cluster halos, but more generally for dark matter halos down to the scale of individual galaxies (Ludlow et al. 2013). In view of this finding, our lens model can be used just as well for studying two other

astrophysical scenarios. First, it can describe the lensing effect of a substructure or a dwarf satellite galaxy in the dark matter halo of a host galaxy (e.g., Hezaveh et al. 2016). Second, it can describe the lensing by a (super)massive black hole in a galaxy (e.g., Mao et al. 2001, Bowman et al. 2004). We note that observational data on galactic dark-matter distributions indicate a preference for profiles with a central core rather than a cusp (Salucci 2019). Nevertheless, the NFW profile can be used as a reasonable approximation for the halos of elliptical (e.g., Shajib et al. 2021) or even massive spiral galaxies (e.g., Rodrigues et al. 2017).

In this article we describe the basic lensing properties of the model, focusing on the structure of its critical curves and caustics. In a companion article we explore the effect of the point mass on the shear and on the images formed by the lens. The content presented here is organized as follows. In Section 2.2 we give a brief overview of lensing by a NFW halo, illustrating the dependence of critical-curve and caustic radii on the halo convergence parameter. We select a fiducial value of the parameter and use it for computing most of the subsequently presented results. In Section 2.3 we explore the properties of the combined NFW halo + point-mass lens model. For a centrally positioned point mass we study the different lensing regimes as a function of its mass in Section 2.3.3. For a general position of the point mass we explore the critical-curve transitions and caustic metamorphoses and map the corresponding boundaries in the parameter space of the point mass in Section 2.3.4. In Section 2.4 we comment on the effect of varying the halo convergence parameter, and discuss the relevance of the results in different astrophysical scenarios. We summarize our main findings in Section 2.5. In Appendix A.1 we present useful analytic results and approximations. In Appendix A.2 we describe the unusual lensing properties for a critical-mass point positioned at the halo center.

2.2 Lensing by an NFW halo

2.2.1 Density profile and convergence

The three-dimensional density profile of a spherical dark-matter halo can be described by the Navarro–Frenk–White profile (Navarro et al. 1996),

$$\rho(r) = \rho_\mathrm{s} \left(\frac{r}{r_\mathrm{s}}\right)^{-1} \left(1 + \frac{r}{r_\mathrm{s}}\right)^{-2} , \tag{2.1}$$

where r is the three-dimensional radial distance from the center, r_s is the scale radius and ρ_s is a characteristic density such that $\rho(r_\mathrm{s}) = \rho_\mathrm{s}/4$. At small radii $r \ll r_\mathrm{s}$ the density diverges as $\rho \sim r^{-1}$, at large radii $r \gg r_\mathrm{s}$ the density drops as $\rho \sim r^{-3}$, and at the scale radius $\mathrm{d}\ln\rho\,/\mathrm{d}\ln r\,|_{r=r_\mathrm{s}} = -2$. The halo mass enclosed in a sphere of radius r is

$$M(r) = 4\pi \int_0^r r'^2 \rho(r')\,\mathrm{d}r' = 4\pi r_\mathrm{s}^3 \rho_\mathrm{s} \left[\ln\left(1 + \frac{r}{r_\mathrm{s}}\right) - \frac{r}{r + r_\mathrm{s}}\right] . \tag{2.2}$$

Due to the logarithmic divergence of the NFW halo mass for $r \gg r_\mathrm{s}$, the profile is extended only to a certain distance such as r_{200}, at which the mean density within the enclosed sphere is 200 times the critical density at the redshift of the

halo, $\rho_{\rm crit}(z)$. The ratio of the two characteristic radii defines the concentration parameter of the halo, $c_{\rm s} = r_{200}/r_{\rm s}$.

Despite its density divergence at the center and its mass divergence at large radii, for a broad range of intermediate radii the NFW profile presents a good fit to cold dark matter halo profiles. For galaxy cluster halos this agreement has been demonstrated by cluster lensing analyses (Okabe et al. 2013, Umetsu and Diemer 2017) or by X-ray emission analyses (Ettori et al. 2013).

In order to compute light deflection by the NFW halo we first integrate Equation (2.1) along the line of sight to obtain the NFW surface density. We express $r = r_{\rm s}\sqrt{x^2 + l^2}$ in terms of the distances x projected in the plane of the sky and l along the line of sight, both in units of the scale radius $r_{\rm s}$. The convergence

$$\kappa(x) = \frac{r_{\rm s}}{\Sigma_{\rm cr}} \int_{-\infty}^{\infty} \rho(r_{\rm s}\sqrt{x^2 + l^2})\, {\rm d}\, l \tag{2.3}$$

is defined as the surface density expressed in units of the critical surface density

$$\Sigma_{\rm cr} = \frac{c^2}{4\pi G} \frac{D_{\rm s}}{D_{\rm l}\, D_{\rm ls}}\,, \tag{2.4}$$

where c is the speed of light, G the gravitational constant, and $D_{\rm l}$, $D_{\rm s}$, and $D_{\rm ls}$ are the angular diameter distances from the observer to the lens (i.e., the halo in our case), from the observer to the source of light (e.g., a background galaxy or quasar), and from the lens to the source, respectively.

For the NFW density from Equation (2.1) the integral in Equation (2.3) can be performed analytically (e.g., Bartelmann 1996, Wright and Brainerd 2000, Keeton 2001, Golse and Kneib 2002), yielding the NFW convergence as a function of the plane-of-the-sky radial position x,

$$\kappa(x) = 2\,\kappa_{\rm s}\, \frac{1 - \mathcal{F}(x)}{x^2 - 1}\,, \tag{2.5}$$

where the dimensionless halo convergence parameter $\kappa_{\rm s} = \rho_{\rm s}\, r_{\rm s}/\Sigma_{\rm cr}$ and the function

$$\mathcal{F}(x) = \begin{cases} \dfrac{\operatorname{arctanh}\sqrt{1 - x^2}}{\sqrt{1 - x^2}} & \text{for } x < 1\,, \\ 1 & \text{for } x = 1\,, \\ \dfrac{\arctan\sqrt{x^2 - 1}}{\sqrt{x^2 - 1}} & \text{for } x > 1\,. \end{cases} \tag{2.6}$$

The NFW convergence decreases monotonically and smoothly with radial position x throughout its range. As shown in Equation (A.3), it has a logarithmic divergence for $x \to 0$, where $\kappa(x) \approx -2\,\kappa_{\rm s} \ln x$. It drops to $\kappa(1) = 2\,\kappa_{\rm s}/3$ at the scale radius, as shown in Equation (A.9), and decreases further to zero as $\kappa(x) \approx 2\,\kappa_{\rm s}\, x^{-2}$ for $x \gg 1$. The unit-convergence radius x_0 has a special significance from the perspective of lensing. It can be determined for a given value of $\kappa_{\rm s}$ by setting $\kappa(x_0) = 1$ in Equation (2.5),

$$\frac{1 - x_0^2}{\mathcal{F}(x_0) - 1} = 2\,\kappa_{\rm s}\,, \tag{2.7}$$

which can be solved numerically. The solutions are illustrated and discussed further in Section 2.2.3.

2.2.2 Lens equation

The gravitational field of the halo deflects a light ray passing at point $\boldsymbol{x}$ in the plane of the sky by the deflection angle

$$\boldsymbol{\alpha}(\boldsymbol{x}) = \frac{4\,G\,M_{\rm cyl}(x\,r_{\rm s})}{c^2\,r_{\rm s}}\;\frac{\boldsymbol{x}}{x^2}\,, \tag{2.8}$$

where $M_{\rm cyl}(x\,r_{\rm s})$ is the mass within a radius $x\,r_{\rm s}$ along the line of sight through the halo center,

$$M_{\rm cyl}(x\,r_{\rm s}) = 2\,\pi\,r_{\rm s}^2\,\Sigma_{\rm cr}\int_0^x \kappa(x')\,x'\,{\rm d}\,x' = 4\,\pi\,r_{\rm s}^3\,\rho_{\rm s}\,\left[\ln\frac{x}{2} + \mathcal{F}(x)\right]\,, \tag{2.9}$$

where we used the NFW convergence from Equation (2.5). The deflection angle for the NFW halo thus is

$$\boldsymbol{\alpha}(\boldsymbol{x}) = \frac{16\,\pi\,G\,r_{\rm s}^2\,\rho_{\rm s}}{c^2}\,\left[\ln\frac{x}{2} + \mathcal{F}(x)\right]\,\frac{\boldsymbol{x}}{x^2} = \frac{4\,\kappa_{\rm s}\,r_{\rm s}\,D_{\rm s}}{D_{\rm l}\,D_{\rm ls}}\,\left[\ln\frac{x}{2} + \mathcal{F}(x)\right]\,\frac{\boldsymbol{x}}{x^2}\,, \tag{2.10}$$

where we used Equation (2.4) and the definition of $\kappa_{\rm s}$ under Equation (2.5) to get the second expression. The deflection angle can be used in the general lens equation,

$$\boldsymbol{\beta} = \boldsymbol{\theta} - \frac{D_{\rm ls}}{D_{\rm s}}\boldsymbol{\alpha}\,, \tag{2.11}$$

connecting the angular position $\boldsymbol{\beta}$ of a background source with the angular position $\boldsymbol{\theta}$ of its image formed by the lens. In gravitational lensing the angles are often expressed in units of the Einstein radius[2] of the lens,

$$\theta_{\rm E} = \sqrt{\frac{4\,G\,M_{\rm NFW}}{c^2}\,\frac{D_{\rm ls}}{D_{\rm l}\,D_{\rm s}}}\,, \tag{2.12}$$

where we set $M_{\rm NFW} = M(c_{\rm s}\,r_{\rm s})$ as the total mass within radius r_{200} using Equation (2.2),

$$M_{\rm NFW} = 4\,\pi\,r_{\rm s}^3\,\rho_{\rm s}\,[\,\ln(1+c_{\rm s}) - c_{\rm s}/(1+c_{\rm s})\,]\,. \tag{2.13}$$

If we introduce the angular scale radius in units of the Einstein radius $\theta_{\rm s}^* = r_{\rm s}/(D_{\rm l}\,\theta_{\rm E})$, we may write the lens equation for the NFW profile as

$$\boldsymbol{\beta}^* = \boldsymbol{\theta}^* - [\,\ln(1+c_{\rm s}) - c_{\rm s}/(1+c_{\rm s})\,]^{-1}\,\left[\ln\frac{\theta^*}{2\,\theta_{\rm s}^*} + \mathcal{F}\left(\frac{\theta^*}{\theta_{\rm s}^*}\right)\right]\,\frac{\boldsymbol{\theta}^*}{(\theta^*)^2}\,, \tag{2.14}$$

where $\boldsymbol{\beta}^* = \boldsymbol{\beta}/\theta_{\rm E}$ = and $\boldsymbol{\theta}^* = \boldsymbol{\theta}/\theta_{\rm E}$. Alternatively, we may express the angles in units of the angular scale length of the halo, $r_{\rm s}/D_{\rm l}$. In these units the source position $\boldsymbol{y} = \boldsymbol{\beta}\,D_{\rm l}/r_{\rm s}$ and the image position $\boldsymbol{x} = \boldsymbol{\theta}\,D_{\rm l}/r_{\rm s}$, so that the lens equation has the form

$$\boldsymbol{y} = \boldsymbol{x} - 4\,\kappa_{\rm s}\,\left[\ln\frac{x}{2} + \mathcal{F}(x)\right]\,\frac{\boldsymbol{x}}{x^2}\,. \tag{2.15}$$

[2]Here given as the radius of the tangential critical curve of the mass $M_{\rm NFW}$ as a point lens. For a lens with a NFW density profile the radius of the tangential critical curve has to be computed numerically from Equation (2.18).

Equation (2.14), which is expressed in familiar lensing units, explicitly involves two parameters, c_s and θ_s^*. In the rest of this work we use the more compact Equation (2.15), which involves a single parameter κ_s that is related to the two parameters by

$$\kappa_\mathrm{s} = (2\,\theta_\mathrm{s}^*)^{-2}\,[\,\ln(1+c_\mathrm{s}) - c_\mathrm{s}/(1+c_\mathrm{s})\,]^{-1}\,. \tag{2.16}$$

This expression can be derived using Equations (2.4), (2.12), and (2.13) in the definition of κ_s above Equation (2.6).

We illustrate the conversion in Figure 2.1 by the dotted $\kappa_\mathrm{s} = \text{const.}$ contours in a θ_s^* vs. c_s plot including sample observational data. The plot range is set to include the parameter combinations of 19 observed galaxy clusters from the CLASH survey (Merten et al. 2015), marked here by the crosses. We use the Merten et al. cluster scale radii r_s, masses M_{200c} for M_NFW, concentrations c_{200c} for c_s, and cluster redshifts z to compute the angular diameter distance $d_\mathrm{A}(z) = D_\mathrm{l}$ in a FLRW universe with PLANCK 2015 cosmological parameters (Planck Collaboration et al. 2016). To obtain θ_s^* we compute the angular Einstein radius θ_E for asymptotically distant sources, replacing $D_\mathrm{ls}/D_\mathrm{s} \to 1$. This replacement does not hold exactly for angular diameter distances, for which the asymptotic ratio is lens-redshift dependent. However, the approximation overestimates the Einstein radii of the clusters in the sample merely by 3–11 %.

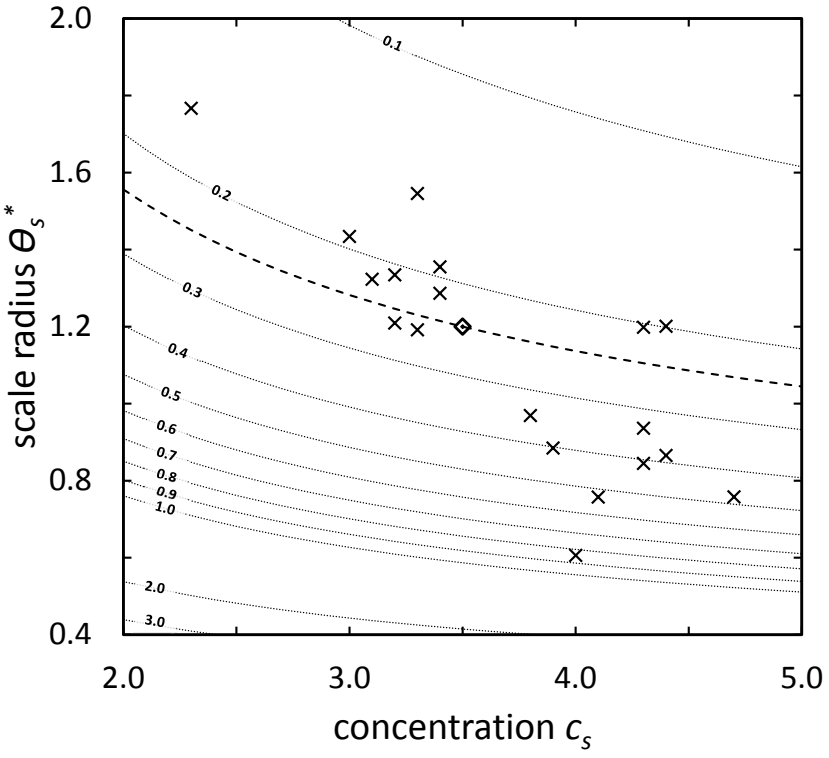

Figure 2.1: Contours of Navarro–Frenk–White halo convergence parameter κ_s as a function of concentration parameter c_s and scale radius in units of Einstein radius θ_s^*, expressed by Equation (2.16). Crosses indicate galaxy cluster data from the Merten et al. (2015) sample. The diamond marks the parameter combination $\{c_\mathrm{s},\, \theta_\mathrm{s}^*\} = \{3.5,\, 1.2\}$; the bold dashed contour passing through it corresponds to the value $\kappa_\mathrm{s} \approx 0.239035$ used for a fiducial NFW halo in this work.

2.2.3 Jacobian, critical curve, caustic

Many important lensing quantities are obtained by computing the Jacobian of the lens equation: the inverse of its absolute value yields the magnification of a point-source image at $\boldsymbol{x}$, its sign indicates the image parity, and its zero contour defines the critical curve, which in turn yields the caustic when mapped back to the source-plane positions $\boldsymbol{y}$.

For the NFW profile, the Jacobian of Equation (2.15) is

$$\det J(\boldsymbol{x}) = \left|\frac{\partial\,\boldsymbol{y}}{\partial\,\boldsymbol{x}}\right| = \left\{1 - \frac{4\,\kappa_\mathrm{s}}{x^2}\,\left[\ln\frac{x}{2} + \mathcal{F}(x)\right]\right\} \times \left\{1 + \frac{4\,\kappa_\mathrm{s}}{x^2}\,\left[\ln\frac{x}{2} + \mathcal{F}(x)\right] - 4\,\kappa_\mathrm{s}\,\frac{\mathcal{F}(x)-1}{1-x^2}\right\}, \quad (2.17)$$

which, due to symmetry, is a purely radial function of image position x. For $x \to 0$ at the halo center $\det J(\boldsymbol{x}) \approx 4\,\kappa_\mathrm{s}^2\,\ln^2 x \to \infty$, as shown in Equation (A.4). For $x \to \infty$ the Jacobian asymptotically reaches unity, $\det J(\boldsymbol{x}) \to 1$.

The factorized form of the Jacobian indicates that the critical curve $\det J(\boldsymbol{x}) = 0$ consists of solutions of two simpler equations. The factor in the first braces yields the tangential critical curve, which is a circle $|\boldsymbol{x}| = x_\mathrm{T}$ with radius obtained by numerically solving

$$1 - \frac{4\,\kappa_\mathrm{s}}{x_\mathrm{T}^2}\,\left[\ln\frac{x_\mathrm{T}}{2} + \mathcal{F}(x_\mathrm{T})\right] = 0\,, \quad (2.18)$$

an equation with a single solution for any value of κ_s. If we introduce the mean convergence within a circle of radius x,

$$\bar{\kappa}(x) = \frac{1}{\pi\,x^2}\,\int_0^x 2\pi\,x'\kappa(x')\,\mathrm{d}\,x' = \frac{4\,\kappa_\mathrm{s}}{x^2}\,\left[\ln\frac{x}{2} + \mathcal{F}(x)\right], \quad (2.19)$$

where we took into account Equation (2.9), we see that Equation (2.18) implies $\bar{\kappa}(x_\mathrm{T}) = 1$. The tangential critical curve thus encloses a circle with unit mean convergence. Recalling that the NFW convergence is a monotonically decreasing function, this means that $\kappa(x_\mathrm{T}) < \bar{\kappa}(x_\mathrm{T}) = 1$ and, thus, $x_\mathrm{T} > x_0$, where the radius of unit convergence x_0 is given by Equation (2.7). Substituting the critical curve $\boldsymbol{x} = x_\mathrm{T}\,(\cos\varphi, \sin\varphi)$ with $\varphi \in [\,0, 2\pi\,]$ in Equation (2.15) and using Equation (2.18), we obtain the corresponding part of the caustic:

$$\boldsymbol{y} = \boldsymbol{x}\,\left\{1 - \frac{4\,\kappa_\mathrm{s}}{x_\mathrm{T}^2}\,\left[\ln\frac{x_\mathrm{T}}{2} + \mathcal{F}(x_\mathrm{T})\right]\right\} = (\,0, 0\,)\,. \quad (2.20)$$

The tangential part of the caustic consists of a single point at the origin.

Setting the second braces in Equation (2.17) equal to zero yields the radial critical curve. This is another circle with radius x_R obtained by numerically solving

$$1 + \frac{4\,\kappa_\mathrm{s}}{x_\mathrm{R}^2}\,\left[\ln\frac{x_\mathrm{R}}{2} + \mathcal{F}(x_\mathrm{R})\right] - 4\,\kappa_\mathrm{s}\,\frac{\mathcal{F}(x_\mathrm{R})-1}{1-x_\mathrm{R}^2} = 0\,, \quad (2.21)$$

which also has a single solution for any κ_s. The l.h.s. can be written as a simple combination of Equation (2.19) and Equation (2.5), yielding

$$1 + \bar{\kappa}(x_\mathrm{R}) - 2\,\kappa(x_\mathrm{R}) = 0\,. \quad (2.22)$$

Therefore, the convergence at the radius of the radial critical curve

$$\kappa(x_\mathrm{R}) = \frac{1}{2}\,[\,1 + \bar{\kappa}(x_\mathrm{R})\,] \tag{2.23}$$

is the average of the mean convergence at the radius and 1. For the monotonically decreasing NFW convergence $\bar{\kappa}(x_\mathrm{R}) > \kappa(x_\mathrm{R}) > 1$ and, thus, $x_\mathrm{R} < x_0$. Substituting the radial critical curve $\boldsymbol{x} = x_\mathrm{R}\,(\cos\varphi, \sin\varphi)$ with $\varphi \in [\,0, 2\pi\,]$ in Equation (2.15) and using Equation (2.21), we obtain the corresponding part of the caustic,

$$\begin{aligned}\boldsymbol{y} &= \boldsymbol{x}\left\{1 - \frac{4\,\kappa_\mathrm{s}}{x_\mathrm{R}^2}\,\left[\ln\frac{x_\mathrm{R}}{2} + \mathcal{F}(x_\mathrm{R})\right]\right\} \\ &= -2\,\left[2\,\kappa_\mathrm{s}\,\frac{\mathcal{F}(x_\mathrm{R}) - 1}{1 - x_\mathrm{R}^2} - 1\right]\,x_\mathrm{R}\,(\cos\varphi, \sin\varphi)\,,\end{aligned} \tag{2.24}$$

where the expression in the square brackets is equal to $\kappa(x_\mathrm{R}) - 1$, which is positive. The radial part of the caustic is thus a circle with radius

$$y_\mathrm{R} = 2\,x_\mathrm{R}\,[\,\kappa(x_\mathrm{R}) - 1\,]\,. \tag{2.25}$$

Figure 2.2 shows the critical curve in the image plane (black, left panel) and caustic in the source plane (red, right panel) for a NFW density profile with $\kappa_\mathrm{s} \approx 0.239035$. This value was obtained from Equation (2.16) for the combination

$$\{c_\mathrm{s},\, \theta_\mathrm{s}^*\} = \{3.5,\, 1.2\} \tag{2.26}$$

chosen to represent the Merten et al. (2015) cluster data and marked by the diamond in Figure 2.1. The outer tangential and inner radial critical curves are plotted over a color map of the Jacobian $\det J(\boldsymbol{x})$, marked red where positive and blue where negative. Lighter areas indicate regions with higher image magnification (brighter images), darker areas regions with lower image magnification (dimmer images). Inside the radial critical curve the Jacobian is positive, increasing divergently toward the origin. Any images appearing close to the origin are thus strongly demagnified. In the annulus between the radial and tangential critical curves the Jacobian is negative, thus any images appearing here have negative parity. Outside the tangential critical curve the Jacobian is positive, increasing monotonically outward, and approaching 1 asymptotically.

The caustic is plotted over a grayscale magnification map, showing the total point-source magnification

$$A(\boldsymbol{y}) = \sum_i |\det J(\boldsymbol{x}_i)|^{-1} \tag{2.27}$$

of all images $\boldsymbol{x}_i$ formed by the lens for a point source at $\boldsymbol{y}$. The magnification map is computed by inverse ray shooting (e.g., Kayser et al. 1986), with the color ranging from black for lowest magnification $A = 1$ to white for highest magnification $A \geq 1000$. The magnification diverges at the caustic, here more prominently at the central point (tangential caustic). At the circular radial caustic the magnification remains finite from the outer side but diverges from the inner side in an extremely narrow high-magnification region (see also Martel and Shapiro 2003).

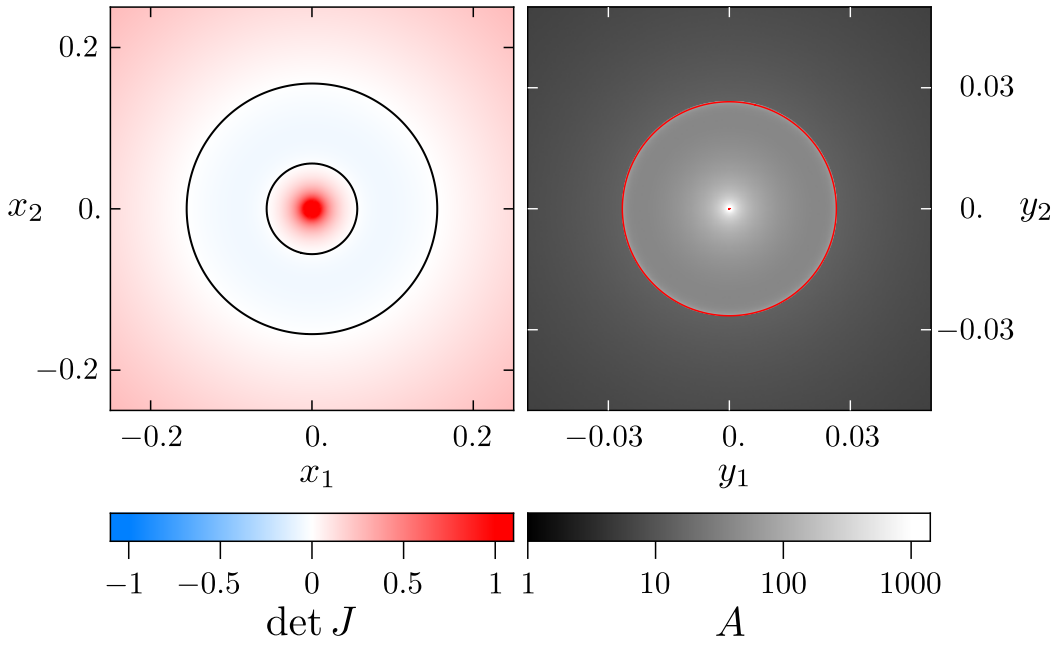

Figure 2.2: Critical curve (left panel, black) and caustic (right panel, red) of a NFW halo with $\kappa_\mathrm{s} \approx 0.239035$. The larger tangential critical curve corresponds to the central point-like caustic; the smaller radial critical curve corresponds to the circular caustic. The image-plane color map in the left panel shows the lens-equation Jacobian $\det J(\boldsymbol{x})$, with colors saturating at $|\det J| = 1$ (the Jacobian is divergent at the origin). The source-plane grayscale map in the right panel shows the total point-source magnification $A(\boldsymbol{y})$, with white saturating at $A = 1000$ (the magnification is divergent at the caustic).

Clearly, sources positioned outside the radial caustic are magnified substantially less than those positioned inside.

Although Figure 2.2 is plotted for a single value of the NFW convergence parameter κ_s, the general character of the critical curve, caustic, Jacobian and magnification maps does not change for other values. What changes are the radii of the tangential and radial critical curves, x_T and x_R, respectively, and the radial caustic radius y_R (Bartelmann 1996, Martel and Shapiro 2003). Figure 2.3 shows the dependence of these radii and the unit convergence radius x_0 on κ_s. All the plotted radii are simple monotonically increasing functions of κ_s. The vertical dot-dashed line indicates the value $\kappa_\mathrm{s} \approx 0.239035$ chosen for illustration in Figure 2.2 as well as in the rest of this work.

While the values of the radii for general κ_s plotted in Figure 2.3 have to be computed numerically, for $\kappa \lesssim 0.2$ they may be approximated by analytic expressions using Equation (A.1) and Equation (A.2) from Appendix A.1.1 in Equation (2.18), Equation (2.7), Equation (2.21), and Equation (2.24). For the critical-curve radii (Dúmet-Montoya et al. 2013) and the unit-convergence radius we find

$$\{x_\mathrm{T},\, x_0,\, x_\mathrm{R}\} \approx 2\,\mathrm{e}^{-(1+3\,\kappa_\mathrm{s})/(2\,\kappa_\mathrm{s})}\,\left\{\mathrm{e},\,\sqrt{\mathrm{e}},1\right\} \tag{2.28}$$

and for the (radial) caustic radius we find

$$y_\mathrm{R} \approx 4\,\kappa_\mathrm{s}\,\mathrm{e}^{-(1+3\,\kappa_\mathrm{s})/(2\,\kappa_\mathrm{s})}\,. \tag{2.29}$$

These approximations are marked by dotted curves in Figure 2.3. All four radii shrink exponentially fast for low values of κ_s. Nevertheless, the ratios between the radii x_T, x_0, x_R are constant in this regime, given by the factors in the braces on the r.h.s. of Equation (2.28).

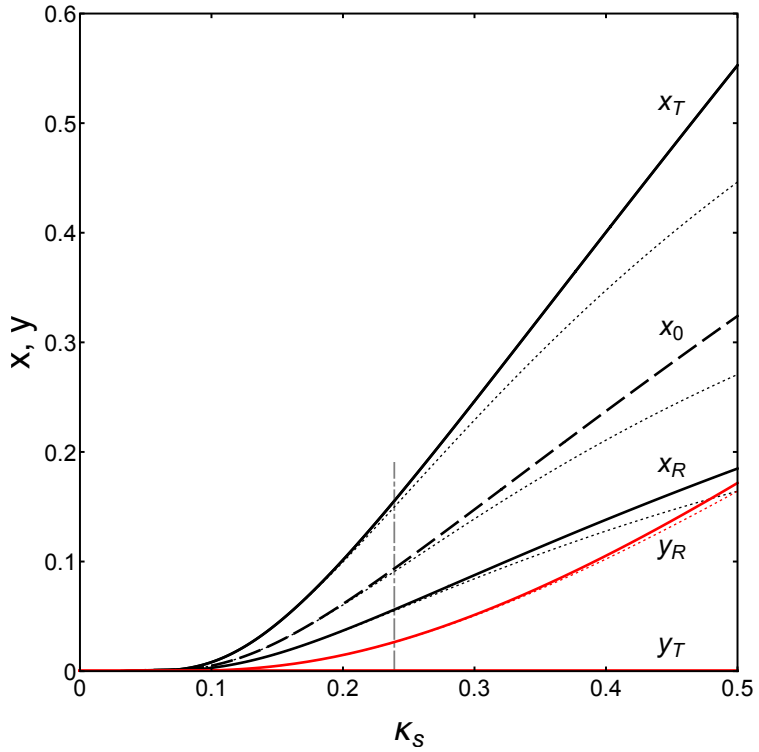

Figure 2.3: Radii of critical curves (solid black: tangential x_T, radial x_R), caustics (solid red: tangential $y_T = 0$, radial y_R), and the unit-convergence circle x_0 (dashed black) of NFW halos as a function of the convergence parameter κ_s. The dotted curves show the low-convergence analytic approximations given by Equation (2.28) and Equation (2.29). The dot-dashed vertical line indicates the fiducial value $\kappa_s \approx 0.239035$ used in Figure 2.2 and the rest of this work.

2.3 Lensing by an NFW halo + point mass

2.3.1 Lens equation

The lensing effect of an additional compact object with mass distributed in a region much smaller than the halo scale radius r_s can be modelled by adding a point-mass deflection term

$$\boldsymbol{\alpha}_P(\boldsymbol{\theta}) = \frac{4\,G\,M_P}{c^2\,D_l}\,\frac{\boldsymbol{\theta}-\boldsymbol{\theta}_P}{|\boldsymbol{\theta}-\boldsymbol{\theta}_P|^2} \tag{2.30}$$

to the deflection angle in Equation (2.11). Here M_P is the mass of the object and $\boldsymbol{\theta}_P$ its angular position from the halo center. If the object acted as an isolated lens, its region of influence could be measured by its angular Einstein radius

$$\theta_{EP} = \sqrt{\frac{4\,G\,M_P}{c^2}\,\frac{D_{ls}}{D_l\,D_s}}\,. \tag{2.31}$$

In our case, with the object embedded in the NFW halo, we will use $\theta_{\rm EP}$ for comparison and illustration purposes.

Adding the point-mass term in units of the NFW-halo Einstein radius to Equation (2.14), we obtain the full lens equation

$$\begin{aligned}\boldsymbol{\beta}^* = \boldsymbol{\theta}^* - [\, \ln(1+c_{\rm s}) - c_{\rm s}/(1+c_{\rm s})\,]^{-1} \\ \times \left[\ln\frac{\theta^*}{2\,\theta_{\rm s}^*} + \mathcal{F}\left(\frac{\theta^*}{\theta_{\rm s}^*}\right)\right]\,\frac{\boldsymbol{\theta}^*}{(\theta^*)^2} - \frac{M_{\rm P}}{M_{\rm NFW}}\,\frac{\boldsymbol{\theta}^* - \boldsymbol{\theta}_{\rm P}^*}{|\boldsymbol{\theta}^* - \boldsymbol{\theta}_{\rm P}^*|^2}\,,\end{aligned} \tag{2.32}$$

where $\boldsymbol{\theta}_{\rm P}^* = \boldsymbol{\theta}_{\rm P}/\theta_{\rm E}$. The influence of the added object is proportional to its relative mass and drops inversely proportionally to the angular separation from its position. Similarly, we may add the term in units of the angular scale length of the halo to Equation (2.15) and obtain the lens equation in the form

$$\boldsymbol{y} = \boldsymbol{x} - 4\,\kappa_{\rm s}\,\left[\ln\frac{x}{2} + \mathcal{F}(x)\right]\,\frac{\boldsymbol{x}}{x^2} - \kappa_{\rm P}\,\frac{\boldsymbol{x} - \boldsymbol{x}_{\rm P}}{|\boldsymbol{x} - \boldsymbol{x}_{\rm P}|^2}\,, \tag{2.33}$$

where the point-mass position $\boldsymbol{x}_{\rm P} = \boldsymbol{\theta}_{\rm P}\,D_{\rm l}/r_{\rm s}$. The newly introduced dimensionless mass parameter $\kappa_{\rm P}$ can be expressed in several equivalent ways,

$$\kappa_{\rm P} = \frac{M_{\rm P}}{M_{\rm NFW}}\,(\theta_{\rm s}^*)^{-2} = \frac{\theta_{\rm EP}^2\,D_{\rm l}^2}{r_{\rm s}^2} = \frac{M_{\rm P}}{\pi\,r_{\rm s}^2\,\Sigma_{\rm cr}}\,, \tag{2.34}$$

where we used the definition of $\theta_{\rm s}^*$ above Equation (2.14), Equation (2.31), and Equation (2.4). The first expression defines the transformation from the parameters appearing in Equation (2.32). The second expression identifies $\kappa_{\rm P}$ as the ratio of the areas (or solid angles) of the point-mass Einstein circle and the halo scale-radius circle. The third expression shows that we may interpret $\kappa_{\rm P}$ as the convergence corresponding to the surface density of the mass $M_{\rm P}$ spread out over the area of the halo scale-radius circle.

In the rest of this work we will use the lens equation in the more compact form provided by Equation (2.33). The equation involves four parameters: the convergences $\kappa_{\rm s}$ and $\kappa_{\rm P}$, and the two components of the point-mass position $\boldsymbol{x}_{\rm P}$. For exploring the lens properties of the model we may always rotate our coordinate axes to position the point mass along the positive horizontal axis, so that $\boldsymbol{x}_{\rm P} = (x_{\rm P}, 0)$ with $x_{\rm P} \geq 0$. With this choice of orientation only three free parameters remain: one describing the NFW halo ($\kappa_{\rm s}$) and two describing the point mass ($\kappa_{\rm P}$ and $x_{\rm P}$).

2.3.2 Jacobian

Computing the determinant of the Jacobi matrix consisting of the partial derivatives $\partial y_i/\partial x_j$ of Equation (2.33) gives us the Jacobian

$$\begin{aligned}\det J(\boldsymbol{x}) = \left\{1 - \frac{4\,\kappa_{\rm s}}{x^2}\,\left[\ln\frac{x}{2} + \mathcal{F}(x)\right] - \frac{\kappa_{\rm P}}{|\boldsymbol{x} - \boldsymbol{x}_{\rm P}|^2}\right\} \\ \times \left\{1 + \frac{4\,\kappa_{\rm s}}{x^2}\,\left[\ln\frac{x}{2} + \mathcal{F}(x)\right] + \frac{\kappa_{\rm P}}{|\boldsymbol{x} - \boldsymbol{x}_{\rm P}|^2} - 4\,\kappa_{\rm s}\,\frac{\mathcal{F}(x) - 1}{1 - x^2}\right\} \\ + 16\,\kappa_{\rm s}\,\kappa_{\rm P}\,\frac{|\,\boldsymbol{x} \times \boldsymbol{x}_{\rm P}\,|^2}{x^4|\boldsymbol{x} - \boldsymbol{x}_{\rm P}|^4}\,\left\{\ln\frac{x}{2} + \mathcal{F}(x) - \frac{x^2}{2}\,\frac{\mathcal{F}(x) - 1}{1 - x^2}\right\}\,,\end{aligned} \tag{2.35}$$

written here in a form independent of coordinate-frame orientation. In the orientation with the point mass on the positive horizontal axis, the norm of the cross product $|\,\boldsymbol{x}\times\boldsymbol{x}_\mathrm{P}\,| = x_\mathrm{P}\,|x_2|$.

Far from the center of the halo ($x=0$) and far from the point mass ($\boldsymbol{x}=\boldsymbol{x}_\mathrm{P}$) the Jacobian $\det J\to 1$. In the general case, with $x_\mathrm{P}\neq 0$, the Jacobian diverges at two distinct locations. As shown in Section 2.2.3, at the center of the halo $\det J(\boldsymbol{x}) \approx 4\,\kappa_\mathrm{s}^2\,\ln^2 x \to \infty$, while at the position of the perturbing point mass $\det J(\boldsymbol{x}) \approx -\kappa_\mathrm{P}^2/|\boldsymbol{x}-\boldsymbol{x}_\mathrm{P}|^4 \to -\infty$.

2.3.3 Point mass at the halo center

In the special case when the point mass is positioned at the center of the halo ($x_\mathrm{P}=0$) the Jacobian loses the entire final term in Equation (2.35), leaving the factorized part

$$\det J(\boldsymbol{x}) = \left\{1-\frac{4\,\kappa_\mathrm{s}}{x^2}\,\left[\ln\frac{x}{2}+\mathcal{F}(x)\right]-\frac{\kappa_\mathrm{P}}{x^2}\right\} \times\left\{1+\frac{4\,\kappa_\mathrm{s}}{x^2}\,\left[\ln\frac{x}{2}+\mathcal{F}(x)\right]+\frac{\kappa_\mathrm{P}}{x^2}-4\,\kappa_\mathrm{s}\,\frac{\mathcal{F}(x)-1}{1-x^2}\right\}. \quad (2.36)$$

Here the situation is peculiar, since the two opposite divergences coincide at the origin. The stronger one due to the point mass prevails, so that $\det J(\boldsymbol{x})\to-\infty$ as $x\to 0$.

The factor in the first braces in Equation (2.36) yields the tangential critical curve, which is a circle $|\boldsymbol{x}| = x_\mathrm{PT}$ with radius obtained by numerically solving

$$1-\frac{4\,\kappa_\mathrm{s}}{x_\mathrm{PT}^2}\,\left[\ln\frac{x_\mathrm{PT}}{2}+\mathcal{F}(x_\mathrm{PT})\right]-\frac{\kappa_\mathrm{P}}{x_\mathrm{PT}^2}=0\,. \quad (2.37)$$

The equation has a single solution for any combination of κ_s and κ_P. Substituting the critical curve $\boldsymbol{x}=x_\mathrm{PT}\,(\cos\varphi,\sin\varphi)$ with $\varphi\in[\,0,2\pi\,]$ in Equation (2.33) and using Equation (2.37), we obtain the corresponding part of the caustic:

$$\boldsymbol{y}=\boldsymbol{x}\left\{1-\frac{4\,\kappa_\mathrm{s}}{x_\mathrm{PT}^2}\,\left[\ln\frac{x_\mathrm{PT}}{2}+\mathcal{F}(x_\mathrm{PT})\right]-\frac{\kappa_\mathrm{P}}{x_\mathrm{PT}^2}\right\}=(\,0,0\,)\,. \quad (2.38)$$

The tangential part of the caustic remains unchanged, consisting of the single point at the origin.

Setting the second braces in Equation (2.36) equal to zero yields the radial critical-curve equation. The solutions are circles with radius x_PR obtained by numerically solving

$$1+\frac{4\,\kappa_\mathrm{s}}{x_\mathrm{PR}^2}\,\left[\ln\frac{x_\mathrm{PR}}{2}+\mathcal{F}(x_\mathrm{PR})\right]+\frac{\kappa_\mathrm{P}}{x_\mathrm{PR}^2}-4\,\kappa_\mathrm{s}\,\frac{\mathcal{F}(x_\mathrm{PR})-1}{1-x_\mathrm{PR}^2}=0\,. \quad (2.39)$$

However, here the number of solutions for a given value of κ_s depends on the value of κ_P. Substituting the radial critical curve $\boldsymbol{x}=x_\mathrm{PR}\,(\cos\varphi,\sin\varphi)$ with $\varphi\in[\,0,2\pi\,]$ in Equation (2.33) and using Equation (2.39), we obtain the corresponding part of the caustic:

$$\boldsymbol{y}=\boldsymbol{x}\left\{1-\frac{4\,\kappa_\mathrm{s}}{x_\mathrm{PR}^2}\,\left[\ln\frac{x_\mathrm{PR}}{2}+\mathcal{F}(x_\mathrm{PR})\right]-\frac{\kappa_\mathrm{P}}{x_\mathrm{PR}^2}\right\} =-2\left[2\,\kappa_\mathrm{s}\,\frac{\mathcal{F}(x_\mathrm{PR})-1}{1-x_\mathrm{PR}^2}-1\right]x_\mathrm{PR}\,(\cos\varphi,\sin\varphi)\,, \quad (2.40)$$

where the expression in the square brackets is equal to $\kappa(x_{\rm PR}) - 1$, which is positive. For each radial critical curve, the corresponding part of the caustic is thus a circle with radius

$$y_{\rm PR} = 2\, x_{\rm PR}\, [\, \kappa(x_{\rm PR}) - 1\,]\,. \tag{2.41}$$

We present the structure of the critical curves and caustics in Figure 2.4 as a function of $\kappa_{\rm P}$ for the cluster with $\kappa_{\rm s} \approx 0.239035$ chosen for illustration in Figure 2.2. The radius of the tangential critical curve $x_{\rm PT}$ is a simple monotonically increasing function of $\kappa_{\rm P}$, which starts on the vertical axis at $x_{\rm T}$, the radius of the NFW tangential critical curve. This growth is just a simple consequence of the increasing mass at the origin.

More interesting are the radial critical curves. For low values of $\kappa_{\rm P}$ Equation (2.39) has two solutions. The larger one ($x_{\rm PR1}$) starts at $x_{\rm R}$, the radius of the NFW radial critical curve, and decreases with $\kappa_{\rm P}$. The smaller one ($x_{\rm PR2}$) starts at 0 and increases with $\kappa_{\rm P}$. As $\kappa_{\rm P}$ grows, the two curves approach each other until they merge at a critical value $\kappa_{\rm P} = \kappa_{\rm PC} \approx 2.714 \cdot 10^{-4}$ (for our choice of $\kappa_{\rm s}$). For super-critical $\kappa_{\rm P} > \kappa_{\rm PC}$ Equation (2.39) has no solution, i.e., there are no radial critical curves.

The two corresponding radial components of the caustic reflect the behavior of the critical curves, with $y_{\rm PR1}$ starting at $y_{\rm R}$, the radius of the NFW radial caustic, and $y_{\rm PR2}$ starting at 0. Even though the larger radial caustic grows with $\kappa_{\rm P}$, the two caustic circles approach each other faster than the corresponding critical-curve circles and vanish beyond $\kappa_{\rm PC}$.

The critical curves and caustics in the two regimes are illustrated by the panels in the bottom row of Figure 2.5.A. The two left columns show the Jacobian plot with critical curves and the total magnification map with caustics in the sub-critical case (for $\kappa_{\rm P} = 10^{-4}$), the two right columns show the corresponding plots in the super-critical case (for $\kappa_{\rm P} = 10^{-3}$). The notation is the same as in Figure 2.2, with the additional cyan circle indicating the position and Einstein ring of the point mass in units of the angular scale radius, $\theta_{\rm EP}\, D_{\rm l}/r_{\rm s}$.

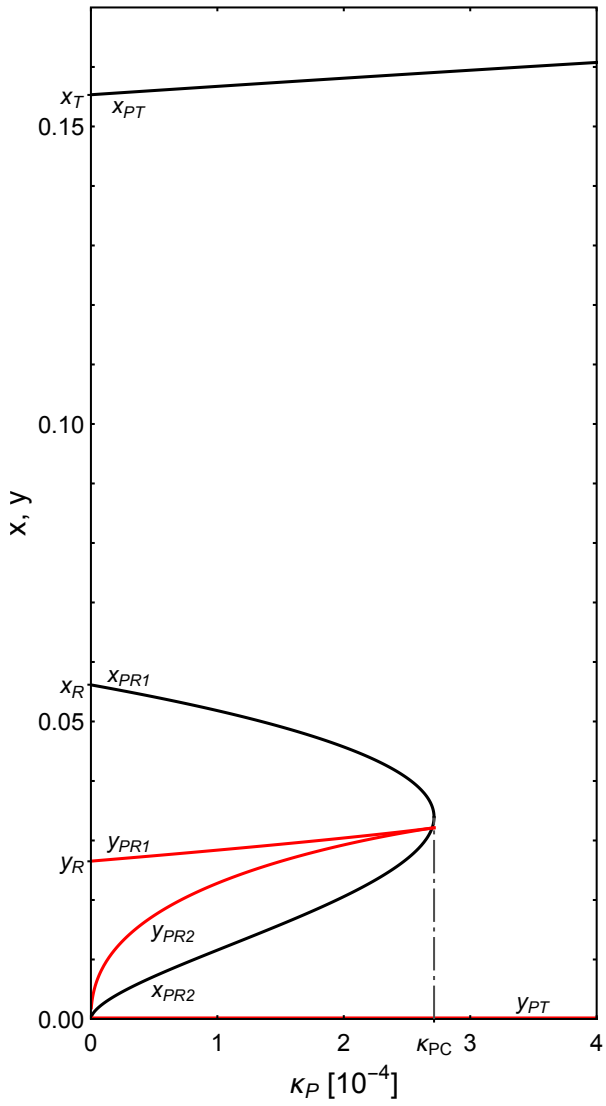

Figure 2.4: Radii of critical curves (black: tangential x_{PT}, radial x_{PR1} and x_{PR2}) and caustics (red: tangential $y_{\mathrm{PT}} = 0$, radial y_{PR1} and y_{PR2}) of a $\kappa_{\mathrm{s}} \approx 0.239035$ NFW halo density profile with a centrally positioned point mass, plotted as a function of its mass parameter κ_{P}. The corresponding radii x_{T}, x_{R}, y_{R} of an unperturbed NFW halo (intersections with the dot-dashed line in Figure 2.3) are marked along the vertical axis. Note the vanishing of the radial critical curves and caustics at $\kappa_{\mathrm{P}} = \kappa_{\mathrm{PC}} \approx 2.714 \cdot 10^{-4}$ (marked by the dot-dashed line).

For the lower-mass case with $\kappa_{\mathrm{P}} = 10^{-4}$, the Jacobian plot resembles the plot from Figure 2.2, except the region near the origin. In this example the additional radial critical curve is marginally larger than the point-mass Einstein radius. Within it the point mass dominates and $\det J < 0$. Between the two radial critical curves $\det J > 0$, between the outer radial and tangential critical curves $\det J < 0$, followed by $\det J > 0$ outside the tangential critical curve. Instead of the single radial caustic of the NFW halo seen in Figure 2.2, there are two circular radial caustics, with the outer and inner one corresponding to the outer and inner radial critical curve, respectively. The total magnification diverges at both caustics from the side of the annular region between them.

As κ_{P} increases, so does the negative-Jacobian region around the origin dominated by the point mass, while the outer radial critical curve and the enclosed positive-Jacobian annulus shrink. The outer radial caustic grows, but the inner one grows faster. At $\kappa_{\mathrm{P}} = \kappa_{\mathrm{PC}}$ the two radial critical curves (as well as the two radial caustics) merge, causing the positive-Jacobian annulus to vanish. This situation is illustrated in the bottom panels of the two central columns of Figure 2.5.B. The peculiar properties of the single merged radial critical curve and caustic are described in Appendix A.2. For larger κ_{P} the radial critical curves and caustics disappear.

For the higher-mass case with $\kappa_{\mathrm{P}} = 10^{-3}$, only the tangential critical curve remains and the negative-Jacobian region around the origin extends all the way to it, as shown in Figure 2.5.A. The caustic is reduced to the single point at the origin, while the magnification shows a brighter central region roughly the size of the vanished radial caustic.

Comparison with Figure 2.2 illustrates how dramatically a single added object may change the lensing properties of the NFW halo. The critical value $\kappa_{\mathrm{PC}} \approx 2.714 \cdot 10^{-4}$ for our halo parameter choice given by Equation (2.26) can be used in Equation (2.34) to compute the corresponding critical mass ratio $M_{\mathrm{P}}/M_{\mathrm{NFW}} \approx 3.91 \cdot 10^{-4}$. Even though such a relative mass may seem low, its gravitational field is strong enough to destroy the radial critical curve and caustic of the NFW halo in which it is embedded.

Similar behavior has been found previously for a central point mass embedded in different axially symmetric mass distributions, such as in a cored isothermal sphere (Mao et al. 2001) or in a Plummer model (Werner and Evans 2006). In either of these models there is a critical mass of the central point, above which the lens has no radial critical curves. Nevertheless, this behaviour is not ubiquitous: a central point mass embedded in a singular isothermal sphere has no radial critical curves, irrespective of its mass (Mao and Witt 2012).

2.3.4 Point mass at a general position

When positioning the point mass at increasing distances x_{P} from the halo center, the critical curve undergoes a sequence of transitions in which its loops connect, disconnect, appear, or vanish. These transitions are accompanied by underlying metamorphoses of the caustic (Schneider et al. 1992). The curves start from the central configurations described in Section 2.3.3 and end with separate critical curves and caustics of a NFW halo and a distant point-mass lens. In Section 2.3.4.1 we describe the overall changes of the critical curves and caustics.

In Section 2.3.4.2 we explore the parameter space of the point mass and identify boundaries at which the critical-curve transitions occur. We illustrate the details of several transitions and transition sequences in Section 2.3.4.3.

2.3.4.1 Critical-curve and caustic galleries

In Figure 2.5.A we present a sample critical-curve and caustic gallery for a sub-critical ($\kappa_\mathrm{P} = 10^{-4}$, left columns) and a super-critical ($\kappa_\mathrm{P} = 10^{-3}$, right columns) point mass. Its positions are marked in the critical-curve plots by the cyan Einstein-radius circles on the horizontal axis. The radial distances from the origin are indicated along the left side of the figure, increasing from $x_\mathrm{P} = 0$ in the bottom row to $x_\mathrm{P} = 0.3$ in the top row, in regular steps of 0.05.

Going up from $x_\mathrm{P} = 0$ to $x_\mathrm{P} = 0.05$ in the sub-critical case, the small critical-curve loop around the point mass connects and merges with the perturbed radial critical curve of the NFW halo. The inner circular caustic connects and merges at its left side with the perturbed radial NFW caustic in a beak-to-beak metamorphosis, while its right side progresses across the origin to the left. The four-cusped perturbed tangential NFW caustic is too tiny to be distinguished from a point at the origin.

By $x_\mathrm{P} = 0.1$ two small critical-curve loops have detached from the perturbed radial NFW critical curve. On the caustic, two small three-cusped loops have detached in simultaneous beak-to-beak metamorphoses from the perturbed radial NFW caustic. Details of this transition are described in Section 2.3.4.3 further below. Between $x_\mathrm{P} = 0.1$ and $x_\mathrm{P} = 0.15$, the two small critical-curve loops connect and merge with the perturbed tangential NFW critical curve. The two small three-cusped caustic loops connect and merge with the perturbed tangential NFW caustic in simultaneous beak-to-beak metamorphoses, forming a central six-cusped caustic loop.

For a more distant position of the point mass, a small critical-curve loop detaches from the perturbed tangential NFW critical curve, as seen for $x_\mathrm{P} = 0.25$. The small loop eventually converges to the point-mass Einstein ring. The horizontally stretched six-cusped caustic loop seen at $x_\mathrm{P} = 0.2$ disconnects in a beak-to-beak metamorphosis, forming two four-cusped loops. The smaller central one eventually shrinks to the point-like tangential NFW caustic. With increasing x_P, the larger one comes to resemble the four-cusped Chang–Refsdal caustic of a point mass with a constant low external shear (Chang and Refsdal 1984). Eventually, it shrinks to the point-like caustic of an isolated point-mass lens.

The influence of the point mass on the critical curve and caustic in the super-critical case is more pronounced and better visible than in the sub-critical case. Nevertheless, for both mass parameters we see that the critical curve is affected in a region reaching multiple Einstein radii from the point mass.

The initial transitions are markedly different in the super-critical case. As described in Section 2.3.3, the critical curve for $x_\mathrm{P} = 0$ consists only of the perturbed tangential NFW critical curve. Nevertheless, a perturbed radial NFW critical curve appears already by $x_\mathrm{P} = 0.05$. The perturbed tangential NFW caustic evolves from a single point at the origin for $x_\mathrm{P} = 0$ to a tiny four-cusped loop for $x_\mathrm{P} = 0.05$. In addition, another caustic loop with two cusps has appeared by $x_\mathrm{P} = 0.05$ in a lips metamorphosis, forming a crescent-shaped rather strongly

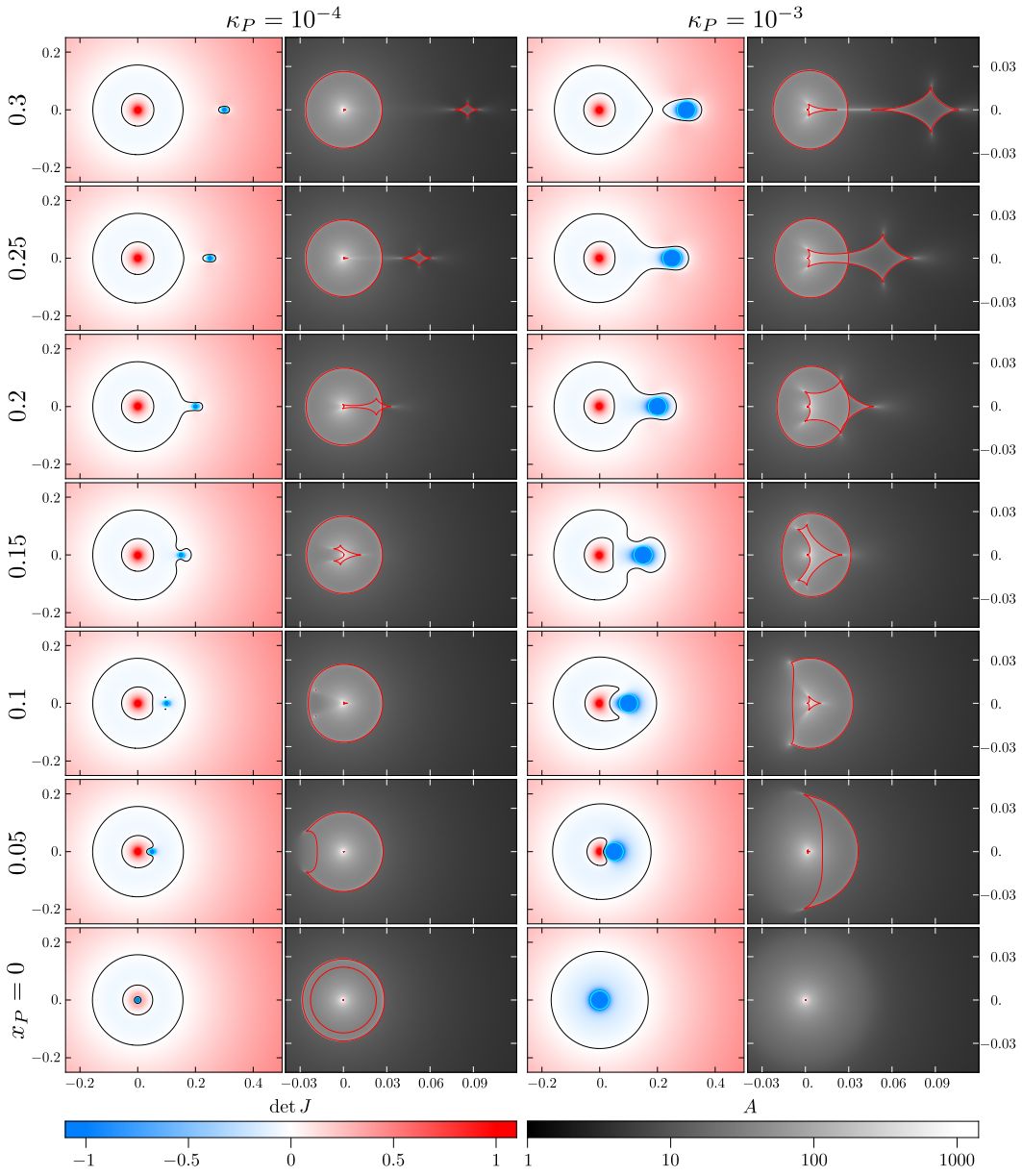

Figure 2.5.A: Critical curves and caustics of a NFW halo + point-mass lens. The left pair of columns corresponds to a sub-critical mass parameter $\kappa_{\rm P} = 10^{-4}$ and the right pair to a super-critical $\kappa_{\rm P} = 10^{-3}$, as marked at the top. The rows correspond to positions of the point mass ranging from $x_{\rm P} = 0$ to $x_{\rm P} = 0.3$, as marked along the left side. The point-mass parameter-combination grid is marked by red crosses in Figure 2.6. The cyan circles indicate the point-mass position and its Einstein ring. Here $\det J \to -\infty$ at the position of the point mass, and $\det J \to \infty$ at the origin (except when the point mass lies there). Remaining notation and color bars same as in Figure 2.2.

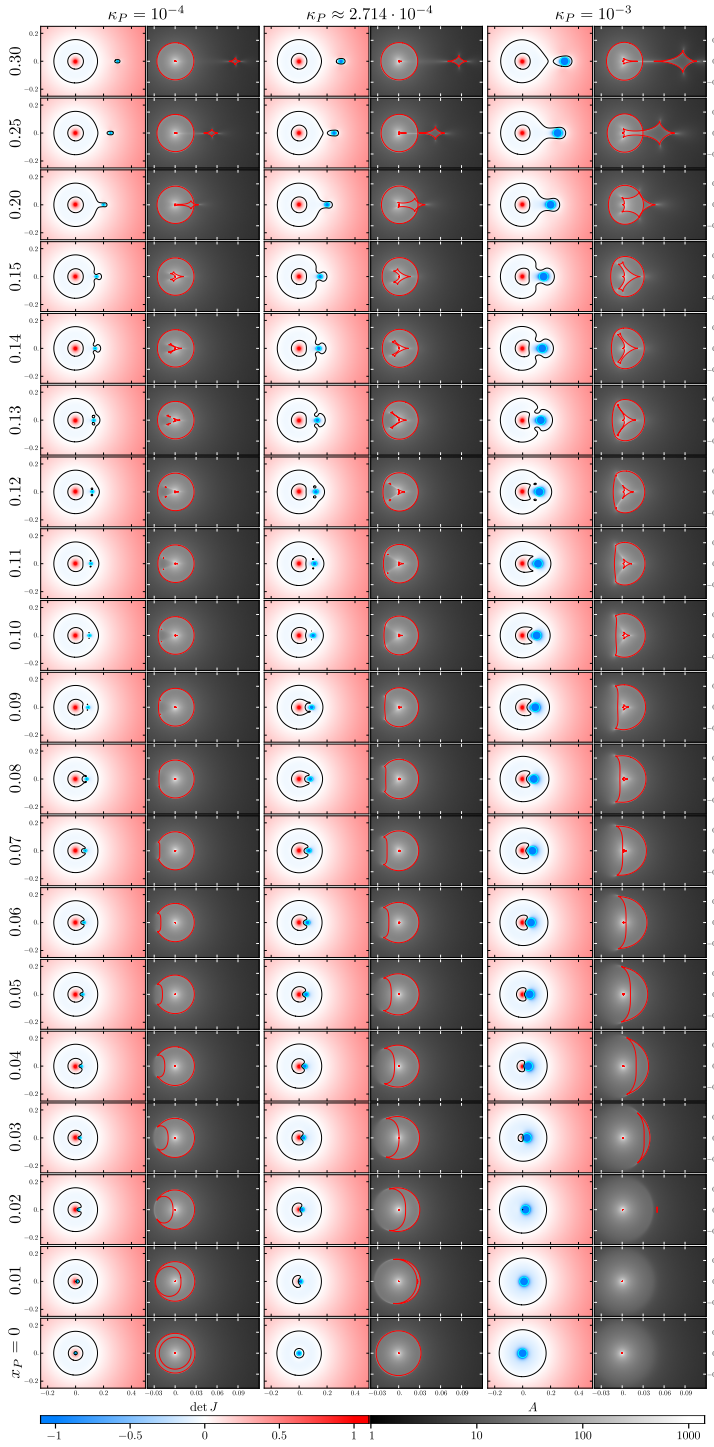

Figure 2.5.B: Critical curves and caustics of a NFW halo + point-mass lens. The left pair of columns corresponds to a sub-critical mass parameter $\kappa_{\rm P} = 10^{-4}$, the central pair to critical $\kappa_{\rm P} = \kappa_{\rm PC} \approx 2.714 \cdot 10^{-4}$, and the right pair to super-critical $\kappa_{\rm P} = 10^{-3}$, as marked at the top. The rows correspond to positions of the point mass ranging from $x_{\rm P} = 0$ to $x_{\rm P} = 0.3$, as marked along the left side. The point-mass parameter-combination grid is marked by red and black crosses in Figure 2.6. Notation same as in Figure 2.5.A. High-resolution plots are available as online figure set associated with Paper I, in arXiv paper or in digital version of this thesis.

perturbed radial NFW caustic. A detailed description of the super- and sub-critical transition sequences for point-mass positions close to the halo center is presented below in Section 2.3.4.3.

The subsequent transitions are similar to the sub-critical case, though some of them are not seen in Figure 2.5.A. This is the case for the two small loops detaching from the perturbed radial NFW critical curve & caustic and connecting to the perturbed tangential NFW critical curve & caustic, which occur here between the $x_\mathrm{P} = 0.1$ and $x_\mathrm{P} = 0.15$ rows. These can be seen in Figure 2.5.B, which shows a more detailed gallery of critical curves and caustics. In addition to the positions and masses from Figure 2.5.A it includes positions from $x_\mathrm{P} = 0$ to $x_\mathrm{P} = 0.15$ in a finer step of 0.01, as well as panels for the critical mass parameter $\kappa_\mathrm{PC} \approx 2.714 \cdot 10^{-4}$ in the central two columns. For this intermediate mass, note in the $x_\mathrm{P} = 0.01$ panels the additional tiny critical-curve loop close to the origin and the corresponding two-cusped caustic loop inside the larger caustic crescent.

More generally, all individual transitions occur at different radial positions for the different mass parameters. For example, the detachment of the two small critical-curve loops from the perturbed radial NFW critical curve occurs between $x_\mathrm{P} = 0.08$ and $x_\mathrm{P} = 0.09$ for $\kappa_\mathrm{P} = 10^{-4}$, between $x_\mathrm{P} = 0.09$ and $x_\mathrm{P} = 0.1$ for $\kappa_\mathrm{P} = \kappa_\mathrm{PC}$, and between $x_\mathrm{P} = 0.11$ and $x_\mathrm{P} = 0.12$ for $\kappa_\mathrm{P} = 10^{-3}$. We illustrate this in detail in the following Section 2.3.4.2, where we map the occurrence of all critical-curve transitions in the parameter space of the point mass.

2.3.4.2 Boundaries in point-mass parameter space

We track the changing structure of critical curves and caustics in the point-mass parameter-space region defined by the intervals $\kappa_\mathrm{P} \in [0,\, 0.0035]$ and $x_\mathrm{P} \in [0,\, 0.4]$. Within this space we identify boundaries at which the overall topology of the critical curve changes in transitions such as those seen in Section 2.3.4.1. These involve situations in which critical-curve loops connect/disconnect, or appear/vanish. In addition, we also identify situations in which loops shrink to a point, or touch without connecting. We chose the upper limits on the parameter intervals empirically: the x_P limit lies above the final transition in the studied κ_P interval; for values above the κ_P limit there are no further changes to the structure of the boundaries.

We note that straightforward use of the first expression for $\mathcal{F}(x)$ from Equation (2.6) leads to numerical instabilities for $x \ll 1$, close to the origin of the image plane. For tracking the changing structure of critical curves in this region it was necessary to use the exact and stable expressions given by Equation (A.5) and Equation (A.6), as shown in Appendix A.1.1.

Finding the boundaries involved several steps. We started by computing the critical curves and caustics on a rough parameter grid, inspecting the results to identify pairs of neighboring grid points with different topologies of the critical curve and different caustic structures. For each such pair we proceeded by interval-halving to pinpoint the intersection of the boundary between the points with the respective grid-line. Where necessary, we added more points in between these grid-line intersections to obtain smoother boundaries. In the emerging boundary plot we checked all mass-parameter intervals with different vertical sequences of boundaries to make sure the changes across the boundaries agreed with the characteristics of the corresponding metamorphoses (such as character-

istic changes in numbers of loops, or changes in numbers of cusps on caustic loops). Finally, we checked the continuity of the critical curves and caustics close to the axes, which correspond to analytically studied axisymmetric lenses: in the zero-mass limit close to the vertical axis (comparison with Section 2.2.3 and Figure 2.2), and in the zero-displacement limit close to the horizonal axis (comparison with Section 2.3.3 and Figure 2.5.B).

The mapped boundaries are presented in a $x_{\rm P}$ vs. $\kappa_{\rm P}$ plot in Figure 2.6. The left panel shows the full explored parameter space; the right panels show two expanded regions in more detail: bottom right for low masses close to the origin; top right for intermediate positions. For better interpretation of the results, the red crosses indicate the parameter combinations for which critical curves and caustics are shown in Figure 2.5.A; the critical curves and caustics for the full set of red and black crosses are shown in Figure 2.5.B. For additional orientation, we mark the NFW halo radial and tangential critical-curve radii ($x_{\rm R}$ and $x_{\rm T}$, respectively) on the vertical axis, and the critical mass parameter $\kappa_{\rm PC}$ on the horizontal axis.

The colors of the boundaries indicate the type and multiplicity of the associated caustic metamorphosis. Single metamorphoses occur in the source plane at a point on the symmetry axis passing through the point mass and the halo center, while two same simultaneous metamorphoses occur at points symmetrically offset from the axis. Cyan color indicates a single beak-to-beak metamorphosis, occurring here at two boundaries: from $x_{\rm R}$ on the vertical axis downward to $\kappa_{\rm PC}$ on the horizontal axis; from $x_{\rm T}$ on the vertical axis upward. Blue indicates two simultaneous beak-to-beak metamorphoses, occurring here at three boundaries: from the origin up to the boundary spike just under $\kappa_{\rm P} = 0.001$ (plotted by a dashed line to reveal the closely adjacent orange lips boundary); from $x_{\rm R}$ on the vertical axis upward to the point marked by the circle; from $x_{\rm T}$ on the vertical axis first downward, then rising to the boundary spike just under $\kappa_{\rm P} = 0.003$.

Orange indicates a single lips metamorphosis, occurring here at three boundaries: from the origin along the entire horizontal axis (corresponding to $x_{\rm P} = 0$); from the origin upward to the boundary spike just under $\kappa_{\rm P} = 0.001$ (just above the closely adjacent dashed blue boundary); from $\kappa_{\rm PC}$ on the horizontal axis upward to the same boundary spike. Dark orange indicates two simultaneous lips metamorphoses, occurring here at one boundary: from the point marked by the circle upward to the boundary spike just under $\kappa_{\rm P} = 0.003$. Green indicates two simultaneous elliptic umbilic metamorphoses, occurring here at one boundary: from the unit-convergence radius $x_0 \approx 0.0936$ on the vertical axis upward to the point marked by the circle. Violet indicates two simultaneous hyperbolic umbilic metamorphoses, occurring here at one boundary: from the point marked by the circle upward. Finally, the point marked by the black circle indicates two simultaneous parabolic umbilics. Four boundaries meet at this point, all of them corresponding to two simultaneous metamorphoses. In clockwise order from lower left these are beak-to-beak, elliptic umbilic, hyperbolic umbilic, and lips boundaries.

In addition to the metamorphoses for which we plotted the parameter-space boundaries in Figure 2.6, the caustic undergoes also the swallow-tail metamorphosis. In it the caustic develops a local "twist" with a self-crossing point and two additional cusps. However, unlike the plotted metamorphoses, the swallow

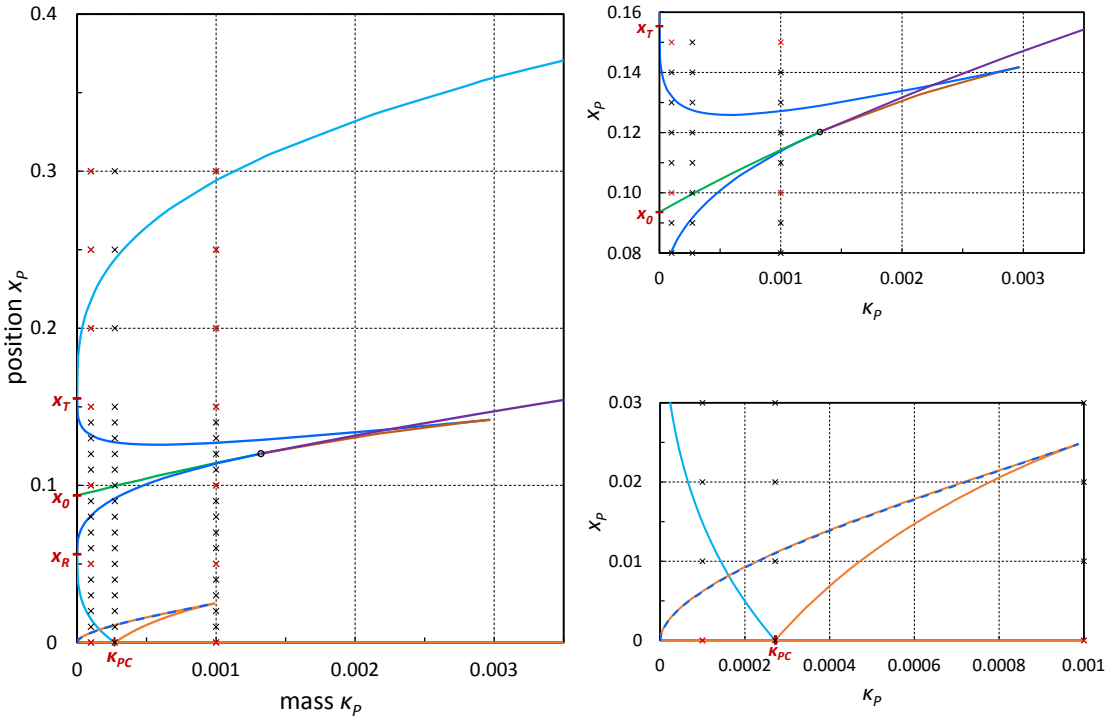

Figure 2.6: Critical-curve transitions in the position x_P vs. mass parameter κ_P parameter space of a point mass in a NFW halo. The transitions occur at boundaries colored according to the corresponding caustic metamorphoses: single beak-to-beak (cyan), two beak-to-beaks (blue), single lips (orange, including the horizontal axis), two lips (dark orange), two elliptic umbilics (green), two hyperbolic umbilics (violet), two parabolic umbilics (point marked by black circle). The blue/orange dashed line at bottom left indicates two closely adjacent transitions: the orange lips occur at larger x_P than the dashed blue beak-to-beaks. Crosses indicate the parameter combinations of the examples illustrated in Figure 2.5.B; red crosses mark the examples illustrated in Figure 2.5.A. Top right panel: detail of the intermediate-position transitions near the umbilics; bottom right panel: detail of the transitions close to the origin. Additional ticks on the axes mark the critical mass parameter $\kappa_\mathrm{PC} \approx 2.714 \cdot 10^{-4}$, the NFW halo tangential (x_T) and radial (x_R) critical-curve radii, and the unit-convergence radius x_0.

tail has no effect on the critical-curve topology. It occurs here always simultaneously in twos, always closely adjacent to simultaneous beak-to-beak boundaries. One such simultaneous swallow-tail pair occurs between the beak-to-beak and lips boundaries extending in Figure 2.6 from the origin upward to the boundary spike just under $\kappa_{\rm P} = 0.001$; two such simultaneous pairs occur in close succession just beneath the beak-to-beak boundary extending from $x_{\rm R}$ on the vertical axis upward to the point marked by the circle.

Before exploring individual transition sequences, metamorphoses, and boundaries in more detail in Section 2.3.4.3, it is worth pointing out the astounding richness of structure, transitions, and lensing regimes between them, which was quite unexpected for us in such a simple lens model.

2.3.4.3 Details of specific transitions and transition sequences

The first interesting transition occurs along the horizontal axis of the parameter-space plot in Figure 2.6, i.e., for an arbitrarily small displacement of the point mass from the halo center. In such a situation the two opposite Jacobian divergences described in Section 2.3.2 no longer coincide, and the Jacobian must cross zero at some point between them. This results in a small new critical-curve loop encircling the weaker $\det J(\boldsymbol{x}) \to \infty$ divergence at the origin of the image plane. The caustic undergoes a lips metamorphosis, in which a new two-cusped loop forms beyond the point-mass position. This particular lips metamorphosis is unusual in its appearance at infinity rather than at a finite distance from the origin of the source plane. A further increase in the point-mass displacement brings the new caustic loop rapidly toward the origin.

Inspecting the changes along the left column of crosses in Figure 2.6 corresponding to the sub-critical $\kappa_{\rm P} = 10^{-4}$ example, we see that the critical curve undergoes a total of eight transitions as we vary the point-mass position from the halo center to an asymptotic distance. Only a few of these can be identified in the galleries in Figure 2.5.A and Figure 2.5.B, as described in Section 2.3.4.1. In order to provide a more comprehensive overview we present the details of three transition sequences below.

After displacing the point mass away from the halo center, the first encountered boundaries are the adjacent dashed blue and orange lines corresponding to the beak-to-beak and lips metamorphoses, respectively. These are illustrated by the critical-curve and caustic details in Figure 2.7, with the entire sequence occurring between $x_{\rm P} = 0$ and $x_{\rm P} = 0.01$ in Figure 2.5.B. The additional third column shows the caustic detail from the second column with the horizontal scale expanded $10\times$ to reveal the caustic structure.

The critical-curve details from bottom to top reveal small positive-Jacobian loop around the origin expanding and approaching the perturbed inner radial NFW critical curve, connecting with it symmetrically at two points in the third row for $x_{\rm P} \approx 0.00617325$, leaving a small negative-Jacobian loop, which shrinks and vanishes between the top two rows. The caustic plot in the bottom row shows the small two-cusped loop approaching the perturbed inner radial NFW caustic from outside. The two caustic loops overlap in the second row. In the third row two simultaneous beak-to-beak metamorphoses occur, in which the outer part of the two-cusped loop touches the perturbed inner radial NFW caustic at two points lying symmetrically above and below the horizontal axis. This pair-wise

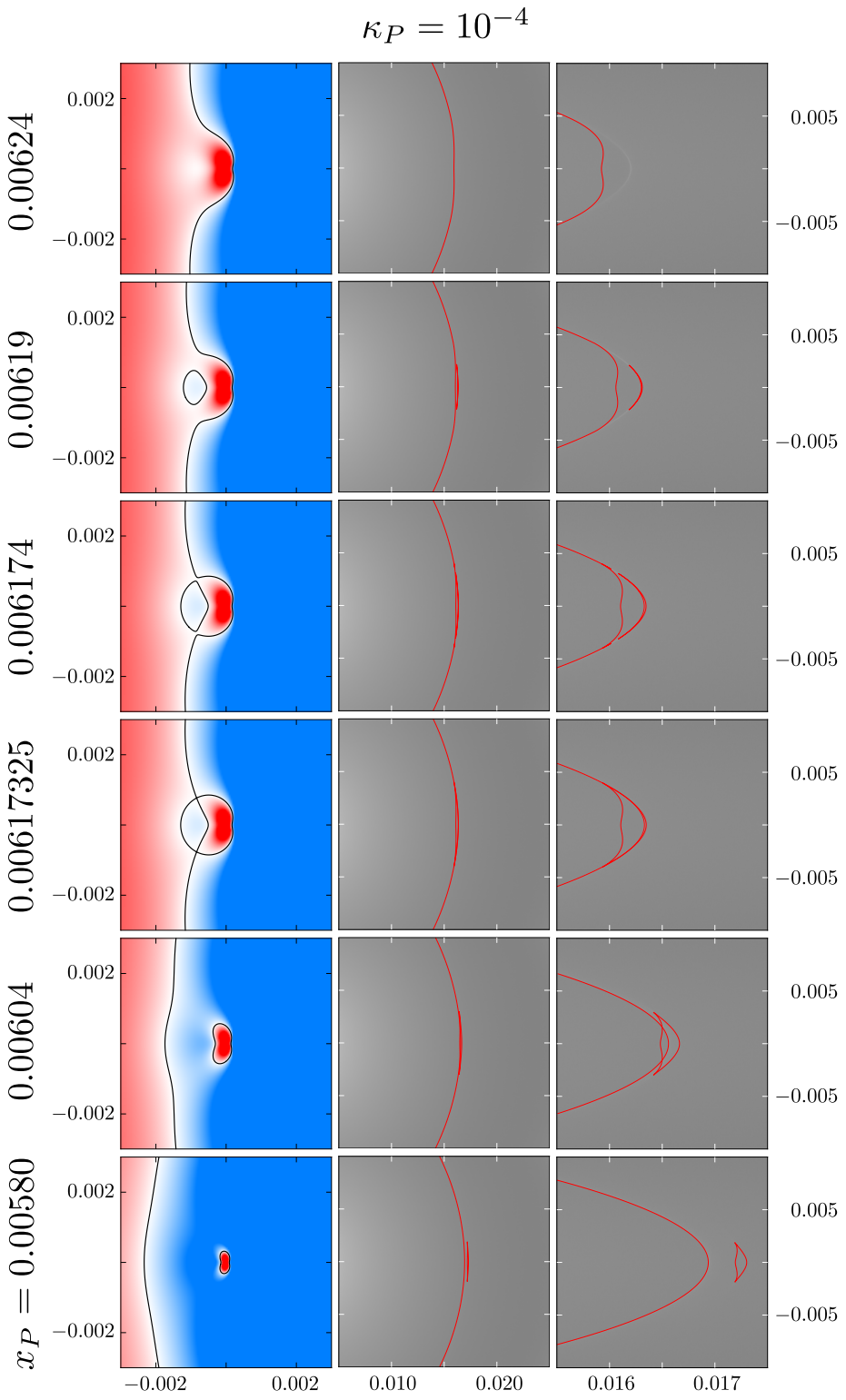

Figure 2.7: Critical-curve and caustic details for a sub-critical $\kappa_{\rm P} = 10^{-4}$ point mass near the halo center. Shown for six radial positions $x_{\rm P}$ marked along the left side, corresponding to transition across the adjacent dashed blue and orange boundaries along the left set of crosses in Figure 2.6. The critical-curve panels are fully inside the Einstein ring of the point mass. The caustic details shown in the central column are expanded in the right column 10× horizontally to reveal the caustic structure. Notation and color bars as in Figure 2.5.A.

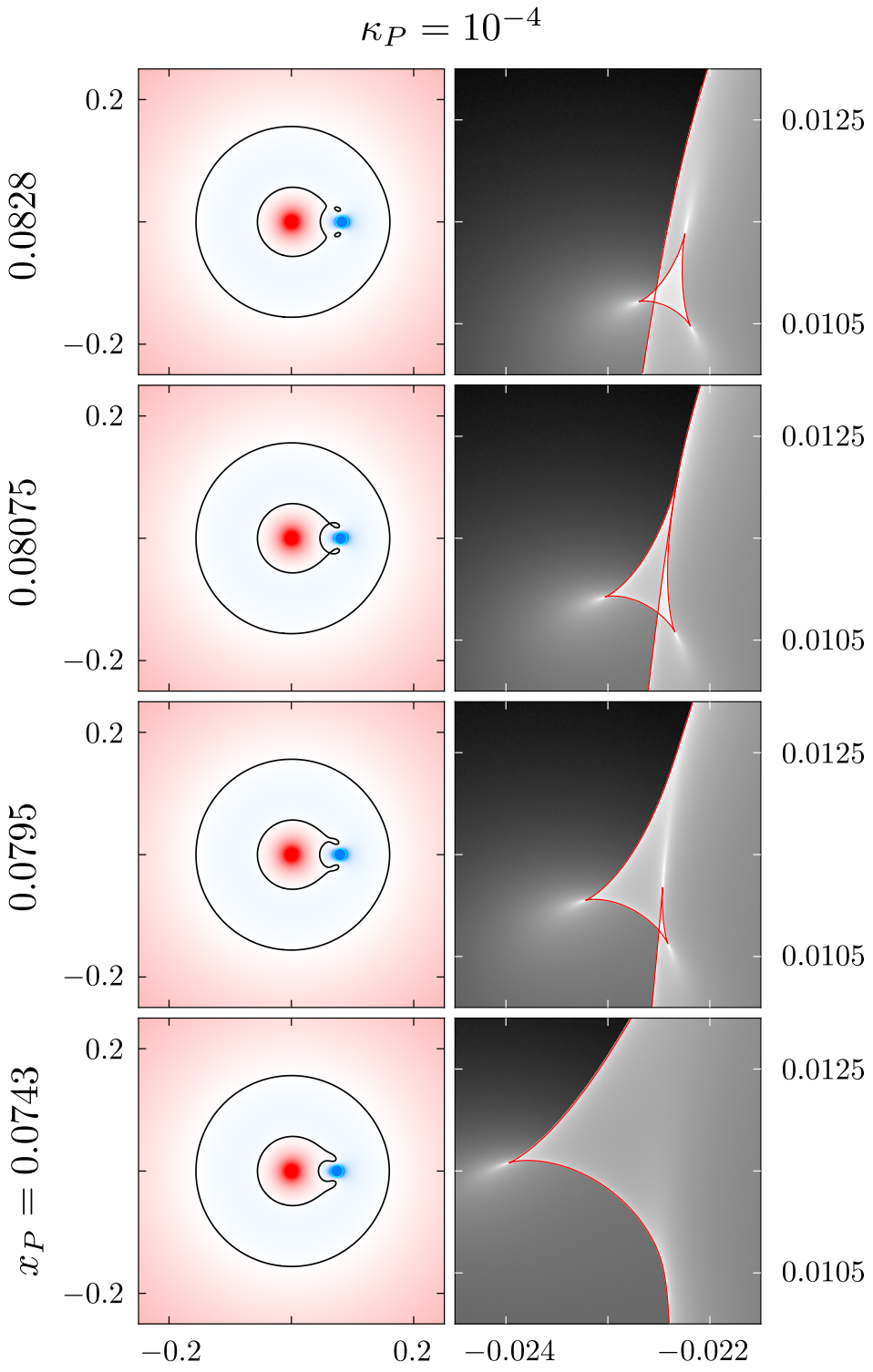

Figure 2.8: Critical curves and caustic details for a $\kappa_{\rm P} = 10^{-4}$ point mass at two simultaneous beak-to-beak metamorphoses (third row from bottom). Shown for four radial positions $x_{\rm P}$ marked along the left side, corresponding to transition across the lower solid blue boundary along the left set of crosses in Figure 2.6. Notation and color bars as in Figure 2.5.A.

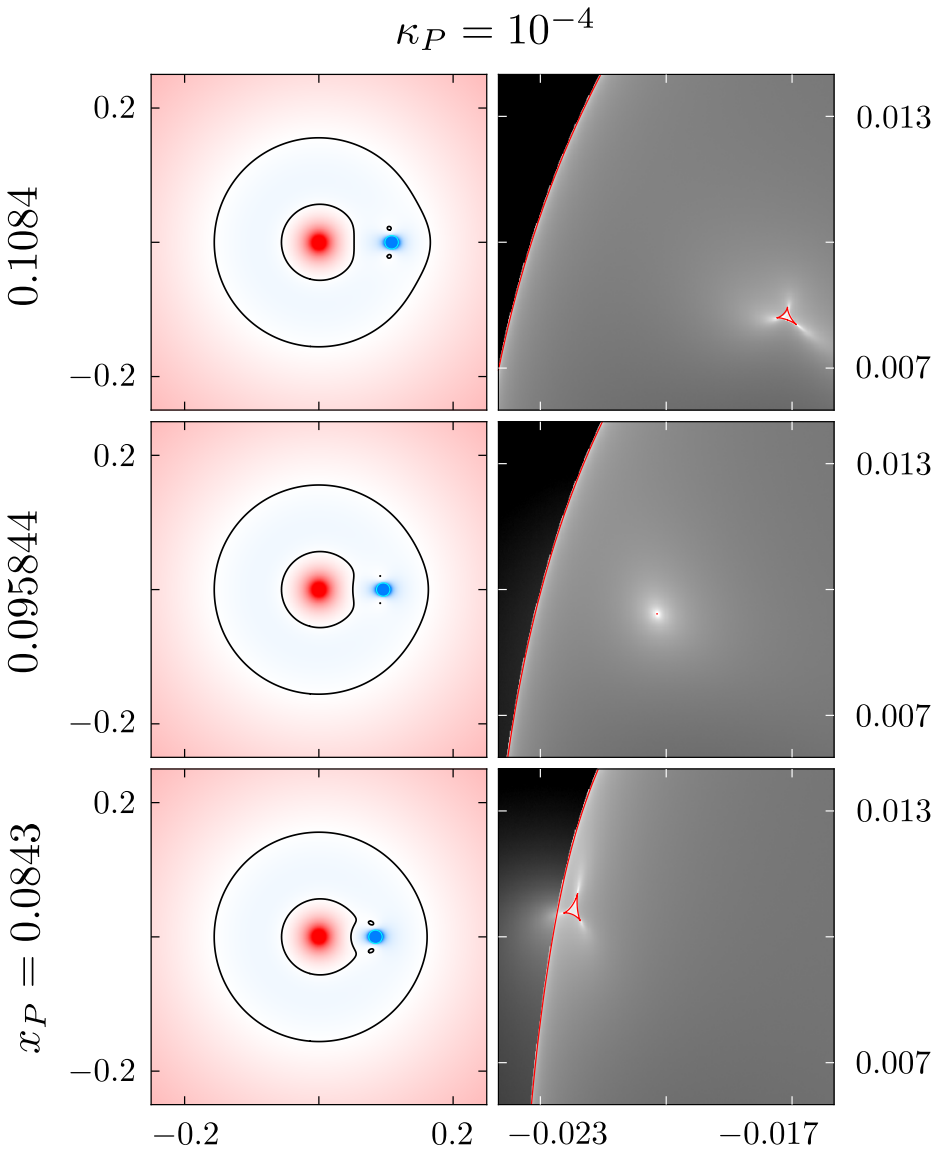

Figure 2.9: Critical curves and caustic details for a $\kappa_{\rm P} = 10^{-4}$ point mass at two simultaneous elliptic umbilics (second row from bottom). Shown for three radial positions $x_{\rm P}$ marked along the left side, corresponding to transition across the green boundary along the left set of crosses in Figure 2.6. Notation and color bars as in Figure 2.5.A.

metamorphosis leads to a thin two-cusped crescent detaching from the caustic on the outer side. The small self-crossing features on the larger caustic in the fourth row vanish by the fifth row in two simultaneous swallow-tail metamorphoses. By the sixth row, the two-cusped crescent vanishes in a lips metamorphosis, leaving a barely noticeable higher-magnification trace in the magnification map.

The detachment of the two small critical-curve loops from the perturbed radial NFW critical curve that occurs between the second and the third row of Figure 2.5.A corresponds to a more complicated sequence of metamorphoses on the caustic, as shown in Figure 2.8. The caustic detail presented in the right panels corresponds to the critical-curve detail below the point mass in the left panels. In the bottom row the caustic detail has a single cusp. By the second row it underwent a swallow-tail metamorphosis, which added a self-intersection and two cusps. A similar swallow-tail metamorphosis occurs on the caustic above the original cusp before the third row, adding a similar smaller feature. In the third row at $x_{\rm P} \approx 0.08075$ two simultaneous beak-to-beak metamorphoses occur, in which the facing cusps of the two swallow-tail features touch and reconnect. In the fourth row the caustic detail consists of a smooth fold and a detached three-cusped loop.

The transition following the detachment of the two loops also occurs between the second and the third row of Figure 2.5.A. The sequence shown in Figure 2.9 corresponds to the green elliptic umbilic boundary in Figure 2.6. The two small critical-curve loops shrink to two points at $x_{\rm P} \approx 0.095844$ in the second row, before expanding again to two loops. A similar effect can be seen in the caustic plots. The two small three-cusped loops shrink to two points at the elliptic umbilic metamorphosis in the second row, before expanding again to three-cusped loops.

Along the right column of crosses in Figure 2.6, which corresponds to the super-critical $\kappa_{\rm P} = 10^{-3}$ example, the sequence is simpler, with the critical curve undergoing only five transitions as the point-mass position varies from the halo center to an asymptotic distance. All the transitions occurring from the second row to the top of Figure 2.5.A are the same as for the sub-critical example. The development from the first to the second row is much simpler than in the sub-critical case, with the small positive-Jacobian critical-curve loop around the origin directly expanding to form the perturbed NFW radial critical curve. The two-cusped caustic loop approaches the origin from the right, forming the crescent-like caustic seen in the first row, and extending further to form the perturbed NFW radial caustic.

However, for super-critical mass parameters $\kappa_{\rm P} \lesssim 9.86 \cdot 10^{-4}$ the sequence of transitions close to the halo center differs markedly from either of the previous examples. For illustration, we demonstrate in Figure 2.10 the transition across the orange, dashed blue, and orange boundaries along the $\kappa_{\rm P} = 8 \cdot 10^{-4}$ grid line in the bottom right panel of Figure 2.6. These correspond to a sequence of lips, two simultaneous beak-to-beak, and lips metamorphoses. The additional third column in Figure 2.10 shows the caustic detail from the second column with the horizontal scale expanded $6\times$ to reveal the caustic structure.

Between the first and the second row, a second small positive-Jacobian critical-curve loop appears to the left of the first one. The two loops expand and connect together symmetrically at two points in the fourth row for $x_{\rm P} \approx 0.0213954$. The detached inner small negative-Jacobian loop shrinks and vanishes between

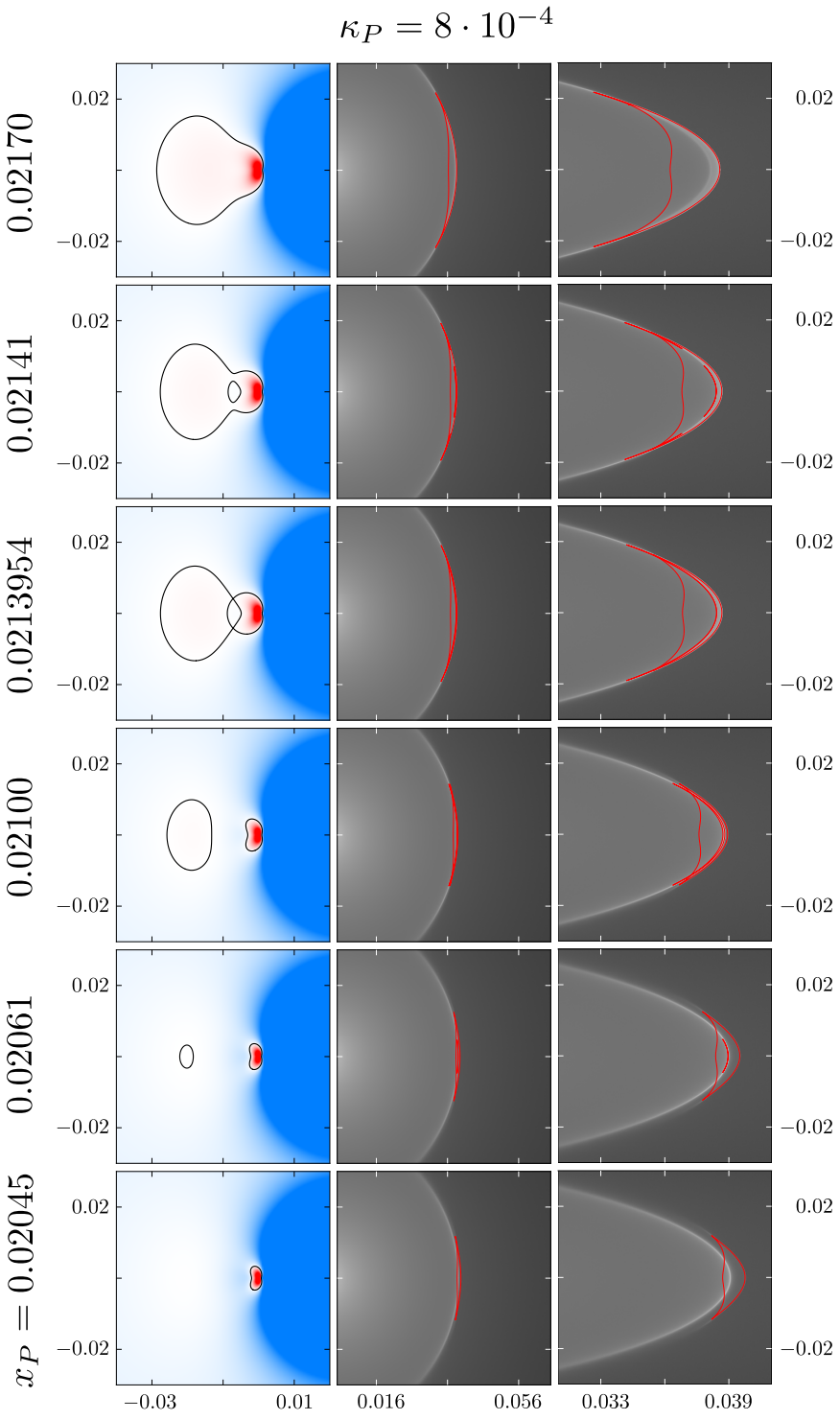

Figure 2.10: Critical-curve and caustic details for a super-critical $\kappa_{\rm P} = 8 \cdot 10^{-4}$ point mass near the halo center. Shown for six radial positions $x_{\rm P}$ marked along the left side, corresponding to transition across the orange, dashed blue, and orange boundaries along the $\kappa_{\rm P} = 8 \cdot 10^{-4}$ vertical line in the bottom right panel of Figure 2.6. The caustic details shown in the central column are expanded in the right column 6× horizontally to reveal the caustic structure. Compare with the corresponding sub-critical sequence in Figure 2.7. Notation and color bars as in Figure 2.5.A.

the top two rows. At larger x_P the remaining positive-Jacobian loop forms the perturbed radial NFW critical curve. In the bottom row the caustic detail shows the small two-cusped loop that arrived from the right to the brighter ring in the magnification map. In the second row the caustic has a second thin two-cusped loop inside the first loop that appeared along the bright ring in a lips metamorphosis. The two caustic loops overlap on the third row. In the fourth row two beak-to-beak metamorphoses occur, in which the outer part of the first loop reconnects symmetrically at two points with the inner part of the second loop. In the fifth row the caustic displays a disconnected thin inner two-cusped loop and small self-crossing features on the outer caustic loop. The features vanish in simultaneous swallow-tail metamorphoses, followed by the vanishing of the small two-cusped loop in a lips metamorphosis. At larger x_P, the two-cusped caustic loop seen in the top row forms the perturbed radial NFW caustic.

For mass parameters $\kappa_\mathrm{P} \gtrsim 1.323 \cdot 10^{-3}$, higher than in the presented examples, the green boundary in Figure 2.6 corresponding to the elliptic umbilic continues as the violet hyperbolic-umbilic boundary. We illustrate in Figure 2.11 the transition across this boundary along the $\kappa_\mathrm{P} = 2 \cdot 10^{-3}$ grid line in Figure 2.6. The two small critical-curve loops touch the perturbed NFW radial critical curve at $x_\mathrm{P} \approx 0.1317$ in the second row, before detaching again, as seen on the third row. In the bottom row the caustic detail shows a single cusp on the larger caustic loop and a closely adjacent small two-cusped loop. At the hyperbolic-umbilic metamorphosis in the second row, both parts of the caustic touch at a blunt angular point. In this metamorphosis a cusp gets transferred from one part of the caustic to another. This can be seen in the third row, where the detached smaller loop has three cusps while there is no cusp on the larger perturbed NFW radial caustic.

For completeness, we mention the parabolic umbilic, which occurs for $\kappa_\mathrm{P} \approx 1.323 \cdot 10^{-3}$ at $x_\mathrm{P} \approx 0.1202$. At this point, which is marked by the black circle in Figure 2.6, boundaries corresponding to four different pair-wise metamorphoses meet, namely: elliptic umbilic, hyperbolic umbilic, lips, and beak-to-beak. When passing through this point in the parameter plot in the sense of increasing x_P, two small loops detach from cusp-like points on the perturbed radial NFW critical curve, starting as points and expanding like in the elliptic umbilic. During the underlying caustic metamorphosis the two cusps on the perturbed radial NFW caustic disappear as two small three-cusped caustic loops detach from them. These caustic loops also start as points and increase in size. Varying the point-mass parameters in the vicinity of the parabolic umbilic point leads to a variety of different changes to the local structure of the caustic (e.g., Godwin 1971, Poston and Stewart 1978).

In Section 2.3.3 we studied the structure of critical curves and caustics for centrally positioned point masses, and demonstrated the distinction between the sub- and super-critical cases. If we look at the transition sequences for different values of κ_P in Figure 2.6, we see that the boundary intersections and limiting points form a finer subdivision into κ_P intervals, each with a specific transition sequence. The approximate values separating these intervals are

$$\kappa_\mathrm{P} \in \Big\{0,\, 1.62 \cdot 10^{-4},\, 2.71 \cdot 10^{-4},\, 9.86 \cdot 10^{-4},\, 1.32 \cdot 10^{-3},\, 2.26 \cdot 10^{-3},\, 2.97 \cdot 10^{-3}\Big\} \,. \quad (2.42)$$

To be precise, the first non-zero value actually should be replaced by two very

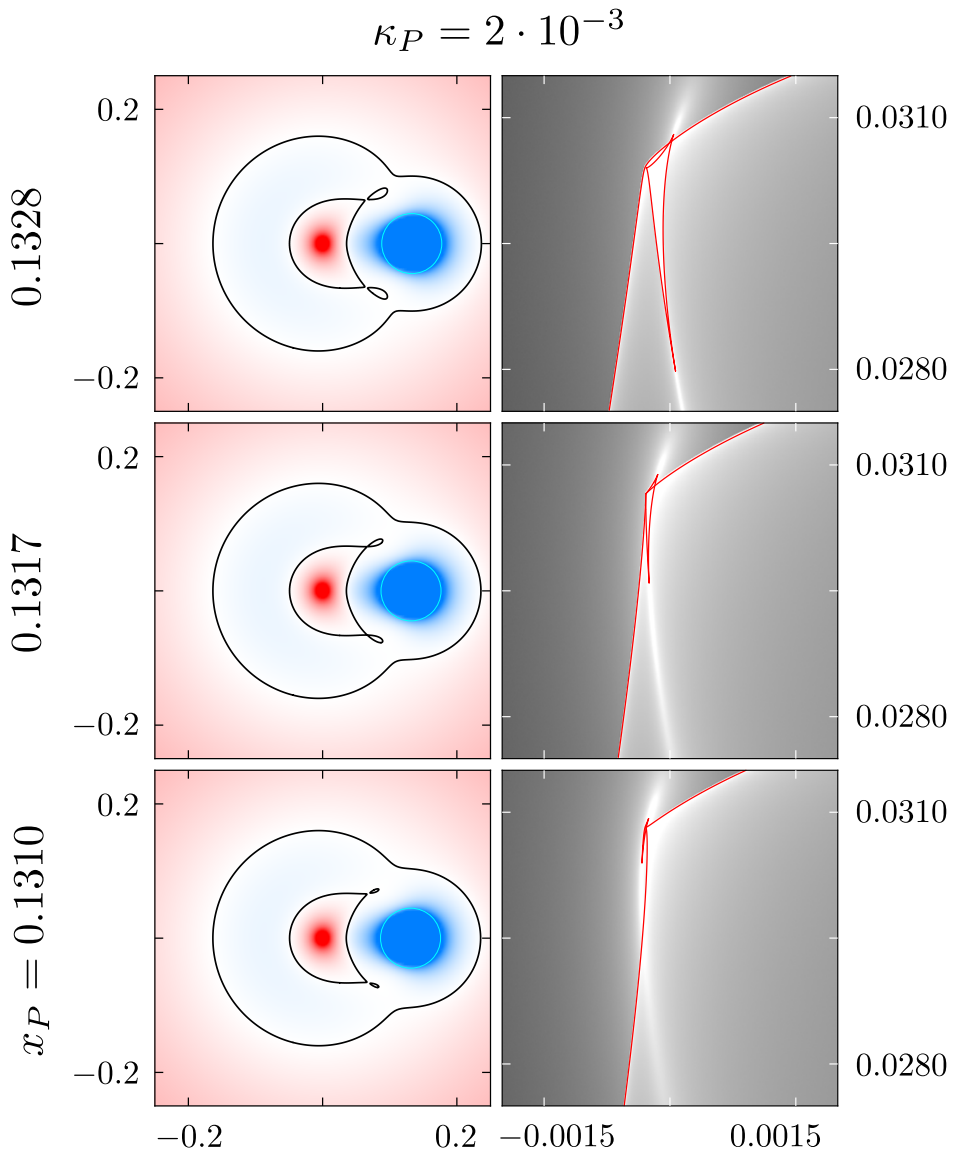

Figure 2.11: Critical curves and caustic details for a $\kappa_{\rm P} = 2 \cdot 10^{-3}$ point mass at two simultaneous hyperbolic umbilics (second row from bottom). Shown for three radial positions $x_{\rm P}$ marked along the left side, corresponding to transition across the violet boundary along the vertical $\kappa_{\rm P} = 2 \cdot 10^{-3}$ line in Figure 2.6. Notation and color bars as in Figure 2.5.A.

close $\kappa_{\rm P}$ values, because the cyan boundary in the bottom right panel of Figure 2.6 intersects the orange before the adjacent dashed blue boundary. The eight different sequences of critical-curve transitions can be read off Figure 2.6, aided by the galleries in Figure 2.5.A and Figure 2.5.B, as well as the transition sequences described in this Section.

Note that the $\kappa_{\rm P} = 10^{-4}$ sub-critical sequence with all the described transitions lies in the first interval defined by the values in Equation (2.42). Hence, any lower-mass point will have the same sequence of critical-curve transitions. Similarly, all point masses with $\kappa_{\rm P} \gtrsim 2.97 \cdot 10^{-3}$ share the same simple sequence, in which the only transition between the appearance of the small critical-curve loop around the origin and the final detachment of the point-mass loop from the perturbed tangential NFW critical curve is the hyperbolic umbilic. In this umbilic transition the perturbed radial and tangential NFW critical curves merely touch at two points. In the underlying caustic metamorphosis, the central four-cusped loop (similar to the caustic in the third row of Figure 2.5.A) extends and touches the two cusps of the crescent-like loop, resulting in a six-cusped central caustic and a smooth perturbed radial NFW caustic.

We point out that the interpretation of the parameter-space structure in Figure 2.6 presented above focused on vertical transitions across the boundaries, which corresponds to placing a fixed-mass point at different positions in the halo. One may interpet the figure just as well by following transitions in the horizontal sense, corresponding to placing points of different masses at a fixed position in the halo. Such explorations reveal that the structure of the critical curve is more sensitive to the mass of the point when it is placed in certain regions of the halo, e.g., close to its center or in a part of the annular region between the radial and tangential NFW critical curves.

2.4 Discussion

Most of the presented results were computed for a single fiducial value of the halo convergence parameter $\kappa_{\rm s} \approx 0.239035$, based on the Merten et al. (2015) galaxy cluster data as shown in Figure 2.1. For these clusters, $\kappa_{\rm s}$ varies from 0.15 to 0.84. Data from other cluster surveys such as OmegaWINGS (Biviano et al. 2017) indicate values as low as $\kappa_{\rm s} \approx 0.01$. In addition, since $\kappa_{\rm s}$ is normalized by the critical surface density defined by Equation (2.4), it also depends on the source redshift due to the direct proportionality $\kappa_{\rm s} \propto D_{\rm ls}/D_{\rm s}$. Plots of this angular diameter distance ratio as a function of source redshift can be found in Asada (1997) or Umetsu (2020).

The main question is what effect will changing $\kappa_{\rm s}$ have on the parameter-space boundaries in Figure 2.6. While a systematic study is in progress, we mention here a few general properties. The overall pattern of the boundaries shrinks toward the origin of the parameter-space plot as $\kappa_{\rm s}$ decreases, and expands from the origin as $\kappa_{\rm s}$ increases. In the vertical direction this can be inferred from the scaling of the NFW critical-curve radii shown in Figure 2.3, due to the importance of these radii on the vertical axis of Figure 2.6. In the horizontal direction this can be inferred from the importance of the relative "mass ratio" $\kappa_{\rm P}/\kappa_{\rm s}$ rather than the absolute value of $\kappa_{\rm P}$. Nevertheless, while the change of the overall scale in the parameter-space plot is most prominent, the shapes of the boundaries change

too, even though more weakly.

Regarding the source redshift, in addition to κ_s it affects also the point-mass parameter κ_P. The critical surface density in the denominator of the last expression in Equation (2.34) reveals that $\kappa_\mathrm{P} \propto D_\mathrm{ls}/D_\mathrm{s}$, the same proportionality seen in κ_s. Indeed, it is the ratio $\kappa_\mathrm{P}/\kappa_\mathrm{s} = M_\mathrm{P}/(\pi\, r_\mathrm{s}^3\, \rho_\mathrm{s})$ that is independent of the source, and is given purely by the properties of the lens. The third parameter of the studied lens system, x_P, does not depend on the source either.

It is worth pointing out the similarity of the structure of the perturbed tangential NFW critical curves and caustics (see Figure 2.5.A) to the critical curves and caustics of the two-point-mass lens (e.g., Erdl and Schneider 1993, Dominik 1999, Pejcha and Heyrovský 2009). For example, with increasing distance x_P the caustic changes from a central four-cusped loop with two three-cusped loops, all of which merge to form a single six-cusped loop, which then splits into two four-cusped loops. The same sequence can be seen in the close, intermediate, and wide regimes of the two-point-mass lens. Even the two topmost beak-to-beak boundaries seen in Figure 2.6 for $\kappa_\mathrm{P} \lesssim 0.002$ resemble the two-point-mass parameter-space boundaries (Erdl and Schneider 1993, top left panel in their Figure 6). In this mass range the lens systems differ in the "fate" of the three-cusped loops which recede from the central four-cusped loop as x_P decreases. In the NFW + point-mass lens they get only as far as the perturbed radial NFW caustic and merge with it, while in the two-point-mass lens they escape to infinity as the separation of the points decreases to zero. Overall, the only caustic loop that escapes to infinity from both components of the NFW + point-mass lens is the small two-cusped loop receding as the point mass approaches the halo center, $x_\mathrm{P} \to 0$.

The lens model explored in this work is relevant for several astrophysical scenarios. The primary motivation was to study the influence of a single galaxy on the overall lensing by a galaxy cluster. For this purpose, replacing the mass distribution within the galaxy by a point mass is the crudest possible approximation. Nevertheless, we may expect the structure of the critical curves to be similar except in the vicinity of the galaxy in the image plane. Clearly, the results in Figure 2.6 will be more relevant for galaxies in a cluster that have lower relative masses and lower scale or cutoff radii of their mass distributions. In addition, we may expect different behavior for galaxies positioned close to the cluster center. Since the Jacobian of galactic mass distributions typically does not have a negative divergence, its combination with the positive Jacobian divergence of the cluster halo will yield different critical-curve structures than those demonstrated above for a point mass. A more complete understanding would be obtained by a comparison study using an extended mass distribution model for the galaxy.

The next astrophysical scenario for which our model is relevant is a (dwarf) satellite galaxy in the dark matter halo of a larger host galaxy. The comments made above for a galaxy within a cluster hold here too. For example, combining the host-galaxy halo with an extended-mass distribution for the satellite could lead to interesting comparisons with binary-galaxy lens models (e.g., Shin and Evans 2008). Our obtained results are more relevant for low-relative-mass compact satellite galaxies. In this scenario, another step toward a more realistic model would be to alter the spherical NFW model for the mass distribution of the host galaxy, e.g., by including ellipticity, adding a core radius, or altering the

central density divergence (Evans and Wilkinson 1998).

Interestingly, our results are most relevant for the third scenario, a massive or super-massive black hole in the dark matter halo of its host galaxy. In such a setting the black hole is perfectly modeled by a simple point-mass lens, since the fraction of the lensed flux in relativistic higher-order images is negligible. In this scenario, the details close to the origin of the halo can be expected to change in mass-distribution models that eliminate the central divergence of the NFW density profile. Regarding the position of the black hole, in most cases it may be expected to lie at the center of the galactic halo. However, in dwarf galaxies massive black holes have been recently found even at their outskirts (Reines et al. 2020). Similar wandering massive black holes are expected to inhabit the outer parts of regular galaxies as well (Guo et al. 2020). Such cases give observational significance to the $x_{\rm P} > 0$ results. For the more typical central position, the main result is the difference between the lensing effects of sub- and super-critical-mass black holes.

2.5 Summary

We explored gravitational lensing by a massive object in a dark matter halo, using the simple model of a point mass in a halo with a NFW density profile. In this work we concentrated on the critical curves and caustics of the lens, in particular on their changes as a function of mass and position of the object. For computing the light deflection angle close to the NFW halo center we derived the numerically stable exact expression given by Equation (A.6).

For a point mass positioned at the center of the halo we demonstrated the existence of a critical mass parameter $\kappa_{\rm PC}$, above which the gravitational influence of the object is strong enough to eliminate the radial critical curve and caustic of the NFW halo, as shown in Figure 2.4. This result is similar to the behavior of a point mass embedded in a cored isothermal sphere (Mao et al. 2001) and in a Plummer model (Werner and Evans 2006), but not in a singular isothermal sphere (Mao and Witt 2012). In Appendix A.2, we demonstrated the peculiar nature of the single radial critical curve and caustic in the critical-mass case, as well as the non-local metamorphosis of their vanishing. Crossing this caustic in the source plane does not change the number of images, and the magnification diverges on both sides of the caustic at a rate typical for a cusp approached perpendicularly, rather than for a fold caustic approached from its inner side.

For a general position of the point mass we found a surprising richness of critical-curve regimes in the point-mass parameter space. Transitions between the regimes occur along boundaries mapped in detail in Figure 2.6, which correspond to underlying caustic metamorphoses. The variety of local metamorphoses occurring in the low-mass regime of this simple lens model is unusually high. In fact, all caustic metamorphoses with three control parameters (beak-to-beak, swallow tail, lips, elliptic umbilic, and hyperbolic umbilic) plus the four-parameter parabolic umbilic occur here (Schneider et al. 1992).

In Section 2.4 we discussed the effect of changing the halo convergence parameter $\kappa_{\rm s}$ on the presented results, and pointed out the similarities between the perturbed tangential NFW caustics for low masses and the caustic regimes of the two-point-mass lens. We commented on the relevance of the results for three

different astrophysical scenarios: a galaxy in a galaxy cluster, a dwarf galaxy in the halo of a host galaxy, and a (super)massive black hole in a galaxy halo. Particularly in the first two cases, similar studies of lens models with an extended mass distribution for the smaller object can be performed for comparison with the presented results of the simplest model.

Acknowledgements

We thank the anonymous referee and Paolo Salucci for helpful comments and suggestions on the manuscript. Work on this project was supported by Charles University Grant Agency project GA UK 1000218.

3. Gravitational Lensing by a Massive Object in a Dark Matter Halo. II. Shear, Phase, and Image Geometry[1]

Abstract

We study the gravitational lensing influence of a massive object in a dark matter halo, using a simple model of a point mass embedded in a spherical Navarro–Frenk–White halo. Building on the analysis of critical curves and caustics presented in the first part of this work, we proceed to explore the geometry of images formed by the lens. First, we analyze several lensing quantities including shear, phase, and their weak-lensing approximations, illustrating the results with image-plane maps. We derive formulae and present a geometric interpretation for the shear and phase of a combination of two axially symmetric mass distributions. In the case of our lens model, we describe the occurrence of zero-shear points and specify the conditions under which they become umbilic points. Second, we use the eigenvalue decomposition of the inverse of the lens-equation Jacobian matrix to compute the magnification and flattening of lensed images. Based on this, we introduce the convergence–shear diagram, a novel and compact way of visualizing the properties of images formed by a particular gravitational lens. We inspect relative deviations of the analyzed lensing quantities in order to evaluate the perturbing effect of the point mass and the applicability of the weak-lensing approximation. We explore the dependence of the results on the point-mass parameters by studying grids of plots for different combinations of its position and mass. We provide analytical explanations for important patterns arising in these plots and discuss the implications for the lensing influence of isolated compact bodies in dark matter halos.

Keywords: gravitational lensing — galaxy clusters — dark matter halos — dwarf galaxies — supermassive black holes

[1]Karamazov and Heyrovský (2022)

3.1 Introduction

Dark matter halos form the basic building blocks in the bottom-up structure formation of ΛCDM cosmology. They constitute the dominant matter component of the astrophysical objects they are associated with: the largest halos with galaxy clusters; smaller halos with individual galaxies and dwarf galaxies. Their properties can be studied by "observations" in the virtual universes arising from large-scale-structure formation simulations (e.g., Zandanel et al. 2018). In our universe, main observational constraints on galaxy-cluster dark matter halos come from the study of the kinematics of cluster galaxies (starting from Zwicky 1933), from measurements of X-ray emission from intracluster baryonic gas (e.g., Ettori et al. 2013), and from analyses of weak and strong gravitational lensing of background galaxies (e.g., Limousin et al. 2007, Okabe et al. 2013). Gravitational lensing analyses are particularly useful as tools for studying the finer-scale substructure of cluster halos, such as subhalos of individual cluster galaxies, local clumps or other inhomogeneities. A detailed analysis of 11 galaxy clusters by Meneghetti et al. (2020) revealed a surprisingly high efficiency of substructure lensing, more than an order of magnitude higher than expected from CDM simulations. This result indicates the need for a better understanding of the lensing effects of individual bodies within the cluster.

The goal of our work is to study the gravitational lensing influence of a compact massive body in a dark matter halo. For this purpose, we use a simple model consisting of a point mass embedded in a spherical Navarro–Frenk–White (NFW) density profile (Navarro et al. 1996). In the first part of this work (Karamazov et al. 2021, hereafter Paper I), we studied the critical curves and caustics of the lens model as a function of the mass and position of the point mass. We discovered that the model exhibited a rich diversity of critical-curve topologies and caustic geometries. We mapped the boundaries separating the corresponding lensing regimes in the point-mass parameter space and identified the accompanying caustic metamorphoses. Among other findings, we demonstrated the existence of a critical value of the mass parameter. For centrally positioned lighter (sub-critical) point masses, the lens has two radial critical curves. Heavier (super-critical) point masses are strong enough to fully eliminate the radial critical curves. For critical point masses the lens has a single radial critical curve with peculiar properties, which are described in Appendix B of Paper I. We discussed the relevance of the model to the lensing by galaxies in galaxy-cluster halos as well as other astrophysical scenarios, such as the lensing influence of a satellite galaxy or a (super-)massive black hole in a galactic dark matter halo.

In this sequel to Paper I, we explore other lensing properties of the model. Here we concentrate on the shear and phase and their relation to the geometric distortions of images formed by the lens. In the weak-lensing regime the relation is tight, with the shear specifying the semi-axis ratio and the phase specifying the orientation of the major axis of the image. However, this will not be the case in the regions with high convergence (near the halo center) or high shear (near the point mass and near the halo center). In Section 3.2 we describe the shear, phase, and image geometry for a NFW-halo-only lens. We study the images in Section 3.2.3, starting from the eigenvalue decomposition of the inverse of the Jacobian matrix and utilizing the convergence–shear diagram, a new tool described in detail in

Appendix A.3. In Section 3.2.4 we introduce the weak shear and weak phase and compare these weak-lensing estimates with the shear and phase.

In Section 3.3 we proceed with the analysis of the NFW halo + point-mass lens in a similar manner. More specifically, in Section 3.3.1 we derive formulae for the shear and phase of the combined mass distribution. We describe the emergence and occurrence of points with zero shear, which may constitute umbilic points under conditions discussed in Section 3.3.2. In Section 3.3.3 we study the properties of images using the convergence–shear diagram. We present the main results in Section 3.3.5 in the form of grids of image-plane maps of different lens characteristics and convergence–shear diagrams, utilizing the same point-mass parameter grid as in Paper I. We discuss the results and their broader relevance in Section 3.4 and summarize our findings in Section 3.5.

3.2 Lensing by an NFW halo

3.2.1 Convergence, shear, and phase

The surface density of a halo with a spherical NFW profile expressed in units of the critical surface density $\Sigma_{\rm cr}$ yields the dimensionless convergence profile (Bartelmann 1996; Paper I),

$$\kappa_{\rm NFW}(x) = 2\,\kappa_{\rm s}\,\frac{1-\mathcal{F}(x)}{x^2-1}\,, \tag{3.1}$$

where x is the plane-of-the-sky distance from the halo center expressed in units of the halo scale radius $r_{\rm s}$, and $\kappa_{\rm s}$ is the halo convergence parameter. The function

$$\mathcal{F}(x) = \begin{cases} \dfrac{\operatorname{arctanh}\sqrt{1-x^2}}{\sqrt{1-x^2}} & \text{for } x<1\,, \\ 1 & \text{for } x=1\,, \\ \dfrac{\arctan\sqrt{x^2-1}}{\sqrt{x^2-1}} & \text{for } x>1\,, \end{cases} \tag{3.2}$$

has a similar radial behavior to the convergence $\kappa_{\rm NFW}(x)$: both decrease monotonically from ∞ at the halo center to 0 for $x \gg 1$ (see Paper I for details). The radius x_0 at which the convergence is equal to 1 can be computed numerically from

$$\frac{1-x_0^2}{\mathcal{F}(x_0)-1} = 2\,\kappa_{\rm s}\,. \tag{3.3}$$

This unit-convergence radius and the circle that it defines play a key role when studying the geometry of images formed by a lens. For the NFW halo x_0 increases monotonically with the convergence parameter $\kappa_{\rm s}$, as illustrated in Paper I. We note here that for $\kappa_{\rm s} = 3/2$ the unit-convergence radius is equal to the scale radius, $x_0 = 1$. For lower values of $\kappa_{\rm s}$ the unit-convergence circle lies inside the scale-radius circle; for higher values outside.

A light ray passing through the halo at a position $\boldsymbol{x}$ in the plane of the sky is deflected by an angle

$$\boldsymbol{\alpha}(\boldsymbol{x}) = \frac{4\,\kappa_{\rm s}\,r_{\rm s}\,D_{\rm s}}{D_{\rm l}\,D_{\rm ls}}\,\left[\ln\frac{x}{2}+\mathcal{F}(x)\right]\,\frac{\boldsymbol{x}}{x^2}\,, \tag{3.4}$$

where D_l, D_s, and D_ls are the angular-diameter distances from the observer to the lens, from the observer to the source, and from the lens to the source, respectively. Expressed in units of the angular scale radius, the position of a source $\boldsymbol{y}$ and the position of its image $\boldsymbol{x}$ formed by the gravitational field of the NFW halo are connected by the lens equation

$$\boldsymbol{y} = \boldsymbol{x} - 4\,\kappa_\mathrm{s}\,\left[\ln\frac{x}{2} + \mathcal{F}(x)\right]\,\frac{\boldsymbol{x}}{x^2}\,. \tag{3.5}$$

For illustration, in the top row of Figure 3.1 we show the lensing of a circular source by a NFW halo with convergence parameter $\kappa_\mathrm{s} \approx 0.239035$, the fiducial value used in Paper I. As seen in the top left panel, in this example the black circular source centered at $\boldsymbol{y}_\mathrm{c} = (0.015,\, -0.005)$ with radius $y_\mathrm{r} = 0.005$ lies inside the radial caustic without overlapping the central point-like tangential caustic. Solving the lens Equation (3.5) numerically for a point $\boldsymbol{y}$ on the circumference of the source yields three points $\boldsymbol{x}$ on the boundaries of the three black images shown in the top right panel. One image lies outside the tangential critical curve, a second image lies between the tangential and radial critical curves, and the smallest third image lies inside the radial critical curve. The dashed circle with

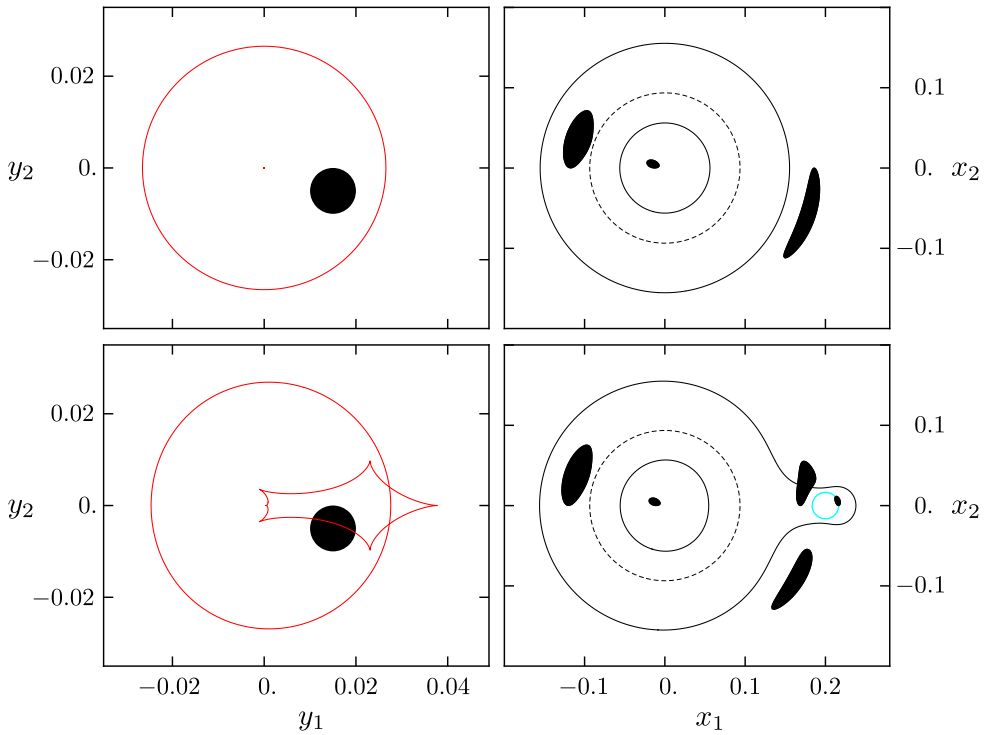

Figure 3.1: Gravitational lensing of a circular source. Top row: lensing by a NFW halo with convergence parameter $\kappa_\mathrm{s} \approx 0.239035$. Bottom row: lensing by the same halo with an additional point mass with mass parameter $\kappa_\mathrm{P} \approx 2.714{\cdot}10^{-4}$ positioned at $\boldsymbol{x}_\mathrm{P} = (0.2,\, 0)$. Left column: source-plane plots indicating the position of the source (black circle) with respect to the lens caustic (red lines). Right column: image-plane plots indicating the positions of images (black patches) with respect to the critical curve (solid black lines). The cyan circle in the bottom right panel marks the Einstein circle of the point mass; the dashed black lines in the right panels mark the unit-convergence circle.

radius $x_0 \approx 0.0936$ is the unit-convergence circle of this halo. In this case, the first two images are elongated in the tangential (azimuthal) direction, while the third image is elongated in the radial direction.

For a source lying inside the radial caustic and overlapping the central tangential caustic, the first two images would merge along the tangential critical curve, forming an Einstein ring. For a smaller source positioned close to the inner side of the radial caustic, the second image would lie inside the unit-convergence circle and be elongated in the radial direction. For a source positioned on the radial caustic, the second and third images would merge at the radial critical curve. For a source lying outside the radial caustic, these two images would vanish, leaving only the first image.

The deformations and orientations of the images are best studied by computing the lens shear and its phase, quantities that may be introduced by means of the lens potential. The deflection angle can be written in terms of the gradient of the lens potential $\psi(x)$, which in this case is circularly symmetric,

$$\boldsymbol{\alpha}(\boldsymbol{x}) = \frac{D_\mathrm{s}}{D_\mathrm{ls}} \nabla_{\boldsymbol{\theta}}\, \psi(x) = \frac{D_\mathrm{s}\, D_\mathrm{l}}{D_\mathrm{ls}\, r_\mathrm{s}}\, \frac{\boldsymbol{x}}{x}\, \frac{\mathrm{d}\psi}{\mathrm{d}x}\,, \tag{3.6}$$

where we converted the angular position in radians $\boldsymbol{\theta}$ to the angular position in scale-radius units, $\boldsymbol{x} = \boldsymbol{\theta}\, D_\mathrm{l}/r_\mathrm{s}$. By substituting for the deflection angle from Equation (3.4) we can express the lens-potential derivative

$$\frac{\mathrm{d}\psi_\mathrm{NFW}}{\mathrm{d}x} = \frac{4\,\kappa_\mathrm{s}\, r_\mathrm{s}^2}{D_\mathrm{l}^2}\, \frac{1}{x}\, \left[\ln \frac{x}{2} + \mathcal{F}(x)\right]\,. \tag{3.7}$$

Integration yields the following expressions for the NFW halo lens potential (Meneghetti et al. 2003, Golse and Kneib 2002):

$$\psi_\mathrm{NFW}(x) = \begin{cases} \frac{2\,\kappa_\mathrm{s}\, r_\mathrm{s}^2}{D_\mathrm{l}^2} \left[\ln x \ln \frac{x}{4} - (\operatorname{arctanh} \sqrt{1-x^2}\,)^2\right] \\ 0 \\ \frac{2\,\kappa_\mathrm{s}\, r_\mathrm{s}^2}{D_\mathrm{l}^2} \left[\ln x \ln \frac{x}{4} + (\arctan \sqrt{x^2-1}\,)^2\right]\,, \end{cases} \tag{3.8}$$

where the expression in the first row holds for $x < 1$, in the second row for $x = 1$, and in the third row for $x > 1$. For $x \ll 1$, the potential close to the halo center

$$\psi_\mathrm{NFW}(x) = -\,\frac{2\,\kappa_\mathrm{s}\, r_\mathrm{s}^2}{D_\mathrm{l}^2} \left(\ln^2 2 + \frac{x^2}{2}\, \ln \frac{x}{2}\right) + \mathcal{O}(x^4\, \ln x)\,, \tag{3.9}$$

starting from a finite negative value and increasing monotonically outward, crossing zero at the scale radius. Note that the expressions for the potential in Meneghetti et al. (2003) and Golse and Kneib (2002) are higher by the constant $-\psi_\mathrm{NFW}(0)$ and thus they start at zero.

For a circularly symmetric lens potential the lens shear γ can be computed as

$$\gamma = \frac{D_\mathrm{l}^2}{2\, r_\mathrm{s}^2} \left|\frac{\mathrm{d}^2\psi}{\mathrm{d}x^2} - \frac{1}{x}\frac{\mathrm{d}\psi}{\mathrm{d}x}\right|\,. \tag{3.10}$$

For the NFW profile the second derivative of the lens potential,

$$\frac{\mathrm{d}^2\psi_\mathrm{NFW}}{\mathrm{d}x^2} = \frac{4\,\kappa_\mathrm{s}\, r_\mathrm{s}^2}{D_\mathrm{l}^2} \left[\frac{1}{x^2-1} + \frac{2x^2-1}{x^2(1-x^2)}\, \mathcal{F}(x) - \frac{1}{x^2} \ln \frac{x}{2}\right]\,, \tag{3.11}$$

can be used together with the first derivative from Equation (3.7) in Equation (3.10) to yield the shear of the NFW halo,

$$\gamma_{\rm NFW}(x) = 2\,\kappa_{\rm s}\left[\frac{2}{x^2}\ln\frac{x}{2} + \frac{1}{1-x^2} + \frac{2-3x^2}{x^2(1-x^2)}\,\mathcal{F}(x)\right], \tag{3.12}$$

as shown by Wright and Brainerd (2000). In order to understand its behavior close to the origin, we expand Equation (3.12) for $x \ll 1$ and obtain

$$\gamma_{\rm NFW}(x) = \kappa_{\rm s}\left[1 + \frac{3}{2}\,x^2\,\ln\frac{x}{2} + \frac{13}{8}\,x^2\right] + \mathcal{O}(x^4\,\ln x)\,. \tag{3.13}$$

By setting $x = 0$ we see that the NFW shear at the center is equal to the convergence parameter of the halo, $\gamma_{\rm NFW}(0) = \kappa_{\rm s}$. From this value the shear decreases outward monotonically. An expansion close to the scale radius shows that for $x \to 1$

$$\gamma_{\rm NFW}(x) = 2\,\kappa_{\rm s}\left[\frac{5}{3} - 2\,\ln 2 - 4\left(\frac{11}{15} - \ln 2\right)(x-1)\right] + \mathcal{O}((x-1)^2)\,, \tag{3.14}$$

which yields $\gamma_{\rm NFW}(1) \approx 0.561\,\kappa_{\rm s}$. The NFW shear decreases for $x \gg 1$ to zero,

$$\gamma_{\rm NFW}(x) = 2\,\kappa_{\rm s}\left[\frac{2}{x^2}\,\ln\frac{x}{2} - x^{-2} + \frac{3\pi}{2}\,x^{-3} - 4\,x^{-4}\right] + \mathcal{O}(x^{-5})\,. \tag{3.15}$$

The first panel in Figure 3.2 shows a contour plot of the shear $\gamma_{\rm NFW}(\boldsymbol{x})$ in the central part of a NFW halo. Going outward from the center, the dotted contours correspond to 95%, 90%, and 85% of the central shear $\gamma_{\rm NFW}(0) = \kappa_{\rm s}$. Clearly, the shear changes very slowly on this scale, as indicated also by the practically homogeneous color, with the color bar set for comparison with further figures. The solid black circles mark the radial (smaller) and tangential (larger) critical curve for the fiducial halo convergence parameter $\kappa_{\rm s} \approx 0.239035$.

The NFW shear can be written in terms of its two components, defined as

$$(\gamma_{\rm NFW1}, \gamma_{\rm NFW2}) = \gamma_{\rm NFW}\,(\cos 2\varphi_{\rm NFW}, \sin 2\varphi_{\rm NFW})\,, \tag{3.16}$$

where the trigonometric functions of the phase $\varphi_{\rm NFW}$ can be computed for a point $\boldsymbol{x} = (x_1, x_2) = x(\cos\phi, \sin\phi)$ in the image plane as

$$(\cos 2\varphi_{\rm NFW}, \sin 2\varphi_{\rm NFW}) = x^{-2}(x_2^2 - x_1^2, -2x_1x_2) = -(\cos 2\phi, \sin 2\phi)\,. \tag{3.17}$$

The negative sign in front of the last parentheses indicates that the phase $\varphi_{\rm NFW} = \phi + \pi/2 + k\pi$, i.e., its orientation is always perpendicular to the position vector of the point. Note that this also means that the phase and the shear components are undefined at $x = 0$, since the phase depends on the direction of approach to the center.

3.2.2 Jacobian

The Jacobian matrix of a general lens equation expressed in terms of the convergence $\kappa(\boldsymbol{x})$, shear $\gamma(\boldsymbol{x})$, and phase $\varphi(\boldsymbol{x})$ has the form (e.g., Schneider et al. 1992)

$$J(\boldsymbol{x}) = \frac{\partial\,\boldsymbol{y}}{\partial\,\boldsymbol{x}} = \begin{pmatrix} 1-\kappa-\gamma\cos 2\varphi & -\gamma\sin 2\varphi \\ -\gamma\sin 2\varphi & 1-\kappa+\gamma\cos 2\varphi \end{pmatrix}. \tag{3.18}$$

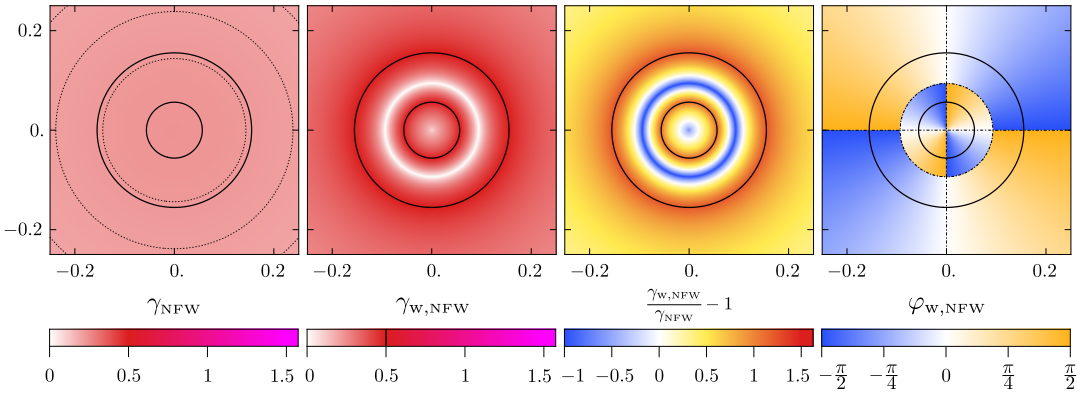

Figure 3.2: Image-plane color maps of lensing characteristics of the NFW halo from the top row of Figure 3.1. For orientation, solid black circles mark the critical curves in all panels. First panel: shear $\gamma_{\rm NFW}(\boldsymbol{x})$ with dotted contours from inside to outside marking 95%, 90%, and 85% of the central shear $\gamma_{\rm NFW}(0) = \kappa_{\rm s} \approx 0.239035$. Second panel: weak shear $\gamma_{\rm w,NFW}(\boldsymbol{x})$ computed from image flattening, using the same color bar as in the first panel. Third panel: relative weak-shear deviation from the shear, $\gamma_{\rm w,NFW}(\boldsymbol{x})/\gamma_{\rm NFW}(\boldsymbol{x}) - 1$. Fourth panel: weak phase $\varphi_{\rm w,NFW}(\boldsymbol{x})$ defined by image orientation, with orange corresponding to images oriented counterclockwise, and blue to images oriented clockwise from the horizontal. Dot-dashed lines mark the unit-convergence circle, and locations of horizontal (white background) and vertical images (high-saturation blue/orange boundary).

Its determinant, the Jacobian, can be computed from the convergence and the shear:

$$\det J(\boldsymbol{x}) = [\,1 - \kappa(\boldsymbol{x}) - \gamma(\boldsymbol{x})\,]\,[\,1 - \kappa(\boldsymbol{x}) + \gamma(\boldsymbol{x})\,]\,. \tag{3.19}$$

The critical curves, explored in detail in Paper I, can be obtained by setting $\det J(\boldsymbol{x}) = 0$. We note here merely that for an axially symmetric lens such as the studied NFW halo, the first term in Equation (3.19) yields the tangential critical curve and the second term yields the radial critical curve. Hence, the shear is related to the convergence by $\gamma(x_{\rm T}) = 1 - \kappa(x_{\rm T})$ at the tangential critical curve, and by $\gamma(x_{\rm R}) = \kappa(x_{\rm R}) - 1$ at the radial critical curve, with the two critical curves separated by the unit-convergence circle.

3.2.3 Geometry of images

To study the geometry of the images, we invert the Jacobian matrix to obtain the mapping from the source plane to the image plane. We can write the inverse matrix in terms of its two eigenvalues,

$$\lambda_{\parallel}(\boldsymbol{x}) = (1 - \kappa - \gamma)^{-1}, \qquad \lambda_{\perp}(\boldsymbol{x}) = (1 - \kappa + \gamma)^{-1}\,, \tag{3.20}$$

as

$$\mathbb{A}(\boldsymbol{x}) = \lambda_{\parallel} \begin{pmatrix} \cos^2\varphi & \cos\varphi\sin\varphi \\ \cos\varphi\sin\varphi & \sin^2\varphi \end{pmatrix} + \lambda_{\perp} \begin{pmatrix} \sin^2\varphi & -\cos\varphi\sin\varphi \\ -\cos\varphi\sin\varphi & \cos^2\varphi \end{pmatrix}\,, \tag{3.21}$$

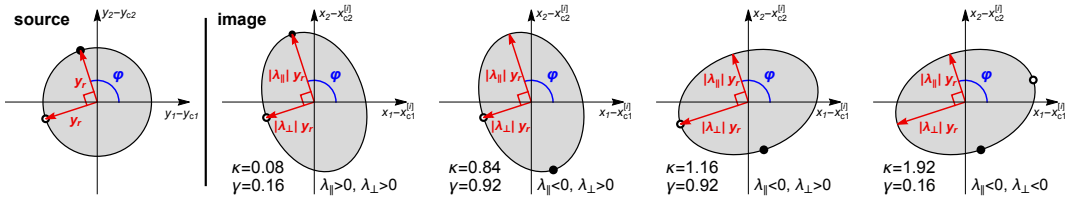

Figure 3.3: Geometry of an image of a small circular source. Left panel: source with radius y_r; the black and white points lie in the directions of the eigenvectors of the inverse Jacobian matrix $\mathbb{A}$ parallel and perpendicular to the phase φ. Right panels: elliptical image for $(\kappa, \gamma) = (0.08, 0.16)$ and the three other combinations producing an ellipse of the same shape and size, as marked at the bottom left of each panel. The sizes of the semi-axes are marked in red; the positions of the images of the two points marked on the circumference are determined by the signs of the eigenvalues marked at the bottom right of each panel.

where κ, γ, and φ are functions of the image-plane position $\boldsymbol{x}$. The matrix accompanying $\lambda_\parallel$ is a projection matrix onto the eigenvector $(\cos\varphi, \sin\varphi)$; the matrix accompanying $\lambda_\perp$ is a projection matrix onto the eigenvector $(-\sin\varphi, \cos\varphi)$. Equation (3.21) shows that an image at position $\boldsymbol{x}$ is scaled by a factor $\lambda_\parallel$ in the direction parallel to the phase φ, and by a factor $\lambda_\perp$ in the direction perpendicular to the phase, $\varphi + \pi/2$.

A small circular source with radius y_r centered at $\boldsymbol{y}_\mathrm{c}$ is thus portrayed by the lens as a set of n small elliptical images with semiaxes $y_\mathrm{r}/|1 - \kappa(\boldsymbol{x}_\mathrm{c}^{[i]}) - \gamma(\boldsymbol{x}_\mathrm{c}^{[i]})|$ and $y_\mathrm{r}/|1 - \kappa(\boldsymbol{x}_\mathrm{c}^{[i]}) + \gamma(\boldsymbol{x}_\mathrm{c}^{[i]})|$. Their positions $\boldsymbol{x}_\mathrm{c}^{[i]}(\boldsymbol{y}_\mathrm{c})$, $i = 1 \ldots n$, can be found by solving the lens equation, i.e., Equation (3.5) for the NFW halo. We illustrate the geometry of one such image in the second panel of Figure 3.3 for convergence $\kappa(\boldsymbol{x}_\mathrm{c}^{[i]}) = \kappa = 0.08$ and shear $\gamma(\boldsymbol{x}_\mathrm{c}^{[i]}) = \gamma = 0.16$. In the three right panels we include all other (κ, γ) combinations that lead to the same combination of semi-axes $|\lambda_\parallel|\, y_\mathrm{r}$ and $|\lambda_\perp|\, y_\mathrm{r}$, i.e., they generate an elliptical image of the same shape and size. The images differ in their orientation and parity. For the combinations in the two right panels with $\kappa > 1$ the major axis is oriented perpendicular to the phase φ rather than parallel to it. The images in the third and fourth panels have negative parity, as indicated by the positions of the images of the black and white points on the circumference of the source. The signs of the eigenvalues are marked in each panel, with negative values indicating mirroring along the corresponding eigenvector.

For a general source, the distortion of its image can be quantified by the dimensionless flattening,

$$f(\kappa, \gamma) = 1 - \min\left(\left|\frac{1-\kappa-\gamma}{1-\kappa+\gamma}\right|, \left|\frac{1-\kappa+\gamma}{1-\kappa-\gamma}\right|\right) , \tag{3.22}$$

defined here using the ratio of the smaller to larger eigenvalues, with their definitions taken from Equation (3.20). For an elliptical image of a circular source, f is equal to its ellipticity. For the sample images in Figure 3.3, $f \approx 0.30$. While the absolute value of the ratio of the eigenvalues determines the distortion of the image, their product determines its magnification and parity. Hence, it is

sufficient to know the convergence κ and shear γ at the position of an image of a small source in order to fully determine its distortion, magnification, parity, and orientation with respect to the phase.

For a given gravitational lens, this information can be condensed into the convergence–shear (hereafter CS) diagram, introduced in Appendix A.3. The geometry of images formed by a NFW halo lens as a function of their radial position x can be easily identified from its CS diagram, shown in Figure 3.4 for the fiducial convergence parameter $\kappa_s \approx 0.239035$. The green curve connecting the $(\kappa_{\rm NFW}(x), \gamma_{\rm NFW}(x))$ points is obtained by using the NFW halo convergence from Equation (3.1) and the NFW halo shear from Equation (3.12). The center of the halo corresponds to position $(\kappa, \gamma) = (\infty, \kappa_s)$ in the diagram, while for $x \to \infty$ the green curve reaches the origin, $(\kappa, \gamma) \to (0, 0)$. The tick marks along the curve correspond to radii (from the right side of the plot) $x \in \{0.002, 0.003, \ldots, 0.01, 0.02, \ldots, 0.1, 0.2, \ldots, 1, 2\}$.

In order to interpret the image geometries in a NFW halo from Figure 3.4, we follow the green curve, starting from the origin for very distant images and progressing toward the halo center. We first recall the discussion following Equation (3.17), which implies that for the NFW profile the direction of the phase corresponds in polar coordinates to the tangential, and the direction perpendicular to the phase to the radial direction, respectively. Initially, the image has

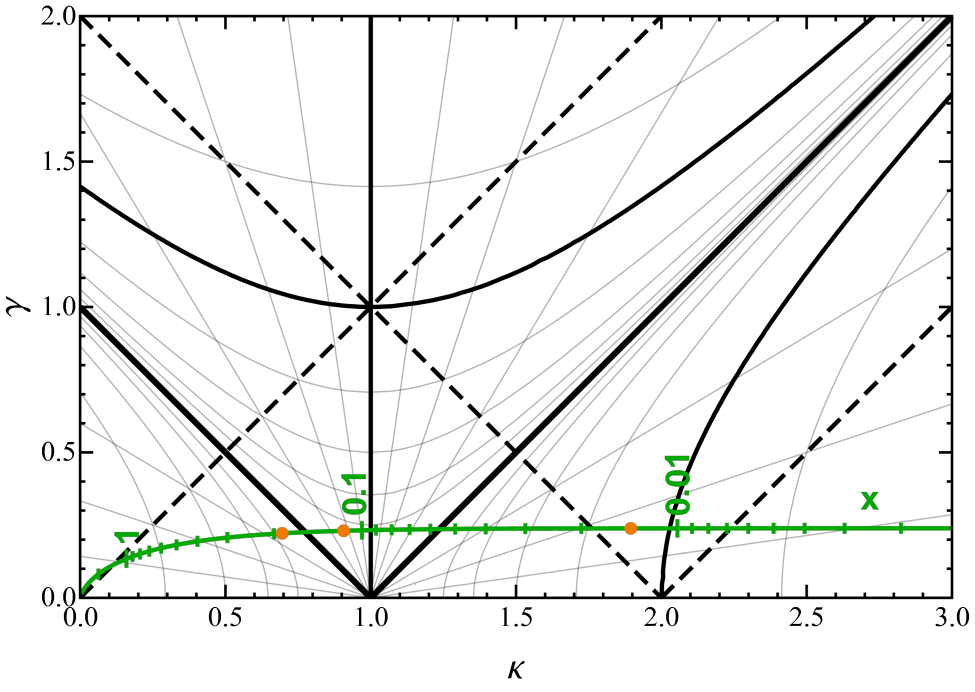

Figure 3.4: CS diagram illustrating the geometry of images formed by the NFW halo from the top row of Figure 3.1 with $\kappa_s \approx 0.239035$. The green line marks all $(\kappa_{\rm NFW}(x), \gamma_{\rm NFW}(x))$ combinations of the lens, with radial positions x marked by tick marks, starting from $x = 0.002$ near the right edge and ending with $x = 2$ close to the origin of the diagram. The orange dots mark the (κ, γ) combinations at the positions of the three images in the top right panel of Figure 3.1. For more details on the diagram and its interpretation see Figure A.2.

positive parity with magnification increasing from 1 and the flattening increasing from 0. The image is expanded tangentially ($|\lambda_\parallel| > 1$) but contracted radially ($|\lambda_\perp| < 1$), as indicated by the position above the dashed line.

Between $x = 2$ and $x = 1$ the green line crosses the diagonal and the image becomes expanded also radially ($|\lambda_\perp| > 1$). For lower x, the green curve approaches the solid black tangential-critical-curve line, along which the magnification and $|\lambda_\parallel|$ become infinite, the flattening increases to 1, and $|\lambda_\perp|$ remains finite. After crossing the tangential critical curve at $x = x_\mathrm{T} \approx 0.155$, the image parity changes to negative (due to the sign of $\lambda_\parallel$ changing to negative) and the magnification and flattening decrease. The maximum distortion stays oriented tangentially until reaching the unit-convergence circle, $x = x_0 \approx 0.0936$, corresponding to the vertical solid black line at $\kappa = 1$. To the right of this line the maximum distortion is oriented radially. At the unit-convergence radius the negative-parity image is close to its lowest magnification (though it stays higher than 16 in this case, as indicated by the hyperbolic contours), and with zero flattening its shape is undistorted.

Proceeding further toward the halo center, the magnification and flattening increase again, with the radial expansion $|\lambda_\perp|$ growing rapidly while the tangential expansion $|\lambda_\parallel|$ decreases. At the solid black radial-critical-curve line, which corresponds to $x = x_\mathrm{R} \approx 0.056$, the magnification and $|\lambda_\perp|$ become infinite, the flattening increases to 1, and $|\lambda_\parallel|$ remains finite. For lower radii, image parity changes back to positive (due to the sign of $\lambda_\perp$ changing to negative), and the magnification and flattening decrease. The expansion in both perpendicular directions decreases, until the intersection with the dashed black line at $x \approx 0.019$. Images lying closer to the halo center are tangentially contracted rather than expanded ($|\lambda_\parallel| < 1$). After crossing the solid black unit-magnification hyperbola at $x \approx 0.0105$, all images are demagnified. The last important intersection occurs at $x \approx 0.0068$; images to the right of the last dashed black line are contracted even radially ($|\lambda_\perp| < 1$), and their magnification and flattening decrease to 0 at the halo center.

The three orange points marked along the green curve in Figure 3.4 correspond to the radial positions of the centers of the three images in the top right panel of Figure 3.1. The first point at $x \approx 0.188$ corresponds to the image outside the tangential critical curve at the right side of the panel. The second point at $x \approx 0.115$ corresponds to the image between the tangential critical curve and the unit-convergence circle at the left side of the panel. The third point at $x \approx 0.014$ corresponds to the smallest image inside the radial critical curve. The magnification, parity, flattening, orientation, and the two scaling factors of the corresponding images can be determined from the positions of these points in the diagram in Figure 3.4. Note that the values obtained from the diagram are technically valid at the positions of the source-center images and thus correspond to the local "point-source" values. Taking into account the radial extent of each image, their position (and the relevant range of their properties) should be marked by line segments along the green line in Figure 3.4 rather than by points.

3.2.4 Weak shear and phase

Weak-lensing cluster-mass reconstructions are based on statistical analyses of the images of background galaxies (Kaiser and Squires 1993). The convergence map is computed from maps of the shear components. These are constructed from the shear and the phase, which are in turn determined from the shapes and orientations of the images. In the weak-lensing limit, the geometry of the elliptical image of a small circular source corresponds to the second panel of Figure 3.3. Its axis ratio yields the shear and the orientation angle of its major axis is equal to the phase. The semi-minor to semi-major axis ratio b/a is obtained by expanding the ratio $\lambda_\perp/\lambda_\parallel$ of the eigenvalues from Equation (3.20) to first order in κ and γ. The ellipticity, which is equal to the flattening of the image defined in Equation (3.22), reduces in this limit to

$$f = 1 - b/a \simeq 2\,\gamma\,, \tag{3.23}$$

i.e., double the value of the local shear. For illustration, for the image in the second panel of Figure 3.3 Equation (3.23) yields an approximate flattening $2\,\gamma = 0.32$, which is an 8% overestimate of the actual value $f \approx 0.30$ from Equation (3.22).

Based on the weak-lensing regime, we introduce the weak shear and weak phase, which are computed from the images using the weak-lensing relations from the previous paragraph. We define the weak shear as

$$\gamma_\mathrm{w}(\boldsymbol{x}) = \frac{1}{2}\,f\left(\kappa(\boldsymbol{x}), \gamma(\boldsymbol{x})\right)\,, \tag{3.24}$$

where the flattening f is computed from Equation (3.22) using lens-specific convergence and shear functions. Note that γ_w by its definition attains only values from the interval [0, 0.5]. In the weak-lensing regime $\gamma_\mathrm{w} \approx \gamma$, but as γ and κ increase, the weak shear computed from the image flattening deviates from the shear.

For the NFW halo we compute the weak shear $\gamma_{\mathrm{w,NFW}}(\boldsymbol{x})$ from Equation (3.24) using its convergence from Equation (3.1) and shear from Equation (3.12). The second panel in Figure 3.2 shows a plot of $\gamma_{\mathrm{w,NFW}}(\boldsymbol{x})$ in the central part of a NFW halo, using the same color scale as for the shear in the first panel of the figure. Due to its relation to the flattening in Equation (3.24), the plot can be interpreted following the f values along the green curve in the diagram in Figure 3.4. At the halo center the flattening and thus also the weak shear are equal to zero. Going outward from the center, the weak shear increases to its maximum value of 0.5 at the radial critical curve, marked by the inner black circle. From there it drops to 0 at the unit-convergence radius and increases back to 0.5 at the tangential critical curve, marked by the outer black circle. Beyond the tangential critical curve the weak shear drops asymptotically to 0. Comparison with the left panel shows the substantial difference between the shears in the central region of the NFW halo, in terms of amplitude as well as radial pattern. Here the variations in image distortion are primarily driven by the convergence rather than by the shear.

In the third panel of Figure 3.2 we illustrate the difference between the first two panels by plotting the relative deviation of the weak shear from the shear, $\gamma_{\mathrm{w,NFW}}/\gamma_{\mathrm{NFW}} - 1$. The blue regions in which the weak shear underestimates

the shear are limited to the vicinity of the origin and the vicinity of the unit-convergence circle. In both cases the weak shear drops to zero and the relative deviation thus reaches -1, its minimum possible value. Everywhere else the weak shear overestimates the shear, with the positive deviation peaking at the critical curves and dropping to 0 asymptotically. Note that the maxima at the critical curves may be negative for NFW halos with a sufficiently high convergence parameter κ_s, for which $\gamma_\mathrm{NFW}(x_\mathrm{R})$ or even $\gamma_\mathrm{NFW}(x_\mathrm{T})$ exceeds the weak-shear value at critical curves (i.e., 0.5).

In addition to the weak shear, we define the image-based weak phase φ_w as the angle between the major axis of the image of a small circular source and the horizontal (x_1) axis of the image plane. Taking into account Figure 3.3 and the discussion preceding Equation (3.22), in the case of the NFW halo it is related to the phase φ_NFW as follows:

$$\varphi_{\mathrm{w,NFW}}(\boldsymbol{x}) = \begin{cases} \varphi_\mathrm{NFW}(\boldsymbol{x}) & \text{for } \kappa_\mathrm{NFW}(\boldsymbol{x}) < 1\,, \\ \varphi_\mathrm{NFW}(\boldsymbol{x}) + \pi/2 & \text{for } \kappa_\mathrm{NFW}(\boldsymbol{x}) > 1\,. \end{cases} \tag{3.25}$$

We use values from the interval $[-\pi/2,\, \pi/2]$ for both φ_NFW and $\varphi_{\mathrm{w,NFW}}$.

The fourth panel of Figure 3.2 shows a color map of the weak phase $\varphi_{\mathrm{w,NFW}}$ of the NFW halo. The white regions with $\varphi_{\mathrm{w,NFW}} = 0$ correspond to horizontally elongated images, in the orange regions with $\varphi_{\mathrm{w,NFW}} > 0$ the images are oriented counterclockwise and in the blue regions with $\varphi_{\mathrm{w,NFW}} < 0$ the images are oriented clockwise from the horizontal. The bright orange/blue boundaries correspond to images elongated exactly vertically, with $|\varphi_{\mathrm{w,NFW}}| = \pi/2$. The weak phase flips by $\pi/2$ along the unit-convergence circle, separating the inner radially oriented from the outer tangentially oriented images. The weak phase is undefined along this circle as well as at the origin, which corresponds to zero flattening. The dot-dashed lines added for orientation mark the positions of all images with exactly horizontal, exactly vertical, or undefined orientation.

Since the weak phase differs from the phase only by the $\pi/2$ flip inside the unit-convergence circle, a similar color map of the phase $\varphi_\mathrm{NFW}(\boldsymbol{x})$ would differ merely by having inverted color and saturation inside the circle. In other words, the color and saturation outside the circle in the fourth panel of Figure 3.2 would be radially extended to the halo center. Hence, the first and third quadrants would be entirely blue and the second and fourth quadrants would be entirely orange.

The plots of the different quantities in Figure 3.2 are presented as reference plots to aid the interpretation of the results for the NFW halo + point-mass lens model presented in Section 3.3.5.

3.3 Lensing by an NFW halo + point mass

3.3.1 Convergence, shear, and phase

Adding a compact massive object modeled by a point mass positioned at $\boldsymbol{x}_\mathrm{P}$ changes the convergence to

$$\kappa(\boldsymbol{x}) = 2\,\kappa_\mathrm{s}\,\frac{1-\mathcal{F}(x)}{x^2-1} + \pi\,\kappa_\mathrm{P}\,\delta(\boldsymbol{x}-\boldsymbol{x}_\mathrm{P})\,, \tag{3.26}$$

where the mass parameter κ_P corresponds to the ratio of the solid angles subtended by the point-mass Einstein circle and by the halo scale-radius circle (for more details, see Paper I). Hence, $\sqrt{\kappa_\mathrm{P}}$ is the point-mass Einstein radius in units of the halo scale radius. The convergence in Equation (3.26) is identical to the NFW halo convergence from Equation (3.1), except exactly at the position of the added point mass. The lens equation can be written as

$$\boldsymbol{y} = \boldsymbol{x} - 4\,\kappa_\mathrm{s}\,\left[\ln\frac{x}{2} + \mathcal{F}(x)\right]\,\frac{\boldsymbol{x}}{x^2} - \kappa_\mathrm{P}\,\frac{\boldsymbol{x}-\boldsymbol{x}_\mathrm{P}}{|\boldsymbol{x}-\boldsymbol{x}_\mathrm{P}|^2}\,, \tag{3.27}$$

in the form used in Paper I.

For illustration, in the bottom row of Figure 3.1 we show the lensing of the same circular source as in the top row, by the same NFW halo with an additional point mass with mass parameter $\kappa_\mathrm{P} \approx 2.714 \cdot 10^{-4}$ positioned at $\boldsymbol{x}_\mathrm{P} = (0.2,\,0)$. This parameter combination is selected from the parameter-space grid used in Paper I. The position of the point mass is indicated by its Einstein circle (cyan) in the bottom right panel. As seen in the bottom left panel, the black circular source lies inside the weakly perturbed radial caustic, with its upper part lying also inside the strongly perturbed tangential caustic. For a source not lying on the caustic, lens Equation (3.27) yields $2, 4$, or 6 images. For a source lying on the caustic, several images appear combined into a lower number of macro-images. In the example shown in the bottom right panel there are five macro-images. Four of them are images of the full source; the fifth macro-image to the top left of the point mass consists of two additional images of the upper part of the source joined along the critical curve. Comparing the images with those in the top right panel, we see that the left and central images are affected only weakly by the point mass. The right image is affected more strongly, plus there are two new images closer to the point mass. For these images in particular, their distortion cannot be simply classified as tangential or radial.

In order to compute the shear we start from the lens potential, which has an additional term due to the point mass,

$$\psi(\boldsymbol{x}) = \psi_\mathrm{NFW}(x) + \frac{r_\mathrm{s}^2}{D_\mathrm{l}^2}\,\kappa_\mathrm{P}\,\ln|\boldsymbol{x}-\boldsymbol{x}_\mathrm{P}|\,, \tag{3.28}$$

where $\psi_\mathrm{NFW}(x)$ is given by Equation (3.8).

The point-mass shear has the simple form

$$\gamma_\mathrm{P}(\boldsymbol{x}) = \frac{\kappa_\mathrm{P}}{|\boldsymbol{x}-\boldsymbol{x}_\mathrm{P}|^2}\,, \tag{3.29}$$

divergent at the point-mass position and dropping rapidly outward. Since the NFW halo shear peaks at its central value κ_s, the added point mass will dominate

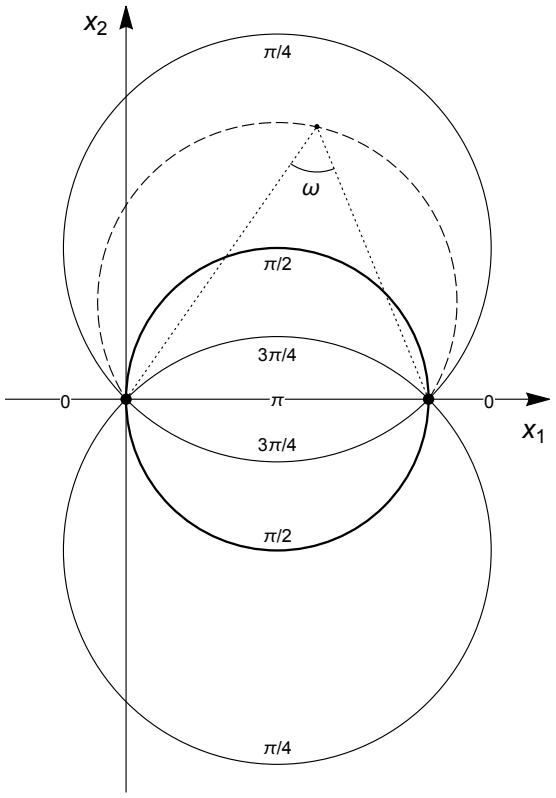

Figure 3.5: Viewing angle $\omega(\boldsymbol{x})$ of the line segment from the halo center to the point mass, appearing in Equation (3.31) for computing the shear $\gamma(\boldsymbol{x})$ of the combined lens. Points on the horizontal axis mark the halo center and the point-mass position $\boldsymbol{x}_{\rm P}$; the dot at the vertex of the angle marks the position $\boldsymbol{x}$. Contours of constant ω are symmetric pairs of circular arcs connecting the centers of the two lens components, with the dashed line marking the arc passing through position $\boldsymbol{x}$. The values of ω range from π along the line segment to 0 along the rest of the horizontal axis.

the lens shear in its vicinity, wherever it may be positioned. The shear can be generally computed from the second derivatives of the lens potential, namely

$$\gamma = \frac{D_{\rm l}^2}{r_{\rm s}^2} \sqrt{\frac{1}{4} \left(\psi_{,11} - \psi_{,22} \right)^2 + \left(\psi_{,12} \right)^2} \,, \tag{3.30}$$

where the commas denote partial derivatives with respect to image-plane coordinates (x_1, x_2). For our combined lens we compute the derivatives of the lens potential from Equation (3.28) and get

$$\gamma(\boldsymbol{x}) = \sqrt{\left[\gamma_{\rm NFW}(x) - \gamma_{\rm P}(\boldsymbol{x})\right]^2 + 4\,\gamma_{\rm NFW}(x)\,\gamma_{\rm P}(\boldsymbol{x})\,\cos^2\omega(\boldsymbol{x})} \,, \tag{3.31}$$

where $\gamma_{\rm NFW}(x)$ and $\gamma_{\rm P}(\boldsymbol{x})$ are given by Equation (3.12) and Equation (3.29), respectively, and

$$\cos\omega(\boldsymbol{x}) = \frac{\boldsymbol{x} \cdot (\boldsymbol{x} - \boldsymbol{x}_{\rm P})}{x\,|\boldsymbol{x} - \boldsymbol{x}_{\rm P}|} \tag{3.32}$$

is the dot product of the unit vectors pointing to $\boldsymbol{x}$ from the halo center and from the point-mass position. In terms of image-plane geometry, ω is the viewing

angle from point $\boldsymbol{x}$ of the line segment connecting the halo center and the point-mass position. As shown in Figure 3.5, curves of constant ω are circular arcs connecting symmetrically the halo center and the point-mass position. Note that ω is also equal to the angle between the tangent to the arc at either of its end points and the outward horizontal direction, as follows from the tangent–chord theorem (alternate segment theorem).

Along the line segment connecting the center and the point mass the viewing angle reaches its maximum, $\omega = \pi$, while along the rest of the horizontal axis it reaches its minimum, $\omega = 0$. In both cases, $\cos^2\omega = 1$ and the total shear from Equation (3.31) is $\gamma(\boldsymbol{x}) = \gamma_{\mathrm{NFW}}(x) + \gamma_{\mathrm{P}}(\boldsymbol{x})$. In this case both shears act in the same orientation, so that their combination is maximal. Along the circle bisected by the line segment, we find $\omega = \pi/2$ according to Thales's theorem and the total shear is $\gamma(\boldsymbol{x}) = |\gamma_{\mathrm{NFW}}(x) - \gamma_{\mathrm{P}}(\boldsymbol{x})|$. In this case the two shears act in perpendicular directions, so that their combination is minimal. For the pair of small arcs in Figure 3.5 with $\omega = 3\pi/4$ and for the pair of large arcs with $\omega = \pi/4$ we get $\cos^2\omega = 1/2$ and the total shear is $\gamma(\boldsymbol{x}) = \sqrt{\gamma^2_{\mathrm{NFW}}(x) + \gamma^2_{\mathrm{P}}(\boldsymbol{x})}$.

As discussed in Section 3.2.1, for the NFW halo the central shear is defined, $\gamma_{\mathrm{NFW}}(0) = \kappa_{\mathrm{s}}$, while the phase and shear components are undefined. The same holds for the central properties of the point-mass lens. However, for the combined lens even the shear at the halo center is undefined. For $x \to 0$ Equation (3.31) yields

$$\gamma(\boldsymbol{x}) \to \sqrt{\left[\kappa_{\mathrm{s}} - \kappa_{\mathrm{P}}\, x_{\mathrm{P}}^{-2}\right]^2 + 4\,\kappa_{\mathrm{s}}\kappa_{\mathrm{P}}\, x_{\mathrm{P}}^{-2}\,\cos^2\omega}\,, \tag{3.33}$$

a value that depends on the direction of approach to the center, due to the directional dependence of ω. As seen from Figure 3.5 and as explained in the discussion above, approaching the center along the horizontal axis leads to the highest value (the sum of the two shears) while an approach along the vertical axis leads to the lowest value (the absolute value of the difference of the two shears). The situation at the position of the point mass is similar, though here the angular differences are suppressed by the divergence of γ_{P}.

The range of values of the shear occurring in the studied central region of the image plane is larger than for the halo or the point mass separately. Its upper limit is ∞, due to the divergence of γ_{P} at the point-mass position $\boldsymbol{x}_{\mathrm{P}}$. Its lower limit may reach 0. As seen from the form of Equation (3.31), this may occur only along the $\omega = \pi/2$ circle at points where $\gamma_{\mathrm{NFW}}(x) = \gamma_{\mathrm{P}}(\boldsymbol{x})$. Following the circle from the halo center to the point mass, γ_{NFW} decreases while γ_{P} increases. Zero-shear points thus exist only if γ_{NFW} is equal to or larger than γ_{P} at the halo center. Hence, for $x_{\mathrm{P}} < \sqrt{\kappa_{\mathrm{P}}/\kappa_{\mathrm{s}}}$ there are no zero-shear points. In this range, for point masses closest to the halo center, the minimum shear $\gamma = \kappa_{\mathrm{P}}\, x_{\mathrm{P}}^{-2} - \kappa_{\mathrm{s}}$ occurs at the halo center when approached along the vertical axis.

Zero-shear points exist for all larger point-mass distances from the halo center. For $x_{\mathrm{P}} = \sqrt{\kappa_{\mathrm{P}}/\kappa_{\mathrm{s}}}$ there is one zero-shear point located directly at the halo center. For any $x_{\mathrm{P}} > \sqrt{\kappa_{\mathrm{P}}/\kappa_{\mathrm{s}}}$ there are two zero-shear points lying symmetrically above and below the horizontal axis on the $\omega = \pi/2$ circle. With increasing distance of the point mass from the halo center the zero-shear points shift along the circle toward the position of the point mass, so that for larger distances they lie nearly vertically above and below the point mass. Their separation from the point mass,

which is approximately $\sqrt{\kappa_{\rm P}/\gamma_{\rm NFW}(x_{\rm P})}$ in this regime, increases with distance as the halo shear decreases.

Image-plane maps of the shear $\gamma(\boldsymbol{x})$ for different masses and positions of the point mass are presented and discussed in Section 3.3.5.1.

The shear components are defined by

$$(\gamma_1, \gamma_2) = \gamma\,(\cos 2\varphi, \sin 2\varphi)\,, \tag{3.34}$$

where the trigonometric functions of the phase φ can be computed for a point $\boldsymbol{x} = (x_1, x_2)$ in the image plane as

$$\begin{aligned} \cos 2\varphi &= \frac{1}{\gamma(\boldsymbol{x})}\left[\frac{x_2^2 - x_1^2}{x^2}\,\gamma_{\rm NFW}(x) + \frac{(x_2 - x_{\rm P2})^2 - (x_1 - x_{\rm P1})^2}{|\boldsymbol{x} - \boldsymbol{x}_{\rm P}|^2}\,\gamma_{\rm P}(\boldsymbol{x})\right] \\ \sin 2\varphi &= \frac{-2}{\gamma(\boldsymbol{x})}\left[\frac{x_1 x_2}{x^2}\,\gamma_{\rm NFW}(x) + \frac{(x_1 - x_{\rm P1})(x_2 - x_{\rm P2})}{|\boldsymbol{x} - \boldsymbol{x}_{\rm P}|^2}\,\gamma_{\rm P}(\boldsymbol{x})\right], \end{aligned} \tag{3.35}$$

where the shears $\gamma(\boldsymbol{x}), \gamma_{\rm NFW}(x)$, and $\gamma_{\rm P}(\boldsymbol{x})$ are given by Equations (3.31), (3.12), and (3.29), respectively. Note that in this case the phase and the shear components are undefined at the halo center and at the point-mass position, since the phase as well as the shear $\gamma(\boldsymbol{x})$ depend on the direction of approach to these points.

We would like to point out that Equation (3.31) is a special case of the more general formula

$$\gamma = \sqrt{(\gamma_{\rm A} - \gamma_{\rm B})^2 + 4\,\gamma_{\rm A}\gamma_{\rm B}\cos^2(\varphi_{\rm A} - \varphi_{\rm B})} \tag{3.36}$$

for the shear of a combination of two mass distributions with shears $\gamma_{\rm A}, \gamma_{\rm B}$ and phases $\varphi_{\rm A}, \varphi_{\rm B}$. For two circularly symmetric mass distributions with the same sign of the expression $\psi'' - x^{-1}\psi'$ that appears in Equation (3.10), the absolute value of the phase difference in Equation (3.36) is equal to the viewing angle ω.

The expression $\psi'' - x^{-1}\psi'$ is globally negative for a range of mass distributions, such as for the NFW profile, for a point mass, for a singular or a non-singular (cored) isothermal sphere. For a combination of two such distributions, the formula for the shear in Equation (3.31), the following discussion, and the formulae for the phase in Equation (3.35) are valid. For example, the case of two point masses was studied by Schneider and Weiss (1986), and the case of two isothermal spheres was studied by Shin and Evans (2008).

3.3.2 Jacobian and umbilic points

The Jacobian of the lens equation can be computed from Equation (3.19) using the convergence from Equation (3.26) and the shear from Equation (3.31). Its explicit form is presented in Paper I, together with a detailed analysis of the critical curves which are obtained by setting the Jacobian equal to zero. The parts of the critical curve lying outside the unit-convergence circle ($x > x_0$) satisfy the equation

$$\gamma(\boldsymbol{x}) = 1 - \kappa(\boldsymbol{x})\,, \tag{3.37}$$

which yields the tangential critical curve in absence of the point mass. The parts lying inside the unit-convergence circle ($x < x_0$) satisfy the equation

$$\gamma(\boldsymbol{x}) = \kappa(\boldsymbol{x}) - 1\,, \tag{3.38}$$

which yields the radial critical curve in absence of the point mass.

Equation (3.19) also indicates that for the Jacobian to be equal to zero at a point lying directly on the unit-convergence circle, the shear must be zero at such a point. From the properties of zero-shear points discussed in Section 3.3.1 it follows that such critical-curve points must lie at the intersections of the unit-convergence circle and the $\omega = \pi/2$ circle extending from the halo center to the point-mass position.

For $x_\mathrm{P} < x_0$ these circles have no intersection and, thus, there are no critical-curve points along the unit-convergence circle. For $x_\mathrm{P} = x_0$ these circles have an intersection exactly at the position of the point mass. However, at this point the shear is not zero, so that even in this case there is no critical-curve point along the unit-convergence circle. For any $x_\mathrm{P} > x_0$ these circles have two intersections. In this case the requirement of zero shear leads to the condition

$$x_\mathrm{P} = x_0 \sqrt{1 + \kappa_\mathrm{P} \,/\, \left[4\kappa_\mathrm{s}\left(1 + \ln\frac{x_0}{2}\right) + 2 - 3x_0^2\right]}\,. \tag{3.39}$$

We conclude that for any value of the mass parameter κ_P Equation (3.39) yields a single corresponding distance of the point mass from the halo center, for which the critical curve has points lying on the unit-convergence circle.

If we place the point mass along the horizontal axis in the image plane at $\boldsymbol{x}_\mathrm{P} = (x_\mathrm{P}, 0)$, the positions of these critical-curve points are

$$\boldsymbol{x} = \left(\frac{x_0}{x_\mathrm{P}}, \pm\sqrt{1 - \frac{x_0^2}{x_\mathrm{P}^2}}\right) x_0\,, \tag{3.40}$$

with the value of x_P given by Equation (3.39). These points with $\kappa = 1$ and $\gamma = 0$ have special significance. As discussed in Appendix A.3, such critical-curve points correspond to umbilics. Equation (3.39) thus presents a condition for the existence of umbilics in the studied lens system. In the $(\kappa_\mathrm{P}, x_\mathrm{P})$ parameter-space plots in Figure 6 of Paper I, Equation (3.39) describes the green and violet umbilic boundary, starting at $x_\mathrm{P} = x_0$ at the $\kappa_\mathrm{P} = 0$ vertical axis and increasing monotonically for higher κ_P. In the image plane, the umbilic points lie along the unit-convergence circle. For $\kappa_\mathrm{P} \ll 1$ they are located close to the horizontal axis in the direction of the point mass. Their displacement from the axis increases with increasing κ_P.

3.3.3 Geometry of images

The geometry of the images can be studied using the eigenvalue decomposition of the inverse of the Jacobian matrix given by Equation (3.21) and the convergence–shear (CS) diagram introduced in Appendix A.3. For a point mass placed at the center of the halo, the convergence and shear are purely radial functions. Hence, the range of their possible combinations is limited to the $(\kappa(x), \gamma(x))$ curve in the

CS diagram. In this case the analysis of possible image geometries can directly follow the example presented in Section 3.2.3 for images formed by the NFW halo.

Even when the point mass is positioned away from the halo center, the convergence given by Equation (3.26) preserves its circular symmetry (with the exception of the single point at the position of the point mass). This means that any convergence value κ can be one-to-one translated to the corresponding radial distance from the halo center x. However, the shear given by Equation (3.31) loses circular symmetry. In the CS diagram this results in the range of possible $(\kappa(\boldsymbol{x}), \gamma(\boldsymbol{x}))$ combinations covering a two-dimensional region. In terms of image distortions and orientations, the lack of symmetry means that instead of the terms "tangential" and "radial" we revert to the more general "in the direction of the phase" and "perpendicular to the phase", respectively.

For illustration, in Figure 3.6 we present the CS diagram for a NFW halo

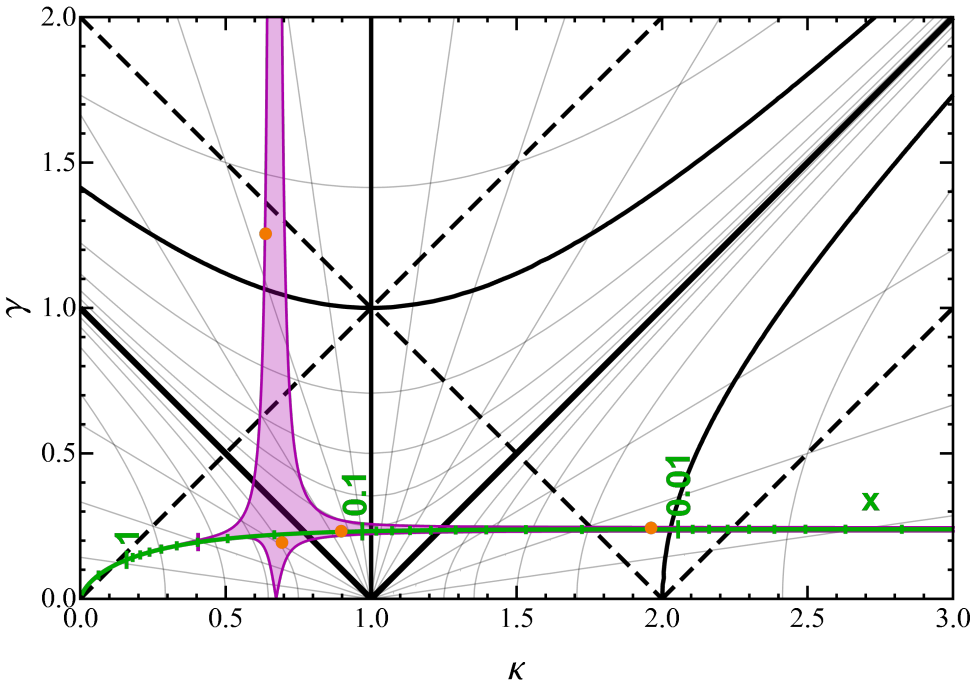

Figure 3.6: CS diagram illustrating the geometry of images formed by the NFW halo with a $\kappa_{\mathrm{P}} \approx 2.714 \cdot 10^{-4}$ point mass at $x_{\mathrm{P}} = 0.2$, from the bottom row of Figure 3.1. The purple-shaded area marks the range of $(\kappa(\boldsymbol{x}), \gamma(\boldsymbol{x}))$ combinations of the lens; the green line marks the $(\kappa_{\mathrm{NFW}}(x), \gamma_{\mathrm{NFW}}(x))$ combinations of the halo-only lens from Figure 3.4. The green tick marks and labels indicate the radial distance x along vertical lines in this diagram. The top purple line marks the maximum shear along a circle with radius x centered on the halo, which always occurs in the direction of the point mass. The bottom purple line marks the minimum shear along the circle; for larger radii x (to the left of the purple tick mark) this occurs in the direction opposite the point mass; for smaller radii x (to the right of the purple tick mark) this occurs at two symmetric off-axis points along the circle. The orange dots mark the (κ, γ) combinations at the positions of the four full images in the bottom right panel of Figure 3.1.

with a $\kappa_{\mathrm{P}} \approx 2.714 \cdot 10^{-4}$ point mass located at $x_{\mathrm{P}} = 0.2$. The purple-shaded region bounded by the bold purple lines shows the range of (κ, γ) combinations occurring in the image plane. Added for orientation is the green curve from Figure 3.4 showing the (κ, γ) combinations of the NFW halo without the point mass. As in Figure 3.4, the tick marks along the curve mark radial distances from the halo center. At any value of x along this axis, the vertical extent between the bold purple lines indicates the range of shear values $\gamma(\boldsymbol{x})$ occurring along the circle $|\boldsymbol{x}| = x$. The maximum shear always occurs in the direction of the point mass, i.e., for $\boldsymbol{x} = (x, 0)$. At large distances x, the minimum shear occurs in the direction opposite to the point mass, i.e., for $\boldsymbol{x} = (-x, 0)$. At lower distances, to the right of the purple vertical tick mark (in the case of Figure 3.6 near $x = 0.4$), minimum shear occurs at two points offset symmetrically from the axis connecting the halo center and the point mass. Close to the halo center, at the right edge of the diagram, minimum shear occurs at points offset nearly perpendicularly from the halo center, i.e., for $\boldsymbol{x} \approx (0, \pm\, x)$. Equation (3.33) shows that at the center of the halo the maximum shear is $\kappa_{\mathrm{s}} + \kappa_{\mathrm{P}}\, x_{\mathrm{P}}^{-2}$ and the minimum shear is $|\kappa_{\mathrm{s}} - \kappa_{\mathrm{P}}\, x_{\mathrm{P}}^{-2}|$.

In the example shown in Figure 3.6, the shear range at large radii does not visibly deviate from the green NFW halo shear. At radii lower than the purple tick mark near $x = 0.4$, the maximum shear starts to deviate substantially from the green curve. The minimum shear starts to deviate visibly between $x = 0.3$ and $x = 0.2$. Along the circle with the radius of the point-mass distance, $x = x_{\mathrm{P}} = 0.2$, the maximum shear diverges at the position of the point mass. At a slightly lower radius, the minimum shear reaches 0 at the positions of the off-axis zero-shear points. For lower radii, the shear interval shrinks back toward the NFW shear at the green curve. However, instead of reaching the central NFW shear $\gamma_{\mathrm{NFW}}(0) = \kappa_s \approx 0.2390$, the limiting shear at $x = 0$ varies within the interval $[0.2322, 0.2458]$, as discussed in the previous paragraph.

The four orange points marked in the purple region in Figure 3.6 correspond to the positions of the four images of the source center in the bottom right panel of Figure 3.1. Note that the fifth macro-image lying on the critical curve in Figure 3.1 does not include an image of the source center. The point appearing at $(\kappa, \gamma) \approx (0.637, 1.255)$ corresponds to the image just to the right of the point mass in Figure 3.1. The three remaining points in Figure 3.6 correspond to perturbed versions of the three images appearing in the absence of the point mass in the top right panel of Figure 3.1. The point at $(\kappa, \gamma) \approx (0.694, 0.194)$ corresponds to the lower right image outside the critical curve in the bottom right panel of Figure 3.1. The point at $(\kappa, \gamma) \approx (0.897, 0.233)$ corresponds to the image just outside the unit-convergence circle at the left side of the panel in Figure 3.1. The fourth point at $(\kappa, \gamma) \approx (1.962, 0.244)$ corresponds to the small image close to the halo center in Figure 3.1.

The properties of the images can be determined from the positions of the points in the diagram; the changes in the properties of the latter three due to the presence of the point mass can be studied by comparing the diagrams in Figures 3.6 and 3.4. Note that, in this case, taking into account the full extent of each image would require marking them in the CS diagram by exact patches covering the corresponding range of (κ, γ) combinations instead of by the points used in Figure 3.6. This would permit including even partial images that do

not contain an image of the source center, such as the fifth macro-image in the bottom right panel of Figure 3.1.

CS diagrams for different masses and positions of the point mass are presented and discussed in Section 3.3.5.3.

3.3.4 Weak shear and phase

Following the example in Section 3.2.4, we use the geometry of image distortions to introduce the weak-lensing shear and phase estimates for the NFW halo + point-mass lens. We compute the weak shear γ_{w} from Equation (3.24), substituting the convergence from Equation (3.26) for $\kappa(\boldsymbol{x})$, and the shear from Equation (3.31) for $\gamma(\boldsymbol{x})$.

The angle between the major axis of the image of a small circular source and the x_1 axis of the image plane is equal to the phase outside the unit-convergence circle; it is perpendicular to the phase inside the unit-convergence circle. Hence, the weak phase φ_{w} is related to the phase φ as follows:

$$\varphi_{\mathrm{w}}(\boldsymbol{x}) = \begin{cases} \varphi(\boldsymbol{x}) & \text{for } \kappa(\boldsymbol{x}) < 1\,, \\ \varphi(\boldsymbol{x}) + \pi/2 & \text{for } \kappa(\boldsymbol{x}) > 1\,, \end{cases} \tag{3.41}$$

where $\varphi(\boldsymbol{x})$ is given by Equation (3.35) and $\kappa(\boldsymbol{x})$ by Equation (3.26). We use values from the interval $[-\pi/2,\, \pi/2]$ for both φ and φ_{w}.

Image-plane maps of the weak shear $\gamma_{\mathrm{w}}(\boldsymbol{x})$ and weak phase $\varphi_{\mathrm{w}}(\boldsymbol{x})$ for different masses and positions of the point mass are presented and discussed in Section 3.3.5.4 and Section 3.3.5.7, respectively.

3.3.5 Lens Characteristics as a Function of Point-mass Parameters

In Sections 3.3.1–3.3.4 we defined the lensing quantities of interest and described their general properties. In this section we present plots illustrating these lens characteristics for different point masses embedded in a NFW halo with a fiducial convergence parameter $\kappa_{\mathrm{s}} \approx 0.239035$. With the exception of Figure 3.9.A and Figure 3.9.B, all of the plots are presented as color maps in the image plane. For better orientation in these maps, we plot the critical curves (solid black) and mark the point-mass position by its Einstein ring (cyan).

In each of the following figures, the three columns of the plot grid correspond to the same three values of the mass parameter κ_{P} of the point mass used in Paper I. These differ in the number of radial critical curves they generate for $x_{\mathrm{P}} = 0$: sub-critical $\kappa_{\mathrm{P}} = 10^{-4}$ with two radial critical curves; critical $\kappa_{\mathrm{P}} = \kappa_{\mathrm{PC}} \approx 2.714 \cdot 10^{-4}$ with one radial critical curve; super-critical $\kappa_{\mathrm{P}} = 10^{-3}$ with no radial critical curve.

For each of the characteristics discussed in Sections 3.3.5.1–3.3.5.8 we present two plot grids. The rows in the first grid correspond to seven values of the point-mass position x_{P} increasing in steps of 0.05 from 0 to 0.3. These parameter combinations correspond to the critical-curve and caustic gallery in Figure 5 of Paper I; they are marked by red crosses in the parameter-space plot in Figure 6 of Paper I. The rows in the second grid correspond to nineteen values of x_{P}

Symbol	Description; First appearance
γ	Shear (combined model or general); Equation (3.18)
γ_{NFW}	Shear of NFW-halo lens; Equation (3.12)
γ_{P}	Shear of a point-mass lens; Equation (3.29)
γ_{w}	Weak shear (combined model or general); Equation (3.24)
$\gamma_{\mathrm{w,NFW}}$	Weak shear of NFW-halo lens; Section 3.2.4
$\delta\varphi_{\mathrm{w}}$	Weak-phase deviation due to the point mass; Section 3.3.5.8
κ	Convergence (combined model or general); Equation (3.18)
κ_{NFW}	Convergence of NFW-halo lens; Equation (3.1)
κ_{P}, κ_{PC}	Mass parameter of a point mass and its critical value; Equation (3.26)
κ_{s}	NFW halo convergence parameter; Equation (3.1)
φ	Phase (combined model or general); Equation (3.18)
φ_{NFW}	Phase of NFW-halo lens; Equation (3.16)
φ_{w}	Weak phase (combined model or general); Equation (3.41)
$\varphi_{\mathrm{w,NFW}}$	Weak phase of NFW-halo lens; Equation (3.25)
ψ	Lens potential (combined model or general); Equation (3.6)
ψ_{NFW}	Lens potential of NFW-halo lens; Equation (3.8)
ω	Viewing angle of the line segment connecting the halo center and the point-mass position; Equation (3.32)

Table 3.1: List of symbols.

increasing in steps of 0.01 from 0 to 0.15, then in steps of 0.05 to 0.3 in the top row. These parameter combinations are marked by red and black crosses in Figure 6 of Paper I.

For better orientation in the notation of the different shears, convergences, phases, and other lensing quantities, we list selected symbols together with their first appearance in the text in Table 3.1.

3.3.5.1 Shear

Image-plane maps of the shear $\gamma(\boldsymbol{x})$ are presented in Figure 3.7.A. The shear color scale is the same as in the first two panels of Figure 3.2, ranging from white for $\gamma = 0$ to magenta for all positions with $\gamma \geq 1.5$. In the absence of the point mass the shear varies very slowly in this region, as indicated by the featureless plot in the first panel of Figure 3.2.

In the bottom row ($x_{\mathrm{P}} = 0$) of Figure 3.7.A the point mass is located at the center of the halo and the whole system thus exhibits axial symmetry. From Equations (3.31) and (3.32) it follows that in this case the total shear at any position is a simple sum of the NFW and point-mass shears. Near the halo center the NFW shear $\gamma_{\mathrm{NFW}}(x)$, shown in the first panel of Figure 3.2, is surpassed by the point-mass shear $\gamma_{\mathrm{P}}(\boldsymbol{x})$ which diverges at the origin. A comparison of the

bottom row in the three columns shows that the magenta high-shear region with the strongest point-mass influence naturally increases with its mass parameter κ_{P}.

Next, we focus on the left column illustrating the sub-critical case with $\kappa_{\mathrm{P}} = 10^{-4}$. Already in the second plot from the bottom ($x_{\mathrm{P}} = 0.05$), many phenomena described in detail in Section 3.3.1 can be clearly seen. A pale circle corresponding to viewing angle $\omega = \pi/2$ connects the point mass and the halo center, marking a region with decreased shear. The shear drops to zero at two points of this circle located above and below the horizontal axis of symmetry. These zero-shear points lie inside the perturbed NFW radial critical curve close to the point mass. Their presence restricts the bright red high-shear region around the point-mass divergence to a smaller extent than in the $x_{\mathrm{P}} = 0$ case. The value of the shear in the vicinity of the halo center depends on the direction of approach. Maximum shear can be seen in the horizontal and minimum shear can be seen in the vertical direction, tangent to the $\omega = \pi/2$ circle.

Going further to $x_{\mathrm{P}} = 0.1$, we see that the paler lower-shear circle and the directional dependence near the origin become less pronounced, and the zero-shear points move even closer to the point mass, lying almost vertically above and below it. They are positioned inside the pair of tiny critical curves seen in the white low-shear areas. This hints at the fact that umbilics can only occur at zero-shear points that lie at the intersection of the $\omega = \pi/2$ circle and the $\kappa = 1$ circle, as explained in Section 3.3.2.

For even higher values of x_{P} in the sub-critical case, the directional dependence at the halo center becomes indiscernible and the pattern close to the point mass becomes more regular. The region of high shear around the point mass has a horizontally elongated oval shape and the zero-shear points lie above and below it in the white spots outside the critical curve. With increasing x_{P}, this shear pattern around the point mass resembles the total shear of the Chang–Refsdal model, which consists of a point mass and a constant external shear (Chang and Refsdal 1984).

The preceding discussion made for the sub-critical case holds also for the critical case ($\kappa_{\mathrm{P}} = \kappa_{\mathrm{PC}} \approx 2.714 \cdot 10^{-4}$) in the central column. In terms of shear, the corresponding plots portray qualitatively the same sequence of situations as in the left column; the difference is merely quantitative. More specifically, the pattern around the point mass is considerably larger and the directional dependence around the halo center is more pronounced, observable even for higher values of x_{P}.

These patterns are even larger and more distinct in the right column illustrating the super-critical case with $\kappa_{\mathrm{P}} = 10^{-3}$. However, there are some important differences. In the second plot from the bottom, $x_{\mathrm{P}} = 0.05$ does not exceed the threshold value of $\sqrt{\kappa_{\mathrm{P}}/\kappa_{\mathrm{s}}} \approx 0.0647$. Hence, there are no zero-shear points. Minimum shear, which is now non-zero in the central region, can be found at the halo center when approached vertically. For point-mass positions $x_{\mathrm{P}} \gtrsim 0.0647$ this minimum shear drops to zero and its position detaches from the origin, moving along the $\omega = \pi/2$ circle. In addition, the third plot from the bottom now depicts the situation before the detachment of the two small critical curves and, thus, the zero-shear points still lie inside the perturbed NFW radial critical curve. Note that in this case the directional dependence of the shear at the halo center can

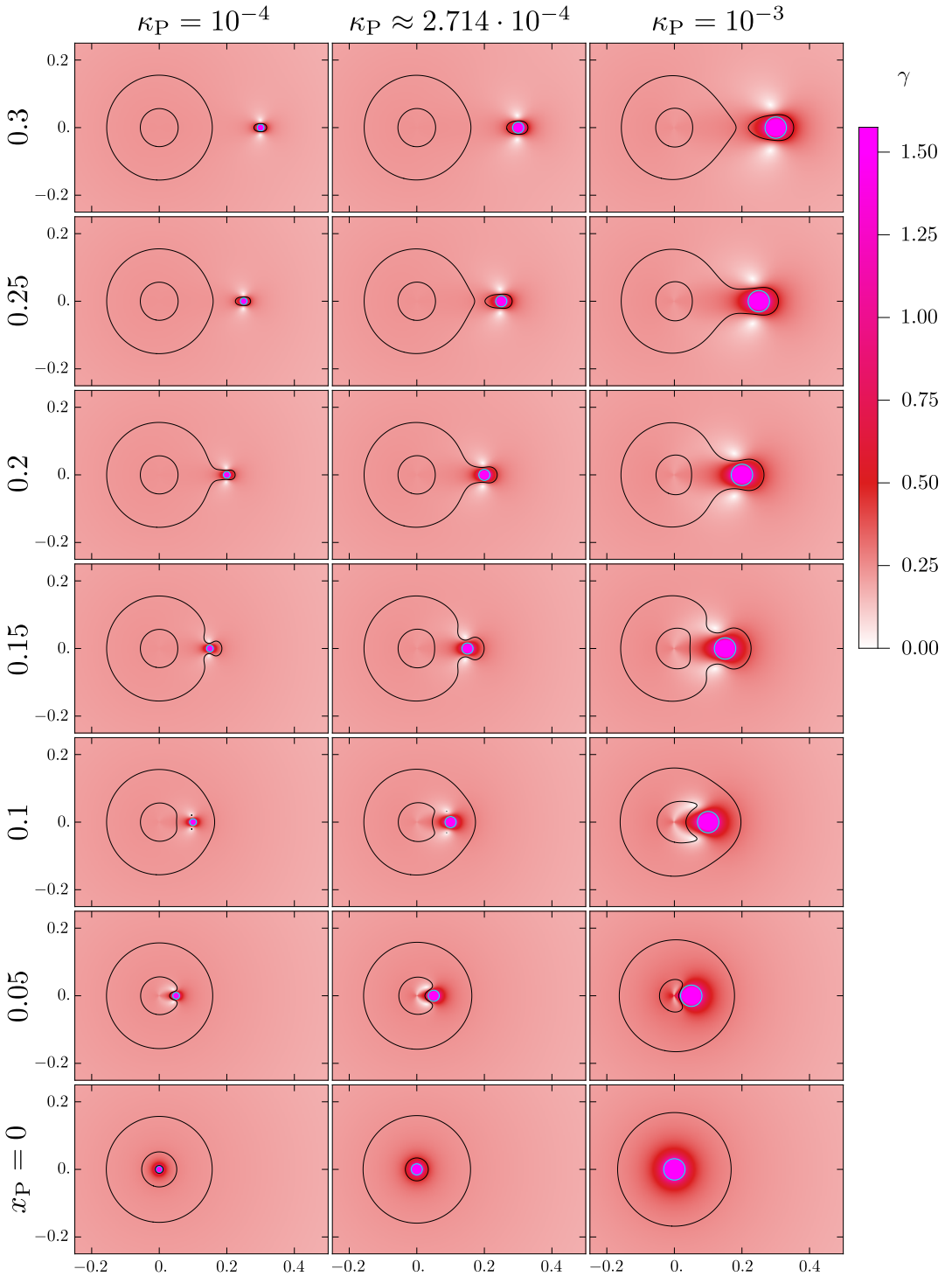

Figure 3.7.A: Image-plane maps of the shear $\gamma(\boldsymbol{x})$ of a NFW halo + point-mass lens, described in Section 3.3.5.1. Columns correspond to sub-critical, critical, and super-critical mass parameters κ_P marked at the top; rows correspond to point-mass positions x_P marked along the left side. Critical curves are plotted in black, and the point-mass location is marked by its Einstein ring (cyan). Magenta marks all positions with $\gamma \geq 1.5$.

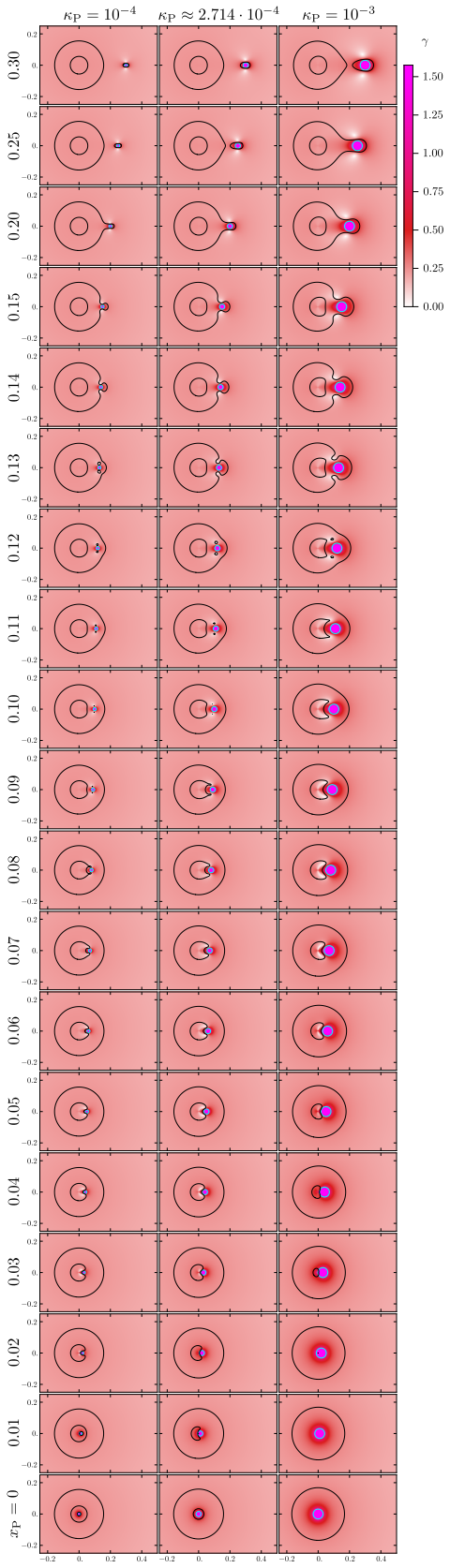

Figure 3.7.B: Image-plane maps of the shear $\gamma(\boldsymbol{x})$ of a NFW halo + point-mass lens, for a finer grid of point-mass positions than in Figure 3.7.A. Notation same as in Figure 3.7.A.

be seen up to the top row.

The dependence of the shear $\gamma(\boldsymbol{x})$ on the point-mass position $x_{\rm P}$ can be examined in more detail in Figure 3.7.B, which includes plots for a finer grid in terms of $x_{\rm P}$. Zero-shear points appear at the halo center at point-mass positions $\{0.0205, 0.0337, 0.0647\}$ in the sub-critical, critical, and super-critical cases. Other key values of $x_{\rm P}$ correspond to changes in the critical-curve topology, as indicated by the color boundaries in Figure 6 of Paper I.

Notice that the zero-shear points always occur in a positive-Jacobian region, as indicated by Equation (3.19): inside the perturbed NFW radial critical curve, inside the symmetric pair of small critical-curve loops, or outside all critical-curve loops. Apart from this, there is hardly any correlation between the shear pattern and the critical-curve geometry.

3.3.5.2 Shear deviation due to the point mass

In Figure 3.8.A, we present image-plane maps of the shear deviation $\gamma/\gamma_{\rm NFW} - 1$ caused by the presence of the point mass. As indicated by the formula, this quantity represents the relative difference between the shear $\gamma(\boldsymbol{x})$ of the NFW halo + point-mass lens (shown in Figure 3.7.A) and the shear $\gamma_{\rm NFW}(x)$ of the NFW halo alone (shown in the first panel of Figure 3.2). As the deviation falls rather quickly with increasing distance from the point mass, we introduce a semi-logarithmic color scale to visualize even minor changes in the deviation. In the positive yellow- and orange-hued regions the shear is increased, while in the negative blue regions it is decreased by the point mass. Darkest blue is used for -1, the lowest possible deviation. From -1 to -10^{-3}, blue saturation decreases logarithmically, and then to 0 linearly, where it reaches white. From 0 to 10^{-3}, yellow saturation increases linearly, and then to 10^{-1} logarithmically. The logarithmic scale then continues to color red at deviation 10, beyond which the color is kept constant even though the shear deviation can reach arbitrarily large values near the point mass.

For better orientation, we also include contours for a few specific values of the shear deviation. The dot-dashed lines represent the zero-deviation contour, along which the shears are equal. Paler and darker shades of orange are used for positive-deviation contours with values 10^{-2} and 10^{-1}, respectively. Similarly, paler and darker shades of blue indicate negative deviations -10^{-2} and -10^{-1}, respectively.

We first inspect the deviation map for a centrally positioned sub-critical point mass (bottom left plot). In this case the deviation is equal to $\gamma_{\rm P}/\gamma_{\rm NFW}$, which is positive in the entire image plane, i.e., the shear is globally increased by the point mass. The deviation diverges at the halo center, since the point-mass shear increases to ∞ while the halo shear tends to the constant $\kappa_{\rm s}$. Further from the halo center the deviation approaches zero, as the point-mass shear given by Equation (3.29) falls quickly with distance. Contours representing deviations 10^{-1} and 10^{-2} are slightly larger than the outer radial and tangential critical curves, respectively.

In the second row ($x_{\rm P} = 0.05$) the point mass is displaced from the center and a pair of blue regions with negative deviation appears. These regions reach the halo center from the vertical direction, while the deviation is positive along the full horizontal axis, as indicated by the orange and yellow color and by the dot-dashed

zero contour pinched at the halo center. In fact, the deviation along the horizontal axis is always positive for any x_P and κ_P, since here $\gamma/\gamma_\mathrm{NFW} - 1 = \gamma_\mathrm{P}/\gamma_\mathrm{NFW}$ according to the discussion in the paragraphs following Equation (3.31). The pattern near the halo center arises from the directional dependence of the shear shown in Equation (3.33). Places with the darkest blue color lie above and below the point mass, with the lowest shear deviation -1 occurring at the zero-shear points. The region with a deviation larger than 10% in absolute value is now roughly centered on the point mass, while the region with a deviation lower than 1% in absolute value lies outside the near-circular pale orange contour and in narrow bands along the dot-dashed zero-deviation contour.

At $x_\mathrm{P} = 0.1$ on the third row we see that the affected area becomes more asymmetric, with the pale orange contour with 10^{-2} deviation now broken into two lobes extending to the left of the center and to the right of the point mass. In this case there is a single region with deviation lower than 1% in absolute value, reaching inside the critical curves, including the zero-deviation contour, and reaching the halo center along it.

For higher values of x_P, the blue regions of negative deviation expand as the point mass shifts to the right. Their borders indicated by the zero-deviation contour become more and more circular except for the vicinity of the point mass, where they enclose the zero-shear points but avoid the vicinity of the point mass. These dot-dashed contours intersect at the halo center at a right angle and the deviation remains positive in the spindle-shaped region along the horizontal axis from the halo center to the point mass. The orange and blue contours gradually detach from the halo center and for $x_\mathrm{P} \geq 0.25$ they form a four-lobed structure around the point mass, with positive lobes extending horizontally from the point mass and negative lobes separated vertically from the point mass. The single region with deviation lower than 1% in absolute value includes the halo center as well as a progressively larger area around it, including the entire image plane except the four lobes around the point mass.

In the critical and super-critical cases in the two right columns, the plots look similar to those in the sub-critical case, with the colors getting progressively more saturated indicating higher shears γ_P from heavier point masses. Naturally, the orange and blue contours also expand with increasing mass. On the other hand, the blue regions of negative deviation inside the dot-dashed contours do not expand with increasing κ_P. On the contrary, they shrink as they recede from a heavier point mass. Away from the point mass, the dot-dashed zero contours are almost circular. They intersect at the halo center at a right angle and reach nearly to the point mass before avoiding it.

Comparing the columns in the different rows, we see that the geometry of the zero-deviation contour is generic, with increasing κ_P affecting only the vicinity of the point mass, and increasing x_P only enlarging the scale. The pattern arises naturally from Equation (3.31) in the regime $\gamma_\mathrm{P} \ll \gamma_\mathrm{NFW}$ valid anywhere except in the immediate vicinity of the point mass. In this case we expand the shear and get the simple result $\gamma/\gamma_\mathrm{NFW} - 1 \simeq (\gamma_\mathrm{P}/\gamma_\mathrm{NFW}) \cos 2\omega$. The ratio in the parentheses is always positive, hence, the zero-deviation contour is purely given by the condition on the viewing angle requiring $\cos 2\omega = 0$. Figure 3.5 shows that the corresponding $\omega = \pi/4$ and $\omega = 3\pi/4$ circles describe the dot-dashed contours seen in Figure 3.8.A practically exactly, except in the point-mass vicinity

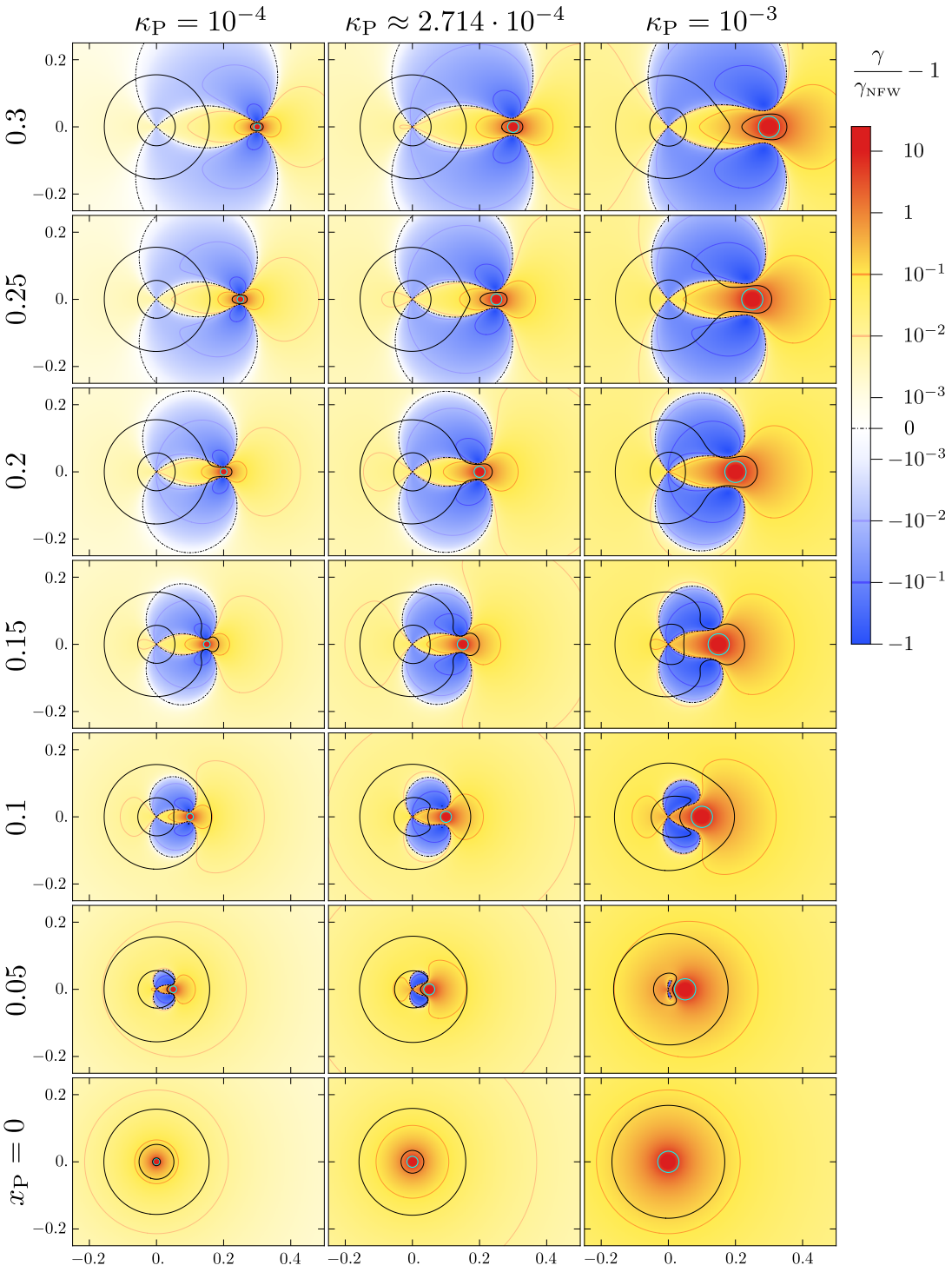

Figure 3.8.A: Image-plane maps of the relative shear deviation, $\gamma/\gamma_{\mathrm{NFW}} - 1$, caused by the presence of the point mass, described in Section 3.3.5.2. The color scale changes from logarithmic to linear in the interval $[-10^{-3}, 10^{-3}]$. All positions with deviation greater than 10 are marked in red. Contours are plotted for five deviation values indicated in the color bar. Remaining notation as in Figure 3.7.A.

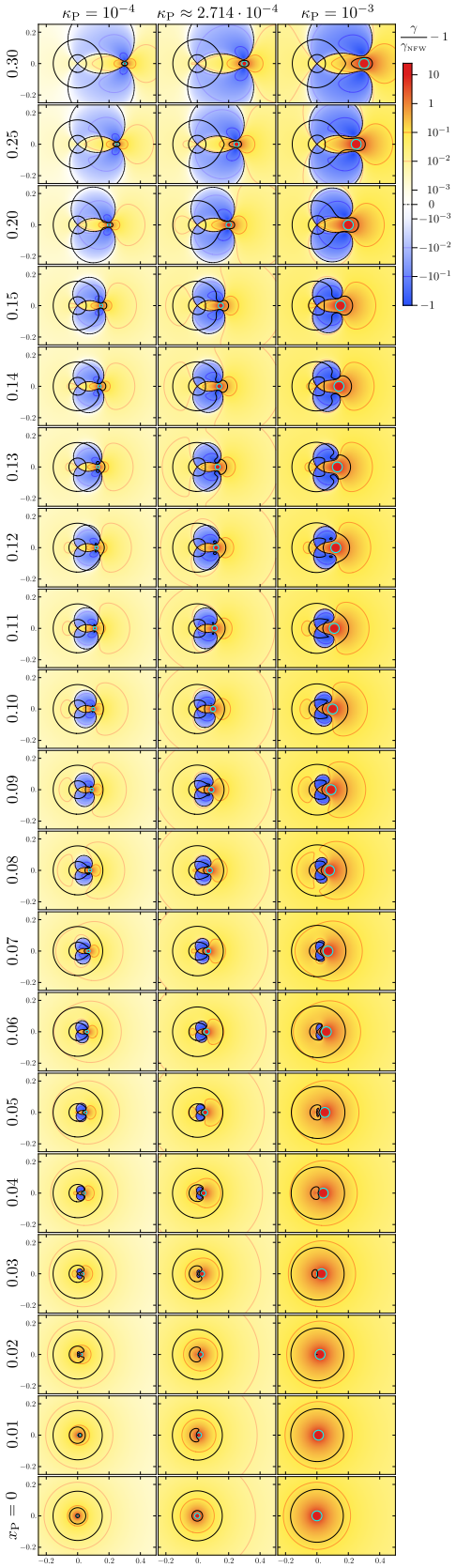

Figure 3.8.B: Image-plane maps of the relative shear deviation, $\gamma/\gamma_{\rm NFW} - 1$, caused by the presence of the point mass, for a finer grid of point-mass positions than in Figure 3.8.A. Notation same as in Figure 3.8.A.

where $\gamma_{\rm P} \gtrsim \gamma_{\rm NFW}$.

In the bottom row of the critical and super-critical columns we see the same pattern of globally positive shear deviation as in the sub-critical column. What differs is the larger extent of the orange contours. In fact, in the super-critical case the entire paler-orange contour of deviation 10^{-2} lies outside the plotted area. Within the plotted area in all other panels in the right column, the regions with a deviation lower than 1% in absolute value are limited to a band along the zero-deviation contour. This band expands as $x_{\rm P}$ increases, and eventually connects with the outer low-deviation region. For $x_{\rm P} = 0.05$ in the super-critical case we can see very small blue regions of negative deviation without zero-shear points inside, as these appear at a higher separation, for $x_{\rm P} \geq 0.0645$. Moreover, here the angle of intersection of the dot-dashed contours is very different from a right angle. In this case the influence of the point mass at the halo center is too strong ($\gamma_{\rm P}/\gamma_{\rm NFW} \approx 1.7$), so that the expansion illustrating the generic shape of the zero-deviation contour is not valid here.

A more detailed view of the changing deviation patterns with point-mass position can be seen in Figure 3.8.B. Its closer inspection reveals that the deviation is globally positive not only for centrally-positioned point masses, but also for plots up to $x_{\rm P} = 0.01$ in the sub-critical case, up to 0.02 in the critical case, and up to 0.04 in the super-critical case. Imposing the condition $\gamma \leq \gamma_{\rm NFW}$ on Equation (3.31) reveals that negative deviation first appears at the halo center in the $\omega = \pi/2$ vertical direction once the point-mass shear at the center decreases to $\gamma_{\rm P} = 2\,\gamma_{\rm NFW}$. Using Equation (3.13) and Equation (3.29) with $\boldsymbol{x} = (0, 0)$ then yields the condition for the existence of negative-deviation regions: $x_{\rm P} \geq \sqrt{\kappa_{\rm P}/(2\,\kappa_{\rm s})}$. In the sub-critical case we find $x_{\rm P} \geq 0.0145$, in the critical $x_{\rm P} \geq 0.0238$, and in the super-critical $x_{\rm P} \geq 0.0457$, in agreement with the deviation maps.

The sizes of the contours can be used to estimate the areas with a strong effect on the shear due to the presence of the point mass. As an example, for the three different masses we find that at the moment of separation of the critical curve surrounding the point mass from the perturbed NFW tangential critical curve, the darker contours of deviation $\pm\,10^{-1}$ extend roughly seven Einstein radii from the point mass.

3.3.5.3 Convergence–Shear diagrams

In Figure 3.9.A we present a grid of CS diagrams, which provide a description complementary to the image-plane plots of the shear, its deviation due to the point mass, and the quantities discussed in the following sections. For a general understanding of CS diagrams see Appendix A.3 with Figure A.2, Section 3.2.3 with Figure 3.4, and, in particular, Section 3.3.3 with Figure 3.6.

The purple-shaded area marks the full range of (κ, γ) combinations of the NFW halo + point-mass lens. Its intersection with the green curve corresponds to the dot-dashed zero-deviation curve in Figure 3.8.A. The part of the area above the green curve then corresponds to the yellow- and orange-hued positive-deviation regions, and the part below the green curve corresponds to the blue negative-deviation regions in Figure 3.8.A.

We start by describing the sub-critical case shown in the left column. For

$x_\mathrm{P} = 0$ the point mass lies at the center of the halo and the system therefore has axial symmetry. In addition, the radial dependence of the convergence is monotonic. This implies that only one value of the shear $\gamma(x)$ can occur for any value of the convergence $\kappa(x)$. These combinations $(\kappa(x), \gamma(x))$ are plotted here as the bold purple curve. For positions far from the halo center (at the left side of the plot), this curve closely follows the unperturbed-halo green curve, which starts at the origin of the plot. Proceeding to the right (closer to the halo center), the purple curve reaches the bold black line with slope -1 representing the tangential critical curve. Here the magnification is infinite and the flattening reaches 1.

Further to the right, the curve enters an area of negative parity, where the magnification decreases and the flattening drops to 0 at the bold vertical $\kappa = 1$ line corresponding to the unit-convergence radius $x_0 \approx 0.0936$. To the right of this line, images are elongated perpendicularly to the phase. Roughly here, the purple curve of $(\kappa(x), \gamma(x))$ combinations starts to deviate significantly from the green curve. It rises rapidly and eventually leaves the plot, as the shear diverges at the location of the point mass. Close to the point mass the parity is always negative and both magnification and flattening approach zero. Before this happens, the purple curve intersects the bold black line with slope 1 twice. The first intersection represents the outer radial critical curve and the second intersection represents the inner radial critical curve. Between them, images have positive parity.

Increasing the point-mass position from $x_\mathrm{P} = 0$ to $x_\mathrm{P} = 0.05$ brings about several important changes. As the system loses its axial symmetry, for each value of convergence $\kappa(x)$ there is a continuous interval of shear values $\gamma(\boldsymbol{x})$ in the image plane and the set of convergence–shear combinations is represented by a two-dimensional region. At the left side of the plot, far from the halo center, these combinations remain limited to the close vicinity of the green curve of the unperturbed halo. At the right side, close to the halo center, the set of combinations forms a horizontal band, with shear values $\gamma \in [\gamma_\mathrm{NFW} - \gamma_\mathrm{P}, \gamma_\mathrm{NFW} + \gamma_\mathrm{P}]$ corresponding to its directional dependence at the halo center, demonstrated by Equations (3.31) and (3.33). In the vicinity of $x = x_\mathrm{P}$ we see the broadest range of shear values. On the one hand, the shear diverges at the position of the point mass while on the other hand, the shear drops to 0 at the zero-shear points occurring here at a radius slightly lower than x_P. Overall, the set of $(\kappa(\boldsymbol{x}), \gamma(\boldsymbol{x}))$ combinations looks similar to the case illustrated in Figure 3.6 and described in detail in Section 3.3.3, with one important difference. The shear divergence and the zero-shear points both lie in the area of $\kappa > 1$, meaning that nearby images would now be elongated perpendicularly to the phase.

As x_P increases in the following rows, both the shear divergence and the zero-shear point shift to the left, indicating that the point mass moves to locations with progressively lower halo convergence. By the third row from the bottom ($x_\mathrm{P} = 0.1$), the purple region touches the horizontal axis to the left of the vertical $\kappa = 1$ line, indicating that the lens underwent an umbilic transition at a slightly lower x_P value. The surroundings of the shear divergence and the zero-shear point now lie in the region $\kappa < 1$, where images are elongated parallel to the phase. The purple regions in the diagram also become narrower with increasing x_P. In the case of the divergence this is due to the changing scale of CS diagrams in terms of image-plane positions, as indicated by the green ticks. In the case of the

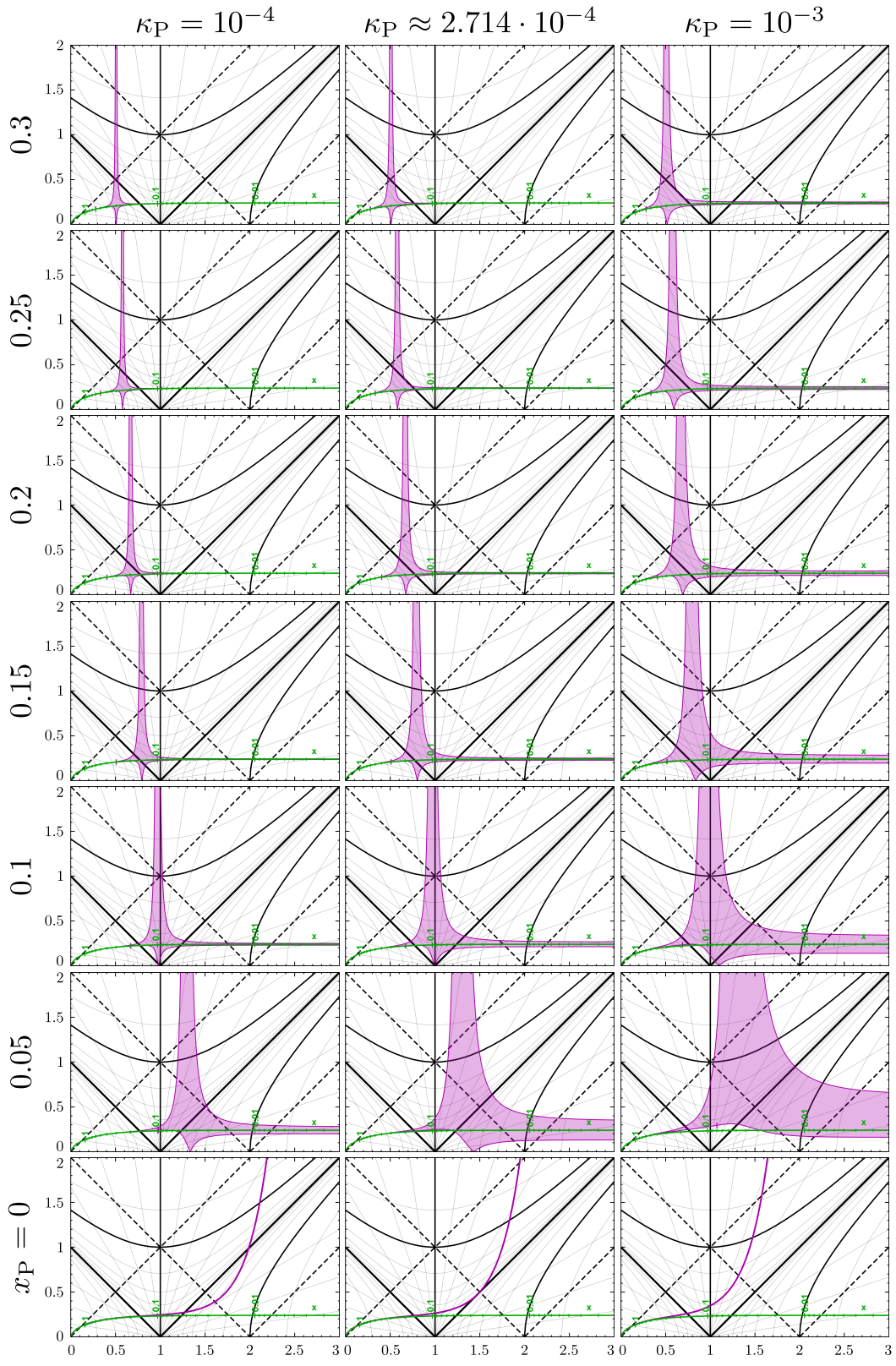

Figure 3.9.A: Convergence–shear (CS) diagrams of a NFW halo + point-mass lens, described in Section 3.3.5.3. Combinations $(\kappa(\boldsymbol{x}), \gamma(\boldsymbol{x}))$ occurring in each of the lens configurations are marked by the purple regions or curves. The green curve corresponds to the NFW-halo lens from Figure 3.4. For further details on the notation see Figure 3.6; for the interpretation of CS diagrams see Figure A.2.

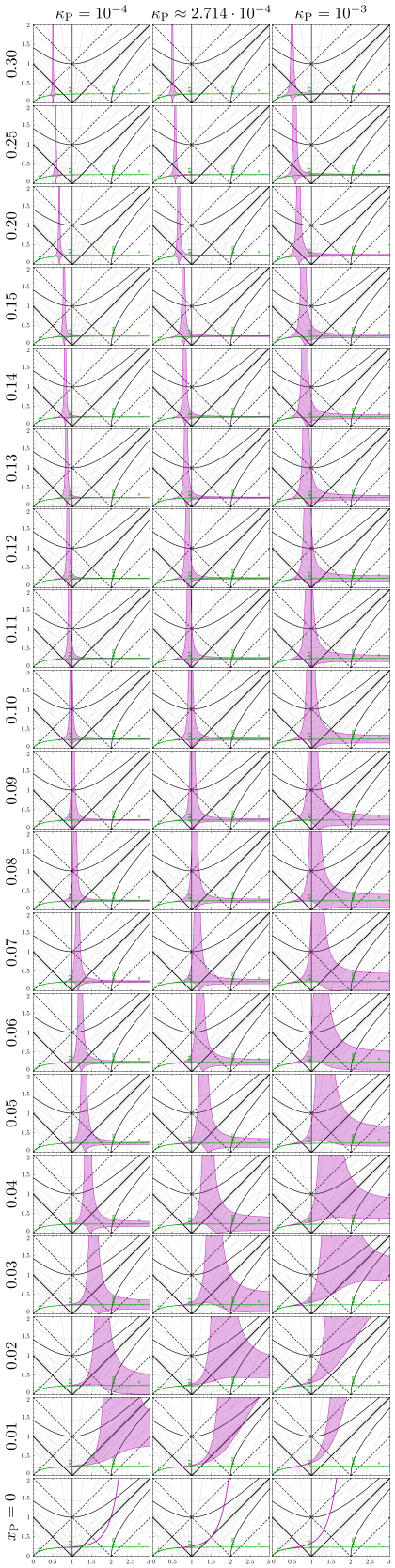

Figure 3.9.B: Convergence–shear (CS) diagrams of a NFW halo + point-mass lens, for a finer grid of point-mass positions than in Figure 3.9.A. Notation same as in Figure 3.9.A.

horizontal band this is due to the decreasing value of $\gamma_{\rm P}(0)$, i.e., the shear due to the point mass at the halo center.

There are a few differences to notice in the critical case, which is shown in the central column of Figure 3.9.A. For a centrally positioned point mass ($x_{\rm P} = 0$), the purple curve of the $(\kappa(x), \gamma(x))$ combinations deviates from the green curve of halo combinations similarly as it does in the sub-critical case. However, instead of intersecting the bold black line with slope 1, the curve merely touches it at a single point. This indicates the disappearance of the inner positive-parity region and the presence of a degenerate radial critical curve, described in detail in Appendix B of Paper I. The plot in the third row from the bottom ($x_{\rm P} = 0.1$) depicts a configuration extremely close to the elliptic umbilic, as the zero-shear points now occur almost precisely at $(\kappa, \gamma) = (1, 0)$. Generally speaking, the purple regions of convergence–shear combinations are broader than in the sub-critical case, meaning that at a given distance from the halo center a greater range of shear values occurs.

For the super-critical mass in the right column, in the axially symmetric $x_{\rm P} = 0$ case the purple curve of the $(\kappa(x), \gamma(x))$ combinations does not touch the black line with slope 1 at all. This means that there are no radial critical curves. The second plot from the bottom ($x_{\rm P} = 0.05$) is now profoundly different than in previous cases. Here, the purple area does not touch the horizontal axis of the plot. As discussed in Section 3.3.5.1, in this case there are no zero-shear points and minimum shear can be found at the halo center when approached vertically. Moreover, unlike in the lower-mass cases, at the halo center the horizontal band does not spread symmetrically around the green line. In this case, at the center the shear due to the point mass is higher than the shear due to the halo, so that $\gamma \in [\gamma_{\rm P} - \gamma_{\rm NFW}, \gamma_{\rm P} + \gamma_{\rm NFW}]$ as shown by Equation (3.33) and discussed in the following paragraphs and in Section 3.3.3.

The variation of the CS diagrams with point-mass position can be inspected in more detail in Figure 3.9.B. Note that the shear interval at the halo center is centered on $\gamma_{\rm P}$ rather than on $\gamma_{\rm NFW}$ in all cases with $x_{\rm P} < \sqrt{\kappa_{\rm P}/\kappa_{\rm s}}$, namely: from $x_{\rm P} = 0$ to $x_{\rm P} = 0.02$ in the sub-critical case; to $x_{\rm P} = 0.03$ in the critical case; to $x_{\rm P} = 0.06$ in the super-critical case. The $x_{\rm P} = 0.01$ diagrams illustrate the nature of the transition from the axially symmetric lens configurations at $x_{\rm P} = 0$, best seen in the right panel. The bold purple curve from $x_{\rm P} = 0$ gradually expands to a broader band at lower radii for $x_{\rm P} = 0.01$. The remaining structure of the purple region lies outside the plotted area in the right panel, but it has a similar nature to the plot in the left panel (also similar to the right panels for higher $x_{\rm P}$ values): shear divergence at the lens position ($x_{\rm P} = 0.01$), and the shear interval shrinking to a horizontal band centered on $\gamma_{\rm P}$.

Another feature to notice for the lower $x_{\rm P}$ values is that the entire purple region lies above the green curve, which means that for such configurations the shear is higher than in the absence of the point mass everywhere in the image plane. As shown in Section 3.3.5.2, this is the case for $x_{\rm P} < \sqrt{\kappa_{\rm P}/(2\,\kappa_{\rm s})}$, namely: plots up to $x_{\rm P} = 0.01$ in the sub-critical case; up to $x_{\rm P} = 0.02$ in the critical case; up to $x_{\rm P} = 0.04$ in the super-critical case. For higher values of $x_{\rm P}$ the shear may be lower than in the absence of the point mass, but only in limited parts of the image plane. For example, along the horizontal axis of the lens the shear always stays higher than in the absence of the point mass, as shown in

Section 3.3.5.2. For lower masses at higher separations x_P, the generic geometry of the zero-deviation contour discussed in Section 3.3.5.2 shows that the regions of lower shear are limited to radial distances $x < x_\mathrm{P}\sqrt{2}$.

3.3.5.4 Weak shear

The plots in Figure 3.10.A show image-plane color maps of the weak shear $\gamma_\mathrm{w}(\boldsymbol{x})$, which we defined in Section 3.2.4 as the shear that would be measured from image deformations using weak-lensing analysis. At the same time, these maps illustrate image flattening, since $f(\boldsymbol{x}) = 2\,\gamma_\mathrm{w}(\boldsymbol{x})$, as shown in Equation (3.24). This equality also implies that weak shear values range from 0 (corresponding to white color in the maps) to 0.5 (bright red color), with the maximum value occurring exclusively along the full length of the critical curve. In spite of this limited range, for purposes of comparison we retain the same color scale as in the first two panels of Figure 3.2 and in Figure 3.7.A.

We begin our description in the left column of Figure 3.10.A with a sub-critical point mass, starting from the bottom row corresponding to its central position in the NFW halo. Directly at the center the weak shear is equal to zero, since the image cannot be flattened in any direction due to the axial symmetry of the lens configuration. Going further from the halo center, the weak shear reaches 0.5 at the small inner radial critical curve, then it decreases slightly before returning to 0.5 at the outer radial critical curve. The weak shear then drops to zero at the unit-convergence circle, along which images are undistorted, increasing again to 0.5 at the tangential critical curve, beyond which it drops asymptotically to zero.

In the second row ($x_\mathrm{P} = 0.05$), the outer red ring of high weak shear along the perturbed NFW tangential critical curve is preserved. The same holds for the white $\gamma_\mathrm{w} = 0$ ring along the unit-convergence circle, which is in fact preserved exactly in all the configurations for all point masses. However, several changes can be seen closer to the halo center, where there are now four points with zero weak shear. These points coincide with the halo center, the point-mass position, and the pair of zero-shear points. This can be understood by inspecting Equation (3.22) and taking its limit at these points. At the halo center, the difference of signs before γ is suppressed by diverging κ, which also suppresses the directional dependence of the shear close to the center. Both fractions in Equation (3.22) tend to 1, which results in zero flattening. At the position of the point mass, both numerators and denominators are dominated by the diverging shear and the fractions thus again approach unity. At the zero-shear points, the fractions for $\gamma = 0$ are directly equal to 1. It is worth noting here that zero shear γ implies zero weak shear γ_w, but not vice versa. All four points are connected by a paler low-weak-shear region corresponding to the $\omega = \pi/2$ circle, which is interrupted between the zero-shear points and the point-mass position by the perturbed NFW radial critical curve, along which the weak shear reaches 0.5.

At $x_\mathrm{P} = 0.1$ the region of low weak shear surrounding the point mass is superimposed over the white ring of the unit-convergence circle, while the pair of $\gamma_\mathrm{w} = 0$ zero-shear points is now trapped inside tiny critical curves, here very close to the elliptic umbilic transition. For higher values of x_P, a lobe forms on the perturbed NFW tangential critical curve with the point mass inside and the zero-shear points outside. By $x_\mathrm{P} = 0.25$ the curve splits and the point mass is surrounded by a small oval critical-curve loop elongated toward the halo center.

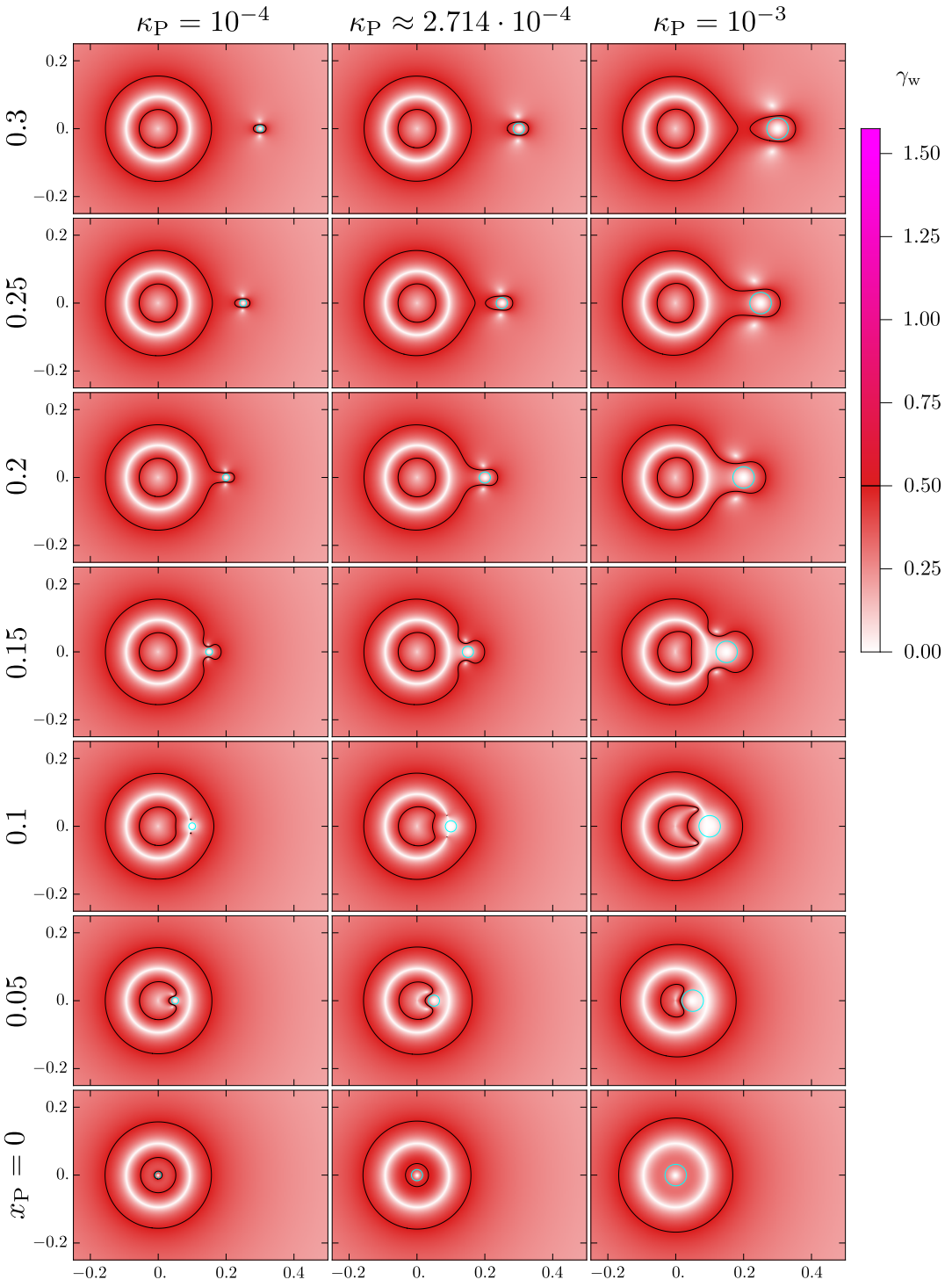

Figure 3.10.A: Image-plane maps of the weak shear $\gamma_{\rm w}(\boldsymbol{x})$ of a NFW halo + point-mass lens, described in Section 3.3.5.4. These maps also illustrate image flattening with values $f(\boldsymbol{x}) = 2\,\gamma_{\rm w}(\boldsymbol{x})$. Maximum weak shear $\gamma_{\rm w} = 0.5$ occurs exclusively along the critical curves. Remaining notation as in Figure 3.7.A.

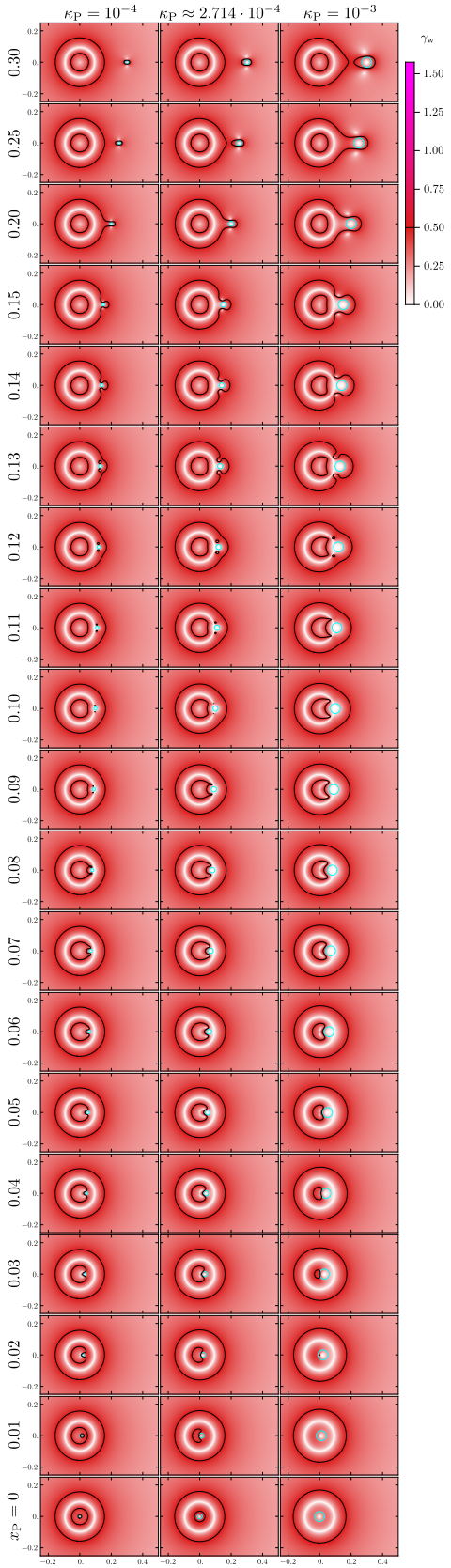

Figure 3.10.B: Image-plane maps of the weak shear $\gamma_{\rm w}(\boldsymbol{x})$ of a NFW halo + point-mass lens, for a finer grid of point-mass positions than in Figure 3.10.A. Notation same as in Figure 3.10.A.

Three points with zero weak shear remain associated with this loop: the point-mass position inside, and the two zero-shear points directly above and below the loop. Similar but larger weak-shear patterns near the tangential-critical-curve lobes and the detached ovals can be seen in the two right columns showing the critical and super-critical cases, in the rows with $x_\mathrm{P} \geq 0.15$.

In the critical case with a centrally located point mass (bottom plot in central column), there is only one $\gamma_\mathrm{w} = 0.5$ circle along the single radial critical curve between the white center and the white $\kappa = 1$ circle. The third row ($x_\mathrm{P} = 0.1$) illustrates the peculiar situation in the presence of elliptic umbilic points (technically, these occur at $x_\mathrm{P} \approx 0.0996$, but the plot is visually identical). These are zero-shear points lying directly on the unit-convergence circle. At these points the weak shear (and flattening) is undefined, as can be seen by substituting $\gamma = 0$ and $\kappa = 1$ in Equation (3.22). In the plot we can see them as point-like interruptions of the white unit-convergence circle.

In the super-critical case with $x_\mathrm{P} = 0$ (bottom right plot) there is no radial critical curve. Hence, the weak shear increases only slightly between the center and the $\kappa = 1$ circle without reaching 0.5. In the $x_\mathrm{P} = 0.05$ plot the pair of vertically offset zero-weak-shear points is missing, since the condition $x_\mathrm{P} > \sqrt{\kappa_\mathrm{P}/\kappa_\mathrm{s}}$ for the existence of zero-shear points is not fulfilled here. Note in the same plot that the weak-shear pattern near the halo center resembles the central directionally dependent shear pattern. However, while the shear is undefined at the center, the weak shear reaches 0 from any direction, with only the rate of convergence depending on the direction. The rate is slowest in the horizontal direction with $\gamma_\mathrm{w} \sim (\gamma_\mathrm{P} + \gamma_\mathrm{NFW})/(\kappa - 1)$, and fastest in the vertical direction with $\gamma_\mathrm{w} \sim |\gamma_\mathrm{P} - \gamma_\mathrm{NFW}|/(\kappa - 1)$ to first order in $1/(\kappa - 1)$. Clearly, the directionality will be most pronounced when $\gamma_\mathrm{P} = \gamma_\mathrm{NFW}$ at the halo center, i.e., at the appearance of the zero-shear points. The directionality will be least pronounced when either of the component shears $\gamma_\mathrm{NFW}, \gamma_\mathrm{P}$ dominates over the other at the halo center.

The emergence and evolution of the features and structures discussed above can be studied in more detail in Figure 3.10.B. For example, the formation of the tiny critical-curve loops around the zero-(weak)-shear points is well visible in the sub-critical case at $x_\mathrm{P} = 0.08$ or in the critical case at $x_\mathrm{P} = 0.09$. The location of the white zero-(weak)-shear points inside these loops is best visible for $x_\mathrm{P} = 0.12$ for all three masses, as well as for $x_\mathrm{P} = 0.13$ in the sub-critical case.

3.3.5.5 Weak-shear deviation due to the point mass

The plots in Figure 3.11.A depict the weak-shear deviation caused by the presence of the point mass, given by $\gamma_\mathrm{w}/\gamma_\mathrm{w,NFW} - 1$. As indicated by the formula, it is defined as the relative difference between the weak shear $\gamma_\mathrm{w}(\boldsymbol{x})$ of a NFW halo with a point mass (see Figure 3.10.A) and the weak shear $\gamma_\mathrm{w,NFW}(\boldsymbol{x})$ of a NFW halo alone (see the second panel of Figure 3.2). This means that the plots are the weak-shear equivalents of the plots from Figure 3.8.A described in Section 3.3.5.2. Therefore, we use the same color scale and the same set of contours as in Figure 3.8.A. Note that due to Equation (3.24), the plots in Figure 3.11.A also exactly portray the relative image-flattening deviation, including the color bar and the values of the contours. The yellow- and orange-hued regions thus correspond to higher flattening and weak shear, while the blue regions correspond

to lower flattening and weak shear than in the absence of the point mass.

The striking patterns of the colored areas in Figure 3.11.A look remarkably complex at first. However, especially in the top rows, away from the halo center and from the vicinity of the point mass, the plots are very similar to those in Figure 3.8.A. This should be expected, since in these regions with low values of γ and κ the weak shear is a good approximation of the shear. Closest to the point mass, the plots differ from those in Figure 3.8.A fundamentally. In Figure 3.8.A, the relative shear deviation diverges to ∞ at the position of the point mass. In Figure 3.11.A, even inside the positive weak-shear deviation contours in the top rows, there is a blue negative area in which the deviation falls to the minimum possible value of -1 at the point-mass position. This is a consequence of the weak shear γ_{w} converging to 0, while the shear γ diverges there. Interestingly, this result holds even for $x_{\mathrm{P}} = 0$ at the halo center, where even $\gamma_{\mathrm{w,NFW}}$ converges to 0. Nevertheless, in the immediate vicinity of the center the weak-shear ratio $\gamma_{\mathrm{w}}/\gamma_{\mathrm{w,NFW}} \simeq 4\,(x\,\ln x)^2\,\kappa_{\mathrm{s}}/\kappa_{\mathrm{P}} \to 0$, so that even in this case the weak-shear deviation at the point-mass position is -1.

In order to decipher the alternating positive and negative regions in Figure 3.11.A, we concentrate on their boundaries which are indicated by the dot-dashed zero-weak-shear-deviation contour. Especially in the top rows, for higher x_{P}, we can see that parts of the contours look identical to the zero-shear-deviation contours from Figure 3.8.A. However, here there is an additional strong effect closely associated with the critical curve, unlike in the case of the shear-deviation patterns which show very little influence of the critical curve. More specifically, this additional effect reflects the relative deformations of the critical curve caused by the point mass.

The zero-weak-shear-deviation contour can be defined using the flattening from Equation (3.22) by setting $f(\kappa,\gamma) = f(\kappa,\gamma_{\mathrm{NFW}})$. Since the convergence is the same with or without the point mass (except at the point-mass position), we immediately see that the zero-shear-deviation contour

$$\gamma(\boldsymbol{x}) = \gamma_{\mathrm{NFW}}(x) \tag{3.42}$$

automatically also forms a component of the zero-weak-shear-deviation contour. All dot-dashed contours from Figure 3.8.A thus appear also in Figure 3.11.A. The remaining components can be obtained by solving the flattening equality, which yields the additional non-trivial solution

$$\gamma(\boldsymbol{x})\,\gamma_{\mathrm{NFW}}(x) = [\,1-\kappa(x)\,]^2\ . \tag{3.43}$$

This equation describes all components of the zero-weak-shear-deviation contour that do not appear in Figure 3.8.A.

In particular, these include components closely associated with the critical curves, which is best illustrated when the NFW critical curves are only weakly perturbed by the point mass. Along the NFW tangential critical curve we recall that $\gamma_{\mathrm{NFW}}(x) = 1-\kappa(x)$, as discussed in Section 3.2.2. Similarly, along the perturbed NFW tangential critical curve which lies outside the unit-convergence circle, the shear satisfies $\gamma(\boldsymbol{x}) = 1-\kappa(x)$, as discussed in Section 3.3.2. It is straightforward to show that the product of the two shears is lower than $[\,1-\kappa(x)\,]^2$ along a section of one of these critical curves and at the same time it is higher than

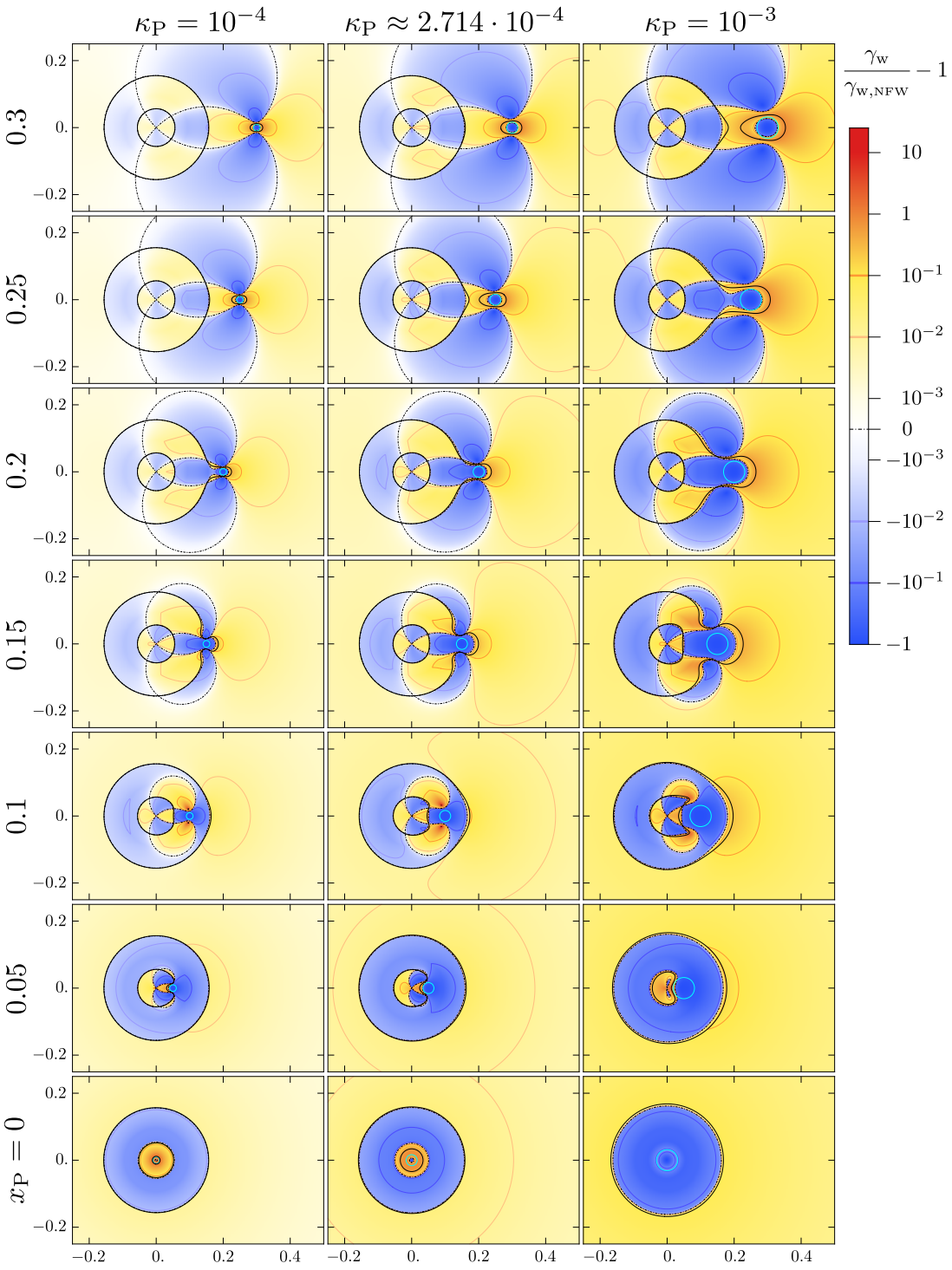

Figure 3.11.A: Image-plane maps of the relative weak-shear deviation, $\gamma_{\rm w}/\gamma_{\rm w,NFW} - 1$, caused by the presence of the point mass, described in Section 3.3.5.5. The maps also exactly portray the relative deviation in image flattening due to the point mass. Color scale, contours, and remaining notation as in Figure 3.8.A.

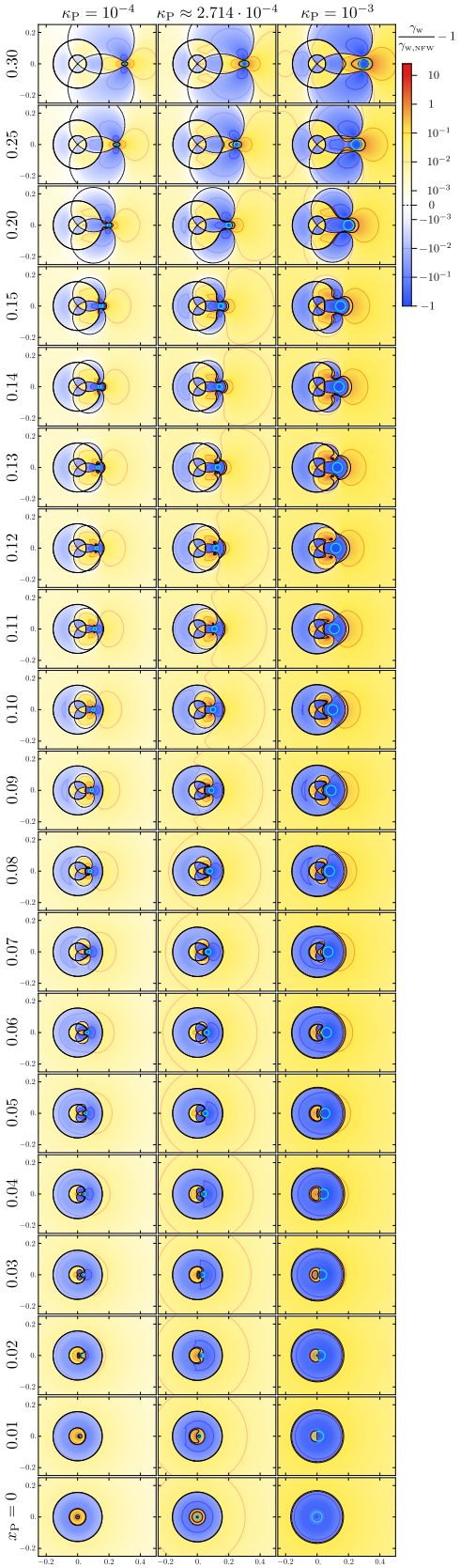

Figure 3.11.B: Image-plane maps of the relative weak-shear deviation, $\gamma_w/\gamma_{w,NFW} - 1$, caused by the presence of the point mass, for a finer grid of point-mass positions than in Figure 3.11.A. Notation same as in Figure 3.11.A.

$[\,1-\kappa(x)\,]^2$ along the corresponding section of the other critical curve. Due to continuity, there is a contour between the critical curves of the two models along which Equation (3.43) is satisfied. When the point-mass perturbation is weak, such as in the top left plot in Figure 3.11.A, the corresponding component of the zero-weak-shear-deviation contour is indistinguishable from the perturbed NFW tangential critical curve. The contour can be distinguished for example in the top right plot near the horizontal axis in the direction of the point mass.

A similar argument can be made for the NFW radial critical curve, along which $\gamma_{\mathrm{NFW}}(x) = \kappa(x) - 1$, as discussed in Section 3.2.2, and for the perturbed NFW radial critical curve inside the unit-convergence circle with $\gamma(\boldsymbol{x}) = \kappa(x) - 1$, as discussed in Section 3.3.2. Even in this case there is a contour between the two critical curves along which Equation (3.43) is satisfied. The contour can be distinguished from the perturbed NFW radial critical curve in Figure 3.11.A for example in the super-critical $x_{\mathrm{P}} = 0.15$ plot near the horizontal axis in the direction of the point mass. Note that Equation (3.43) also accounts for other components of the zero-weak-shear-deviation contour, such as the loop around the point mass in the top row of Figure 3.11.A.

At the mutual intersections of the components of zero-weak-shear-deviation contour, Equation (3.42) and Equation (3.43) have to be satisfied simultaneously. This implies that these points also represent the intersections of the critical curves of the NFW halo with and without the point mass. The combined geometry of the components with their mutual intersections explains the partitioning of the image plane into the color patterns seen in Figure 3.11.A.

Starting with a centrally positioned sub-critical point mass (bottom left plot), the deviation shows a very small negative region around the point mass inside the inner radial critical curve, followed by a positive annulus reaching just beyond the outer radial critical curve, a negative annulus almost to the tangential critical curve, and a positive outer region. All three boundaries separating these regions are described by Equation (3.43). At $x_{\mathrm{P}} = 0.05$, the negative region around the point mass is connected with the larger negative annulus. In addition, the zero-shear-deviation boundary given by Equation (3.42) can be seen, introducing negative areas above and below the halo center, with positive crescents where it reaches beyond the zero-weak-shear-deviation contour associated with the perturbed NFW radial critical curve. At $x_{\mathrm{P}} = 0.1$, strong positive deviation can be seen close to the two tiny critical-curve loops, along which $\gamma_{\mathrm{w}} = 0.5$ while $\gamma_{\mathrm{w,NFW}} \approx 0$. However, note that at the zero-shear points inside the loops the weak-shear deviation equals -1, with the indiscernible negative regions around them bordered by contour loops obeying Equation (3.43). At $x_{\mathrm{P}} = 0.15$, the region inside the zero-shear-deviation contour flips color again as it crosses the zero-weak-shear-deviation contour associated with the perturbed NFW tangential critical curve. At $x_{\mathrm{P}} = 0.25$, the point-mass critical-curve loop is detached from the NFW-halo critical curve, showing the characteristic four-lobed contour pattern seen in Figure 3.8.A, here with the central negative region described above.

A similar sequence can be seen in the two right columns, in which the structures are larger and the deviations more prominent. In particular, the zero-weak-shear-deviation contours near the critical curves are better visible in some of the plots here. Note also the change with increasing mass for a central position of

the point mass in the bottom row. In the critical case there is only a single degenerate radial critical curve, with the accompanying zero-weak-shear-deviation contour well separated from it. The positive-deviation annulus is narrower as the central negative region is larger, and for a higher mass it disappears entirely. This can be seen in the super-critical case, where there is only a single large negative-deviation region reaching almost to the tangential critical curve.

The transitions of the patterns with increasing point-mass position x_P can be studied in more detail in Figure 3.11.B. For example, note the appearance of a positive-deviation region in the super-critical case at $x_\mathrm{P} = 0.01$, as soon as the point mass is displaced from the halo center. For larger separations the boundary of this region forms the zero-weak-shear-deviation contour associated with the perturbed NFW radial critical curve. The small negative regions inside the tiny critical-curve loops can be seen here at $x_\mathrm{P} = 0.13$ in the sub-critical case, or at $x_\mathrm{P} = 0.12$ in all cases. In the critical and super-critical cases at $x_\mathrm{P} = 0.13$, we see that these regions persist even after the loops merge with the outer critical curve.

Studying the colored contours, we see that the regions with the strongest negative weak-shear deviation occur close to the point mass and near the zero-shear points (except when they lie between the perturbed NFW radial and tangential critical curves). The strongest positive deviation occurs close to the point mass along the horizontal axis outside its Einstein radius, and just outside the tiny critical-curve loops enclosing the zero-shear points. A closer inspection of the contours reveals that some of them display sharp bends at specific positions. These may appear at three types of locations. First, at the unit-convergence circle, as can be seen for example in the critical case at $x_\mathrm{P} = 0.15$ on the pale blue, pale orange, and dark orange contours. These kinks are caused by the switching of the minimum fractions in Equation (3.22) at $\kappa = 1$, which causes a discontinuity in the derivatives.

Second, at the critical curves, as can be seen for example in the super-critical case at $x_\mathrm{P} = 0.25$ on the pale orange and pale blue contours at the left side of the plot, or in the sub-critical case at $x_\mathrm{P} = 0.15$ on the pale orange and pale blue contours above and below the halo center. These kinks are caused by crossing the zero points of the absolute values in Equation (3.22), which also causes a discontinuity in the derivatives. Third, at the NFW-halo critical curves, as can be seen for example in the super-critical case at $x_\mathrm{P} = 0.15$ on the dark blue contours around the zero-shear points above and below the point mass, or in the critical case at $x_\mathrm{P} = 0.20$ on the dark blue contour extending from the point mass toward the halo center. These kinks are similar to the previous ones, being caused by crossing the zero points of the absolute values in Equation (3.22) when evaluating the NFW halo weak shear.

Regarding the extent of the contours, they are generally slightly smaller than those in Figure 3.8.A, indicating that the weak-shear deviation falls more quickly with the distance from the point mass than the shear deviation. As a rough estimate, at the moment of separation of the critical curve surrounding the point mass from the perturbed NFW tangential critical curve, the $\gamma_\mathrm{w}/\gamma_{\mathrm{w,NFW}} - 1 = \pm 10^{-1}$ contours extend roughly six Einstein radii from the point mass.

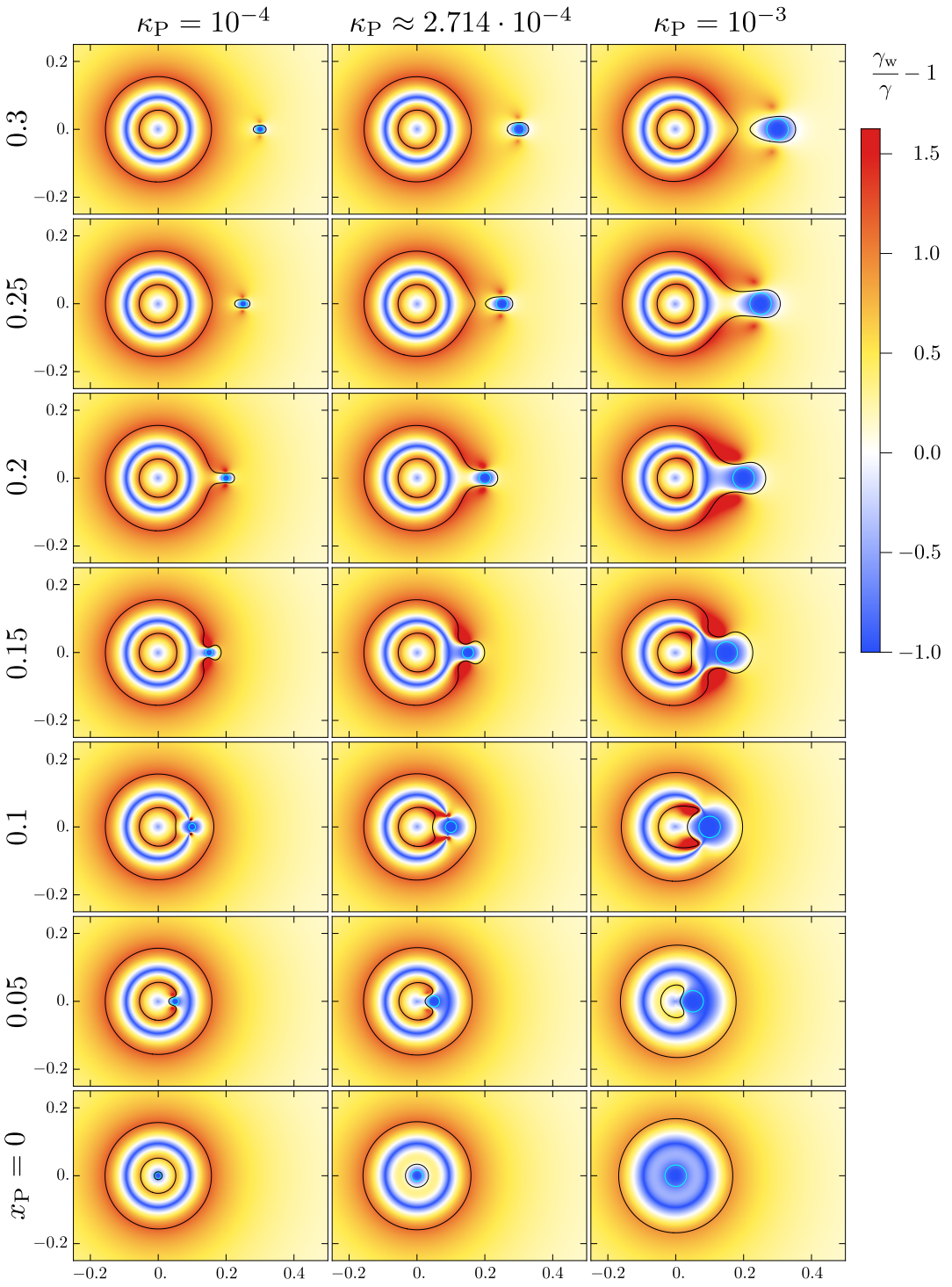

Figure 3.12.A: Image-plane maps of the relative weak-shear deviation from the shear, $\gamma_\mathrm{w}/\gamma - 1$, of a NFW halo + point-mass lens, described in Section 3.3.5.6. The maps illustrate the relative error of the weak-lensing shear estimate. All positions with deviation greater than 1.5 are marked in red. Remaining notation as in Figure 3.7.A.

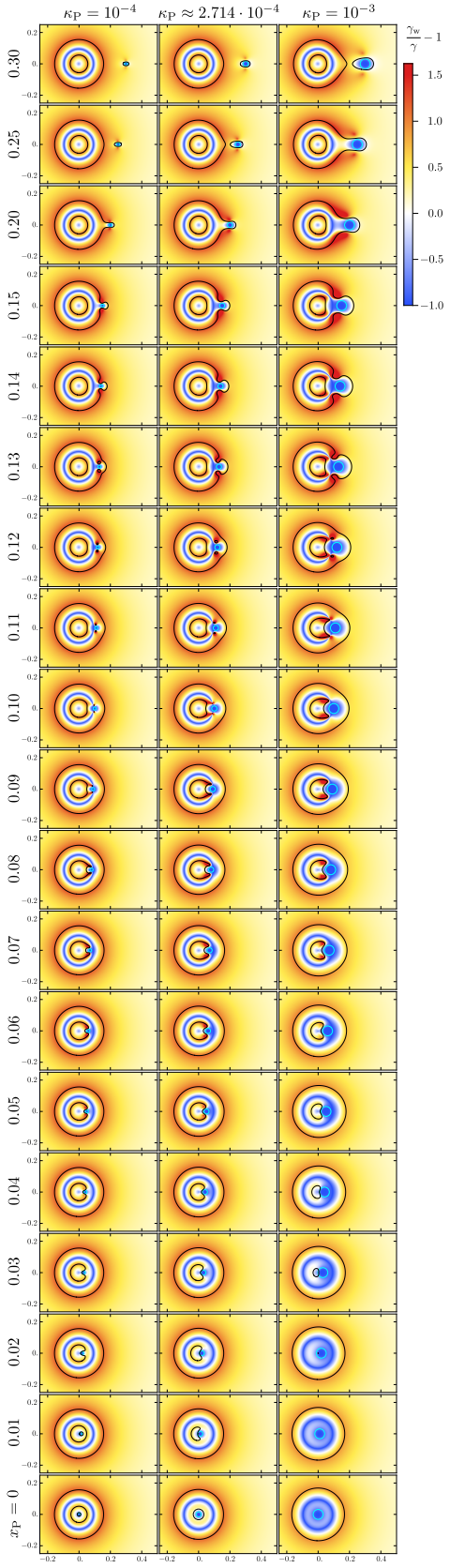

Figure 3.12.B: Image-plane maps of the relative weak-shear deviation from the shear, $\gamma_w/\gamma - 1$, of a NFW halo + point-mass lens, for a finer grid of point-mass positions than in Figure 3.12.A. Notation same as in Figure 3.12.A.

3.3.5.6 Weak-shear deviation from the shear

The relative deviation $\gamma_w/\gamma - 1$ of the weak shear (shown in Figure 3.10.A) from the shear (shown in Figure 3.7.A) is plotted in the image-plane color maps in Figure 3.12.A. We use the same color scale as in the third panel of Figure 3.2, which shows the same quantity plotted for the NFW halo alone. By its definition, this deviation shows the relative error of shear estimation using the weak-lensing approximation.

In the case of the sub-critical mass (left column), the plots are very similar to the plot in the third panel of Figure 3.2, with the point mass affecting only its nearby surroundings. Note that the weak shear is always zero at the position of the point mass, so that the deviation reaches its minimum value of -1 there, leading to a dark blue spot similar to the one associated with the point mass in Figure 3.11.A. In the bottom row, the central negative spot is thus more prominent than in the absence of the point mass and it includes even the inner radial critical curve. At $x_P = 0.05$, there is a pair of red spots with a strong positive deviation close to the zero-shear points above and below the point mass. At these points, both γ_w and γ drop to 0, but their ratio γ_w/γ converges to $1/|\kappa - 1|$. The deviation is thus positive as long as $\kappa < 2$, corresponding to zero-shear points located more than circa 0.011 from the center of our fiducial halo.

As the point mass crosses the unit-convergence circle near $x_P = 0.1$, the red spots shrink but their peak deviation increases. When the zero-shear points approach the perturbed NFW tangential critical curve at $x_P = 0.15$, the spots expand to their largest as they merge with the positive-deviation band along the critical curve. When the point-mass critical-curve loop is detached from the perturbed tangential critical curve of the NFW halo as seen in the two top rows, the positive-deviation spots remain associated with the zero-shear points above and below the point mass, even though their peak deviation declines with increasing point-mass position x_P. The pattern around the halo center at $x_P = 0.3$ is virtually identical to the unperturbed-halo pattern in the third panel of Figure 3.2.

The plots for a critical mass in the central column follow a similar sequence, with larger affected regions around the point mass. When it is positioned at the halo center (bottom row), we see that the single radial critical curve shows practically zero deviation, and between it and the blue unit-convergence circle the positive deviation reaches lower values. At $x_P = 0.1$, the red areas of high deviation extend from the perturbed NFW radial critical curve past the zero-shear points and beyond the unit-convergence circle. The pinched pattern at its intersection with the circle is indicative of the elliptic umbilic at which the weak shear is undefined, as discussed in Section 3.3.5.4.

The regions strongly influenced by the super-critical mass in the right column are much larger, with nearly half of the pattern around the NFW halo critical curve affected for $x_P = 0.1, 0.15$, and 0.2. For $x_P = 0$ there is no region of positive deviation between the halo center and the unit-convergence circle. For $x_P = 0.05$ a positive region is present but there are no red spots, as there are no zero-shear points at this configuration. At $x_P = 0.1$ the red spots are very large and prominent. At $x_P = 0.15$, in addition to the zero-shear-point red spots there are two adjacent smaller red spots along the perturbed NFW radial critical

curve.

The changing patterns can be studied with a finer step in point-mass positions in Figure 3.12.B. For example, the pattern around the tiny critical-curve loops can be seen at $x_{\rm P} = 0.12$ and in a few neighboring panels. We also point out the $x_{\rm P} = 0.03$ panel in the sub-critical case and the $x_{\rm P} = 0.04$ panel in the critical case. In these panels there are no red spots close to the zero-shear points, which lie still too close to the halo center. However, in the super-critical case at $x_{\rm P} = 0.06$ we see red (or rather orange) spots at the tips of the perturbed NFW radial critical curve even though the zero-shear points are not present yet. One panel higher, at $x_{\rm P} = 0.07$, these red spots are more prominent while the zero-shear points are located near their edge closer to the halo center. Clearly, the red spots develop at the perturbed NFW radial critical curve even for lower point-mass positions at which there are no zero-shear points. With a slight increase in $x_{\rm P}$, the points reach the red spots, which then remain associated with them at more distant point-mass positions.

Overall, the pattern of the blue areas shows that the weak shear underestimates the shear near the halo center, along the unit-convergence circle, and roughly within an Einstein radius of the point mass (extending further when it overlaps with the unit-convergence circle). Practically everywhere else the weak shear overestimates the shear, most prominently in the red and orange areas: close to the zero-shear points, along the perturbed NFW tangential critical curve, and along the perturbed NFW radial critical curve (except when a super-critical mass is positioned close to the halo center). Further from the halo center, e.g., close to the right edge of the plots in Figure 3.12.A for our fiducial halo, the positive deviation is very low, so that the weak shear may serve as a good approximation of the shear. However, the agreement fails in the vicinity of the point mass. This occurs primarily inside its Einstein radius, but also further to the tangentially offset zero-shear points. Note that for $\kappa_{\rm NFW}(x_{\rm P}) \ll 1$ the deviation at the zero-shear points reaches a value $\gamma_{\rm w}/\gamma - 1 \approx \kappa_{\rm NFW}(x_{\rm P})$, so that their influence decreases as the halo convergence declines for higher $x_{\rm P}$.

3.3.5.7 Weak phase

In Figure 3.13.A we present image-plane plots of the weak phase $\varphi_{\rm w}$ of the NFW halo + point-mass lens, given by Equation (3.41). We defined the weak phase in Section 3.2.4 as the phase that would be measured from the orientation of image deformations using weak-lensing analysis. For an elliptical image of a small circular source the weak phase is simply the angle between its major axis and the horizontal axis in the plots. Thus, $\varphi_{\rm w} = 0$ corresponds to horizontally and $|\varphi_{\rm w}| = \pi/2$ to vertically elongated images. The weak phase of the NFW-halo lens is described in Section 3.2.4 and shown in the fourth panel of Figure 3.2. Without the point mass, outside the unit-convergence circle the weak phase is equal to the phase and images are oriented tangentially. Inside the unit-convergence circle the weak phase is perpendicular to the phase and images are oriented radially.

In Figure 3.13.A we use the same weak-shear color scale as in the fourth panel of Figure 3.2, with white corresponding to horizontal images, orange to images oriented counterclockwise from the horizontal, and blue to images oriented clockwise from the horizontal. The saturation of both colors increases with the angle from the horizontal, from zero saturation for angle 0 to maximum saturation

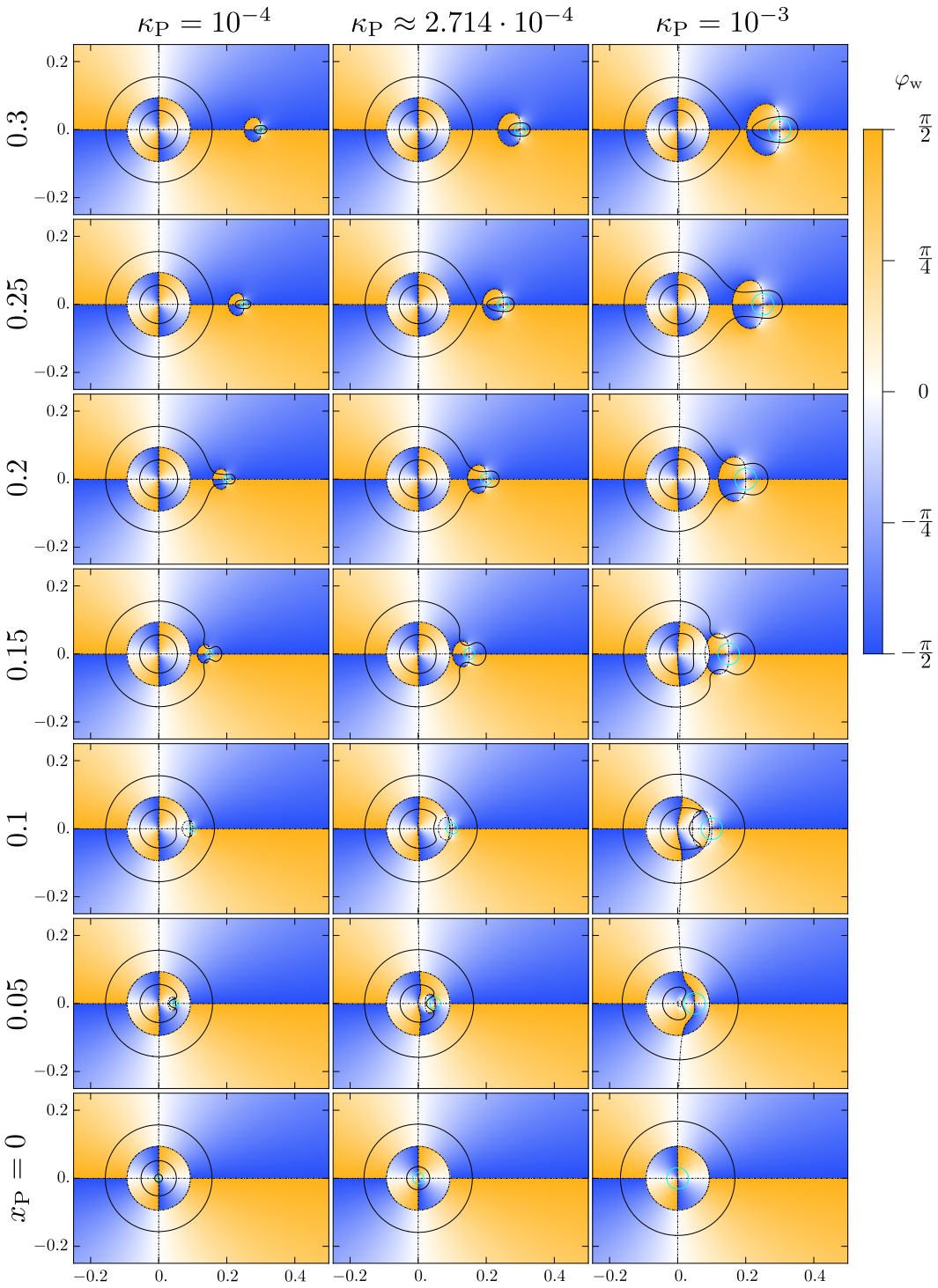

Figure 3.13.A: Image-plane maps of the weak phase $\varphi_{\mathrm{w}}(\boldsymbol{x})$ of a NFW halo + point-mass lens, described in Section 3.3.5.7. Orange and blue correspond to images oriented counterclockwise and clockwise, respectively, from the horizontal. Dot-dashed curves indicate exactly horizontal, exactly vertical, or undefined image orientation. Remaining notation as in Figure 3.7.A.

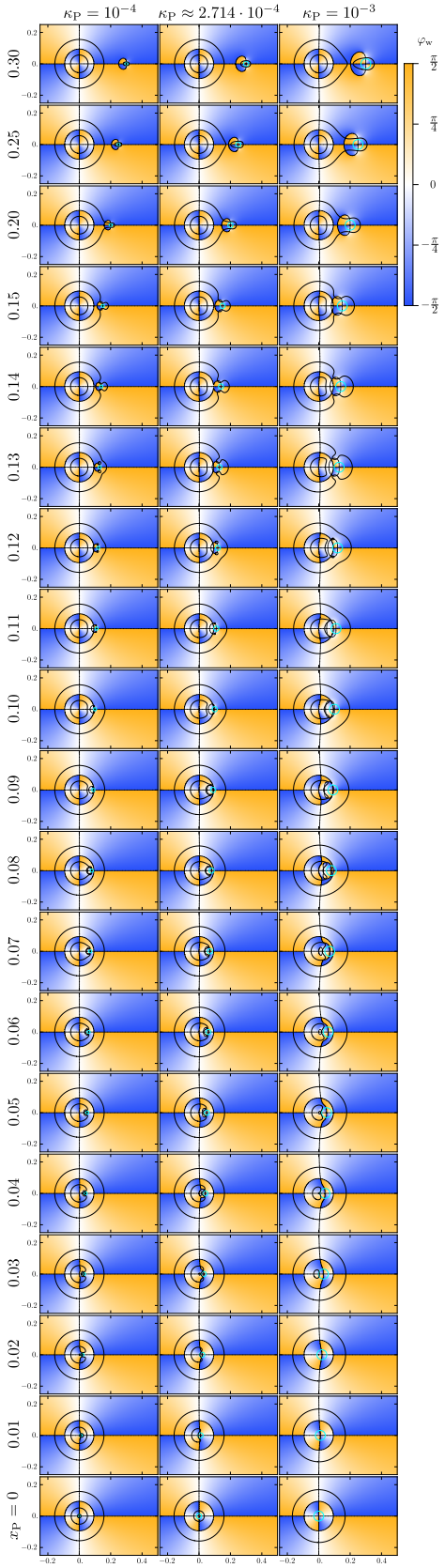

Figure 3.13.B: Image-plane maps of the weak phase $\varphi_{\rm w}(\boldsymbol{x})$ of a NFW halo + point-mass lens, for a finer grid of point-mass positions than in Figure 3.13.A. Notation same as in Figure 3.13.A.

for angle $\pi/2$. The dot-dashed contour marks several special orientations: $\varphi_\mathrm{w} = 0$, $|\varphi_\mathrm{w}| = \pi/2$, and undefined φ_w. The weak phase is undefined at all points with zero weak shear, as described in Section 3.3.5.4. These include the halo center, the point-mass position, the zero-shear points, and the unit-convergence circle. All of these points thus play an important role in the patterns seen in the color maps in Figure 3.13.A.

Thanks to the axial symmetry of the lens configurations with $x_\mathrm{P} = 0$ in the bottom row of Figure 3.13.A, the color maps are identical to that of the unperturbed halo, as seen in the fourth panel of Figure 3.2. This means that outside the $\kappa = 1$ circle images are oriented tangentially, while inside the circle the weak phase is flipped by $\pi/2$ and images are oriented radially. Exactly at the halo center the weak phase is undefined. Note the colors alternating around the center with orange in the first quadrant and the saturation varying from zero along the horizontal to maximum along the vertical axis. Such a pattern corresponds to radial orientation of images around the center.

The variation of the weak-phase maps with point-mass position x_P is best seen in the super-critical case (right column). In the top row with $x_\mathrm{P} = 0.3$ the point mass is well separated from the halo center. The left part of the plot closer to the halo center is similar to the unperturbed pattern seen also in the bottom row. Note here the slight shift toward the point mass of the dot-dashed contour extending vertically outward from the unit-convergence circle, which corresponds to horizontal images. The main new feature is the oval region with inverted colors bordered by a loop of the dot-dashed contour, which passes through the position of the point mass at its right side and extends in the direction of the halo center on its left side. The pattern seen around the point mass also has colors alternating around the center, however, here with blue in the first quadrant. In addition, the saturation varies from zero along the vertical to maximum along the horizontal axis. This pattern corresponds to tangential orientation of images around the point mass.

The left part of the dot-dashed border of the oval separates high-saturation regions and, thus, corresponds to vertically oriented images. The right part of the border lies in the white band separating low-saturation regions and, thus, corresponds to horizontally oriented images. The two parts of the boundary meet at the zero-shear points that lie above and below the point mass. In this panel, horizontal images occur along the horizontal axis inside the unit-convergence circle, along the vertical dot-dashed contour outside the unit-convergence circle, and along the right boundary of the oval region connecting the zero-shear points vertically through the point-mass position. Vertical images occur along the horizontal axis outside the unit-convergence circle, along the vertical dot-dashed contour inside the unit-convergence circle, and along the left boundary of the oval region connecting the zero-shear points and passing vertically through a point between the halo center and the point mass.

Going down in the right column, the inverted-color oval shrinks slightly as it moves with the point mass closer to the halo center. At $x_\mathrm{P} = 0.15$, the oval partly overlaps the unit-convergence circle. The very pale color in the region of their overlap indicates near-horizontal orientation of images there. At the boundary of the oval in this plot, images are oriented horizontally along its left part inside the unit-convergence circle and along its right part from the zero-shear points to the

point-mass position. Along the segments extending from the zero-shear points to the left till the unit-convergence circle, images are oriented vertically. Image orientations along the other parts of the dot-dashed contour remain unchanged.

At $x_\mathrm{P} = 0.1$, the zero-shear points now lie inside the unit-convergence circle, so that horizontally oriented images now occur along the left boundary of the oval up to the zero-shear points and along the part of the right boundary outside the unit-convergence circle passing through the point-mass position. Vertically oriented images occur along the segments extending from the zero-shear points to the right till the unit-convergence circle. The pattern inside the overlap of the oval and the unit-convergence circle reflects two general properties of its boundaries. Crossing the boundary of the oval inverts only the color at $\varphi_\mathrm{w} = 0$ or $|\varphi_\mathrm{w}| = \pi/2$, which corresponds to a continuous change in orientation. Crossing the unit-convergence circle inverts the color as well as the saturation, which corresponds to a $\pi/2$ flip in orientation. Note here also the more prominent bulging of the vertical dot-dashed contour passing through the halo center as the point mass lies closer.

Between $x_\mathrm{P} = 0.1$ and $x_\mathrm{P} = 0.05$, the boundary of the inverted-color oval undergoes reconnection with the bulging vertical dot-dashed contour. At $x_\mathrm{P} = 0.05$ this contour passes through the point-mass position, while a small inverted-color oval lies to the left of it, with its left boundary passing through the halo center. Note that at $x_\mathrm{P} = 0.05$ there are no zero-shear points, so that here the entire boundary of the small oval corresponds to horizontal images. What is more striking in this plot is the pattern around the point mass, which now lies inside the unit-convergence circle. Orange in the first quadrant and zero saturation along the horizontal axis indicate that images are now oriented radially around the point mass. As the point mass moves closer to the halo center, at a certain value $0 \leq x_\mathrm{P} < 0.05$ the small oval disappears and the dot-dashed vertical curve passes through the origin for $x_\mathrm{P} = 0$.

In the critical and sub-critical cases (the central and left columns, respectively) the same sequence of changes occurs as in the super-critical case, although for slightly different values of x_P. Note that the inverted-color oval increases in size with increasing mass parameter κ_P. In the top rows, the point at which the left side of its boundary crosses the horizontal axis marks a boundary of influence of the halo and the point mass (at least as far as image orientation is concerned). Both boundaries passing through this point correspond to vertically oriented images. However, images located off the horizontal axis to the left of this point are tilted tangentially to the halo, while those to the right of this point are tilted tangentially to the point mass.

Details of the changing patterns and contours can be studied in more detail in Figure 3.13.B. For example, it can be seen that the reconnection of the vertical and oval dot-dashed contours occurs at the zero-shear points. At higher values of x_P the points lie on the larger oval passing through the point-mass position, while at lower values they lie on the smaller oval passing through the halo center. For progressively lower point-mass distances, the zero-shear points move along the smaller oval to the center, where they disappear at $x_\mathrm{P} = \sqrt{\kappa_\mathrm{P}/\kappa_\mathrm{s}}$.

The plot for the critical case at $x_\mathrm{P} = 0.1$ illustrates the situation at the elliptic umbilics, which occur for a slightly lower point-mass distance. In this case, the full length of the oval contour corresponds to horizontal image orientations (except

the point-mass position and the zero-shear points with undefined orientation). Similarly, the $x_\mathrm{P} = 0.09$ plots for the critical and super-critical cases indicate the interesting pattern near the point mass when it lies on the unit-convergence circle (in both cases for a slightly higher point-mass distance). To the right of the point mass images are oriented vertically (tangentially), to the left horizontally (radially), and above and below the orientation is undefined (i.e., the images are circular).

The weak-phase plots presented in Figure 3.13.A can also be used to visualize the phase, which we do not present in a separate plot. The reason is indicated by Equation (3.41), which shows that outside the unit-convergence circle the phase is equal to the weak phase, while inside it differs by $\pi/2$. The phase plots would thus differ from the weak-phase plots in Figure 3.13.A by having the colors and saturations flipped inside the unit-convergence circle around the halo center. The circle would disappear in such plots, and the color and saturation outside would extend continuously inside all the way to the halo center. The dot-dashed contour would then consist only of the horizontal axis, the perturbed vertical line through the halo center, and the large oval associated with the point mass reconnecting to the small oval associated with the halo center.

Overall, note that unlike the weak shear in Figure 3.10.A, the weak phase in Figure 3.13.A shows very little correlation with the geometry of the critical curve. Finally, we point out that placing the point mass off the horizontal axis would not lead to a simple rotation of the patterns as in the other presented plot grids. Instead, the overall halo pattern and the pattern close to the point mass would remain unchanged. A point mass in a blue region of the halo would thus locally generate a pair of orange lobes, while in an orange region it would generate a pair of blue lobes.

3.3.5.8 Weak-phase deviation due to the point mass

The image-plane color maps presented in Figure 3.14.A depict the weak-phase deviation due to the point mass, defined as the difference between the weak shear of the NFW halo + point-mass lens (shown in Figure 3.13.A) and the weak shear of the NFW halo alone (shown in the fourth panel of Figure 3.2), $\delta\varphi_\mathrm{w}(\boldsymbol{x}) = \varphi_\mathrm{w} - \varphi_\mathrm{w,NFW}$. We correct the difference if necessary by adding or subtracting π to keep $\delta\varphi_\mathrm{w}$ in the interval $[-\pi/2, \pi/2]$. The deviation is also equal to the angle by which the orientation of an image changes due to the presence of the point mass. Red positive values of $\delta\varphi_\mathrm{w}$ correspond to a counterclockwise change, blue negative values to a clockwise change in orientation. The color saturation is scaled linearly for $|\delta\varphi_\mathrm{w}| \leq \pi/2000$ and logarithmically for $|\delta\varphi_\mathrm{w}| \geq \pi/2000$. Contours are plotted for $|\delta\varphi_\mathrm{w}| = \pi/20 = 9^\circ$ (dark red and blue), and for $|\delta\varphi_\mathrm{w}| = \pi/200 = 0.9^\circ$ (light red and blue).

When the point mass is located exactly at the center of the halo (bottom row of Figure 3.14.A), the lens has axial symmetry and the weak-phase deviation is zero everywhere, which explains the completely white plots. Note that this result also reflects the fact that images are oriented radially around a point mass lying inside the unit-convergence circle, as shown in Section 3.3.5.7.

All the other plots with an off-center point mass share the same characteristic color pattern; they differ only in its scale and in color saturation. The blue and red regions are separated by the dot-dashed contour, which marks all positions

with zero deviation $\delta\varphi_{\rm w} = 0$ or maximum deviation $|\delta\varphi_{\rm w}| = \pi/2$. The geometry of the contour is simple and independent of the mass parameter $\kappa_{\rm P}$: it includes the horizontal axis and the $\omega = \pi/2$ circle reaching from the halo center to the position of the point mass (see Figure 3.5). Along the horizontal axis, images are always horizontal inside and vertical outside the unit-convergence circle, unaffected by the presence of a point mass, as shown in Section 3.3.5.7. Hence, this part of the dot-dashed contour corresponds to $\delta\varphi_{\rm w} = 0$.

Along the $\omega = \pi/2$ circle, there is a right angle between the direction to the halo center and the direction to the point mass. The shear from the halo and the shear from the point mass thus act in perpendicular directions. Going from the halo center along the $\omega = \pi/2$ circle, the halo shear decreases and the point-mass shear increases, as described in Section 3.3.1. Hence, from the halo center to the zero-shear points the halo shear dominates and the image orientation remains unchanged, so that $\delta\varphi_{\rm w} = 0$ along this part of the circle. From the zero-shear points to the point mass, the point-mass shear dominates and the images are oriented perpendicular to the orientation they would have in absence of the point mass, so that $|\delta\varphi_{\rm w}| = \pi/2$ along the remaining part of the circle. For point-mass positions $x_{\rm P} < \sqrt{\kappa_{\rm P}/\kappa_{\rm s}}$, there are no zero-shear points and the entire $\omega = \pi/2$ circle corresponds to $|\delta\varphi_{\rm w}| = \pi/2$.

Above the horizontal axis and outside the $\omega = \pi/2$ circle, the weak-shear deviation is positive meaning that in this region the image orientation changes counterclockwise. Conversely, under the axis and outside the circle, the deviation is negative and the image orientation changes clockwise. Inside the $\omega = \pi/2$ circle, the sign of the deviation in either half-plane is switched and image orientations change in the opposite sense. At the center of the halo and at the location of the point mass, four regions of alternating positive and negative deviation meet.

Deviations $|\delta\varphi_{\rm w}|$ peak close to the point mass (particularly along the $\omega = \pi/2$ circle), and fall rapidly with increasing distance from it. The color pattern near the point mass indicates that images are oriented tangentially around it (when it lies outside the unit-convergence circle) or radially around it (when it lies inside the unit-convergence circle). The color pattern around the halo center indicates that the point mass orients the images more horizontally there. When zero-shear points are present, zero deviations occur in the horizontal and vertical directions from the center and strongest deviations occur along the diagonals. In the absence of zero-shear points, for $x_{\rm P} < \sqrt{\kappa_{\rm P}/\kappa_{\rm s}}$, zero deviations occur in the horizontal directions and strongest $|\delta\varphi_{\rm w}| = \pi/2$ deviations occur in the vertical directions.

The areas with high deviation $|\delta\varphi_{\rm w}|$ extend further from the point mass for greater values of $\kappa_{\rm P}$, as seen in the central and right columns of Figure 3.14.A. For point masses far from the halo center (in the top rows), all contours form four-lobed butterfly-like shapes. For point masses closer to the halo center, the left lobes of the contours become pointy (e.g., $x_{\rm P} = 0.2$ in the central column) and eventually they extend to the halo center (e.g., $x_{\rm P} = 0.15$ in the central column). To illustrate the area affected by the point mass, we estimate the extent of the contours at the moment of separation of the critical curve surrounding the point mass from the perturbed NFW tangential critical curve, i.e., between $x_{\rm P} = 0.20$ and $x_{\rm P} = 0.25$ for the sub-critical and critical cases, and between $x_{\rm P} = 0.25$ and $x_{\rm P} = 0.30$ in the super-critical case. In all three cases, the inner $|\delta\varphi_{\rm w}| = \pi/20$

contours extend about four Einstein radii, while the outer $|\delta\varphi_{\rm w}| = \pi/200$ contours extend as far as twelve Einstein radii from the point mass.

The changes in the contours for different point-mass positions can be studied in more detail in Figure 3.14.B. The abrupt change from zero deviation to $|\delta\varphi_{\rm w}| = \pi/2$ along the $\omega = \pi/2$ circle at the zero-shear points can be best seen in the presence of the small critical-curve loops surrounding them, e.g., for $x_{\rm P} = 0.12$. Note also the very small extent of the colored regions for the lowest separations $x_{\rm P}$.

Similarly to Figure 3.13.A, the weak-phase deviation in Figure 3.14.A shows very little correlation with the geometry of the critical curve. However, unlike Figure 3.13.A, it also shows no influence of the unit-convergence circle.

3.4 Discussion

The examples of images formed by the NFW halo + point-mass lens in the bottom right panel of Figure 3.1 can be compared with the results presented in Section 3.3.5, specifically with the corresponding $x_{\rm P} = 0.2$, $\kappa_{\rm P} \approx 2.714 \cdot 10^{-4}$ panels of the plot grids. In particular, the weak-shear map in Figure 3.10.A shows the image flattening, the weak-phase map in Figure 3.13.A shows the image orientation, and the weak-shear-deviation-from-shear map in Figure 3.12.A shows the relative shear error that would be incurred by assuming the weak-lensing relation between image distortion and shear.

A few points should be noted regarding the interpretation of such comparisons. First, Figures 3.7.A–3.14.A present maps of their respective quantities for point-like sources. For images of extended sources such as those shown in Figure 3.1, one has to consider the full variation of the quantities within the area of the image. For example, an image lying on the unit-convergence circle will have its inner part extended radially and its outer part tangentially, as seen from Figure 3.13.A.

Second, when studying the changes in image shape and orientation due to the point mass using Figure 3.1 with Figure 3.11.A or Figure 3.14.A, a direct comparison can be made when there is at least a partial overlap of the images formed by halos with and without the point mass. In the bottom right panel of Figure 3.1, the left and central images have a large overlap with the images in the top right panel, the lower right image has a smaller overlap, and the two images close to the point mass have no overlap. For these two images, Figure 3.11.A and Figure 3.14.A show the deviations from images formed at the same positions by the halo-only lens, but for different source positions. In this particular case, the sources would lie above the horizontal axis at different radial distances in the top left panel of Figure 3.1. In fact, even in the case of overlapping images, the overlapping parts may be images of different parts of the source. Thus, Figure 3.11.A and Figure 3.14.A compare the properties of images formed by the two lens models at a same position in the image plane of sources at different positions in the source plane. They do not compare the properties of images of a fixed source formed by a halo with and without a point mass.

Third, in this work we do not explore the changes in image positions due to the point mass. This would be difficult to present in general, if only due to the change in the number of images. However, it could be done in a perturbative regime, by studying the displacement and distortion of particular images of a

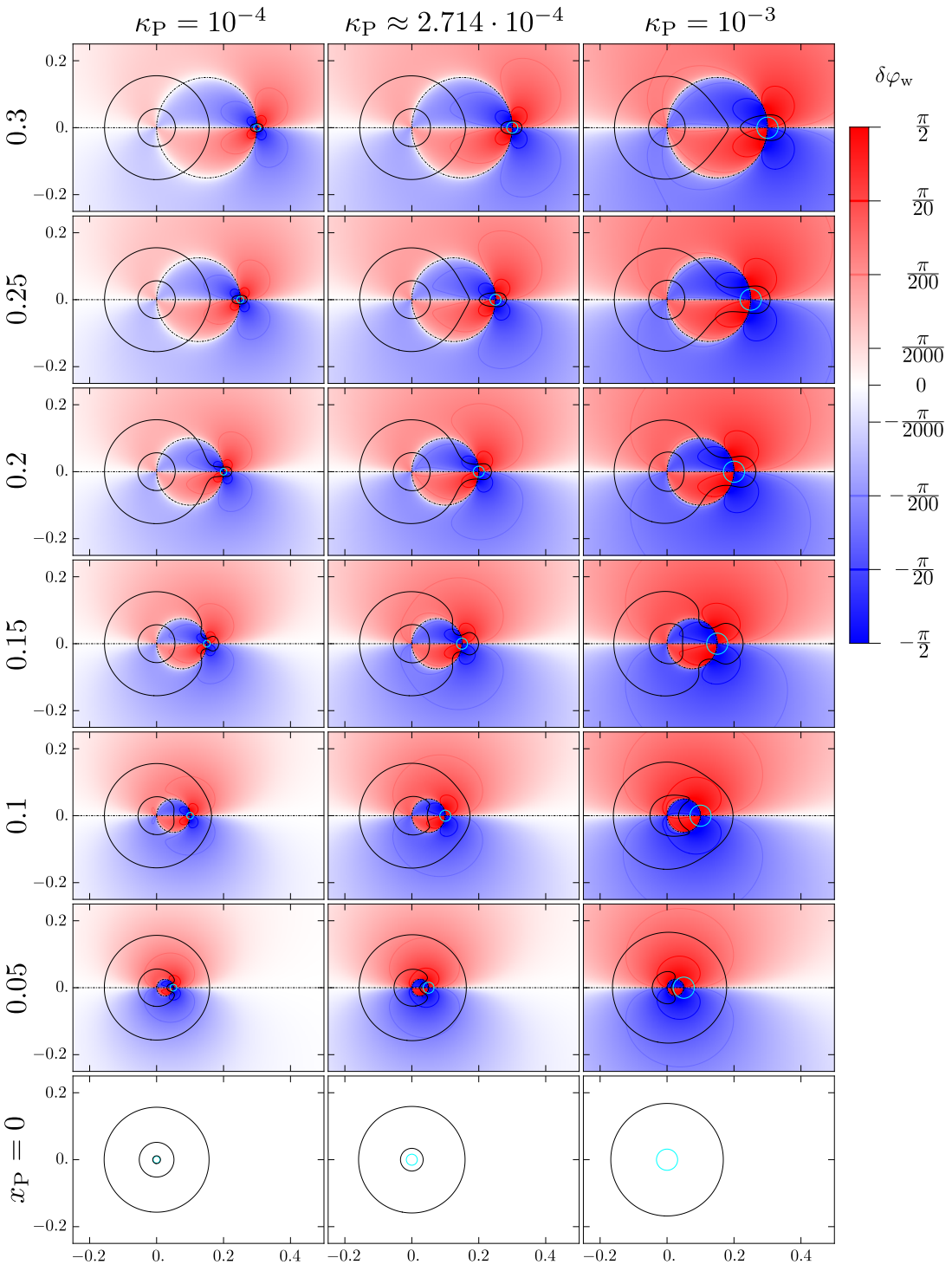

Figure 3.14.A: Image-plane maps of the weak-phase deviation $\delta\varphi_{\mathrm{w}}(\boldsymbol{x})$ caused by the presence of the point mass, described in Section 3.3.5.8. The maps also exactly portray the change in image orientation due to the point mass. Red and blue indicate counterclockwise and clockwise deviation, respectively. The color scale changes from logarithmic to linear in the interval $[-\pi/2000, \pi/2000]$. Four colored contours correspond to $\delta\varphi_{\mathrm{w}}$ values indicated in the color bar; the dot-dashed contour corresponds to $\delta\varphi_{\mathrm{w}} = 0$ and $\delta\varphi_{\mathrm{w}} = \pm\pi/2$. Remaining notation as in Figure 3.7.A.

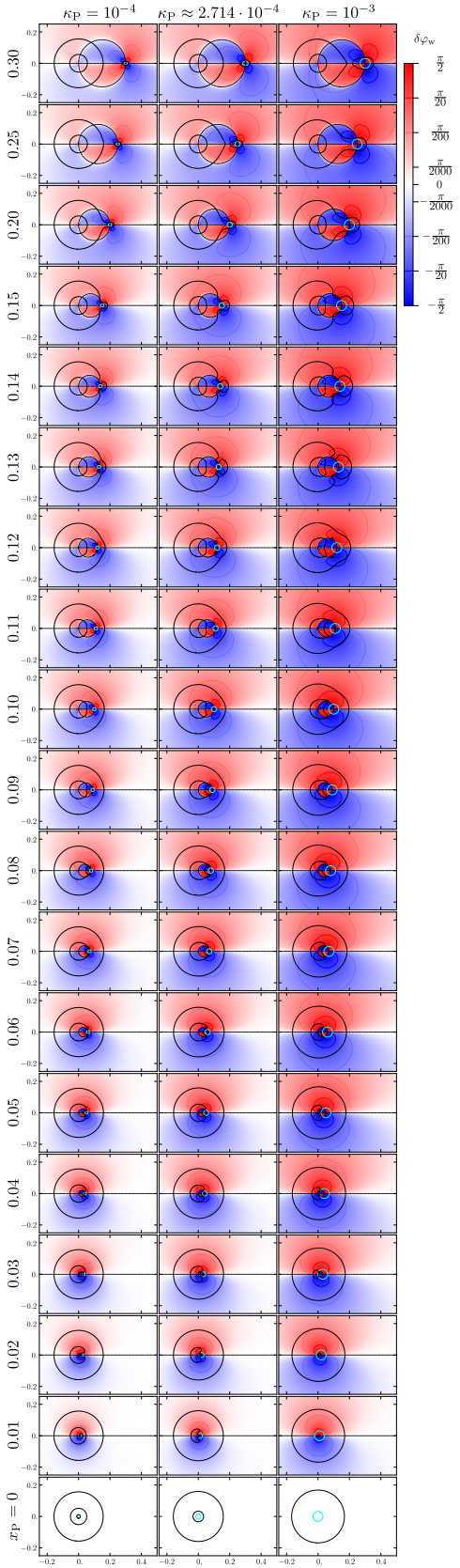

Figure 3.14.B: Image-plane maps of the weak-phase deviation $\delta\varphi_{\mathrm{w}}(\boldsymbol{x})$ caused by the presence of the point mass, for a finer grid of point-mass positions than in Figure 3.14.A. Notation same as in Figure 3.14.A.

fixed source due to the presence of a point mass. This approach was taken by Wagner (2018), who studied general perturbations of large arc-like images along the tangential critical curve of axisymmetric lenses. One provided example shows the influence of a point-mass perturber on the radii and lengths of arcs formed by a singular isothermal sphere lens. Even though NFW halos have different lensing properties, the generic pattern of angular distortions seen for example in the $x_\mathrm{P} = 0.25$, $\kappa_\mathrm{P} = 10^{-4}$ panel of Figure 3.14.A indicates that an arc-like image between the tangential critical curve and the point mass inside the $\omega = \pi/2$ circle would be straightened by its influence. Hence, its radius of curvature would be increased, in agreement with the example in Wagner (2018). Overall, image-plane maps such as those in Figures 3.11.A and 3.14.A are suitable for assessing the influence of compact masses in observed lensing clusters or galaxies where the image positions are fixed.

The results presented in this work correspond to one fiducial value of the halo convergence parameter κ_s. The variation of the critical curves and the unit-convergence circle with κ_s, as well as the variation of κ_s and κ_P with source redshift are discussed in Paper I. The plots presented above in Sections 3.3.5.1–3.3.5.8 can be expected to follow the combined geometry of the critical curve, the unit-convergence circle, and the $\omega = \pi/2$ circle. Note that the last mentioned circle is given purely by the value of x_P, which is independent of the source redshift and the halo convergence parameter.

Some of the obtained results have more general relevance than just for a point mass embedded in a spherically symmetric NFW halo. These include some of the analytic results, such as the shear of a combination of two mass distributions described in Section 3.3.1. Among the numerical results shown in Figures 3.7.A–3.14.A, the patterns seen around the point mass at sufficient separation from the halo critical curves will be very similar for other halo mass distributions with low spatial variation on the scale of the point-mass Einstein radius (e.g., Chang and Refsdal 1984), as discussed further below. Best seen in the top left plots for $x_\mathrm{P} = 0.30$, $\kappa_\mathrm{P} = 10^{-4}$, the patterns are relevant not only for point masses separated from other mass concentrations, but also for extended bodies with compact mass distributions that do not extend significantly beyond their Einstein radius.

The applicability of the studied lens model to the astrophysical scenarios of a galaxy within a galaxy cluster, of a satellite galaxy within a galactic halo, and of a massive black hole in a galactic halo is discussed in Paper I. In addition, possible extensions toward more advanced models are pointed out there, such as replacing the point mass by an extended mass distribution. For distributions that do not extend significantly beyond their total-mass Einstein radius, the lensing quantities in the surroundings will not differ significantly from the patterns seen in Figures 3.7.A–3.14.A. However, for more extended distributions the patterns will be affected more substantially. Nevertheless, at large separations the lensing impact of any compact object may be approximated by that of a point mass.

The explored model can be extended also by altering the properties of the NFW halo. On the one hand, one may change its central properties by adding a core radius, or by changing its density divergence (Evans and Wilkinson 1998). Such changes would alter the radii of the halo critical curves and caustics, the reference plots in Figure 3.2, and the critical value κ_PC of the mass parameter of

the point mass. This would impact the presented results primarily for point-mass positions close to the halo center. Regardless of the nature of the alterations, for sufficiently large distances the point-mass critical-curve loop disconnects from the halo critical curves. In this distant regime the patterns in the vicinity of the point mass will have the same character as seen in the figures.

On the other hand, one may abandon spherical symmetry and study the effect of a massive object embedded in a more realistic elliptical NFW halo. The lensing properties of an NFW halo with an elliptically symmetric mass distribution are poorly studied due to the lack of simple analytic expressions to describe them (Oguri 2021). Nevertheless, for low values of the halo ellipticity the properties can be approximated by those of the pseudo-elliptical model, which has an elliptically symmetric lens potential (Golse and Kneib 2002, Meneghetti et al. 2003, Dúmet-Montoya et al. 2012). In this model the critical curve typically consists of two nested oval loops instead of the two circles of the spherical model. The point-like tangential caustic of the spherical model is replaced by a four-cusped loop; the circular radial caustic by an oval loop. In this model one may expect an even more complex dependence of the critical curves and caustics of the combined lens on the mass and two-dimensional position of the point mass than in the spherical case described in Paper I.

In the elliptical model, the unit-convergence circle which plays a key role in the spherical model when studying the geometry of images is replaced by a unit-convergence ellipse. The grids of the plots corresponding to those in Figures 3.7.A–3.14.A would be complicated by an additional parameter, the angular position of the point mass with respect to the axes of the elliptical halo. Nevertheless, the main factors driving the patterns described in the text, such as the existence and location of zero-shear points or the geometry of the perturbations of the critical curve, would remain the same. The asymptotic patterns would have the same nature as seen in the spherical model, as mentioned above. However, they would be less symmetric and the extent of the contours would additionally depend on the angular position within the halo.

The presented single-point-mass results will be useful for interpreting the properties of cluster lens models with multiple (point) masses embedded in an NFW halo. Masses that are sufficiently separated from the perturbed NFW halo critical curves as well as from other masses should display similar patterns in their vicinity, as discussed above. Each of these masses will also produce deviation patterns near the halo center similar to those seen in the top left plots in Figures 3.8.A, 3.11.A, or 3.14.A. Due to the directional dependence of these patterns, their superposition for a sufficient number of isotropically distributed masses would drive the amplitude of the central deviations to zero. Strong differences can be expected when one or more of the masses are positioned close to the halo center, or when two or more neighboring masses are mutually separated by less than a few Einstein radii. These situations cannot be simply extrapolated from the results presented in this work and their study requires direct simulations.

3.5 Summary

In this paper we proceeded in our study of gravitational lensing by a compact massive object in a dark matter halo. In Paper I we analyzed the critical curves

and caustics of a lens consisting of a point mass embedded in a spherical NFW halo. Here we concentrated on the shear and phase of the same lens model, focusing on their relation to the geometry of images formed by the lens.

In Section 3.2.1, we described the properties of the shear and phase of a lens consisting only of a NFW halo. In order to study the images, we used the eigenvalue decomposition of the inverse matrix of a general lens-equation Jacobian matrix presented in Equation (3.21). Based on it, we introduced the convergence–shear diagram (CS diagram) in Appendix A.3, which illustrates concisely the connection between arbitrary convergence and shear values and the geometry of an image corresponding to them. Specific lens models occupy characteristic regions in the diagram, which then define the properties of all images that could be formed by the lens. We described the properties of images formed by the NFW halo by reading them off the CS diagram in Section 3.2.3. In Section 3.2.4 we defined the weak shear and weak phase as the shear and phase values obtained by assuming weak-lensing relations involving the semiaxes of images and their orientation.

We followed the same outline for the NFW halo + point-mass lens in Section 3.3. In particular, we derived the formula for the shear in Equation (3.31) which provides a geometric interpretation in terms of the halo and point-mass shears and the viewing angle ω of the line segment separating them. The formula which is valid for combinations of other axisymmetric lenses is a special case of the more general formula in Equation (3.36) for the shear of a combination of two arbitrary lenses. For the NFW halo + point-mass lens, we discuss the appearance and location of zero-shear points in Section 3.3.1 and describe the conditions under which they form umbilic points in Section 3.3.2.

Figures 3.7.A–3.14.A illustrate the main results in terms of image-plane maps of different lens characteristics and CS diagrams, all presented for the same grid of point-mass parameter combinations as the grid used in Paper I. Important features and trends seen in the figures are described in the corresponding Sections 3.3.5.1–3.3.5.8. As discussed in Section 3.4, the obtained results have broader implications beyond the specific properties of the studied lens model.

We thank the anonymous referee for comments and suggestions that helped improve the manuscript. Work on this project was supported by Charles University Grant Agency project GA UK 1000218.

4. Gravitational Lensing by a Galaxy Cluster

So far we have studied gravitational lensing by substructures in dark-matter halos in the simplest possible model consisting of a single point mass embedded in an NFW halo. In this chapter, we make a major step forward towards a realistic model of a galaxy cluster. We compose the model by combining an ellipsoidal NFW mass distribution as a main cluster halo with multiple truncated ellipsoidal NFW distributions as individual subhalos.

We choose parameters of the main halo to reflect real observed lensing clusters, while for the subhalos, where necessary observations are not available, we use probability distributions of their parameters fitted from cosmological simulations. Our goal is to simulate a galaxy cluster similar to clusters analysed in astronomical lensing surveys (e.g., Merten et al. 2015). We use formulae for deflection angles of both truncated and non-truncated ellipsoidal NFW halo lenses and sum them into a deflection angle of the complete cluster lens.

Once the lens model is complete, we use it to generate image-plane and source-plane maps of several lensing quantities analogous to the maps presented in Chapter 2 and Chapter 3. We discuss the current results for the cluster lens with a help of former results obtained from the simpler model.

4.1 Cluster construction

In this section, we construct a model of a galaxy cluster in two steps. First, we introduce a main dark-matter halo as a triaxial ellipsoidal mass distribution with NFW profile (Section 4.1.1). In order to mimic the real physical galaxy clusters, we base our choice of the halo parameters on the analyses of observed lensing clusters (Merten et al. 2015). Next, we generate properties and positions of cluster subhalos by sampling them from probability distributions. Generally, such probability distributions of real physical subhalos are not available. Instead, we will use distributions fitted from N-body cosmological simulations. In doing so, we will loosely follow the choices made by Giocoli et al. (2012). Subsequently, we model each subhalo as a *truncated* triaxial ellipsoidal mass distribution with NFW profile (Section 4.1.2).

When needed, we use cosmological parameters from Planck Collaboration et al. (2016) to compute the required quantities.

4.1.1 Cluster halo

Merten et al. (2015) analysed 19 lensing clusters from the *Cluster Lensing and Supernova Survey with Hubble* (CLASH). We choose parameters of the main NFW halo to be fairly average with respect to their dataset. Therefore, we choose virial concentration parameter $c_{\mathrm{vir}} = 4.5$ and scale parameter $r_{\mathrm{s}} = 0.580\,\mathrm{Mpc}$. Apart from yielding a typical lensing halo, this choice has another convenient property. The scale radius is equal to the Einstein radius ($r_{\mathrm{s}} = r_{\mathrm{E}}$).

We also choose the redshift at which our cluster is positioned, $z_\mathrm{l} = 0.4$, based on the dataset of Merten et al. (2015). This value of reshift corresponds to the angular diameter distance of the lens $D_\mathrm{l} = 1142\,\mathrm{Mpc}$. For the source plane, we choose the redshift $z_\mathrm{s} = 7$, which in turn corresponds to the distance $D_\mathrm{s} = 1102\,\mathrm{Mpc}$. To study gravitational lensing, we also need to compute the distance between the lens and the source, D_ls. This can be done using the formula

$$D_\mathrm{ls} = D_\mathrm{s} - \frac{1+z_\mathrm{l}}{1+z_\mathrm{s}}\, D_\mathrm{l}\,, \tag{4.1}$$

which yields $D_\mathrm{ls} = 902\,\mathrm{Mpc}$.

Now, we can calculate the virial mass of the main halo, which we will need for the subsequent generation of the subhalo masses. The virial mass is defined as a mass of the sphere with radius $r_\mathrm{vir} = r_\mathrm{s}\, c_\mathrm{vir}$ and a mean density equal to the critical density ρ_crit multiplied by the virial overdensity Δ_vir,

$$M_\mathrm{vir} = \frac{4}{3}\,\pi\, r_\mathrm{vir}^3\, \Delta_\mathrm{vir}(z_\mathrm{l})\rho_\mathrm{crit}(z_\mathrm{l})\,. \tag{4.2}$$

In the ΛCDM cosmology using the parameters from PLANCK survey (Planck Collaboration et al. 2016), we get critical density $\rho_\mathrm{crit}(0.4) = 1.3276 \times 10^{-26}\,\mathrm{kg\,m^{-3}}$ and the virial overdensity can be approximated (Stoehr 1999) as

$$\Delta_\mathrm{vir}(z) = 9\,\pi^2 \left[1 + \Omega_\mathrm{m}(z)^{\widetilde{\beta}} - \widetilde{\alpha}\left(1 - \Omega_\mathrm{m}(z)\right)\right], \tag{4.3}$$

where $\widetilde{\alpha} = 0.7076$ and $\widetilde{\beta} = 0.4403$. We obtain the cosmological matter-density parameter at the redshift of the lens, $\Omega_\mathrm{m}(z)$, from the approximation formula (Longair 2008)

$$\Omega_\mathrm{m}(z) = \Omega_\mathrm{m} \Bigg/ \left[\left(\frac{\Omega_\mathrm{m}\, z + 1}{1+z}\right) - \Omega_\Lambda \left(\frac{1}{1+z} - \frac{1}{(1+z)^3}\right)\right], \tag{4.4}$$

where Ω_m and Ω_Λ are density parameters at $z = 0$. Using this approach we obtain the virial mass of our fiduacial halo $M_\mathrm{vir} = 1.88 \times 10^{15}\, M_\odot$.

Next, we choose the shape of the triaxial halo, i.e., the ratios of its semiaxes. For this, we use the results of Jing and Suto (2002), who determined probability distributions of semiaxis ratios of simulated halos. They introduce the quantity

$$\tilde{r}_{13} = \left(\frac{a_1}{a_3}\right)\left(\frac{M_\mathrm{vir}}{M_\star}\right)^{0.07\,[\Omega_\mathrm{m}(z)]^{0.7}} \tag{4.5}$$

and they determine that it follows the normal probability distribution $\tilde{r}_{13} \sim \mathcal{N}(\mu = 0.54, \sigma = 0.113)$, where μ is the mean of the distribution and σ is its standard deviation. (Symbols a_1, a_2 and a_3 are used to denote semiaxes of the ellipsoid.) For ΛCDM cosmology and redshifts $z = 0$, 0.5, 1.0 they provide values of mass parameter $M_\star$ equal to $9.4 \times 10^{12}\, h^{-1} M_\odot$, $2.0 \times 10^{12}\, h^{-1} M_\odot$ and $3.8 \times 10^{11}\, h^{-1} M_\odot$, respectively, which we use to interpolate for our chosen value of z_l. When quantity $\tilde{r}_{13}$ is known, Equation (4.5) can be used to obtain the ratio of the ellipsoid semiaxes $a_1/a_3 = \sqrt{1 - e_2^2}$. The second axis ratio, $a_1/a_2 = \sqrt{1 - e_1^2}$,

can then be obtained from the conditional probability distribution (Jing and Suto 2002)

$$p(a_1/a_2 \,|\, a_1/a_3) = \frac{3}{2(1-r_{\rm min})}\left[1-\left(\frac{2\,a_1/a_2-1-r_{\rm min}}{1-r_{\rm min}}\right)^2\right], \qquad (4.6)$$

for $a_1/a_2 \geq r_{\rm min}$ and $p(a_1/a_2 \,|\, a_1/a_3) = 0$ for $a_1/a_2 \leq r_{\rm min}$ while $r_{\rm min} = a_1/a_3$ for $a_1/a_3 \geq 0.5$ and $r_{\rm min} = 0.5$ for $a_1/a_3 < 0.5$. In the next subsection, we use these formulae to generate the axis ratios of the subhalos. Here, we use them merely to choose typical axis ratios of the main halo $a_1/a_3 = 0.4$ a $a_1/a_2 = 0.8$.

The orientation of the halo can be chosen arbitrarily. However, it may be noted that studied lensing clusters tend to be oriented along the line of sight of the observer. This way, the projected density is more concentrated and the strong-lensing phenomena are thus more likely. For simplicity, we choose the values of Euler angles defining the cluster orientation with respect to the direction to the observer and coordinate axes in the plane of the sky $\widehat{\vartheta} = \widehat{\psi} = \widehat{\phi} = \pi/6$.

Finally, it is necessary to express the scale semiaxis $a_{\rm s0}$ of the ellipsoidal halo in terms of the scale radius $r_{\rm s}$. We require for the mass of an elliptically flattened halo,

$$M_{\rm vir,ell} = \frac{4}{3}\,\pi\, a_{\rm s0}^3\, c_{\rm vir}^3\, \sqrt{1-e_1^2}\,\sqrt{1-e_2^2}\,\Delta_{\rm vir}(z_{\rm l})\rho_{\rm crit}(z_{\rm l})\,, \qquad (4.7)$$

to be equal to the mass of the spherical halo from Equation (4.2). Conveniently, this is simply achieved by choosing the scale semiaxis $a_{\rm s0}$ so that $r_{\rm s}$ is the geometric mean of all three semiaxes of the scale ellipsoid,

$$a_{\rm s0} = r_{\rm s}\left[(1-e_1^2)(1-e_2^2)\right]^{-\frac{1}{6}}\,. \qquad (4.8)$$

4.1.2 Subhalos

To generate the subhalo masses $m_{\rm sub}$, we use the halo-mass function devised by Giocoli et al. (2010, 2012)[1],

$$\frac{{\rm d}N(M_{\rm vir}, c_{\rm vir}, z)}{{\rm d}m_{\rm sub}} = \widehat{A}\, M_{\rm vir}\sqrt{1+z}\,\frac{\bar{c}}{c_{\rm vir}}\, m_{\rm sub}^{-1.9}\exp\left[-\widehat{\beta}\left(\frac{m_{\rm sub}}{M_{\rm vir}}\right)^3\right], \qquad (4.9)$$

where $\widehat{A} = 9.33\times10^{-4}$ and $\widehat{\beta} = 12.2715$. The parameter $\bar{c}$ is the mean concentration of a halo with mass $M_{\rm vir}$ at redshift z. Since we wish to model a typical halo, we set $\bar{c}/c_{\rm vir} = 1$. Based on the halo masses analysed by Giocoli et al. (2010), we choose the minimum subhalo mass $m_{\rm min} = 10^{-4.2}M_{\rm vir}$. The total number of the subhalos is then computed by integrating the Equation (4.9) from $m_{\rm min}$ to $M_{\rm vir}$, which yields $N = 249$ subhalos. Using this value to normalize Equation (4.9), we obtain a cumulative distribution function (CDF), which we use in turn to generate subhalo masses of N subhalos.

We sample the concentration parameters of the subhalos $c_{\rm vir,sub}$, from a log-normal probability distribution,

$$\log_{10} c_{\rm vir,sub} \sim \mathcal{N}(\mu = \bar{a}\log_{10} m_{\rm sub} + \bar{b},\, \sigma = 0.12)\,, \qquad (4.10)$$

[1]There seems to be a typo in Giocoli et al. (2012). The derivative in their Equation (7) was probably supposed to be taken with respect to $\ln m$.

where the mass-dependence, including parameters $\bar{a} = -0.114$ and $\bar{b} = 2.49$, is again adapted from Giocoli et al. (2010). Various values of the deviation σ can be found in the literature. We base our choice on works of, e.g., Neto et al. (2007) and Duffy et al. (2008).

We generate the axis ratios of the ellipsoidal subhalos according to Equations (4.5, 4.6), which we introduced in the previous subsection, and we compute the respective eccentricities $e_{1,\mathrm{sub}}$ and $e_{2,\mathrm{sub}}$. We sample the Euler angles orienting the subhalo $\widehat{\vartheta}_{\mathrm{sub}}$, $\widehat{\psi}_{\mathrm{sub}}$ and $\widehat{\phi}_{\mathrm{sub}}$ from an uniform probability distribution on the interval $[0, 2\pi]$.

Next, we can compute the scale semiaxis of the subhalo $a_{\mathrm{s0,sub}}$. Again, we require for the elliptically flattened subhalo to have the same mass as its spherical version, i.e., m_{sub}. We express the LHS using Equation (4.2) and the RHS using Equation (4.7). Then we can express the scale semiaxis

$$a_{\mathrm{s0,sub}} = \sqrt[3]{\frac{m_{\mathrm{sub}}}{M_{\mathrm{vir}}}}\,\frac{c_{\mathrm{vir}}}{c_{\mathrm{vir,sub}}}\,r_{\mathrm{s}}\,\left[(1-e_{1,\mathrm{sub}}^2)(1-e_{2,\mathrm{sub}}^2)\right]^{-\frac{1}{6}}\,. \tag{4.11}$$

To conclude the generation of subhalos, we have to sample their positions within the galaxy cluster. For the spherical distribution of subhalos, Gao et al. (2004) provide the following formula for the fraction of subhalos in a sphere with radius r,

$$\frac{n(<x)}{N} = \frac{(1+0.244\,c_{200})\,x^{2.75}}{1+0.244\,c_{200}\,x^2}\,, \tag{4.12}$$

where $x = r/r_{200}$, while r_{200} is the radius of a sphere around the halo, in which the mean density is $200\,\rho_{\mathrm{crit}}(z_{\mathrm{l}})$, and $c_{200} = r_{200}/r_{\mathrm{s}}$. The formula is in fact a CDF for the random variable x. To translate between r_{vir} a r_{200}, we use the formula (Giocoli et al. 2010)

$$\frac{r_{200}}{r_{\mathrm{vir}}} = 0.746\left[\frac{\Delta_{\mathrm{vir}}(z)}{\Delta_{\mathrm{vir}}(0)}\right]^{0.395}\,. \tag{4.13}$$

To generate a projected position of a subhalo, we thus first sample a random point on a 3D unit sphere, keep two of its cartesian coordinates and scale them by multiplying by $r = x\,r_{200}$ generated using the Equation (4.12). Finally, we deform and rotate this 2D subhalo position in order to align it with the main cluster halo. Therefore, we multiply one of the coordinates and divide the other by the square root of the axes ratio of the projected main halo, $\sqrt[4]{1-e^2}$, to conserve the size of an elliptical area where the subhalos reside. We rotate the position by the angle $\widehat{\phi}$.

4.2 Deflection angles of ellipsoidal NFW lenses

In this section, we provide formulae for deflection angles of triaxially ellipsoidal NFW lenses. First, for an untruncated NFW mass distribution (Heyrovský and Karamazov 2022a) and then for an ellipsoidally truncated mass distribution (Heyrovský and Karamazov 2022b), for which we also provide approximate asymptotic formula, that hold at a sufficient distance from the halo center.

4.2.1 Ellipsoidal NFW lens

We start with a density profile of a general triaxially ellipsoidal NFW halo,

$$\rho(a_0) = \frac{\rho_\mathrm{s}}{a_0\,(1+a_0)^2}\,, \tag{4.14}$$

expressed as a function of the dimensionless semi-major axis of the ellipsoidal surface passing through point $(x',\,y',\,z')$,

$$a_0 = \frac{1}{a_{\mathrm{s}0}}\sqrt{x'^2 + \frac{y'^2}{1-e_1^2} + \frac{z'^2}{1-e_2^2}}\,. \tag{4.15}$$

The parameter $a_{\mathrm{s}0}$ is the three-dimensional scale semi-major axis of the NFW profile, x', y', z' are Cartesian coordinates aligned with the orientation of major, median and minor symmetry axes of the halo, respectively, and $e_1 \leq e_2$ are corresponding eccentricities.

Integrating the density profile along the line of sight yields a two-dimensional elliptically symmetric convergence profile. We can express its scale semi-major axis a_s and eccentricity e in terms of the the three-dimensional parameters of the halo and the Euler angles $\widehat{\vartheta}$, $\widehat{\psi}$ describing the orientation as

$$a_\mathrm{s} = a_{\mathrm{s}0}\sqrt{\frac{2 - e_2^2\sin^2\widehat{\vartheta} - (1-\cos^2\widehat{\psi}\sin^2\widehat{\vartheta})e_1^2 + \sqrt{\left[e_2^2\sin^2\widehat{\vartheta} + (1-\cos^2\widehat{\psi}\sin^2\widehat{\vartheta})e_1^2\right]^2 - 4\,e_1^2\,e_2^2\sin^2\widehat{\psi}\sin^2\widehat{\vartheta}}}{2}}\,, \tag{4.16}$$

$$e = \sqrt{\frac{2}{1 + \frac{2 - e_2^2\sin^2\widehat{\vartheta} - (1-\cos^2\widehat{\psi}\sin^2\widehat{\vartheta})e_1^2}{\sqrt{\left[e_2^2\sin^2\widehat{\vartheta} + (1-\cos^2\widehat{\psi}\sin^2\widehat{\vartheta})e_1^2\right]^2 - 4\,e_1^2e_2^2\sin^2\widehat{\psi}\sin^2\widehat{\vartheta}}}}}\,. \tag{4.17}$$

We express the angular position in the lens plane in units of the angular scale semi-major axis,

$$\boldsymbol{x} = \frac{\boldsymbol{\theta} D_\mathrm{L}}{a_\mathrm{s}}\,, \tag{4.18}$$

and align its component x_1 with the projected major axis. The dimensionless semi-major axis of an ellipse passing through point $(x_1,\,x_2)$ is then

$$a = \sqrt{x_1^2 + \frac{x_2^2}{1-e^2}}\,. \tag{4.19}$$

The convergence profile of the triaxial NFW halo can then be expressed as

$$\kappa(a) = 2\,\kappa_\mathrm{s}\,\frac{\mathcal{F}(a) - 1}{1-a^2}\,, \tag{4.20}$$

where

$$\mathcal{F}(a) = \begin{cases} \dfrac{\operatorname{arctanh}\sqrt{1-a^2}}{\sqrt{1-a^2}} & \text{for } a < 1\,, \\ 1 & \text{for } a = 1\,, \\ \dfrac{\arctan\sqrt{a^2-1}}{\sqrt{a^2-1}} & \text{for } a > 1\,, \end{cases} \tag{4.21}$$

and

$$\kappa_\mathrm{s} = \sqrt{\frac{(1-e_1^2)(1-e_2^2)}{(1-e_1^2)\cos^2\widehat{\vartheta} + (1-e_2^2)(1-e_1^2\sin^2\widehat{\psi})\sin^2\widehat{\vartheta}}}\,\frac{\rho_\mathrm{s}\,a_{\mathrm{s}0}}{\Sigma_\mathrm{cr}}\,. \tag{4.22}$$

The convergence parameter κ_s can be understood as

$$\kappa_\mathrm{s} = \frac{3}{4}\frac{\rho_\mathrm{s}}{\Sigma_\mathrm{cr}}\frac{V(a_{\mathrm{s}0})}{S(a_{\mathrm{s}0})}\,, \tag{4.23}$$

where $V(a_{\mathrm{s}0})$ is a volume of the ellipsoid with semi-major axis $a_{\mathrm{s}0}$ and $S_\mathrm{proj}(a_{\mathrm{s}0})$ is its sky-projected area.

Finally, we can obtain the deflection angle of the (untruncated) ellipsoidal NFW halo using image-plane integration as shown in Equation (1.3),

$$\begin{aligned}
\alpha_1(\boldsymbol{x}) &= \frac{D_\mathrm{S}\,a_\mathrm{s}}{D_\mathrm{L}D_\mathrm{LS}}\frac{4\,\kappa_\mathrm{s}\,x_1\sqrt{1-e^2}}{[(x_1-e)^2+x_2^2]\,[(x_1+e)^2+x_2^2]}\Bigg\{\left[(x_1^2-e^2)(1-e^2)+x_2^2(1+e^2)\right]\frac{\mathcal{F}(a)}{\sqrt{1-e^2}}\\
&\quad + (x_1^2+x_2^2-e^2)\ln\frac{\sqrt{x_1^2+x_2^2}}{1+\sqrt{1-e^2}} - \frac{x_2}{x_1}(x_1^2+x_2^2+e^2)\arctan\frac{x_1x_2(1-\sqrt{1-e^2})}{x_1^2\sqrt{1-e^2}+x_2^2}\Bigg\}\,,\\
\alpha_2(\boldsymbol{x}) &= \frac{D_\mathrm{S}\,a_\mathrm{s}}{D_\mathrm{L}D_\mathrm{LS}}\frac{4\,\kappa_\mathrm{s}\,x_2\sqrt{1-e^2}}{[(x_1-e)^2+x_2^2]\,[(x_1+e)^2+x_2^2]}\Bigg\{\left[x_1^2(1-2\,e^2)+x_2^2+e^2\right]\frac{\mathcal{F}(a)}{\sqrt{1-e^2}}\\
&\quad + (x_1^2+x_2^2+e^2)\ln\frac{\sqrt{x_1^2+x_2^2}}{1+\sqrt{1-e^2}} + \frac{x_1}{x_2}(x_1^2+x_2^2-e^2)\arctan\frac{x_1x_2(1-\sqrt{1-e^2})}{x_1^2\sqrt{1-e^2}+x_2^2}\Bigg\}\,.
\end{aligned} \tag{4.24}$$

These expressions are exact and stable for arbitrary value of projected eccentricity $e \in [0,\,1)$. As explained above, the coordinate axes x_1, x_2 are aligned with the semiaxes of the projected ellipse. To get the deflection angle of an arbitrarily oriented halo, one simply needs to rotate the deflection angle vector $\boldsymbol{\alpha}(\boldsymbol{x})$ from Equation (4.24) by the Euler angle $\widehat{\varphi}$. For details see Heyrovský and Karamazov (2022a).

4.2.2 Truncated ellipsoidal NFW lens

To derive the deflection-angle formulae for an ellipsoidal NFW lens with mass distribution truncated at a certain ellipsoidal surface, we use the complex formalism presented by Bourassa and Kantowski (1975) (and corrected by Bray 1984). In this formalism, components of the deflection angle of an axes-aligned ellipsoidal lens are obtained as real and imaginary components of a complex conjugate of integral I:

$$\alpha_1 + \mathrm{i}\,\alpha_2 = \frac{4\,G}{c^2}\,I^*\,.$$

The integral itself is given by the expression

$$I = \frac{2\,\pi\,a_\mathrm{s}\,\sqrt{1-e^2}}{x_1+\mathrm{i}\,x_2}\int_0^{a(x_1,x_2)}\frac{\sigma(a')\,a'\,\mathrm{d}a'}{\sqrt{1-\frac{e^2}{(x_1+\mathrm{i}\,x_2)^2}\,a'^2}}\,.$$

Here the position in the image plane (x_1, x_2) is given in units of the scale semi-major axis a_s and, again,

$$a(x_1,x_2) = \sqrt{x_1^2 + x_2^2/(1-e^2)}$$

is the semimajor axis of the ellipse with eccentricity e centered on the origin passing through this point. For a triaxial ellipsoid, this eccentricity can expressed by Equation (4.17). The $\sigma(a) = \Sigma_{\rm cr}\,\kappa(a)$ is a 2D projected mass density. Using the convergence of an untruncated NFW lens (Equation 4.20) we can obtain the integral

$$I = \frac{4\,\pi\,\Sigma_{\rm cr}\,\kappa_{\rm s}\,a_{\rm s}\,\sqrt{1-e^2}}{(x_1+{\rm i}\,x_2)^2-e^2}\,\left[\sqrt{(x_1+{\rm i}\,x_2)^2-e^2\,\left(x_1^2+\frac{x_2^2}{1-e^2}\right)}\right.$$
$$\left.\times\,\mathcal{F}\left(\sqrt{x_1^2+\frac{x_2^2}{1-e^2}}\right)+(x_1+{\rm i}\,x_2)\,\ln\frac{\sqrt{x_1^2+\frac{x_2^2}{1-e^2}}}{1+\sqrt{1-\frac{e^2}{(x_1+{\rm i}\,x_2)^2}\left(x_1^2+\frac{x_2^2}{1-e^2}\right)}}\right],$$

which yields the deflection angle equivalent to Equation (4.24).

Next, for a density profile truncated at $a = c_{\rm T}$, the integral I becomes

$$I = \frac{2\,\pi\,a_{\rm s}\,\sqrt{1-e^2}}{x_1+{\rm i}\,x_2}\,\int_0^{\min(c_{\rm T}\,,\,a(x_1,x_2))}\frac{\sigma(a')\,a'\,{\rm d}a'}{\sqrt{1-\frac{e^2}{(x_1+{\rm i}\,x_2)^2}\,a'^2}}\,.$$

We truncate the subhalos at their virial distances and therefore use $c_{\rm T} = c_{\rm vir}$.

Using the truncated NFW surface density $\sigma(a) = \Sigma_{\rm cr}\,\kappa_{\rm T}(a)$, where

$$\kappa_T(a) = 2\,\kappa_{\rm s}\,\frac{1}{1-a^2}\,\left[\frac{\sqrt{c_{\rm T}^2-a^2}}{c_{\rm T}+1}-\mathcal{F}_{\rm T}(a)\right] \tag{4.25}$$

and

$$\mathcal{F}_{\rm T}(a) = \begin{cases} \dfrac{\operatorname{arctanh}\dfrac{\sqrt{(1-a^2)(c_{\rm T}^2-a^2)}}{a^2+c_{\rm T}}}{\sqrt{1-a^2}} & \text{for } a<1\,,\\[2ex] \sqrt{\dfrac{c_{\rm T}-1}{c_{\rm T}+1}} & \text{for } a=1\,,\\[2ex] \dfrac{\arctan\dfrac{\sqrt{(a^2-1)(c_{\rm T}^2-a^2)}}{a^2+c_{\rm T}}}{\sqrt{a^2-1}} & \text{for } 1<a<c_{\rm T}\,,\\[2ex] 0 & \text{for } a\geq c_{\rm T}\,, \end{cases}$$

we get for $a < c_{\rm T}$

$$I = \frac{4\,\pi\,\Sigma_{\rm cr}\,\kappa_{\rm s}\,a_{\rm s}\,\sqrt{1-e^2}}{(x_1+{\rm i}\,x_2)^2-e^2}\,\left[\sqrt{(x_1+{\rm i}\,x_2)^2-e^2\,(x_1^2+\frac{x_2^2}{1-e^2})}\,\mathcal{F}_{\rm T}\left(\sqrt{x_1^2+\frac{x_2^2}{1-e^2}}\right)\right.$$
$$-\,(x_1+{\rm i}\,x_2)\,\ln\frac{\sqrt{c_{\rm T}^2-x_1^2-\frac{x_2^2}{1-e^2}}+c_{\rm T}\sqrt{1-\frac{e^2}{(x_1+{\rm i}\,x_2)^2}\,(x_1^2+\frac{x_2^2}{1-e^2})}}{(1+c_{\rm T})\sqrt{x_1^2+\frac{x_2^2}{1-e^2}}}$$
$$\left.+\,\frac{(x_1+{\rm i}\,x_2)^2+e^2c_{\rm T}}{e(1+c_{\rm T})}\,\ln\frac{e\,\sqrt{c_{\rm T}^2-x_1^2-\frac{x_2^2}{1-e^2}}+\sqrt{(x_1+{\rm i}\,x_2)^2-e^2\,(x_1^2+\frac{x_2^2}{1-e^2})}}{x_1+{\rm i}\,x_2+e\,c_{\rm T}}\right], \tag{4.26}$$

and for $a \geq c_\mathrm{T}$

$$I = \frac{4\,\pi\,\Sigma_\mathrm{cr}\,\kappa_\mathrm{s}\,a_\mathrm{s}\,\sqrt{1-e^2}}{(x_1+\mathrm{i}\,x_2)^2-e^2} \times \left[\frac{x_1+\mathrm{i}\,x_2}{2}\,\ln\frac{(1+c_\mathrm{T})^2}{1-\frac{e^2 c_\mathrm{T}^2}{(x_1+\mathrm{i}\,x_2)^2}} - \frac{(x_1+\mathrm{i}\,x_2)^2+e^2 c_\mathrm{T}}{e(1+c_\mathrm{T})}\,\operatorname{arctanh}\frac{e\,c_\mathrm{T}}{x_1+\mathrm{i}\,x_2}\right]. \quad (4.27)$$

Special care must be taken when numerically evaluating these formulae with respect to multiple branches of present complex functions. For details of the derivation see Heyrovský and Karamazov (2022b). For now, we do not rule out the possibility of decomposing the formulae into pairs of purely real ones. However, in this thesis we proceed with their complex forms and, in order to use them in parallel GPU computations, we precompute a multidimensional table of integrals I and interpolate between its values.

4.2.3 Truncated ellipsoidal NFW lens – asymptotics

Far from the center ($|\boldsymbol{x}| \gg 1$), the deflection angle of the truncated ellipsoidal NFW halo can be expanded and approximated as

$$\alpha_1(\boldsymbol{x}) \simeq \frac{4\,GM_\mathrm{vir,ell}}{c^2\,a_\mathrm{s}}\left(\frac{x_1}{x_1^2+x_2^2} + e^2\,\frac{(c_\mathrm{T}+1)\ln(c_\mathrm{T}+1)-c_\mathrm{T}(1+\frac{c_\mathrm{T}}{2}-\frac{c_\mathrm{T}^2}{6})}{(c_\mathrm{T}+1)\ln(c_\mathrm{T}+1)-c_\mathrm{T}}\,\frac{x_1(x_1^2-3\,x_2^2)}{(x_1^2+x_2^2)^3}\right),$$

$$\alpha_2(\boldsymbol{x}) \simeq \frac{4\,GM_\mathrm{vir,ell}}{c^2\,a_\mathrm{s}}\left(\frac{x_2}{x_1^2+x_2^2} + e^2\,\frac{(c_\mathrm{T}+1)\ln(c_\mathrm{T}+1)-c_\mathrm{T}(1+\frac{c_\mathrm{T}}{2}-\frac{c_\mathrm{T}^2}{6})}{(c_\mathrm{T}+1)\ln(c_\mathrm{T}+1)-c_\mathrm{T}}\,\frac{x_2(3\,x_1^2-x_2^2)}{(x_1^2+x_2^2)^3}\right). \quad (4.28)$$

4.3 Computation of lensing quantities

So far, we have described three individual lens models to be used for halo and subhalos and chose parameters of our fiducial galaxy cluster. Now, we put everything together and generate several image-plane and source-plane maps of the lensing quantities of the cluster lens, similar to those shown in previous chapters for the simpler lens model with a single point-like perturbation.

4.3.1 Deflection angle of the cluster lens

To plot and study both image-plane and source-plane quantities, we need to compute the deflection angle $\boldsymbol{\alpha}(\boldsymbol{\theta})$ of the cluster lens. It can be easily done by simply adding deflection angles of individual cluster constituents, i.e., its main halo and subhalos. This is true, because the deflection angle is proportional to the gradient of the lens potential ψ, which is the solution to the Poisson's equation (1.7).

The additivity of the deflection angles then results from the linearity of Poisson's equation. To get the deflection angle $\boldsymbol{\alpha}(\boldsymbol{\theta})$ of the combined cluster lens, we thus add the deflection angles of the halo and subhalos, while accounting for positions of the subhalos by shifting the image-plane-position parameter $\boldsymbol{\theta}$ and for the orientation of halo and subhalos by first rotating the shifted image-plane-position by a negative value of the Euler angle $\widehat{\phi}$ orienting the halo (or $\widehat{\phi}_{\mathrm{sub}}$ in case of subhalo) and then rotating the resulting deflection angle back by $\widehat{\phi}$.

We model the main cluster halo using the ellipsoidal NFW model. In Section 4.2.1 we have presented formulas for the deflection angle of this model, which we may use directly. On the other hand, the situation with subhalos is more complicated. We wish to model the them as truncated ellipsoidal NFW mass distributions, for which we have presented the deflection-angle formulas in Section 4.2.2. The deflection angle for this truncated mass distribution was derived in the complex formalism of Bourassa and Kantowski (1975) and is represented by complicated formulas composed of numerous instances of inverse hyperbolic functions of complex variables. Since we wish to generate the amplification map using the inverse-ray-shooting method, which is highly computationally expensive, we implement our lensing simulation in CUDA so that it runs parallelly on the computer graphics card (GPU). Due to the poor support of complex-number computations in CUDA, we instead precompute a table of values of function I (Equations 4.26, 4.27) for a four-dimensional grid of image-plane positions and subhalo parameters and, when needed, we compute the deflection angle of a subhalo by interpolating between the grid values.

Two dimensions of the table of precomputed values of the function I represent different two-dimensional positions in the image plane, i.e., different values of the vector argument $\boldsymbol{\theta}$ of the deflection angle $\boldsymbol{\alpha}(\boldsymbol{\theta})$ of the truncated ellipsoidal NFW lens. It suffices to consider only positive values of components of $\boldsymbol{\theta}$ since, due to the symmetry, the deflection angle for negative or mixed components can be obtained simply by inverting signs. To balance the discretization error of the grid and GPU-memory consumption, we precompute the function for 1001 values in each component of $\boldsymbol{\theta}$ ranging from 0 to 40 in units of the projected scale semiaxis a_{s}. The other two dimensions of the table represent values of subhalo virial concentration parameter c_{vir} and subhalo projected axes ratio $\sqrt{1-e^2}$. We precompute the integrals for 51 values of concentration parameter ranging from 0 to 50 and for 6 values of projected axes ratio ranging from 0 to 1. For the bicubic interpolation between the table values we also need first and mixed second derivatives of these values. We compute them using a second-order central finite difference method.[2]

Using the described method we can get the deflection angle of the subhalo within the square area defined by the table grid. To obtain the deflection angle for image-plane positions lying outside the grid we resort to using the approximate asymptotic formulas presented in Section 4.2.3. We smooth the transition by gradually mixing the bicubic interpolation and the asymptotics inside an annulus between the radius 32, measured in projected ellipse axes ratio, and the border

[2]It is convenient to precompute function I without the multiplicative prefactors and multiply by them only after the interpolation. However, it is necessary to include $1/[\log(1+c_{\mathrm{T}}) - c_{\mathrm{T}}/(1+c_{\mathrm{T}})]$, which appears in κ_{s}, in the precomputed I. Otherwise, the interpolation would be imprecise due to significant variation of precomputed values.

of the grid. To ensure the smoothness of the transition, within the annulus we mix the interpolated and asymptotic values there. We multiply the interpolated values by the factor $1-(2\,r_{\mathrm{mix}}^3+3\,r_{\mathrm{mix}}^2)$, where r_{mix} is the relative radial distance within the annulus, such that $r_{\mathrm{mix}}=0$ at the inner boundary of the annulus and $r_{\mathrm{mix}}=1$ at the outer boundary of the annulus, and we multiply the asymptotic values by $-2\,r_{\mathrm{mix}}^3+3\,r_{\mathrm{mix}}^2$. The mixing factor was chosen so that its derivatives vanish at the annulus boundaries.

4.3.2 Generating the image-plane and source-plane maps

To plot the maps of the image-plane lensing quantities we start with computing maps of components of the deflection angle $\boldsymbol{\alpha}(\boldsymbol{\theta})$ of the cluster lens. Next, we multiply these maps by the ratio of angular diameter distances $D_{\mathrm{ls}}/D_{\mathrm{s}}$ to obtain the first derivatives of the lens potential $\psi_{,1}$ and $\psi_{,2}$ (see Equation 1.6). We differentiate these first derivatives numerically to get the second derivatives $\psi_{,11}$, $\psi_{,12}$ and $\psi_{,22}$, which we in turn use to compute the convergence κ (see Equation 1.12), shear γ and phase φ (see Equation 1.13). From these, we compute the Jacobian J and find the critical curves as its zero-contours. As in Chapter 3, we also compute the weak shear and weak phase (image orientation), the relative difference between the shear and weak shear, and also the differences in shear and image orientation due to the presence of subhalos. For these two differences we need to compute the deflection-angle maps of the main halo alone. In addition to these quantities, which we already studied in Chapters 2 and 3 for the simple pertubed halo model, we also introduce a map of inverse Jacobian $|\det J(\boldsymbol{\theta})|^{-1}$ as an image-plane complement to the source-plane amplification map.

We compute the source-plane amplification map by the inverse-ray-shooting method (Kayser et al. 1986), i.e., we randomly sample one billion positions from the square area of the image plane and project them back to the source plane using the lens equation (1.1), into which we have inserted the cluster-lens deflection angle computed as described in the previous subsection. Subsequently, we count the number of light rays that fell into each pixel of a defined source-plane grid. The amplification $A(\boldsymbol{\beta})$ is then computed as a ratio of the light rays that fell into each source-plane pixel in presence of the lens to the number of light rays that would fall there in absence of the lens, which is simply given by the areas of considered regions, number of rays and resolution of the pixel grid. The number of light rays necessary to obtain a smooth amplification map without excessive noise together with the complexity of the deflection-angle formulas makes the whole process very computationally intensive, which is the reason why we run it in parallel on GPU using the code written in CUDA.

4.4 Results

In the following subsections, we present and describe our results in the form of image-plane and source-plane maps of the lensing quantities produced as described in Section 4.3 for a single fiducial cluster constructed according to the procedure from Section 4.1.

Most of the lensing quantities that we plot here are the same as those that we studied in Chapters 2 and 3 for the simple model of an NFW halo perturbed

by a single point mass. Moreover, we use the same color scales as before. This allows us to use the knowledge acquired by studying the simple model to better understand the lensing by a more realistic model of the galaxy cluster.

Primarily, we focus on the inner parts of the fiducial cluster, since the most of interesting lensing phenomena occur there. However, when beneficent, we also present zoomed-out versions of the maps to get a view of the whole cluster and to reveal the asymptotic behavior of the plotted quantities. Furthermore, we find the critical curves and include them in those maps, where it makes sense. The resolution of all the maps presented in the figures is 1024×1024 pixels and the angular positions indicated by the ticks on frames of the plots are measured in units of the projected scale semiaxis of the main ellipsoidal halo a_s. In other words, values on axes of the plots represent components x_1 and x_2 of the dimensionless position vector $\boldsymbol{x} = \boldsymbol{\theta} D_\mathrm{L}/a_\mathrm{s}$ in the case of image-plane maps and components y_1 and y_2 of the dimensionless position vector $\boldsymbol{y} = \boldsymbol{\beta} D_\mathrm{L}/a_\mathrm{s}$ in the case of the source-plane amplification map.

4.4.1 Convergence

Figure 3.1 is an image-plane map of the convergence $\kappa(\boldsymbol{\theta})$ (Equation 1.12). In other words, it represents the projected two-dimensional density of the mass in the galaxy cluster. The same color scale is used for the convergence as is used for the shear, since both quantities are closely related (they are both non-negative quantities composed of second derivatives of the lens potential).

We see that the convergence computed from the combined deflection angles of the cluster constituents is in agreement with our construction of the galaxy cluster in Section 4.1. As expected, the plotted distribution is composed of a central elliptical, tilted and highly concentrated convergence peak corresponding to the main halo and smaller elliptical peaks corresponding to the subhalos. The convergence diverges at the cluster center and falls to zero at an infinite distance.

The numerous subhalos are obviously elliptical, randomly rotated and their sizes vary greatly with larger subhalos being comparatively rarer. The subhalos are located in an elliptical area, which is aligned with the main halo. A projected number density of subhalos rises towards the cluster center. However, it rises only slightly and much less than the mass density of the main halo. This is a result of the subhalo radial distribution (Equation 4.12) combined with a projection along the line of sight.

The top left panel of Figure 3.2 shows a detail of the convergence map focused on the center of the cluster. The critical curves are now included in the plot. For our fiducial lens configuration, the main tangential critical curve appears at positions with values of convergence ranging roughly between $\kappa = 0.5$ and $\kappa = 1$.

4.4.2 Jacobian and critical curves

The top right panel of Figure 3.2 is a map of the Jacobian of the lens equation $J(\boldsymbol{\theta})$ (Equation 1.14) of the galaxy-cluster lens. Similarities with the Jacobian map of the unperturbed NFW lens (Figure 2.2) are clearly visible. At the center of the main halo, the Jacobian approaches positive infinity indicating infinite demagnification. The small central area of positive Jacobian (red) is then sur-

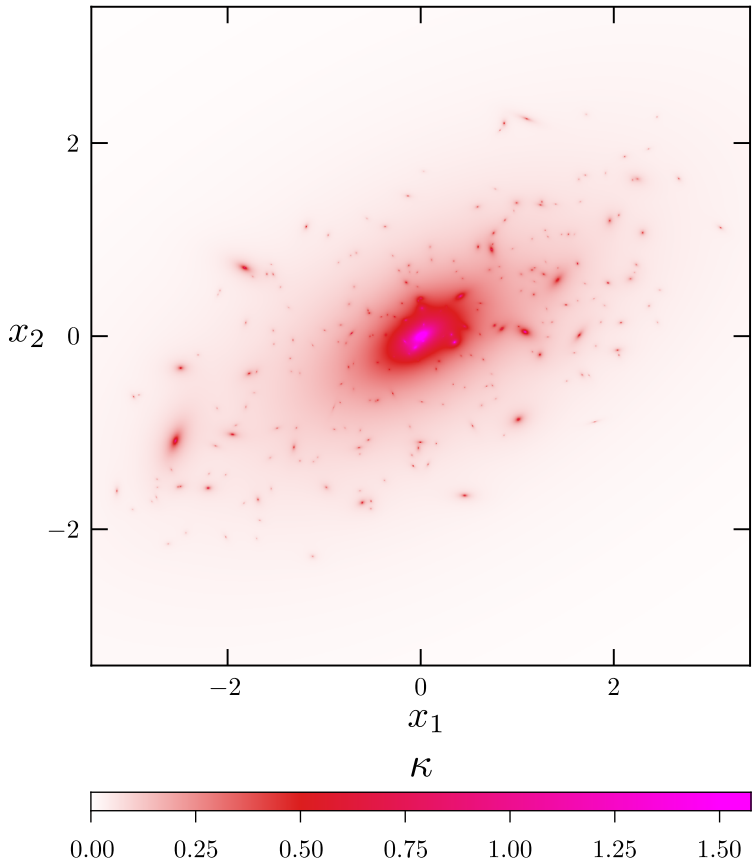

Figure 3.1: A map of the convergence showing the projected mass density of the fiducial cluster. The image-plane position is measured in the units of projected scale semiaxis of the main ellipsoidal halo a_s.

rounded by a larger area of negative Jacobian (blue), where the parity of images would be negative. Outside the blue area, the Jacobian is again positive (color red) and asymptotically approaches unity, meaning that images sufficiently removed from the halo center would be virtually unaffected by the lens. Unlike in the spherical case in Chapter 2, the blue area of the negative Jacobian is now elongated and aligned with the orientation of the halo.

A similar structure of central positive divergence surrounded by an area of negative Jacobian is generally present also for individual subhalos with structures being more pronounced for larger subhalos and those closer to the cluster center. Interestingly, the subhalos lying inside the large blue area of negative parity are accompanied by a local anisotropy in the Jacobian. In their vicinity, the Jacobian is more negative in the radial direction with respect to the cluster center while being closer to zero in the perpendicular (tangential) direction.

Critical curves at which the amplification is infinite are found as zero contours of the Jacobian. Thus, they appear in the white areas of the Jacobian map and form natural boundaries between areas of positive (red) and negative (blue) parity. We use black color to plot them. The largest critical curve is the tangential critical curve of the main halo, which forms the outer boundary of the large blue area. It is slightly dumbbell-shaped and aligned with the projected ellipse of the main halo. Inside it, at the very center of the Jacobian map, lies a somewhat

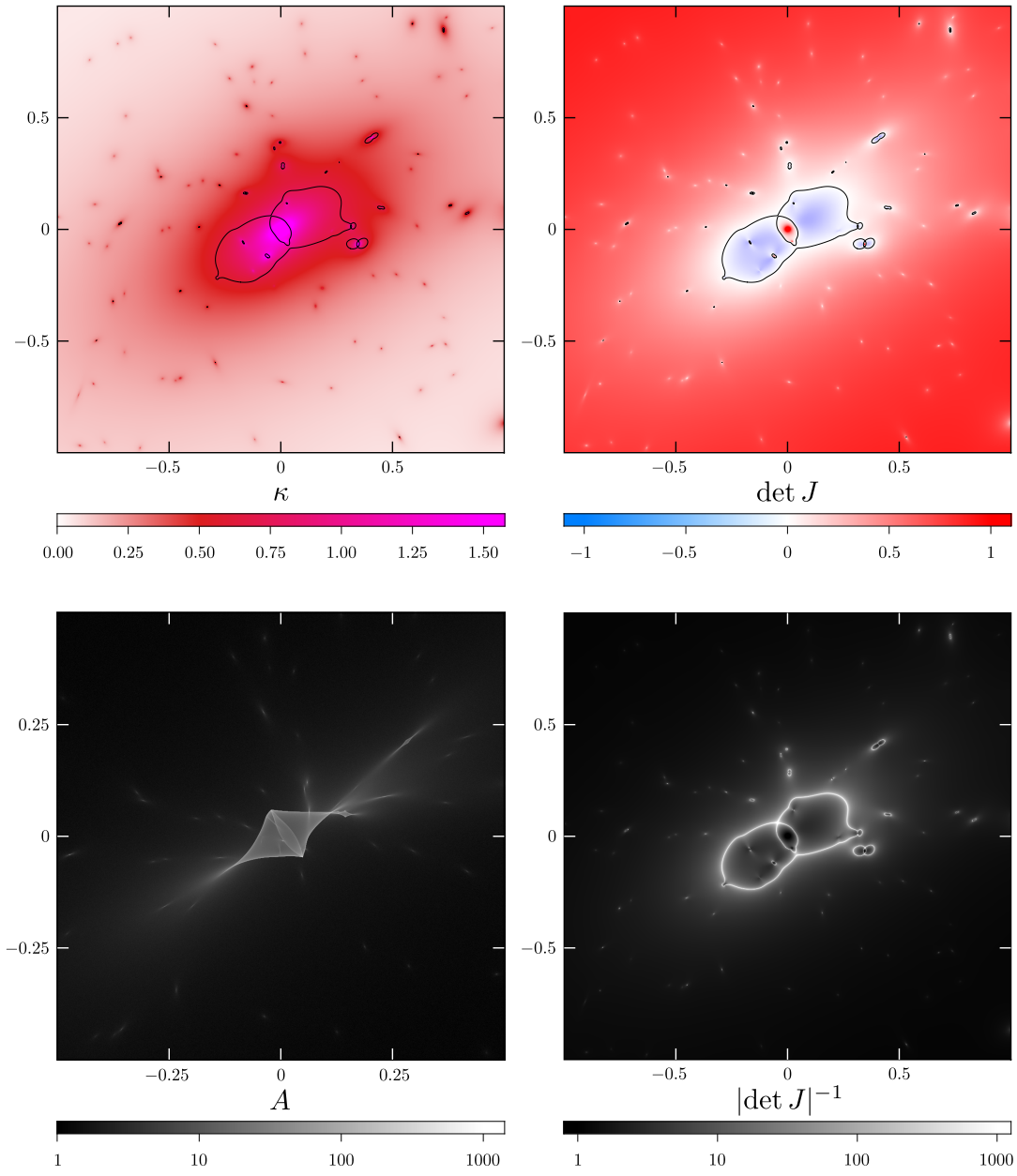

Figure 3.2: Lensing quantities in the central region of the galaxy cluster. Top left: image-plane map of the convergence. Top right: image-plane map of the Jacobian of the lens equation. Bottom right: image plane of the inverse of the absolute value of the Jacobian, i.e., the amplification observed at a given image-plane position. Bottom left: source-plane amplification map, i.e., amplification of a point source at given source-plane position. Both image-plane and source-plane positions are measured in the units of the projected scale semiaxis of the main ellipsoidal halo a_s.

spindle-shaped radial critical curve oriented perpendicularly to the halo. These two critical curves are almost touching indicating that the lens is close to the umbilic transition.

Similar structures and shapes of the critical curves are also present for the subhalos. However, they are mostly oriented radially, pointing towards the cluster center. Some critical curves (especially the inner radial ones) of the subhalos are too small to be visible as zero-contours of the Jacobian in our map. Fixing this would require a substantial increase in the resolution of the map. In general, larger subhalo critical curves appear close to the tangential main-halo critical curve and if they are too close, they merge with it forming protruding lobes. Subhalos lying directly inside the main tangential critical curve merely form additional small radial critical curves inside it.

4.4.3 Inverse Jacobian

The bottom right panel of Figure 3.2 is a map of the inverse absolute value of the lens-equation Jacobian, i.e., $|\det J|^{-1}$. It is closely related to the Jacobian map plotted in the panel above and it represents the amplification that would be observed at the given image-plane position $\boldsymbol{x}$. Therefore, this image plane-map is complementary to the standard source-plane amplification map, which we present in the bottom left panel. We also introduce a black-and-white logarithmic color scale similar to that, which we use for the source-plane amplification maps. The inverse Jacobian diverges (white color) at positions, where we have located the critical curves and plotted them in other image-plane maps. In fact, this is the definition of critical curves. At large distance from the cluster center, the amplification falls to 1 (black color), which corresponds to unamplified images. Close to the centers of the halo and the subhalos, areas with $|\det J|^{-1} < 1$ occur, indicating possibility of demagnified images. Overall, the structures visible in this map are close analogues of those in the Jacobian map including, e.g., the visible anisotropies surrounding the subhalos lying inside the main tangential critical curve.

4.4.4 Amplification

The last (bottom left) panel of Figure 3.2 is a standard source-plane amplification map generated using the inverse-ray-shooting method as described in Section 4.3.2. This amplification map shows the amplification $A(\boldsymbol{\beta})$ of a point source located at a given source-plane position $\boldsymbol{y}$. Although a substantial amount of light rays (one billion) was used to generate the map, when zoomed in sufficiently, some noise is still visible. We use the same black-and-white color scale as in Chapter 2 with color black indicating an amplification equal to one, which occurs at an asymptotic distance from the cluster center. On the other hand, the white color indicates $A(\boldsymbol{\beta}) > 1000$. Ultimately, the amplification diverges at caustics, which appear as very sharp brightness transitions in the amplification map. In general, the amplification is high inside the caustics.

The largest caustic corresponds to the tangential critical curve of the main halo. This caustic is somewhat diamond-shaped with sides bending slightly inwards. The orientation of this caustic is aligned with the orientation of the halo.

There are two areas of high amplification extending far beyond the two cusps of the caustic. At some places, the main caustic is visibly deformed by the presence of smaller subhalo caustics and the right cusp of the main caustic is actually merged with one of them. Inside the largest diamond-shaped caustic there is a smaller spindle-shaped caustic oriented perpendicularly to the orientation of the cluster. This caustic corresponds to the radial critical curve of the main halo. The side angles of the "diamond" and cusps of the "spindle" are almost touching, since the lens is close to the umbilic transition.

In general, caustics associated with subhalos have the same "diamond and spindle" structure as caustics of the main halo. However, they are predominantly oriented so that they point towards the cluster center with their long cusps. Some subhalo caustics are too small to be discernible. Nevertheless, there always is a visible elongated area of high ampification, usually oriented towards the cluster center, associated with every subhalo.

4.4.5 Shear

In the top left panel of Figure 3.3, we present an image-plane map of the shear $\gamma(\boldsymbol{\theta})$ using the same color scale as we did in Chapter 3 and as we subsequently used for the convergence.

At the center of the cluster, the value of shear diverges to infinity (color magenta). Moving from the center, the shear decreases with a rate that is strongly dependent on the direction. In the direction of the major axis of the main cluster halo, the rate of the decrease is the lowest and two red lobes of high shear are formed inside the main critical curve. On the other hand, in the perpendicular direction, that is towards the pair of areas where the tangential and radial critical curves almost touch, the shear falls rapidly, eventually reaching points of zero shear (white) lying just beyond the tangential critical curve. Unlike in the case of a spherical halo with a point perturbation discussed in Section 3.3.5.1, the central pattern and the pair of zero shear points is now caused by the ellipticity of the halo.

Further from the center, apart from being perturbed by smaller subhalo patterns, the shear slowly decreases asymptotically towards zero. Shear patterns around subhalos mimic the large pattern of the main halo (directional dependence around the center and pair of zero shear points). At the same time the present subhalo shear pattern is related to the pattern described in Section 3.3.5.1, i.e., roughly speaking, there is an elongated area of higher shear with two zero-shear points above and below. However, areas of low shear around the zero-shear points are now more elongated tangentially with respect to the main halo. The elongation and curvature of these low-shear areas are reminiscent of the low-shear circle spanned between the halo center and the point perturbation identified in Section 3.3.5.1.

As before, the zero-shear points are closely related to umbilics. As already noted, the zero-shear points appear near the place where tangential and radial critical curves almost touch. Should they reach the umbilic (for a different configuration of the cluster) the zero-shear points would coincide with the points of umbilics, i.e., they would lie at the intersections of the critical curve and the curve of $\kappa = 1$.

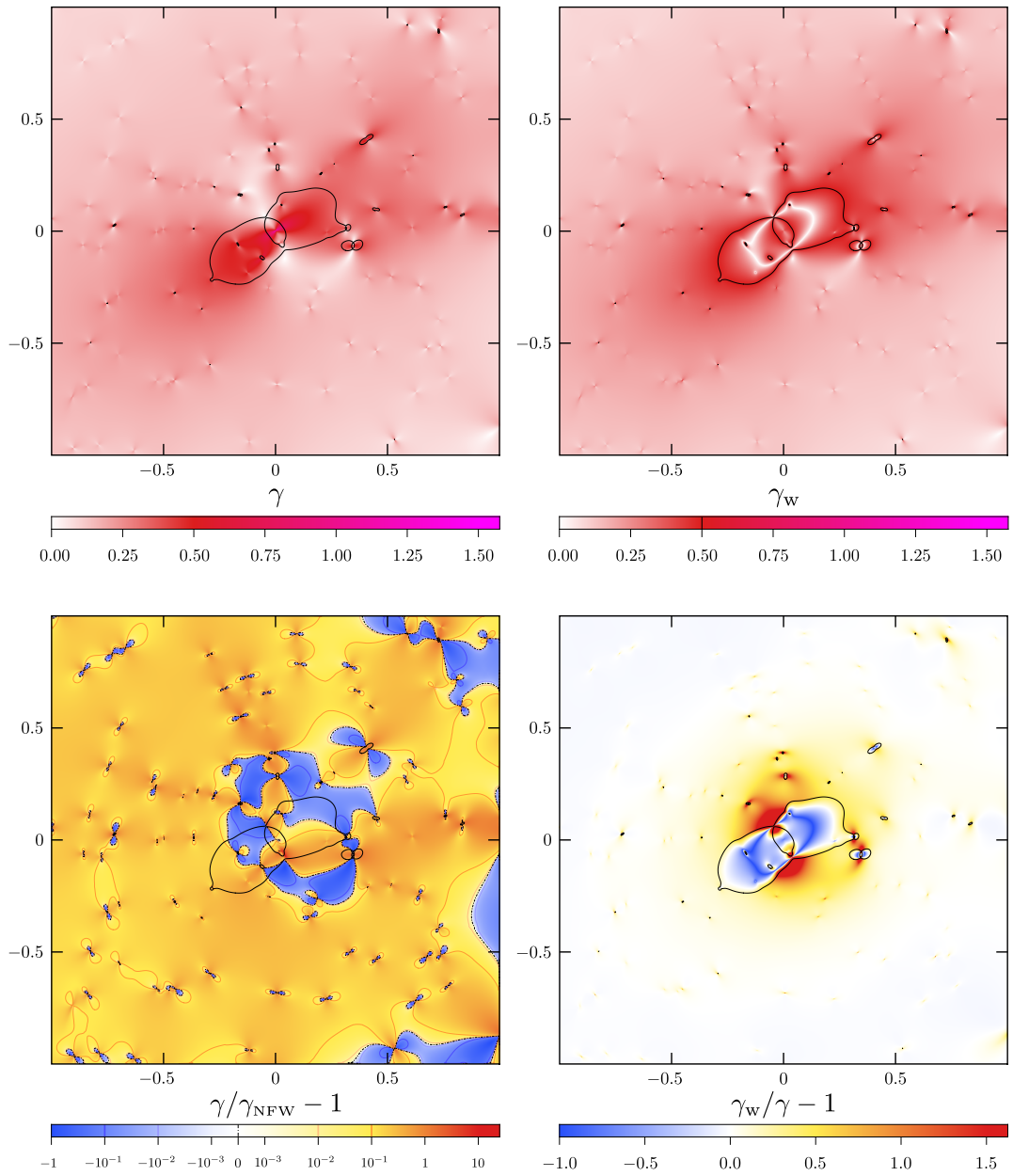

Figure 3.3: Shear and related image-plane quantities near the center of the galaxy cluster. Top left: shear. Top right: weak shear, i.e., half the flattening of a small circular image at given position. Bottom left: shear deviation due to the subhalos. Bottom right: weak-shear deviation from the shear.

4.4.6 Weak shear

The top right panel of Figure 3.3 is an image-plane map of the weak shear $\gamma_{\mathrm{w}}(\boldsymbol{\theta})$, defined in Section 3.2.4. It represents the shear that would be measured from image deformations in the weak-lensing analysis. The same map also serves as a map of the flattening, since $f(\boldsymbol{x}) = 2\,\gamma_{\mathrm{w}}(\boldsymbol{x})$.

At first glance, the map of weak shear looks quite similar to the map of shear. Beyond the central region, the weak shear is slowly decreasing while being perturbed by local tangentially oriented patterns of the subhalos. However, the weak shear differs from the shear greatly close to the critical curves. Along all of the critical curves, the weak shear reaches its maximum possible value $\gamma_{\mathrm{w}} = 1/2$ (color red), indicating maximal flattening. On the other hand, the weak shear falls to 0 at $\kappa = 1$, which occurs along the white perturbed ellipse lying between the radial and tangential critical curves. Along this bright curve, minimally deformed images would occur. Unlike in the case of the point perturbation in Chapter 3, the shape of the unit-convergence curve is now affected by the presence of adjacent subhalos. This discussion of the critical curves and the unit-convergence curve holds for the main halo as well as for the subhalos.

At the main-halo center inside the radial critical curve, a directional dependence of the weak shear is visible. Once again, the values are highest along the direction of the semi-major axis of the main halo and lowest in the perpendicular direction. Directly at the center, the weak shear converges to a value between 0 and 1/2 depending on the eccentricity of the main halo.

The weak shear also drops to zero at zero-shear points. However, the bright areas of low weak shear surrounding the zero-shear points are somewhat smaller than the analogous areas of low shear. This is due to the significant influence of convergence on image shapes in this region.

4.4.7 Shear deviation due to the subhalos

The relative difference in shear incurred by the presence of subhalos is plotted in the bottom left panel of the Figure 3.3. As in Section 3.3.5.2, we define it as $\gamma/\gamma_{\mathrm{NFW}} - 1$, where γ is the total shear of the combined cluster model plotted in the panel above, while γ_{NFW} is the shear of only the main NFW halo, which, however, is now elliptically deformed. In the current image-plane map, we use the same semi-logarithmic color scale and the same set of contours as in Figure 3.8.A.

The plotted deviation is predominantly positive (colors yellow and orange) in most of the image-plane map. Far from the halo center, the shear deviation does not reach zero asymptotically. Instead, it converges to a positive value of approximately 5% in the presented simulation. The specific value depends on the total mass of all subhalos.

The predominantly positive deviation is perturbed by pairs of blue lobes of negative deviation oriented tangentially with respect to the main halo. These lobes are associated with areas of low shear close to the subhalos. They surround the zero-shear points, where the deviation falls to the minimum possible value -1 (saturated blue). The shape of the lobes is influenced by the proximity of other (sub)halos and two lobes associated with subhalos lying close to each other can even merge. One of the blue areas of low deviation extends to the center of the cluster. This resembles the configuration described in Section 3.3.5.2, where

two blue lobes above and below the point perturbation extend towards the halo center and touch there.

There are also darker orange areas of more positive deviation, i.e., increased shear, lying in front of and behind the subhalo radially with respect to the main halo. This effect arises from the combination of shears due to the main halo and the subhalos. It is in agreement with similar results seen in the point-mass-perturbation case in Section 3.3.5.2.

4.4.8 Weak-shear deviation from the shear

The bottom right panel of Figure 3.3 is an image-plane map of the weak-shear deviation from the shear, $\gamma_{\mathrm{w}}/\gamma - 1$, i.e., the relative error of shear estimation using the weak-lensing approximation. The color scale is the same as in Section 3.3.5.6. Unlike in the previous panel, the current color scale is linear, which is more suitable to reveal the strong effects occurring in the cluster center.

We see that the weak shear strongly overestimates (color red) the shear in the vicinity of the zero-shear points as already mentioned in Section 4.4.6. The red areas of high deviation are pinched, where the unit-convergence curve passes between the critical curves, and they partially reach inside the radial critical curve. The deviation then falls to the minimum possible value -1 (color blue) at the cluster center and at the unit-convergence curve, since at these image-plane positions the weak shear is negligible compared to the shear or it drops to zero. Along the tangential critical curve, the deviation is positive everywhere. This description of the deviation pattern holds both for the main halo and the subhalos.

Further from the main critical curve, the deviation drops to zero (color white) and continues falling towards slightly negative values (light blue). In the corners of the plot, the deviation is still approximately -0.016. However, asymptotically, the deviation decreases to zero. Overall, the deviation is low everywhere except for the vicinity of the critical curves. Except in the vicinity of the (sub)halo centers the weak-lensing approximation is thus applicable.

4.4.9 Weak phase

The left panel of Figure 3.4 is an image-plane map of the weak phase φ_{w} (see Section 3.3.4). It represents the value of phase that would be determined in the weak lensing analysis. For a small circular source, the weak phase is the angle between the semi-major axis of its elliptical image and the horizontal axis of the plot. For $\kappa < 1$, the weak phase is equal to the phase, while for $\kappa > 1$ the weak phase is perpendicular to the phase. The color scale is the same as in Section 3.3.5.7 and the dot-dashed contours once again denote positions, where the orientation of images is exactly horizontal (color white), exactly vertical (orange-blue transition) or undefined.

The basic pattern of changing colors and saturations (i.e., the division into four quadrants) at a sufficient distance from the cluster center resembles the similar pattern in the simpler lens discussed in Section 3.3.5.7. This pattern simply means that images lying at sufficient distance from the center are oriented tangentially around the main halo. However, in the present model, the pattern

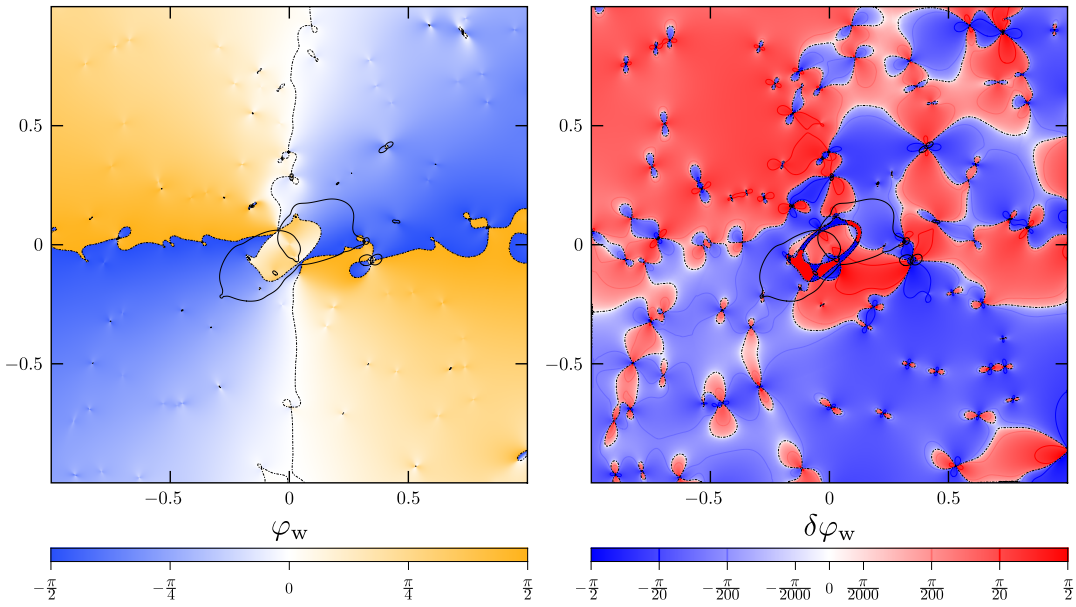

Figure 3.4: Left: weak phase, i.e., image orientation at given position. Right: weak-phase deviation due to the subhalos.

is perturbed close to the subhalos, where the influence of these subhalos prevails over the influence of the main halo and images are oriented tangentially around them. Pairs of lobes of inverted colors thus appear adjacent to the subhalos. The orientation depends on the position of the subhalo with respect to the main halo. Some lobes merged with the main horizontal or vertical contour or with lobes associated with other subhalos.

The weak phase is undefined at positions with zero weak shear, where small images would remain undeformed. These are zero-shear points and the unit-convergence curve. At these points, the orientation changes along the dot-dashed contours abruptly between parallel and perpendicular to the phase.

Unlike in the case of the spherical halo discussed in Section 3.3.5.7, the weak phase is now positive (color orange) everywhere inside the the unit-convergence curve around the cluster center. Minor exceptions to this are associated with subhalos lying inside the unit-convergence curve. This means that close to the center of a sufficiently elliptical halo, the images would be oriented more or less in the direction of the halo's projected semi-major axis. Nevertheless, the orientation of images close to the center still varies with their positions, since the color orange is darker along the vertical and brighter along the horizontal direction.

Interesting asymptotic behavior of the weak phase is revealed in the zoomed-out version of the plot in the left panel of Figure 3.5. Both horizontal and vertical contours are tilted slightly towards the orientation of the projected semi-major axis of the main halo, meaning that the orientation of the images follows the elliptical shape of the halo.

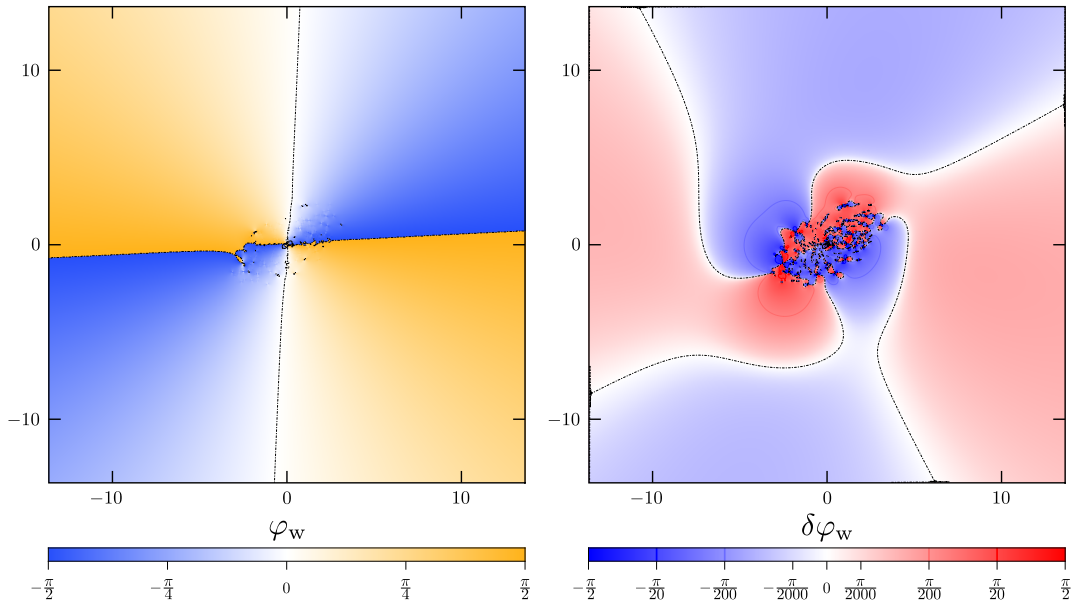

Figure 3.5: Zoomed out version of Figure 3.4 revealing the asymptotic behavior of angular lensing quantities.

4.4.10 Weak-phase deviation due to the subhalos

Finally, the right panel of Figure 3.4 is an image-plane map of the weak-phase deviation due to the subhalos, $\delta\varphi_{\mathrm{w}}(\boldsymbol{x})$, which we defined in Section 3.3.5.8. It can be understood as a change in the orientation of an image at a given position incurred by the presence of subhalos. We use the same semi-logarithmic color scale and set of contours as before. Overall, the deviation is relatively low; its absolute value rarely exceeds 9° (dark contours).

The plotted deviation pattern around the cluster center is obviously very disorganised. It seems that above the center the deviation is predominantly positive (color red) and the orientation of images is changed counterclockwise there. On the other hand, below the cluster center, negative deviation (color blue) dominates and the images are reoriented in a clockwise direction.

Since the subhalos in regions with subcritical convergence orient nearby images tangentially around themselves, there are two areas of positive deviation (red) and two areas of negative deviation (blue) around each subhalo. Because of this, pairs of lobes of inverted color appear in larger areas of positive or negative deviation. The orientation of the lobes depends on the position around the center. In general, in top left and bottom right quadrants of the plot, areas of positive deviation lie roughly on the left and right from the subhalos and areas of negative deviation lie above and below. In top right and bottom left quadrants the situation is inverted. The size of the lobes strongly depends on the subhalo mass and nearby lobes merge forming complicated patterns.

Since the orientation of the images changes by $\pi/2$ inside the unit-convergence curve and since the unit-convergence curve is affected by the presence of the subhalos, there is an area of strong deviation encircling the center of cluster. The inner border of this area is the unit-convergence curve of the main halo alone and

it is shaped as a perfect ellipse. The outer border is the unit-convergence curve of the complete model. This kind of pattern was not present in Section 3.3.5.8, since the point-mass perturbation does not affect the convergence anywhere else than at the position of the point mass itself.

Some of the contours appear to be slightly broken at certain points, typically in low-deviation areas. This is a minor artefact caused by an imperfect transition between the interpolated and asymptotic regimes used to compute the deflection angles of the subhalos.

A zoomed-out version of the deviation map is plotted in the right panel of Figure 3.5. We see that at a sufficient distance from the halo center four quadrants of alternating positive and negative deviation form. Interestingly, these quadrants are aligned with the orientation of the main halo and do not depend on the particular distribution of the subhalos. This is explained by the fact that the elliptical main halo extends to infinity orienting the images tangentially along the ellipse, while the subhalos are truncated and at a sufficient distance, their monopole contribution prevails orienting images roughly along the circle. At intermediate distances between the complex subhalo-dominated pattern in the center and the simple asymptotic pattern of the four quadrants, there is an intermediary regime with zero-deviation contours substantially changing their orientation. Other shapes are possible in this intermediate region for different distributions of the subhalos.

5. Conclusion

Throughout the whole thesis, we explored the role played by small-scale substructures in the gravitational lensing by dark-matter halos. Relevance of the topic follows from the fact that according to the widely accepted ΛCDM paradigm, hierarchically structured concentrated dark-matter halos make up most of the matter content of our universe. At the same time, multiple discrepancies were described between the astronomical observations and cosmological N-body simulations related to the halo substructures. More recently, Meneghetti et al. (2020) discovered a substantial difference in lensing efficiency of galaxy cluster substructures between observed and simulated clusters.

We decided to embrace a bottom-up approach and started our investigation of the topic with the simplest possible relevant lens model, which consists of a single point mass added into an NFW halo. It can be understood, for example, as a very crude model of an individual galaxy in a galaxy-cluster halo or as a reasonable model of a supermassive black hole in a galaxy halo (Mahler et al. 2022). The advantage of this simple model with only few parameters is that it can be studied in detail using analytical methods.

In Chapter 2, we focused on critical curves and caustics of the simple model. We explored its parameter space and discovered an unexpected richness of caustic transitions. For a centrally positioned perturbation, we found a critical mass, at which a pair of radial caustics merge into one with peculiar properties. For an even heavier central point mass, even this peculiar caustic disappears and only the point-like tangential caustic remains.

In Chapter 3, we continued our investigation of the same model concentrating on weak-lensing quantities and the geometry of images. We plotted sets of image-plane maps of lensing quantities and used analytical methods to explain the observed patterns. We discussed the applicability of the weak-lensing approximation and also introduced Convergence–Shear diagrams, a novel and compact way of visualising geometric properties of lensed images. Our analyses of the point-mass-perturbed NFW halo were published in *The Astrophysical Journal* (Karamazov et al. 2021, Karamazov and Heyrovský 2022).

In Chapter 4, our interest moved towards the lensing by a much more realistic model of a galaxy cluster. We have built the model from a large untruncated ellipsoidal NFW halo and multiple truncated ellipsoidal NFW subhalos. We chose the parameters of the model with the intent to simulate a typical lensing cluster. Our choice of the main-halo parameters was based on real galaxy clusters analysed in lensing surveys. While generating the parameters of the subhalos, we had to resort to probability distributions fitted from N-body cosmological simulations. In doing so, we loosely followed the approach taken by Giocoli et al. (2012). We presented formulae for deflection angles for these two lens models and combined them to obtain a deflection angle of the whole cluster lens. We developed a new parallel GPU code for generating both source-plane and image-plane maps of the lensing quantities. We presented these maps in the same form that we used for maps generated from the simple model in the preceding chapters. This allowed us to use our analytical understanding of the simple point-perturbed model to discuss and explain the morphology of patterns in the cluster-lens maps.

Overall, the results generated from our analytically composed model of a sample galaxy cluster indicate agreement with Meneghetti et al. (2020), who simulated lensing by clusters taken straight from cosmological structure-formation simulations and found that the lensing influence of small-scale substructures was substantially lower than in observed clusters. Since our parallel lensing code can be easily modified, in subsequent research it will be possible to closely investigate differences between various models of cluster subhalo populations and hopefully shed more light on the problem of discrepant lensing efficiencies of galaxy cluster substructures.

Bibliography

G. O. Abell. The distribution of rich clusters of galaxies. *The Astrophysical Journal Supplement*, 3:211A, 1958.

R. E. Angulo, O. Hahn, A. D. Ludlow, and S. Bonoli. Earth-mass haloes and the emergence of NFW density profiles. *Monthly Notices of the Royal Astronomical Society*, 417:4687–4701, 2017.

H. Asada. Critical lines in gravitational lenses and the determination of cosmological parameters. *The Astrophysical Journal*, 485:460–464, 1997.

Y. M. Bahé. Strongly lensed cluster substructures are not in tension with ΛCDM. *Monthly Notices of the Royal Astronomical Society*, 505:1458–1463, 2021.

M. Bartelmann. Arcs from a universal dark-matter halo profile. *Astronomy and Astrophysics*, 313:697–702, 1996.

M. Bartelmann, S. Narayan, R.and Seitz, and P. Schneider. Maximum-likelihood cluster reconstruction. *Astrophysical Journal Letters*, 464:L115, 1996.

A. Biviano, A. Moretti, A. Paccagnella, et al. The concentration-mass relation of clusters of galaxies from the OmegaWINGS survey. *Astronomy and Astrophysics*, 607:A81, 2017.

R. R. Bourassa and R. Kantowski. The theory of transparent gravitational lenses. *The Astrophysical Journal*, 195:13–21, 1975.

J. D. Bowman, J. N. Hewitt, and J. R. Kiger. Gravitational lensing signatures of supermassive black holes in future radio surveys. *The Astrophysical Journal*, 617:81–101, 2004.

M. Bradač, P. Schneider, M. Lombardi, and T. Erben. Strong and weak lensing united. i. the combined strong and weak lensing cluster mass reconstruction method. *The Astrophysical Journal*, 437:39, 2005.

I. Bray. Spheroidal gravitational lenses. *Monthly Notices of the Royal Astronomical Society*, 208:511–516, 1984.

J. S. Bullock and M. Boylan-Kolchin. Small-scale challenges to the ΛCDM paradigm. *Annual Review of Astronomy and Astrophysics*, 55:1, 2017.

K. Chang and S. Refsdal. Star disturbances in gravitational lens galaxies. *Astronomy and Astrophysics*, 132:168–178, 1984.

D. Clowe, A. Gonzalez, and M. Markevitch. Weak-lensing mass reconstruction of the interacting cluster 1E 0657-558: Direct evidence for the existence of dark matter. *The Astrophysical Journal*, 604:596, 2004.

A. B. Congdon and C. Keeton. *Principles of Gravitational Lensing*. Springer, Cham, 2018. ISBN 9783030021221.

N. Dalal and C. S. Kochanek. Direct detection of cold dark matter substructure. *The Astrophysical Journal*, 572:25–33, 2002.

G. Despali, C. Giocoli, and G. Tormen. Some like it triaxial: the universality of dark matter halo shapes and their evolution along the cosmic time. *Monthly Notices of the Royal Astronomical Society*, 443:3208–3217, 2014.

J. M. Diego, H. B. Sandvik, P. Protopapas, M. Tegmark, et al. Non-parametric mass reconstruction of A1689 from strong lensing data with the Strong Lensing Analysis Package. *Monthly Notices of the Royal Astronomical Society*, 362: 1247, 2005.

M. Dominik. The binary gravitational lens and its extreme cases. *Astronomy and Astrophysics*, 349:108–125, 1999.

A. R. Duffy, J. Schaye, et al. Dark matter halo concentrations in the wilkinson microwave anisotropy probe year 5 cosmology. *Monthly Notices of the Royal Astronomical Society: Letters*, 390:L64–L68, 2008.

H. S. Dúmet-Montoya, G. B. Caminha, and M. Makler. Domain of validity for pseudo-elliptical NFW lens models. mass distribution, mapping to elliptical models, and arc cross section. *Astronomy & Astrophysics*, 544:A83, 2012.

H. S. Dúmet-Montoya, G. B. Caminha, and M. Makler. Analytic solutions for Navarro-Frenk-White lens models in the strong lensing regime for low characteristic convergences. *Astronomy & Astrophysics*, 560:A86, 2013.

F. W. Dyson, A. S. Eddington, and C. Davidson. A determination of the deflection of light by the sun's gravitational field, from observations made at the total eclipse of May 29, 1919. *Philosophical Transactions of the Royal Society A: Mathematical, Physical and Engineering Sciences*, 220:571–581, 1920.

J. Einasto. Kinematics and dynamics of stellar systems. *Trudy Inst. Astrofiz. Alma-Ata*, 5:87, 1965.

A. Einstein. Lens-like action of a star by the deviation of light in the gravitational field. *Science*, 84:506, 1936.

X. Er and A. Rogers. Two families of astrophysical diverging lens models. *Monthly Notices of the Royal Astronomical Society*, 475:867–878, 2018.

H. Erdl and P. Schneider. Classification of the multiple deflection two point-mass gravitational lens models and application of catastrophe theory in lensing. *Astronomy and Astrophysics*, 268:453–471, 1993.

S. Ettori, A. Donnarumma, E. Pointecouteau, et al. Mass profiles of galaxy clusters from X-ray analysis. *Space Science Reviews*, 177:119–154, 2013.

N. W. Evans and M. I. Wilkinson. Lens models with density cusps. *Monthly Notices of the Royal Astronomical Society*, 296:800–812, 1998.

E. Q. Finney, M. Bradač, K.-H. Huang, et al. Mass modeling of frontier fields cluster MACS J1149.5+2223 using strong and weak lensing. *The Astrophysical Journal*, 859:58, 2018.

C. S. Frenk, S. D. M. White, M. Davis, and G. Efstathiou. The formation of dark halos in a universe dominated by cold dark matter. *The Astrophysical Journal*, 327:507–525, 1988.

L. Gao, S. D. M. White, et al. The subhalo populations of ΛCDM dark haloes. *Monthly Notices of the Royal Astronomical Society*, 355:819–834, 2004.

C. Giocoli, G. Tormen, et al. The substructure hierarchy in dark matter haloes. *Monthly Notices of the Royal Astronomical Society*, 404:502–517, 2010.

C. Giocoli, M. Meneghetti, et al. MOKA: a new tool for strong lensing studies. *Monthly Notices of the Royal Astronomical Society*, 421:3343–3355, 2012.

A. N. Godwin. Three dimensional pictures for Thom's parabolic umbilic. *Publications mathématiques de l'I.H.É.S.*, 40:117–138, 1971.

G. Golse and J.-P. Kneib. Pseudo elliptical lensing mass model: Application to the NFW mass distribution. *Astronomy and Astrophysics*, 390:821–827, 2002.

G. Granata, A. Mercurio, C. Grillo, L. Tortorelli, et al. Improved strong lensing modelling of galaxy clusters using the fundamental plane: Detailed mapping of the baryonic and dark matter mass distribution of Abell S1063. *Astronomy & Astrophysics*, 659:A24, 2022.

M. Guo, K. Inayoshi, T. Michiyama, et al. Hunting for wandering massive black holes. *The Astrophysical Journal*, 901:39, 2020.

A. Halkola, S. Seitz, and M. Pannella. Parametric strong gravitational lensing analysis of Abell 1689. *Monthly Notices of the Royal Astronomical Society*, 372: 1425–1462, 2006.

J. F. Hennawi, M. D. Gladders, M. Oguri, et al. A new survey for giant arcs. *The Astronomical Journal*, 135:664–681, 2008.

D. Heyrovský. Gravitational lensing: From planets to galaxy clusters. *Habilitation thesis, Charles University*, 2021.

D. Heyrovský and M. Karamazov. Paper in preparation. *The Astrophysical Journal, to be submitted*, 2022a.

D. Heyrovský and M. Karamazov. Paper in preparation. *The Astrophysical Journal, to be submitted*, 2022b.

Y. D. Hezaveh, N. Dalal, D. P. Marrone, et al. Detection of lensing substructure using ALMA observations of the dusty galaxy SDP.81. *The Astrophysical Journal*, 823:37, 2016.

M. Jauzac, D. Eckert, M. Schaller, et al. Growing a 'cosmic beast': observations and simulations of MACS J0717.5+3745. *Monthly Notices of the Royal Astronomical Society*, 481:2901–2917, 2018.

Y. P. Jing and Y. Suto. Triaxial modeling of halo density profiles with high-resolution N-body simulations. *The Astrophysical Journal*, 574:538–553, 2002.

E. Jullo, J. P. Kneib, M. Limousin, Á. Elíasdóttir, P. J. Marshall, and T. Verdugo. A bayesian approach to strong lensing modelling of galaxy clusters. *New Journal of Physics*, 9:12, 2007.

N. Kaiser and G. Squires. Mapping the dark matter with weak gravitational lensing. *Astrophysical Journal*, 404:441, 1993.

N. Kaiser, G. Squires, and T. Broadhurst. A method for weak lensing observations. *The Astrophysical Journal*, 449:460, 1995.

J. C. Kapteyn. First attempt at a theory of the arrangement and motion of the sidereal system. *The Astrophysical Journal*, 55:302–327, 1922.

M. Karamazov and D. Heyrovský. Gravitational lensing by a massive object in a dark matter halo. II. shear, phase, and image geometry. *The Astrophysical Journal*, 927:101, 2022. Paper II.

M. Karamazov, L. Timko, and D. Heyrovský. Gravitational lensing by a massive object in a dark matter halo. I. critical curves and caustics. *The Astrophysical Journal*, 922:72, 2021. Paper I.

R. Kayser, S. Refsdal, and R. Stabell. Astrophysical applications of gravitational micro-lensing. *Astronomy and Astrophysics*, 166:36–52, 1986.

C. R. Keeton. A catalog of mass models for gravitational lensing. *arXiv:astro-ph/0102341*, 2001.

P. L. Kelly, J. M. Diego, S. Rodney, et al. Extreme magnification of an individual star at redshift 1.5 by a galaxy-cluster lens. *Nature Astronomy*, 2:334–342, 2018.

J.-P. Kneib and P. Natarajan. Cluster lenses. *The Astronomy and Astrophysics Review*, 19:47, 2011.

R. Li, C. S. Frenk, S. Cole, L. Gao, S. Bose, and W. A. Hellwing. Constraints on the identity of the dark matter from strong gravitational lenses. *Monthly Notices of the Royal Astronomical Society*, 460:363–372, 2016.

M. Limousin, J. Richard, E. Jullo, et al. Combining strong and weak gravitational lensing in Abell 1689. *The Astrophysical Journal*, 668:643–666, 2007.

M. S. Longair. *Galaxy Formation*. Springer, Berlin, 2008. ISBN 9783540734772.

A. D. Ludlow, J. F. Navarro, M. Boylan-Kolchin, et al. The mass profile and accretion history of cold dark matter haloes. *Monthly Notices of the Royal Astronomical Society*, 432:1103–1113, 2013.

D. H. Lyth and A. R. Liddle. *The primordial density perturbation: cosmology, inflation and the origin of structure*. Cambridge University Press, 2009. ISBN 9780521828499.

G. Mahler, P. Natarajan, M. Jauzac, and J. Richard. Gravitational lensing effects of supermassive black holes in cluster environments. *arXiv:2201.10900*, 2022. submitted to MNRAS.

S. Mao and H. J. Witt. Lensing by a singular isothermal sphere and a black hole. *Monthly Notices of the Royal Astronomical Society*, 420:792–799, 2012.

S. Mao, H. J. Witt, and L. V. E. Koopmans. The influence of central black holes on gravitational lenses. *Monthly Notices of the Royal Astronomical Society*, 323:301–307, 2001.

H. Martel and P. R. Shapiro. Gravitational lensing by CDM halos: Singular versus nonsingular profiles. *arXiv:astro-ph/0305174*, 2003.

M. Meneghetti, M. Bartelmann, and L. Moscardini. Cluster cross-sections for strong lensing: analytic and numerical lens models. *Monthly Notice of the Royal Astronomical Society*, 340:105–114, 2003.

M. Meneghetti, P. Natarajan, D. Coe, et al. The frontier fields lens modelling comparison project. *Monthly Notices of the Royal Astronomical Society*, 472: 3177–3216, 2017.

M. Meneghetti, G. Davoli, P. Bergamini, et al. An excess of small-scale gravitational lenses observed in galaxy clusters. *Science*, 369:1347–1351, 2020.

J. Merten, M. Meneghetti, M. Postman, et al. CLASH: The concentration-mass relation of galaxy clusters. *The Astrophysical Journal*, 806:4, 2015.

C. Messier. Catalogue des Nébuleuses & des amas d'Étoiles. *Connoissance des Temps*, 1784:227–267, 1781.

R. B. Metcalf and P. Madau. Compound gravitational lensing as a probe of dark matter substructure within galaxy halos. *The Astrophysical Journal*, 563:9–20, 2001.

R. B. Metcalf, M. Meneghetti, C. Avestruz, et al. The strong gravitational lens finding challenge. *The Astrophysical Journal*, 625:A119, 2019.

J. F. Navarro, C. S. Frenk, and S. D. M. White. The structure of cold dark matter halos. *Astrophysical Journal*, 462:563, 1996.

J. F. Navarro, C. S. Frenk, and S. D. M. White. A universal density profile from hierarchical clustering. *The Astrophysical Journal*, 490:493–508, 1997.

A. F. Neto, L. Gao, et al. The statistics of ΛCDM halo concentrations. *Monthly Notices of the Royal Astronomical Society*, 381:1450–1462, 2007.

A. B. Newman, T. Treu, R. S. Ellis, et al. The density profiles of massive, relaxed galaxy clusters. I. the total density over three decades in radius. *The Astrophysical Journal*, 765:24, 2013.

M. Oguri. Fast calculation of gravitational lensing properties of elliptical Navarro-Frenk-White and Hernquist density profiles. *Publications of the Astronomical Society of the Pacific*, 133:074504, 2021.

N. Okabe, G. P. Smith, K. Umetsu, et al. LoCuSS: The mass density profile of massive galaxy clusters at z = 0.2. *The Astrophysical Journal Letters*, 769:L35, 2013.

P. J. E. Peebles. Structure of the coma cluster of galaxies. *The Astrophysical Journal*, 75:13, 1970.

O. Pejcha and D. Heyrovský. Extended-source effect and chromaticity in two-point-mass microlensing. *The Astrophysical Journal*, 690:1772–1796, 2009.

P. Peter and J.-P. Uzan. *Primordial Cosmology*. Oxford University Press, 2009. ISBN 9780199209910.

Planck Collaboration, P. A. R. Ade, N. Aghanim, et al. Planck 2015 results. I. overview of products and scientific results. *Astronomy & Astrophysics*, 594:A1, 2016.

T. Poston and I. Stewart. *Catastrophe Theory and Its Applications*. Pitman, London, 1978. ISBN 978-0486692715.

D. Potter, J. Stadel, and R. Teyssier. PKDGRAV3: beyond trillion particle cosmological simulations for the next era of galaxy surveys. *Computational Astrophysics and Cosmology*, 4:2, 2017.

S. Refsdal. The gravitational lens effect. *Monthly Notices of the Royal Astronomical Society*, 128:295, 1964.

A. E. Reines, J. J. Condon, J. Darling, et al. A new sample of (wandering) massive black holes in dwarf galaxies from high-resolution radio observations. *The Astrophysical Journal*, 888:36, 2020.

A. Robertson. The galaxy-galaxy strong lensing cross-sections of simulated ΛCDM galaxy clusters. *Monthly Notices of the Royal Astronomical Society*, 504:L7–L11, 2021.

D. C. Rodrigues, A. del Popolo, V. Marra, et al. Evidence against cuspy dark matter haloes in large galaxies. *Monthly Notices of the Royal Astronomical Society*, 470:2410–2426, 2017.

P. Salucci. The distribution of dark matter in galaxies. *The Astronomy and Astrophysics Review*, 27:2, 2019.

P. Schneider. *Extragalactic Astronomy and Cosmology*. Springer-Verlag, Berlin, Heidelberg, 2006. ISBN 978-3-540-33174-2.

P. Schneider and A. Weiss. The two-point-mass lens - detailed investigation of a special asymmetric gravitational lens. *Astronomy and Astrophysics*, 164:237–259, 1986.

P. Schneider, J. Ehlers, and E. E. Falco. *Gravitational Lenses*. Springer-Verlag, Berlin, 1992. ISBN 978-0387970707.

P. Schneider, C. Kochanek, and J. Wambsganss. *Gravitational Lensing: Strong, Weak and Micro*. Springer, Berlin, 2006. ISBN 978-3-540-30310-7.

S. Seitz, P. Schneider, and M. Bartelmann. Entropy-regularized maximum-likelihood cluster mass reconstruction. *Astronomy and Astrophysics*, 337:325–337, 1998.

A. J. Shajib, T. Treu, S. Birrer, et al. Dark matter haloes of massive elliptical galaxies at z $\sim$ 0.2 are well described by the Navarro-Frenk-White profile. *Monthly Notices of the Royal Astronomical Society*, 503:2380–2405, 2021.

E. M. Shin and N. W. Evans. Lensing by binary galaxies modelled as isothermal spheres. *Monthly Notices of the Royal Astronomical Society*, 390:505–522, 2008.

F. Stoehr. High resolution simulations of structure formation in underdense regions. *Master's thesis, Technische Universität München*, 1999.

S. H. Suyu, V. Bonvin, F. Courbin, C. D. Fassnacht, et al. H0LiCOW - I. H0 lenses in COSMOGRAIL's Wellspring: program overview. *Monthly Notices of the Royal Astronomical Society*, 468:3, 2017.

L. Timko. Gravitační čočkování kombinací spojité a diskrétní hmoty. *Bachelor's thesis, Charles University*, 2017.

K. Umetsu. Cluster-galaxy weak lensing. *The Astronomy and Astrophysics Review*, 28:7, 2020.

K. Umetsu and B. Diemer. Lensing constraints on the mass profile shape and the splashback radius of galaxy clusters. *The Astrophysical Journal*, 836:231, 2017.

C. A. Vera-Ciro, L. V. Sales, et al. The shape of dark matter haloes in the Aquarius simulations: evolution and memory. *Monthly Notices of the Royal Astronomical Society*, 416:1377–1391, 2011.

J. Wagner. Generalised model-independent characterisation of strong gravitational lenses. III. perturbed axisymmetric lenses. *Astronomy & Astrophysics*, 615:A102, 2018.

D. Walsh, R. F. Carswell, and R. J. Weymann. 0957+561 A, B: twin quasistellar objects or gravitational lens? *Nature*, 279:381, 1979.

J. Wang, J. F. Navarro, C. S. Frenk, et al. Assembly history and structure of galactic cold dark matter haloes. *Monthly Notices of the Royal Astronomical Society*, 413:1373–1382, 2011.

M. C. Werner and N. W. Evans. A simple model for lensing by black holes in galactic nuclei. *Monthly Notices of the Royal Astronomical Society*, 368:1362–1368, 2006.

C. O. Wright and T. G. Brainerd. Gravitational lensing by NFW halos. *The Astrophysical Journal*, 534:34–40, 2000.

D. Xu, D. Sluse, L. Gao, J. Wang, C. Frenk, S. Mao, P. Schneider, and V. Springel. How well can cold dark matter substructures account for the observed radio flux-ratio anomalies. *Monthly Notices of the Royal Astronomical Society*, 447: 3189–3206, 2015.

F. Zandanel, M. Fornasa, F. Prada, et al. MultiDark clusters: galaxy cluster mock light-cones, eROSITA, and the cluster power spectrum. *Monthly Notices of the Royal Astronomical Society*, 480:987–1005, 2018.

J. Zavala and C. S. Frenk. Dark matter haloes and subhaloes. *Galaxies*, 7:4, 2019.

Ya. B. Zel'dovich. Gravitational instability: An approximate theory for large density perturbations. *Astronomy and Astrophysics*, 5:84–89, 1970.

F. Zwicky. Die Rotverschiebung von extragalaktischen Nebeln. *Helvetica Physica Acta*, 6:110–127, 1933.

F. Zwicky. On the probability of detecting nebulae which act as gravitational lenses. *Physical Review*, 51:290, 1937.

List of publications

1. M. Karamazov, L. Timko and D. Heyrovský. Gravitational Lensing by a Massive Object in a Dark Matter Halo. I. Critical Curves and Caustics. *The Astrophysical Journal*, 922:72, 2021

2. M. Karamazov and D. Heyrovský. Gravitational Lensing by a Massive Object in a Dark Matter Halo. II. Shear, Phase, and Image Geometry. *The Astrophysical Journal*, 927:101, 2022

A. Appendices

A.1 Analytic results and approximations[1]

Studies of gravitational lensing by NFW halos face analytic and numerical challenges due to the properties of the function $\mathcal{F}(x)$, defined here by Equation (2.6). The main difficulties occur close to the origin, for $x \ll 1$, where $\mathcal{F}(x) \to \infty$ but the combination $\ln(x/2)+\mathcal{F}(x)$, appearing in Equation (2.15) and elsewhere, converges to zero. This problem becomes even more pronounced for lower values of the halo convergence parameter κ_s, when all the critical curves and caustics shrink exponentially fast to the origin, as shown in Equation (2.28), Equation (2.29), and Figure 2.3. Even in double-precision arithmetic the expression from the first line of Equation (2.6) would fail to reproduce the results and transitions close to the origin presented in this work.

In the following Appendix A.1.1 we present expansions of different lensing quantities close to the origin to illustrate their local behavior. In addition, we present exact analytic expressions that do not suffer from the described cancellation problem. In Appendix A.1.2 we illustrate the continuous and smooth nature of $\mathcal{F}(x)$ and the convergence $\kappa(x)$ across the scale radius, at $x = 1$.

A.1.1 Lensing near the origin

For $x \ll 1$ the four leading orders of the expansion of $\mathcal{F}(x)$ can be written as

$$\mathcal{F}(x) = -\ln\frac{x}{2} - \frac{x^2}{2}\,\ln\frac{x}{2} - \frac{x^2}{4} + \mathcal{O}(x^4\,\ln x)\,, \tag{A.1}$$

which yields the two leading orders of the expression

$$\ln\frac{x}{2} + \mathcal{F}(x) = -\frac{x^2}{2}\,\ln\frac{x}{2} - \frac{x^2}{4} + \mathcal{O}(x^4\,\ln x)\,, \tag{A.2}$$

in which the logarithmic divergence of $\mathcal{F}(x)$ is cancelled and the combination shrinks to zero as $x^2\,\ln x$. By substituting Equation (A.1) in Equation (2.5) we get four leading orders of the NFW convergence expansion

$$\kappa(x) = -2\,\kappa_\mathrm{s}\,(\,\ln\frac{x}{2} + 1 + \frac{3}{2}\,x^2\,\ln x + \frac{5}{4}\,x^2\,) + \mathcal{O}(x^4\,\ln x)\,, \tag{A.3}$$

showing its logarithmic divergence. The Jacobian behavior close to the origin can be obtained by substituting Equation (A.1) in Equation (2.17), yielding three leading orders of its expansion

$$\det J(\boldsymbol{x}) = 4\,\kappa_\mathrm{s}^2\,\ln^2\frac{x}{2} + 4\,\kappa_\mathrm{s}\,(1+2\,\kappa_\mathrm{s})\,\ln\frac{x}{2} + 1 + 4\,\kappa_\mathrm{s} + 3\,\kappa_\mathrm{s}^2 + \mathcal{O}(x^2\,\ln x)\,. \tag{A.4}$$

Getting higher-order terms would require a higher-order expansion in Equation (A.1). This result reveals the $\ln^2 x$ divergence of the NFW Jacobian at the origin.

[1] Appendix A of Karamazov et al. (2021)

For computing the critical curves and caustics we need exact analytic expressions rather than series expansions. We first express the top row of Equation (2.6) in an equivalent form,

$$\mathcal{F}(x) = \frac{1}{\sqrt{1-x^2}} \ln \frac{1+\sqrt{1-x^2}}{x}\,, \tag{A.5}$$

which can then be combined with $\ln(x/2)$ to cancel the divergence at the origin,

$$\ln \frac{x}{2} + \mathcal{F}(x) = \frac{-x^2}{1-x^2+\sqrt{1-x^2}} \ln \frac{x}{2} + \frac{1}{\sqrt{1-x^2}} \ln \frac{1+\sqrt{1-x^2}}{2}\,. \tag{A.6}$$

The first term reveals the leading order of the expansion at the origin as seen in Equation (A.2), while the second term contributes to higher orders starting from $\mathcal{O}(x^2)$. Both Equation (A.5) and Equation (A.6) are valid for any $x < 1$. These numerically stable expressions can be used in Equation (2.35) to compute the Jacobian and the critical curve, and in Equation (2.33) to compute the caustic.

A.1.2 Lensing near the scale radius

At the halo scale radius the $x < 1$ expression in Equation (2.6) transitions smoothly to the $x > 1$ expression. For illustration, we provide the three leading terms of the expansion valid on both sides of $x = 1$,

$$\mathcal{F}(x) = 1 - \frac{2}{3}(x-1) + \frac{7}{15}(x-1)^2 + \mathcal{O}((x-1)^3)\,. \tag{A.7}$$

Using this result, we may expand the lens-equation combination

$$\ln \frac{x}{2} + \mathcal{F}(x) = 1 - \ln 2 + \frac{x-1}{3} - \frac{(x-1)^2}{30} + \mathcal{O}((x-1)^3)\,. \tag{A.8}$$

Substituting Equation (A.7) in Equation (2.5) yields two leading orders of the NFW convergence expansion

$$\kappa(x) = \kappa_\mathrm{s} \left[\frac{2}{3} - \frac{4}{5}(x-1) \right] + \mathcal{O}((x-1)^2)\,. \tag{A.9}$$

Getting higher-order terms would require a higher-order expansion in Equation (A.7).

A.2 Vanishing radial critical curves and caustics[2]

For a point mass with the critical value of the mass parameter $\kappa_\mathrm{P} = \kappa_\mathrm{PC}$ positioned centrally in a NFW halo, the single radial critical curve and single radial caustic have very unusual properties, as mentioned in Section 2.3.3. We illustrate the situation in Figure A.1, showing from top row to bottom the critical curve plotted over a color map of the Jacobian, the radial profile of the Jacobian, the caustic plotted over the total magnification map, and the radial profile of the total magnification in the vicinity of the (vanishing) radial caustics. The central

[2] Appendix B of Karamazov et al. (2021)

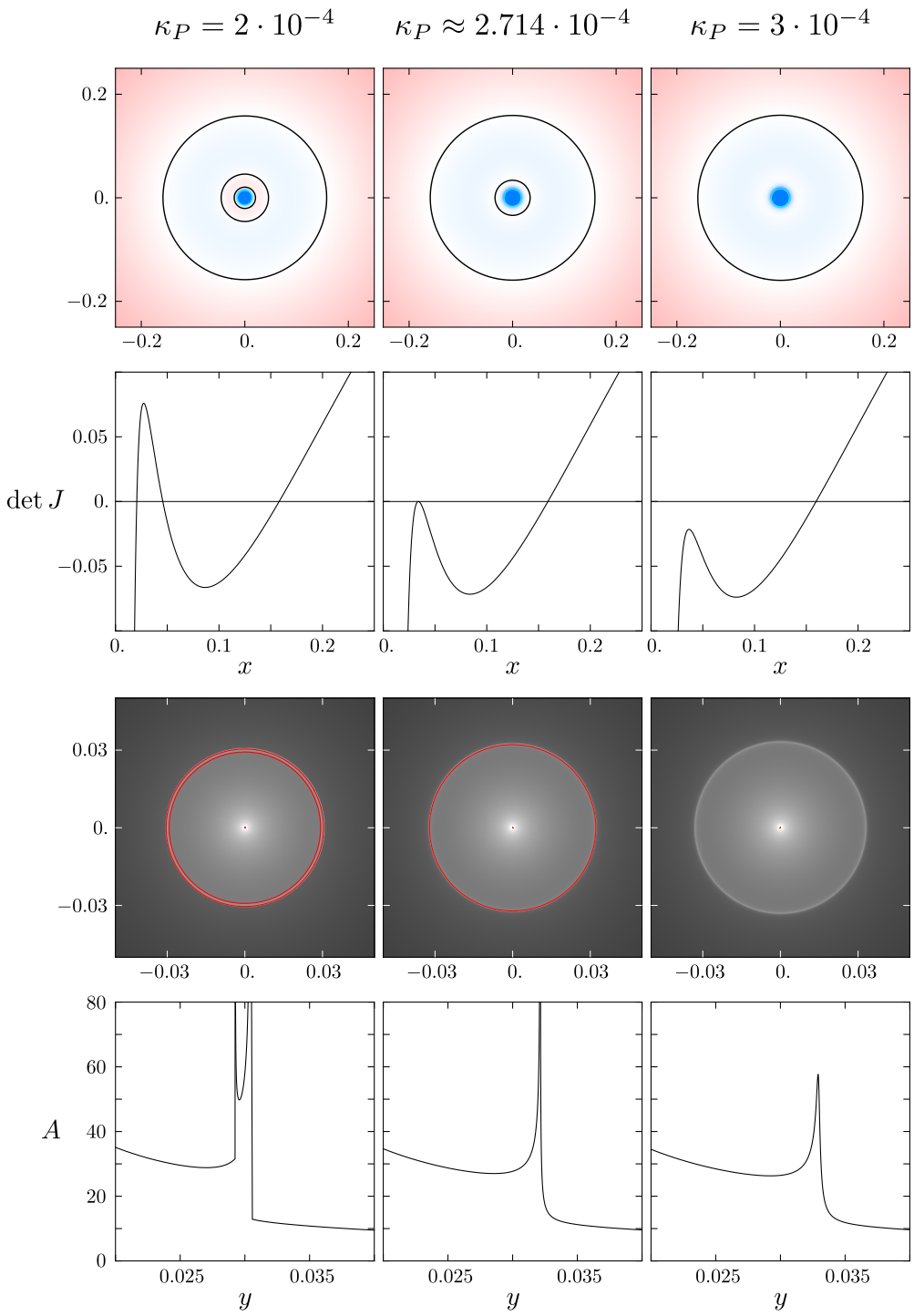

Figure A.1: Vanishing radial critical curves and caustics for a centrally positioned point mass. Rows from top: Jacobian maps with critical curves; radial profiles of Jacobian from halo center; total magnification maps with caustics; radial profiles of total magnification in vicinity of radial caustic position. Columns from left for increasing mass parameter: sub-critical $\kappa_\mathrm{P} = 2 \cdot 10^{-4}$ (two radial critical curves and caustics); critical $\kappa_\mathrm{P} = \kappa_\mathrm{PC} \approx 2.714 \cdot 10^{-4}$ (single radial critical curve and caustic); super-critical $\kappa_\mathrm{P} = 3 \cdot 10^{-4}$ (no radial critical curve and caustic). Note that the single radial caustic in the central column is not a fold caustic (see Appendix A.2). Notation and color bars as in Figure 2.5.A.

column corresponds to the critical value $\kappa_{\rm P} = \kappa_{\rm PC} \approx 2.714 \cdot 10^{-4}$, which is bracketed in the left column by sub-critical $\kappa_{\rm P} = 2 \cdot 10^{-4}$ and in the right column by super-critical $\kappa_{\rm P} = 3 \cdot 10^{-4}$.

Along the critical curve the Jacobian is zero by definition, but for $\kappa_{\rm P} = \kappa_{\rm PC}$ it is negative on both sides of the radial critical curve, as seen in the top two panels of the central column. Thus, images on both sides have the same (negative) parity. The caustic, which is shown in the third panel of the central column, is even more peculiar. Along the caustic the magnification is infinite by definition. However, the number of images of a point source does not change when crossing this radial caustic. What's more, the magnification is divergent from both sides of the radial caustic, as seen in the bottom panel of the central column. This is unlike the usual fold caustic, across which the magnification changes discontinuously, diverging when approached from the inner side but reaching a finite value when approached from the outer side.

We are not aware of any previous example in the gravitational lensing literature of a smooth caustic curve that is not a fold caustic. The same type of caustic clearly should appear even for a critical value of the central mass embedded in a cored isothermal (Mao et al. 2001) or a Plummer (Werner and Evans 2006) density profile. In addition, a similar effect occurs in certain non-gravitational plasma lens models (Er and Rogers 2018). However, to our knowledge the peculiar nature of such a caustic has not been described yet.

The vanishing of the radial critical curves and caustics presents a unique type of caustic metamorphosis. The usual metamorphoses, such as those discussed in Section 2.3.4.3, occur at a single point. Their properties are studied by Taylor-expanding the lens potential and lens equation in the vicinity of the point. This metamorphosis is not point-like; it occurs along the full length of the caustic simultaneously, as a consequence of the axial symmetry of the lens configuration. Nevertheless, it is related to the common beak-to-beak metamorphosis, in which two facing fold caustics approach each other, touch, and reconnect, forming two facing cusps that recede from the metamorphosis point. Here the two facing radial caustics are perfectly parallel, hence they come into contact and the metamorphosis occurs simultaneously along their full length. Instead of forming receding cusps, which do not arise here due to the symmetry, the caustics simply vanish, leaving a ring-like maximum in the magnification map as well as a ring-like maximum in the negative-Jacobian surroundings in the image plane.

This interpretation is supported by the character of the total-magnification divergence at the caustic. For the critical value of $\kappa_{\rm P}$ we find $A(y) \sim |\, y - y_{\rm PR} \,|^{-2/3}$ on both sides of the caustic radius $y_{\rm PR}$, as shown in the bottom panel of the central column. This is the generic magnification decline perpendicular to the axis of a cusp, as seen for example by setting $y_{\parallel} = 0$ in equation (A6) of Pejcha and Heyrovský (2009). For $\kappa_{\rm P} = 2 \cdot 10^{-4}$ the divergence at the outer radial caustic follows $A(y) \sim (y_{\rm PR1} - y)^{-1/2}$ for $y < y_{\rm PR1}$, and the divergence at the inner radial caustic follows $A(y) \sim (y - y_{\rm PR2})^{-1/2}$ for $y > y_{\rm PR2}$, as shown in the bottom panel of the left column. Both are generic fold caustics oriented inside the annulus enclosed by them. Note that the inner radial caustic is weaker than the outer one, as indicated by the more narrow divergence.

The critical value of the mass parameter $\kappa_{\rm PC} \approx 2.714 \cdot 10^{-4}$ corresponds to the fiducial NFW halo convergence parameter $\kappa_{\rm s} \approx 0.239035$ used in this

work. However, the occurrence of such a critical mass and the accompanying metamorphosis is generic, with the critical value depending on the halo in which the mass is embedded: $\kappa_{\mathrm{PC}} = \kappa_{\mathrm{PC}}(\kappa_{\mathrm{s}})$.

A.3 Image geometry as a function of convergence and shear[3]

The mapping from a source to its image is described locally by the inverse of the lens-equation Jacobian matrix. The eigenvalue decomposition of this inverse matrix $\mathbb{A}$ presented in Equation (3.21) shows that the full geometry of an image of a small source, including its shape, size, and orientation with respect to the phase, is given by the lens convergence and shear at the position of the image. We demonstrate here the connection between the geometry of an image and its position in a general convergence–shear diagram.

The properties of an image appearing at position $\boldsymbol{x}$ in the image plane can be determined from the convergence–shear diagram (CS diagram) in Figure A.2 using the combination of the local convergence $\kappa(\boldsymbol{x})$ and shear $\gamma(\boldsymbol{x})$, and the eigenvalues introduced in Equation (3.20) computed from them. The eigenvalue $\lambda_{\parallel}$, which defines the scaling factor in the direction of the phase, is constant in the diagram along straight lines with slope -1. It starts at 1 at the origin of the plot, and increases to ∞ at the solid red line, which corresponds to critical curves (tangential in the case of axially symmetric lenses). Above it $\lambda_{\parallel}$ changes discontinuously to $-\infty$, with the negative sign indicating that the image is flipped in the direction of the phase. The value of $\lambda_{\parallel}$ increases to -1 along the dashed red line, above which the flipped image is contracted rather than expanded in the direction of the phase. Further beyond the top right corner of the diagram, $\lambda_{\parallel}$ increases asymptotically to 0. Overall, below the dashed red line the image is expanded in the direction of the phase, while above it the image is contracted in the direction of the phase.

The scaling factor in the direction perpendicular to the phase is defined by the eigenvalue $\lambda_{\perp}$, which is constant in the diagram along straight lines with slope 1. Along the dashed blue line passing through the origin we find $\lambda_{\perp} = 1$. Above it the image is contracted in the direction perpendicular to the phase, and $\lambda_{\perp}$ decreases asymptotically to 0 above the top left of the diagram. Below the dashed blue line passing through the origin $\lambda_{\perp}$ increases to ∞ at the solid blue line, which corresponds to critical curves (radial in the case of axially symmetric lenses). Below it $\lambda_{\perp}$ changes discontinuously to $-\infty$, with the negative sign indicating that the image is flipped in the direction perpendicular to the phase. The value of $\lambda_{\perp}$ increases to -1 along the right dashed blue line, below which the flipped image is contracted in the direction perpendicular to the phase. Further beyond the bottom right corner of the diagram, $\lambda_{\perp}$ increases asymptotically to 0. Overall, in the band between the dashed blue lines the image is expanded in the direction perpendicular to the phase, while outside it the image is contracted in the direction perpendicular to the phase.

The described scalings in the two perpendicular directions can be combined to yield information about the orientation, shape, and size of the image. Comparing

[3] Appendix A of Karamazov and Heyrovský (2022)

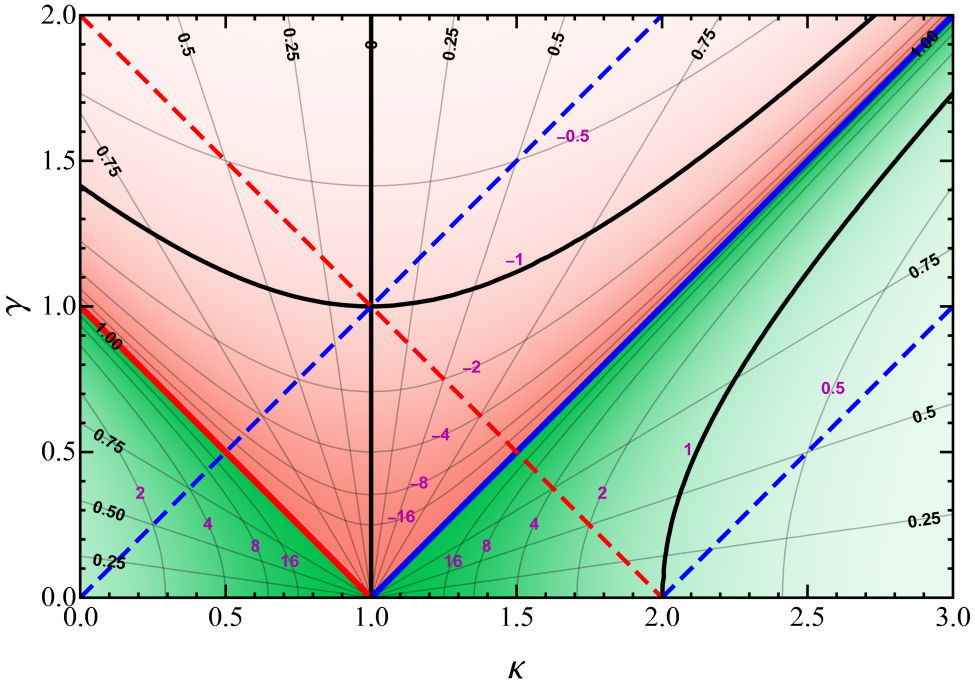

Figure A.2: Convergence–shear diagram (CS diagram) illustrating the geometry of lensed images as determined by the (κ, γ) combination at their position. The color map and the purple-labeled hyperbolic contours show the values of $\det \mathbb{A}$; its absolute value yields the magnification and its sign yields the parity of the image (positive in green, negative in pink areas). Unit magnification occurs at the origin of the diagram and along the bold black hyperbolae; outside the region delimited by them images are demagnified. The black-labeled straight-line contours correspond to constant flattening of the image, given by Equation (3.22). Undistorted images occur along the $\gamma = 0$ axis and the bold black $\kappa = 1$ line. The solid red and solid blue lines correspond to critical-curve points; the combination $(\kappa, \gamma) = (1, 0)$ specifically to umbilic points. Unit absolute values of the eigenvalues of $\mathbb{A}$ occur along the dashed diagonals: $\lambda_\parallel = -1$ (red); $\lambda_\perp = 1$ (blue from origin); $\lambda_\perp = -1$ (blue from $\kappa = 2$). For $\kappa < 1$ images are elongated in the direction of the phase; for $\kappa > 1$ perpendicular to the phase. For more details, see Appendix A.3.

their absolute values for a non-zero shear, $|\lambda_\parallel|$ is larger for $\kappa < 1$ and $|\lambda_\perp|$ is larger for $\kappa > 1$. Hence, the vertical solid black line at $\kappa = 1$ divides images by the orientation of their distortion, i.e., the orientation of the major axis of an elliptical image of a small circular source. To the left of the line, images are oriented in the direction φ (parallel to the phase), while to the right of the line, images are oriented in the direction $\varphi + \pi/2$ (perpendicular to the phase).

The distortion of the shape can be quantified by the flattening, computed from Equation (3.22). In the diagram in Figure A.2, the flattening f is constant along the straight lines radiating from the point $(\kappa, \gamma) = (1, 0)$, labeled by their f value at the outer edge of the plot. The horizontal axis corresponds to $f = 0$, i.e., there is no distortion for zero shear. Clockwise from the direction to the origin of the plot, f values along the lines increase in steps of 0.25 to 1 at the solid red line, corresponding to maximum flattening in the direction of the phase at the

tangential critical curve. For the following lines, f decreases in steps of 0.25 to 0 at the vertical $\kappa = 1$ line, along which there is no distortion either. Continuing clockwise, f increases to 1 at the solid blue line, corresponding to maximum flattening in the direction perpendicular to the phase at the radial critical curve. The flattening along the following lines decreases back to 0 along the horizontal axis.

The change in size of the image is given by the absolute value of the product of the two scale factors. Since they are eigenvalues of $\mathbb{A}$, their product is equal to its determinant,

$$\det \mathbb{A}(\boldsymbol{x}) = \lambda_{\parallel}(\boldsymbol{x})\, \lambda_{\perp}(\boldsymbol{x}) = \left\{ \left[1 - \kappa(\boldsymbol{x})\right]^2 - \gamma^2(\boldsymbol{x}) \right\}^{-1} , \tag{A.10}$$

which is the inverse of the Jacobian $\det J(\boldsymbol{x})$ from Equation (3.19). For an image at $\boldsymbol{x}$, the sign of $\det \mathbb{A}(\boldsymbol{x})$ yields the parity and its absolute value $|\det \mathbb{A}(\boldsymbol{x})|$ yields the (point-source) magnification, the ratio of solid angles subtended by the image and by the source. The values of $\det \mathbb{A}$ are indicated by the purple-labeled hyperbolic contours and the color map in Figure A.2. Shades of pink above the critical-curve lines indicate negative $\det \mathbb{A}$, i.e., all images here are mirror images with negative parity. Positive-parity images lie in the green regions below the critical-curve lines.

The origin of the diagram with zero convergence and shear has unit magnification and positive parity, $\det \mathbb{A} = 1$. Proceeding from the origin, contours are plotted for magnifications increasing in powers of two, corresponding to $\det \mathbb{A} \in \{2, 4, 8, 16\}$. Along the solid red and solid blue lines the magnification is infinite; above them the sign of $\det \mathbb{A}$ flips to negative. Going upward from the critical-curve lines, the magnifications along the plotted hyperbolas decrease in powers of two, corresponding to $\det \mathbb{A} \in \{-16, -8, -4, -2, -1, -0.5\}$. The bold black hyperbola passing through the point $(\kappa, \gamma) = (1, 1)$ thus corresponds to unit magnification. All images above it are demagnified. Below the solid blue radial-critical-curve line the sign of $\det \mathbb{A}$ flips back to positive. Proceeding from it to the right, contours are plotted for $\det \mathbb{A} \in \{16, 8, 4, 2, 1, 0.5\}$. The bold black hyperbola passing through the point $(\kappa, \gamma) = (2, 0)$ thus also corresponds to unit magnification. All images to its right are demagnified.

Note that the values of $\lambda_{\parallel}$ along diagonal lines with slope -1 are equal to the value of $\det \mathbb{A}$ at their intersection with the dashed blue line starting from the origin. The values of $\lambda_{\perp}$ along diagonal lines with slope 1 are equal to $-\det \mathbb{A}$ at their intersection with the dashed red line.

The two perpendicular lines in the diagram corresponding to undistorted images differ by the sign of $\det \mathbb{A}$. Images along the horizontal axis (with $\gamma = 0$) have positive parity; they are magnified for $\kappa < 2$ and demagnified for $\kappa > 2$. Images along the vertical bold line (with $\kappa = 1$) are mirror images with negative parity; they are magnified for $\gamma < 1$ and demagnified for $\gamma > 1$. Clearly, the point $(\kappa, \gamma) = (1, 0)$ lying at the intersection of these lines has special significance. At this point, the entire Jacobian matrix given by Equation (3.18) is equal to zero, and its inverse $\mathbb{A}$ is thus undefined. If such points exist in the image plane of a gravitational lens, they define the position of critical-curve umbilic points (Schneider et al. 1992; Paper I). The properties of images in their vicinity depend on higher-order derivatives of the lens equation.

The structure of the CS diagram shows that in the general non-critical case there are four different (κ, γ) combinations that lead to the same combination of $(f, |\det \mathbb{A}|)$, i.e., an image of the same shape and size. Two of these have positive and two have negative parity, as illustrated in Figure 3.3. In the case of zero flattening, there are three different (κ, γ) combinations with only one negative-parity image.

For any specific gravitational lens, the range of $(\kappa(\boldsymbol{x}), \gamma(\boldsymbol{x}))$ combinations occurring in its image plane defines a region in the diagram which demonstrates the properties of all possible images formed by the lens. For a lens with an axially symmetric mass distribution the region is one-dimensional, described by the curve $(\kappa(x), \gamma(x))$ with the radial position x varying from 0 to ∞. For a spherical NFW halo this case is described in Section 3.2.3 and illustrated in Figure 3.4; for a NFW halo with a centrally positioned point mass see the bottom row of Figure 3.9.A. For more asymmetric lenses with a (non-constant) continuous mass distribution, the region in the diagram is two-dimensional, as shown for the spherical NFW halo with an off-center point mass in Figure 3.6 and 3.9.A (except the bottom row).

For lenses consisting of point masses without continuous matter (e.g., stars and stellar systems in Galactic microlensing), the corresponding one-dimensional region is the $\kappa = 0$ vertical axis, with $\gamma \to \infty$ at the positions of the masses and $\gamma \to 0$ far from them. For quasar microlensing, in which point masses are combined with a constant background convergence κ_0 and shear γ_0, the one-dimensional region lies along the $\kappa = \kappa_0$ vertical line. Finally, the regime of weak lensing with $\kappa \ll 1$ and $\gamma \ll 1$ is confined to the vicinity of the origin of the diagram in Figure A.2.